

PENN  
CENTER for  
MUSCULOSKELETAL  
DISORDERS

# 13<sup>th</sup> Annual Scientific Symposium/Retreat

Wednesday, November 9, 2016  
BRB II/III Auditorium and Lobby  
9:00am-5:30pm  
[www.med.upenn.edu/pcmd/](http://www.med.upenn.edu/pcmd/)

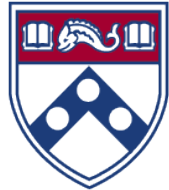
## Table of Contents

	Page
Symposium Agenda.....	1
Penn Center for Musculoskeletal Disorders Components.....	2-13
Center Overview.....	2-3
Core I-Biomechanics.....	4
Core II-Histology.....	5
Core III-MicroCT.....	6
Pilot Grant Program.....	7-10
Visiting Professorship Series.....	11-12
Symposium Participants.....	13-19
Speaker Abstracts.....	20-29
Other Abstracts.....	P1-P67
Biomechanics.....	P1-P16
Histology.....	P17-P28
MicroCT.....	P29-P38
Miscellaneous.....	P39-P67
Notes.....	

We gratefully acknowledge the financial support provided by the National Institute of Arthritis, Musculoskeletal and Skin Diseases of the National Institutes of Health and the University of Pennsylvania Perelman School of Medicine for our Center.



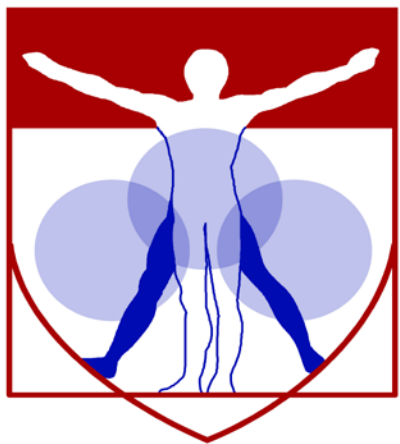
# Penn Center for Musculoskeletal Disorders Scientific Symposium Agenda



November 9, 2016

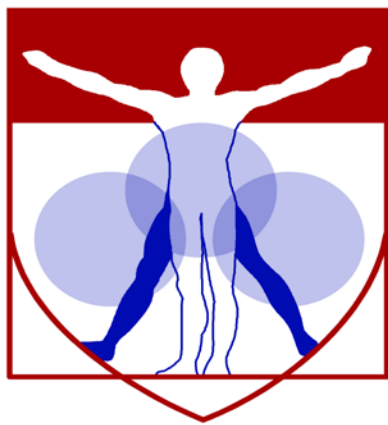
**BRB II/III Auditorium/Lobby ♦ University of Pennsylvania**

9:00 – 10:00am	<b>Registration and Poster Set-up</b>
10:00 – 10:20am	<b>Welcome and Overview</b> <i>Louis Soslowsky, Ph.D.</i>
10:20 – 10:30am	<b>“Histology Core Re-Launch”</b>
10:30 – 11:15am	<b>Session I: New Member Session</b> (Moderator: Lachlan Smith, Ph.D.) <ul style="list-style-type: none"><li>◆ <i>Ellen Casey, M.D. - "Sex Hormones and ACL Injury"</i></li><li>◆ <i>Ronnie Sebro, M.D.- "Statistical Considerations for the Diagnosis of Osteoporosis"</i></li><li>◆ <i>Benjamin Prosser, Ph.D. - “Microtubule Mechanics in Contracting Myocytes”</i></li></ul>
11:15 – 12:00pm	<b>Session II: Affiliate Member Session</b> (Moderator: Ling Qin, Ph.D.) <ul style="list-style-type: none"><li>◆ <i>Karin Silbernagel PT, ATC, Ph.D., University of Delaware - "Patients' Recovery After Tendon Injury"</i></li><li>◆ <i>Gregory Lewis, Ph.D., Penn State College of Medicine - “Simulation-Based Design for Orthopaedic Surgeries”</i></li><li>◆ <i>Mary Barbe, Ph.D., Lewis Katz School of Medicine, Temple - “Substance P Increases Collagen Type I via TGF-β-Dependent and -Independent Pathways in Rat Tenocytes”</i></li></ul>
12:00 – 2:00pm	<b>Poster Session and Lunch (provided) in BRB Lobby</b> <ul style="list-style-type: none"><li>➤ <b>12:40-1:20 Poster Session (Even numbered)</b></li><li>➤ <b>1:20-2:00 Poster Session (Odd numbered)</b></li></ul>
2:00 – 3:00pm	<b>Session III: Pilot Grantee Session</b> (Moderator: Maurizio Pacifici, Ph.D.) <ul style="list-style-type: none"><li>◆ <i>Joshua Baker, M.D., M.S.C.E. - "Intramuscular Fat Accumulation in Rheumatoid Arthritis: A New Perspective on Cachexia"</i></li><li>◆ <i>Foteini Mourkioti, Ph.D. - “Stem Cell Molecular Mechanisms in Chronic Skeletal Muscle Injury”</i></li><li>◆ <i>Russ Carstens, M.D. - “Defining the Roles of Esrp1 Regulated Alternative Splicing in Craniofacial Development”</i></li></ul>
3:00 – 4:00pm	<b>Keynote Speaker</b> (Moderator: Eileen Shore, Ph.D.) <i>"Strategies for Improving Bone Properties in Patients with Osteogenesis Imperfecta."</i> Matthew Warman, M.D., Harriet M. Peabody Professor of Orthopedic Surgery Professor, Department of Genetics, Harvard Medical School Director, Orthopaedic Research Laboratories at Boston Children's Hospital
4:00 – 4:15pm	<b>Final Comments Preceding Poster Session and Reception</b>
4:15 – 5:30pm	<b>Poster Session, Presentation of Poster Awards and Reception in BRB Lobby</b>



PENN  
—  
CENTER for  
MUSCULOSKELETAL  
DISORDERS

# Center Components



PENN  
\_\_\_\_\_  
CENTER for  
MUSCULOSKELETAL  
DISORDERS

# Center Overview

## OVERVIEW OF THE PENN CENTER FOR MUSCULOSKELETAL DISORDERS

**Director:** Louis J. Soslowsky, PhD ([soslowsk@upenn.edu](mailto:soslowsk@upenn.edu))

**Associate Director:** Maurizio Pacifici, PhD ([PacificiM@email.chop.edu](mailto:PacificiM@email.chop.edu))

Musculoskeletal-related conditions in the United States account for 132 million visits to physicians' offices, 29 million visits to emergency rooms, 15 million hospital outpatient visits, and cost over \$850 billion each year. Further, musculoskeletal injuries in the United States cause workers to miss more than 440 million days of work annually. In fact, more than one in four Americans has a musculoskeletal impairment. With the widespread increase in athletic and recreational activities, and the increase of the elderly population at large, these numbers are expected to rise substantially. Musculoskeletal injuries represent a critical health concern which must be better understood and better treated. To do so, a dedicated and focused strategic effort is required that optimizes research translation from the bench to the bedside in an efficient and effective manner.

The Penn Center for Musculoskeletal Disorders (PCMD) will continue to enhance the research productivity of, and provide critical resources and programs to, investigators to address multidisciplinary research strategies for musculoskeletal problems. The overall goal of this Center is to promote cooperative interactions among investigators, accelerate and enrich the effectiveness and efficiency of ongoing research, foster new collaborations and new research, and ultimately, translate our research efforts into better and new therapies for musculoskeletal disorders. The central theme of the Center will continue to be "Musculoskeletal Tissue Injury and Repair". This theme is broad (as it includes all musculoskeletal tissue types, such as bone, cartilage, disc, ligament, meniscus, muscle, and tendon), focused (as takes advantage of commonalities in approaches across tissue types), and clinically significant (as it fosters development of assays, procedures and knowledge in preclinical animal and human models of translational relevance). It is important to note that our PCMD is not a "bone center" nor is it a "muscle center". Rather, it is truly a "musculoskeletal center" and has emerged as the recognized home for musculoskeletal research across the Penn campus and as a technical and intellectual resource for the broader Philadelphia musculoskeletal research community.

One focus of our Center is to translate research themes, approaches, and paradigms that are consistent across different tissues. Musculoskeletal tissues have much in common and their similarities are often overlooked when focus is restricted to a single tissue type. For example, the role of inflammatory cytokines is well studied in several tissue injury and repair scenarios; yet specific findings in one tissue-type are not always known and applied in other tissues. Similarly, the availability of technologies for imaging blood vessel formation in vivo to monitor healing in a given tissue is not always known and available to researchers focusing on other tissues. Given that approaches routinely used to evaluate mechanisms in one tissue could aid researchers in other areas, our Center will work to foster this critical cross-talk.

To provide a further focus for our Center, we will continue to develop programs with an emphasis on small animal models utilizing unique and sophisticated methods that can cross length scales to pre-clinical large animal models and human testing. Although large animal models for many human diseases exist and are essential for translational studies, small animals (e.g., mouse and rat) have become more commonly used for fundamental discovery of disease mechanism and initial therapeutic development due to availability of transgenic and knockout approaches and molecular tools, low cost, ease of handling and housing, and other practical issues. However, performing certain assays and experiments in mice and rats can be challenging and these difficulties often cannot be overcome in single investigator laboratories. The PCMD will provide unique expertise and sophisticated analytical tools to investigate musculoskeletal tissues across length scales.

Thus, the primary overall aims of this Center are to enhance and advance the research productivity of investigators in musculoskeletal tissue injury and repair by:

**Aim 1:** Providing innovation within critical resource core facilities in areas that cross disciplines, length scales, and hierarchies. These core facilities are µCT Imaging, Biomechanics, and Histology.

**Aim 2:** Developing a pilot and feasibility grant program for investigators, with direct mentorship, whereby new approaches, ideas, and collaborations can be developed prior to seeking extramural funding.

**Aim 3:** Developing educational and research enrichment programs spanning tissue types, research approaches, and paradigms, through which members can learn from national leaders and from each other.

High quality musculoskeletal research is currently being conducted by many groups at Penn. While many bring sophisticated approaches to bear on musculoskeletal problems, few groups have the required expertise and facilities to perform high quality and specialized assays in their own labs. Furthermore, most investigators are not aware of approaches utilized, and results obtained, in other tissues that may have direct relevance on their research questions. Ultimately, close cooperation, communication, and collaboration among researchers across musculoskeletal tissue types and from a wide variety of disciplines will significantly enhance the research of our members. The Center will provide opportunities to integrate multi-disciplinary techniques to determine mechanisms for tissue function, injury, degeneration, repair, and regeneration, with the ultimate goal of advancing the diagnosis, treatment, and prevention of diseases and injuries of the musculoskeletal system.

In addition to the specific features described in this proposal, there is an intangible feature of our Center that should not be overlooked. Although our musculoskeletal program is strong nationally, the Penn biomedical research community is large and diverse. As such, the Center serves as an essential mechanism to highlight our successes and the importance and excitement of musculoskeletal research across campus, as well as to institutional leadership. Having a strong voice for musculoskeletal researchers is critical to support our collective and individual research goals. In these ways, the Center - with essential support from the P30 - has become and remains an indispensable resource and advocate for our community.



PENN  
CENTER for  
MUSCULOSKELETAL  
DISORDERS

## Core I

# Biomechanics

## Biomechanics Core

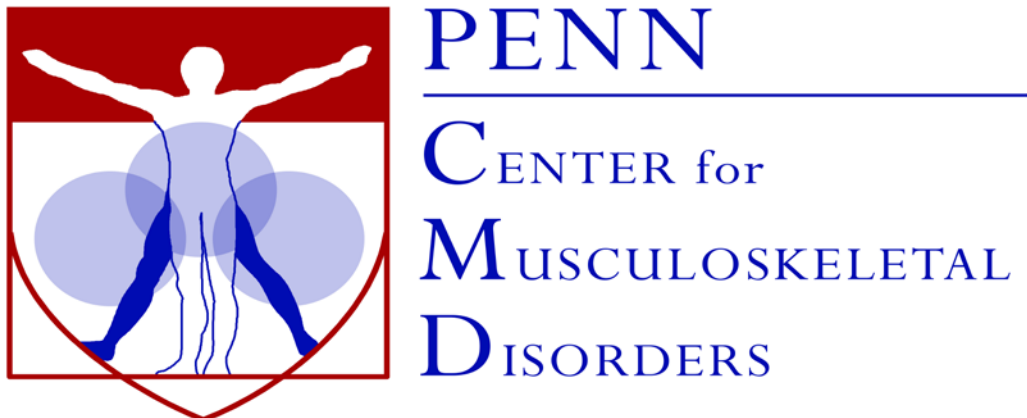
**Core Director:** Robert Mauck, Ph.D. ([lemauck@mail.med.upenn.edu](mailto:lemauck@mail.med.upenn.edu))

**Technical Director:** Snehal Shetye, Ph.D. ([shetye@upenn.edu](mailto:shetye@upenn.edu))

The overall objective of the Biomechanics Core is to develop and provide a wide range of innovative biomechanical approaches to evaluate musculoskeletal tissue function in the context of damage, repair, and regeneration, and to provide training and funding for new projects and collaborations utilizing these assays. Over the last decade, our Biomechanics Core at the Penn Center for Musculoskeletal Disorders (PCMD) has grown into a thriving resource for the University of Pennsylvania and Philadelphia area musculoskeletal research community. In this submission, we will further expand our services to meet the increased demand for specialized techniques and develop new and innovative methods that address the multi-scale mechanics of musculoskeletal tissues. These developments will provide customized services that enhance the research productivity of our members. The Specific Aims of the Biomechanics Core are:

- To provide guidance and training on the capabilities, advantages, and disadvantages of the various methodologies to assess musculoskeletal tissue biomechanical function through formal educational enrichment programs and one-on-one interactions
- To provide expertise and service for biomechanical assays of musculoskeletal tissues
- To develop innovative biomechanical testing techniques that will be applicable to Musculoskeletal research, and in particular those that provide information across tissue length scales
- To provide funding for the development of new projects and collaborations and to develop preliminary and/or feasibility data for investigators.

Successful completion of these aims will significantly enhance the environment and the capabilities of researchers at the University of Pennsylvania, leading to new approaches to address musculoskeletal disorders and new collaborations between Center faculties who may have not previously included biomechanical function approaches in their musculoskeletal research programs.



PENN  
CENTER for  
MUSCULOSKELETAL  
DISORDERS

Core II

Histology

## Histology Core

**Co-Directors:** **Lachlan Smith, Ph.D.** ([lachlans@mail.med.upenn.edu](mailto:lachlans@mail.med.upenn.edu))  
**Ling Qin, Ph.D.** ([qinling@mail.med.upenn.edu](mailto:qinling@mail.med.upenn.edu))

The structure and composition of musculoskeletal tissues are tailored to meet their demanding functions. With injury, aging, and specific diseases, the structure and composition of these tissues deteriorate, resulting in a decline or loss of biological, phenotypic and mechanical function and properties. Musculoskeletal tissues each have a wide array of compositional and structural variety with respect to cellular components, microarchitecture, and extracellular matrix constituents. Careful description and quantification of tissue structural organization and composition, as well as localization and identification of secreted factors, are necessary requirements for elucidation of the biologic mechanisms underlying musculoskeletal integrity, injury, and repair. The overall objective of this Histology Core (HC) is to utilize and develop a wide range of standard and innovative histological and histomorphometric approaches to evaluate musculoskeletal tissue injury and repair, and to provide training and funding for new projects and collaborations utilizing these assays.

There is an increasing demand for specialized histological techniques, development of new histomorphological methods, and customization of histological approaches to musculoskeletal-based problems. The need for these approaches is ever-broadening due to the recognition that many musculoskeletal disorders can affect other systems (indirectly, including muscle, bone, and other connective structures). In addition, some pathologies are true multisystem disorders that also affect musculoskeletal tissues. Thus, investigators whose interests were initially focused on non-musculoskeletal pathology now also require access to the advice and services provided by the HC. In addition, with the proliferation of new animal models, it is critical to be able to characterize their musculoskeletal phenotype, whether it is primarily or secondarily affected by a genetic disorder or other type of musculoskeletal insult..

The Specific Aims of the Histology Core are to:

- To provide guidance and training on the capabilities, advantages, and disadvantages of the various methodologies to assess musculoskeletal tissue structure and composition through formal educational enrichment programs and one-on-one interactions
- To provide high-quality expertise and service for histological and histomorphometric assays of musculoskeletal tissues
- To develop new and innovative histologically-based techniques that will be applicable to musculoskeletal research
- To provide funding for development of new projects and collaborations and to develop preliminary and/or feasibility data for investigators.

Successful completion of these aims will significantly enhance the environment and the capabilities of researchers in the Penn Center for Musculoskeletal Disorders at the University of Pennsylvania (Penn), leading to new approaches to address musculoskeletal disorders and new collaborations between Center faculty who may have not previously included structural and compositional approaches through histological examination in their musculoskeletal research programs.



PENN  
—  
CENTER for  
MUSCULOSKELETAL  
DISORDERS

Core II

MicroCT

## MicroCT Core

**Director: Felix Wehrli, Ph.D.** ([wehrli@mail.med.upenn.edu](mailto:wehrli@mail.med.upenn.edu))

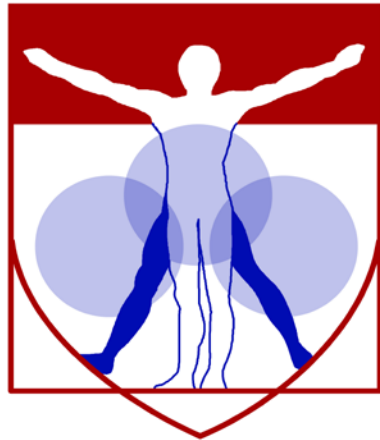
**Associate Director: X. Sherry Liu, Ph.D.** ([xiaowei@mail.med.upenn.edu](mailto:xiaowei@mail.med.upenn.edu))

The development of high-resolution micro-CT ( $\mu$ CT) during the past two decades has revolutionized the quantitative assessment of calcified and X-ray dense tissue morphology. With the capability of non-destructive, three-dimensional (3D) visualization of tissue structure,  $\mu$ CT has largely supplanted traditional histomorphometry and become a gold standard for calcified tissue density and microstructure evaluation for many measures. Due to the low intrinsic X-ray contrast of non-mineralized tissues, traditional applications of  $\mu$ CT in musculoskeletal research have been limited to mineralized tissue. However, the development of contrast-enhanced imaging methods has greatly broadened applications of  $\mu$ CT to include musculoskeletal soft tissues as well. These cutting-edge image-based quantification methods not only enable characterization of soft-tissue morphology, but some also yield insight into tissue composition, such as glycosaminoglycan (GAG) density, which is associated with soft-tissue function and mechanics. Another important advance in the past decade is in vivo  $\mu$ CT imaging of living small animals. Research of musculoskeletal tissue injury and repair has been progressively utilizing animal models of human disease. Unlike many assays that require sacrificing the animal to extract tissues for analysis, in vivo  $\mu$ CT enables longitudinal evaluation of changes in a particular animal non-invasively over time. This new imaging strategy minimizes the number of animals required while enhancing statistical power. With these developments,  $\mu$ CT can now provide a deep and quantitative understanding of the genetic influences on the skeleton, as well as remodeling events in hard and soft tissues during repair, treatment, and with altered loading scenarios. Further, a  $\mu$ CT modality for clinical imaging of calcified tissue microstructure, called high-resolution peripheral quantitative CT (HR-pQCT), has recently been developed. This technology inaugurated a new era of non-invasive quantitative skeletal imaging, and has become a powerful tool for clinical research of musculoskeletal disorders. The overall objective of the  $\mu$ CTIC is to offer a wide range of  $\mu$ CT imaging approaches to evaluate musculoskeletal tissue injury and repair, and to provide training and consultation for new projects and collaborations utilizing these assays.

The Specific Aims for the  $\mu$ CTIC are:

- To provide guidance and expertise on the use of  $\mu$ CT imaging for musculoskeletal research through educational enrichment programs and one-on-one interactions
- To provide a range of  $\mu$ CT imaging resources, expertise, and services for the study of the structure, function and physiology of the musculoskeletal system in laboratory animals and humans
- To develop new  $\mu$ CT imaging-based techniques that will be applicable to musculoskeletal research
- 4) To provide funding for the development of new projects and collaborations and to develop preliminary and/or feasibility data for investigators.

Successful completion of these Aims will significantly enhance the environment and capabilities of researchers at the University of Pennsylvania, leading to novel and innovative approaches to address musculoskeletal disorders and to new collaborations between Core faculty who may not have previously included human and/or animal imaging in their musculoskeletal research programs.



PENN  
CENTER for  
MUSCULOSKELETAL  
DISORDERS

---

## Pilot Grant Program

## **PENN CENTER FOR MUSCULOSKELETAL DISORDERS PILOT AND FEASIBILITY GRANT PROGRAM**

The Penn Center for Musculoskeletal Disorders has an ongoing Pilot and Feasibility Grant Program. Submissions should be related to musculoskeletal tissue injury and repair which is the broad focus of the Center and Grants are only eligible for Center members (if you are not a member but would like to become one, please contact [pcmd@mail.med.upenn.edu](mailto:pcmd@mail.med.upenn.edu)). For more information on our Cores and Center in general, please see our web site at [www.med.upenn.edu/pcmd](http://www.med.upenn.edu/pcmd). We are anticipating that the next Center grant submission deadline will be in Spring 2017.

### Eligibility

- Only Full Center members are eligible. If you are not currently a member, please go to the link: <http://www.med.upenn.edu/pcmd/memberinfo.shtml>
- Categories of applicants include: 1) Established investigators with a proposal to test the feasibility of a new or innovative idea in musculoskeletal tissue injury and repair representing a clear and distinct departure from their ongoing research, 2) Established investigators with no previous work in musculoskeletal tissue injury and repair interested in testing the applicability of their expertise on a problem in this area, and 3) New investigators without significant extramural grant support as a Principal Investigator to develop a new project.
- Pilot and Feasibility Grants must use at least one of the Center's Research Cores.
- Pilot project awardees are eligible for one year, with a second year to be considered (budgets will be for \$20-50,000 per year and timelines should be for one or two years). The second year of funding, the dollar amount of which would only be for up to half the year one budget, will be considered based on the progress report submitted after the first year of funding and funding availability in the Center. Please note that second year funding will often not be awarded, and when awarded, will be done so primarily to new investigators; second year funding to senior investigators will be quite rare.
- It is expected that these Pilot grants will lead to funding through other independent, extramural mechanisms. Therefore, the likelihood of future extramural funding will enter into the evaluation of these proposals.

### Format

- Applications should be formatted loosely in the style of an NIH R03 grant (<http://grants.nih.gov/grants/guide/pa-files/PA-13-304.html>). The main body of the application (Specific Aims through Research Design and Methods-sections 4-7 below) is limited to five pages. The application should be in a single pdf file. The format should be:

- 1) Cover Page (not NIH face page) with grant title, PI name (and co-PI name if applicable), affiliation, contact information
- 2) Budget and brief justification (note that equipment is not allowed)
- 3) NIH Biosketch of PI (and co-PI if applicable)
- 4) Specific Aims
- 5) Significance
- 6) Innovation
- 7) Approach
- 8) Brief Statement of Category of Investigator per guidelines above
- 9) Brief Statement of How this Funding will lead to other Extramural Funding
- 10) Human Subjects and/or Vertebrate Animal Subjects (if applicable)
- 11) Consultants (if applicable)
- 12) Literature Cited
- 13) Certification of Patient Oriented Research (if applicable)

Please do not hesitate to email [pcmd@mail.med.upenn.edu](mailto:pcmd@mail.med.upenn.edu) with any questions or comments.

**Penn Center for Musculoskeletal Disorders Pilot & Feasibility Grants**  
**(all grants awarded since inception of Center)**

**Awarded 2016-2017**

Joseph Baur, Ph.D., Assistant Professor of Physiology Institute for Diabetes, Obesity and Metabolism, “Targeting NAD metabolism in muscular dystrophy”

Yongwon Choi, Ph.D. Leonard Jarett Professor of Pathology and Lab Medicine, “Cell adhesion regulation of multiple-myeloma induced bone destruction”

X. Sherry Liu

Assistant Professor of Orthopaedic Surgery and Bioengineering, “Mechanical Consequences of Modeling- vs. Remodeling-Based Bone Formation”

Hongtao Zhang, Ph.D., Research Assistant Professor, Department of Pathology and Lab Medicine, “Novel cartilage-targeting Fc fusion proteins as novel and effective treatments for osteoarthritis”

**Awarded 2015-2016**

Yejia Zhang, MD, PhD, Department of Physical Medicine and Rehabilitation, “Inhibition of ADAM-8 to reduce intervertebral disc degeneration”

Oren Friedman, MD, Department of Otorhinolaryngology, “Effect of injury to cartilage and recovery treatment with FGF-18”

Harvey Smith, MD, Department of Orthopaedic Surgery, “Impact of Pre-Culture and In Vivo Remobilization on Engineered Disc Replacement”

Tejvir Khurana, MD, PhD, Department of Physiology, “Role of the IL-15 / IL-15R $\alpha$  axis in modulating muscle-tendon-bone adaptation and repair”

**Awarded 2014-2015**

Joshua F. Baker, MD, MSCE, Department of Rheumatology & Epidemiology/Perelman School of Medicine: “Assessment of Intramyocellular Fat Accumulation in Rheumatoid Arthritis Using MR Spectroscopy”

Russ P. Carstens, MD, Department of Renal-Electrolyte and Hypertension Division, Perelman School of Medicine: “Roles of Epithelial Splicing Regulatory Proteins in Craniofacial Development” (*awarded extramural funding from the NIH 1R56DE024749 and awarded R01 NIDCR*)

Foteini Mourkioti, PhD, Department of Orthopaedic Surgery/Perelman School of Medicine: “A Novel Molecular Mechanism in Chronic Skeletal Muscle Injury” (*supported in part from the IRM*)

Chamith Rajapakse, PhD, Department of Radiology/Perelman School of Medicine: “Biomechanics of Hip Fracture Assessed by MRI”

**Awarded 2013-2014**

X. Sherry Liu, PhD, Department of Orthopaedic Surgery, Perelman School of Medicine: “Structure and Strength Recovery in Post-Lactation Bone” (*awarded extramural funding from the NIH R03 AR065145*)

Ling Qin, Ph.D., Department of Orthopaedic Surgery, Perelman School of Medicine: “Novel Anabolic Treatment for Radiation-Induced Osteoporosis” (*awarded extramural funding from the NIH R01AR066098*)

Lachlan Smith, Ph.D. Department of Orthopaedic Surgery, Perelman School of Medicine: “Molecular Mechanisms of Failed Vertebral Bone Formation in Mucopolysaccharidosis VII” (*awarded extramural funding from the NIH R03 AR065142 and the MPS Society*)

Hansell H. Stedman, MD, Department of Surgery, Perelman School of Medicine: “Molecular Pattern Recognition in Acute and Chronic Injury to Muscle and Myotendinous Junction” (*awarded extramural funding from the NIH R01NS094705*)

#### **Awarded 2012-2013**

Jason Burdick, PhD, Department of Bioengineering, School of Engineering and Applied Science: “Acellular Fibrous Scaffolds for Stem Cell Recruitment and Cartilage Repair” (*awarded extramural funding from the NIH R01 EB008722*)

James L. Carey, MD, MPH, Department of Orthopaedic Surgery, Perelman School of Medicine: “Development of a Large Animal Model of Osteochondritis Dissecans” (*awarded extramural funding from the NIH R01 EB008722*)

Andrew Kuntz, MD, Department of Orthopaedic Surgery, Perelman School of Medicine: “Effects of Intra-Articular Glenohumeral Injection of a Nonsteroidal Anti-Inflammatory Drug on Shoulder Joint Mechanics in a Rat Model”

Arjun Raj, PhD, Department of Bioengineering, School of Engineering and Applied Science: “Single Cell Analysis of Molecular and Micromechanical Heterogeneity in Mesenchymal Stem Cells and Engineered Tissues”

#### **Awarded 2011-2012**

Struan F.A. Grant, PhD, Department of Pediatrics, Children’s Hospital of Philadelphia and Perelman School of Medicine: “Utilization of ChIP-seq to Identify Genes Regulated by Osterix”

Motomi Enomoto-Iwamoto, DDS, PhD, Department of Orthopaedic Surgery, Children’s Hospital of Philadelphia and Perelman School of Medicine: “Tendon Repair by Retinoic Acid Receptor Agonists” (*awarded extramural funding from the NIH R21 AR062193*)

Ian N. Jacobs, MD, Department of Otorhinolaryngology: Head and Neck Surgery, Children’s Hospital of Philadelphia and Perelman School of Medicine: “A Pilot Study for the Development of a Rabbit In-Vivo Tissue- Engineered Cartilage Graft for Pediatric Laryngotracheal Reconstruction” (*awarded extramural funding from The Triological Society*)

#### **Awarded 2010-2011**

Susan W. Volk, VMD, PhD, Dipl ACVC, Department of Small Animal Surgery, School of Veterinary Medicine: “The Role of Type III Collagen in Bone Repair and Regeneration”

Jaimo Ahn, MD, PhD, Department of Orthopaedic Surgery, Perelman School of Medicine: “Toward the Identification of Molecular Pathway Alterations in Aged Fracture Healing: A Pilot Study Utilizing a Genetic Model of Senescence” (*awarded extramural funding from the NIH R03 AG040670*)

Shannon Fisher, MD, PhD, Department of Cell and Developmental Biology, Perelman School of Medicine: “Requirement for Osterix in Skull Formation and Maintenance of Adult Bone in Zebrafish” (*awarded extramural funding from the NIH R21 DE021509*)

#### **Awarded 2010-2011 (Jointly with IOA)**

Olena Jacenko, PhD, Department of Animal Biology, School of Veterinary Medicine: “Aging of the hematopoietic niche” (*awarded extramural funding from the NIH R01 DK088334-01*)

Eileen M. Shore, PhD, Departments of Orthopaedic Surgery and Genetics, Perelman School of Medicine: “Modulation of Progenitor Cell Differentiation through BMP Signaling” (*awarded extramural funding from the NIH R01 AR041916-15*)

Kurt D. Hankenson, DVM, PhD, Department of Animal Biology, School of Veterinary Medicine: “Notch Signaling in Bone Regeneration” (*awarded extramural funding from the DOD CDMRP*)

#### **Awarded 2009-2010**

Ling Qin, PhD, Department of Orthopaedic Surgery, Perelman School of Medicine: “Mechanisms of EGFR Action on Bone” (*awarded extramural funding from the NIH R01 DK095803*)

Steven Scherer, MD, PhD, Department of Neurology, Perelman School of Medicine: “Are N-cadherin and L1 Adhesion Molecules Required for Recovery of Muscle Strength after Nerve Injury?”

Nader M. Hebel, MD, Department of Orthopaedic Surgery, Perelman School of Medicine: “A Pre-Clinical Rodent Model of Intervertebral Disc Autograft Transplant” (*awarded extramural funding from the DOD/CDMRP/PROP OR090090*)

#### **Awarded 2008-2009**

Sunday O. Akintoye, BDS, DDS, MS, Department of Oral Medicine, School of Dental Medicine: “Orofacial Bone Marrow Stromal Cells Promote Bisphosphonate-Associated Jaw Osteonecrosis” (*awarded extramural funding from the NIDCR R21 DE022826*)

Margaret M. Chou, PhD, Departments of Cell and Developmental Biology, Perelman School of Medicine: “Mechanisms of TRE17/USP6 Function in the Etiology of Aneurysmal Bone Cyst” (*awarded extramural funding from the NIH-NCI R01 CA168452 and R21-CA18601*)

Kenneth W. Leichty, MD, Department of Surgery, Perelman School of Medicine: “The Role of Inflammation in Regenerative Fetal Tendon Wound Healing” (*awarded extramural funding from the NIH DP2 DK083085*)

Kathleen M. Loomes, MD, Department of Pediatrics, Children’s Hospital of Philadelphia: “The Role of Jag1 in Osteogenesis”

Eileen M. Shore, PhD, Departments of Orthopaedic Surgery and Genetics, Perelman School of Medicine: “Analysis of an ACVR1 Knock-in Mouse Model for FOP” (*awarded extramural funding from the NIH R01 AR041916-15S1*)

#### **Awarded 2007-2008**

Sherrill L. Adams, PhD, Department of Biochemistry, School of Dental Medicine: “Collagen III-deficient Mice as a Model for Musculoskeletal Wound Repair”

Kurt D. Hankenson, DVM, PhD, Department of Animal Biology, School of Veterinary Medicine: “Regulation of Bone Formation by Novel Activators of Canonical Wnt Signaling”

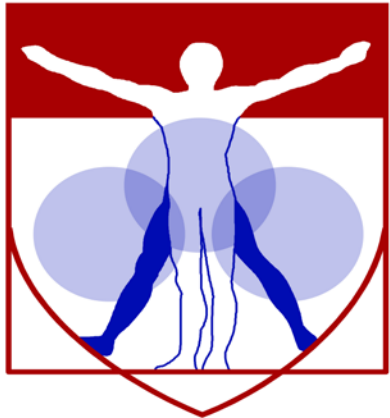
#### **Awarded 2006-2007**

Robert J. Pignolo, MD, PhD, Department of Medicine, Perelman School of Medicine: “Stem Cell Rescue of the Osteoporotic Phenotype in a Mouse Model of Accelerated Aging” (*awarded extramural funding from the NIH R01 AG028873*)

Robert L. Mauck, PhD, Department of Orthopaedic Surgery, Perelman School of Medicine “Meniscus Repair with a Novel Aligned Nanofiber Scaffold” (*awarded extramural funding from the NIH R01 AR056624 and the VA RR & D*)

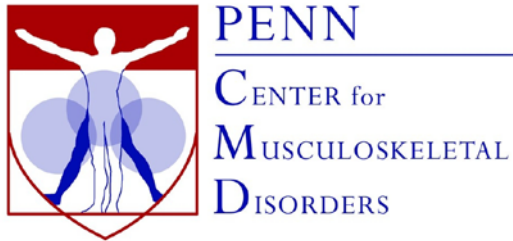
Christopher S. Chen, MD PhD, Department of Bioengineering, School of Engineering and Applied Science: “Mechanotransduction in Mesenchymal Stem Cells” (*awarded partial funding as Co-Investigator on NIH P41 EB001046*)

Pedro K. Beredjiklian, MD, Department of Orthopaedic Surgery, Perelman School of Medicine: “Role of Hyaluronic Acid Receptors in Tendon Healing” (*awarded extramural funding from the NIH R21 AR052393*)



PENN  
CENTER for  
MUSCULOSKELETAL  
DISORDERS

Visiting  
Professorship Series  
**2016-2017**



## Visiting Professorship Series-Academic Year 2016-2017

### Tuesday, September 20, 2016, 1:30-2:30pm/JMB Class of '62 Auditorium

Mechanisms of Chondroprotection by TGF- $\beta$ .

Rosa A. Serra, PhD

Professor, Department of Cell, Developmental and Integrative Biology

University of Alabama at Birmingham

### Tuesday, October 25, 2016, 1:30-2:30pm/ CRB Austrian Auditorium

Musculoskeletal Adaptation to Space Flight.

Henry J. Donahue PhD

Professor and Chair, Department of Biomedical Engineering

Virginia Commonwealth University, Richmond

### ANNUAL SCIENTIFIC SYMPOSIUM (all day event)

#### Wednesday, November 9, 2016, 9:00-5:30pm/BRB Auditorium

Title: *Strategies for Improving Bone Properties in Patients with Osteogenesis Imperfecta*

Matthew Warman, MD

Professor, Department of Genetics, Harvard Medical School

### Tuesday, December 13, 2016, 1:30-2:30pm/ CRB Austrian Auditorium

Osteocytes and Bone Remodeling: They're Just Dying to do the Job.

Mitchell B. Schaffler, PhD

CUNY and Wallace Coulter Distinguished Professor of Biomedical Engineering

Chairman, Department of Biomedical Engineering

The City College of New York, City University of New York

### Tuesday, January 10, 2017, 1:30-2:30pm/CRB Austrian Auditorium

Studying Bone as a Complex Adaptive System Reveals Inter-Individual Differences in Skeletal Growth and Aging.

Karl Jepsen, PhD

Professor, Associate Chair of Research, Department of Orthopaedic Surgery

University of Michigan

### Tuesday, February 7, 2017, 1:30-2:30pm/CRB Austrian Auditorium

Cell-independent Manipulation of Bone Matrix Properties: A Novel Treatment Strategy for Osteoporosis and Type 2 Diabetes.

David Burr, PhD Professor of Anatomy & Cell Biology Professor, Department of Biomedical Engineering

Indiana University

### Tuesday, March 14, 2017, 1:30-2:30pm/CRB Austrian Auditorium

Title TBD

Linda Sandell, PhD, Mildred B. Simon Research Professor and Director of Research

Washington University

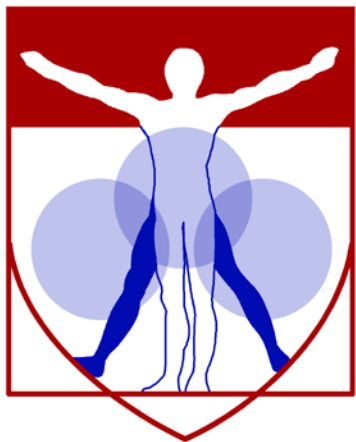
### Tuesday, April 4, 2017, 1:30-2:30pm/CRB Austrian Auditorium

**Title TBD**

Laurie Goodrich, CVM, PhD, Associate Professor of Orthopaedics, Department of Clinical Sciences.  
Colorado State University

**Tuesday, May 2017 TBD**

**Tuesday, June 2017 TBD**



PENN  
CENTER for  
MUSCULOSKELETAL  
DISORDERS

---

# Symposium Participants

Last Name	First Name	Email	Affiliation
Abdul Majeed	Saif	abmajeed@upenn.edu	Penn Dental
Agnello	Kimberly	kagnello@vet.upenn.edu	Penn Vet Clinical Studies
Ailavajhala	Ramya	tub58807@temple.edu	Temple Bioengineering
Alavi	Abass	Abass.alavi@uphs.upenn.edu	Penn Radiology
Allen	Robyn	roallen@vet.upenn.edu	Penn DSRB
Alvarez-Urena	Pedro	pedroau@seas.upenn.edu	Penn Bioengineering
Arany	Zolt	zarany@mail.med.upenn.edu	Penn Cardiology
Ashley	Blair	blair.ashley@uphs.upenn.edu	Penn Ortho
Baker	Joshua	joshua.baker@uphs.upenn.edu	Penn Rheumatology/Epidemiology
Bansal	Sonia	soniab@seas.upenn.edu	Penn Bioengineering
Barbe	Mary	mary.barbe@temple.edu	Temple Univ Anatomy & Cell Biology
Barnum	Carrie	carrie.barnum@gmail.com	Penn Ortho
Baxter	Josh	josh.baxter@uphs.upenn.edu	Penn Ortho
Beach	Zakary	zbeach@seas.upenn.edu	Penn Ortho
Bendigo	Justin	jbendigo@mail.med.upenn.edu	Penn Ortho
Billings	Paul	BillingsP@email.chop.edu	CHOP Ortho
Bonnevie	Eddie	edbon@mail.med.upenn.edu	Penn Ortho
Boorman-Padgett	James	jboorm@mail.med.upenn.edu	Penn Ortho
Brewer	Niambi	nbrewer@mail.med.upenn.edu	Penn Ortho
Carey	James	james.carey@uphs.upenn.edu	Penn Ortho
Caron	Robert	raron@mail.med.upenn.edu	Penn Ortho
Carstens	Russ	russcars@upenn.edu	Penn Renal Electrolyte & Hypertension
Casey	Ellen	Ellen.Casey@uphs.upenn.edu	Penn Physical Medicine & Rehabilitation
Chakkalakal	Salin	salin.chakkalakal@gmail.com	Penn Ortho
Chang	Ting-Han	tinch@upenn.edu	Penn Dental Oral Medicine
Chen	Dongning	dongning@seas.upenn.edu	Penn Bioengineering
Chen	Mengcun	chenmc0603@gmail.com	Penn Ortho
Chery	Daphney	dchery88@gmail.com	Drexel University
Chin	LiKang	likangc@upenn.edu	Penn Gastroenterology
Chin	Matthew	mattchin@upenn.edu	Penn Ortho
Convente	Michael	mconvente@gmail.com	Penn Ortho
Cosgrove	Brian	bdcosgro@gmail.com	Penn Ortho
Cousminer	Diana	cousminerd@email.chop.edu	CHOP Human Genetics

de Bakker	Chantal	chantald@seas.upenn.edu	Penn Ortho
Dekhne	Mihir	mdekhne@sas.upenn.edu	Penn Ortho
Dinella	Susan	sdinella@mail.med.upenn.edu	Penn Ortho
Dodge	George	gdodge@mail.med.upenn.edu	Penn Ortho
Dong	Guangyu	gdong@upenn.edu	Penn Dental Perio
Doolittle	Alexandra	acdoolittle@gmail.com	Thomas Jefferson Univ Cell & Regenerative Medicine
Enomoto-Iwamoto	Motomi	iwamotom1@email.chop.edu	CHOP Ortho
Esterhai	John	john.estherhai@uphs.upenn.edu	Penn Ortho
Farber	Daniel	Daniel.farber@uphs.upenn.edu	Penn Ortho
Feldman	George	george.feldman@jefferson.edu	Thomas Jefferson Univ Ortho
Fong	John	johnfong@alumni.upenn.edu	Penn Ortho
Francois	Noelle	francoisn@email.chop.edu	CHOP Ortho
Frara	Nagat	tuc36797@temple.edu	Temple Univ Anatomy/Cell Biology
Freedman	Benjamin	freedman.br@gmail.com	Penn Ortho
Freeman	Theresa	theresa.freeman@jefferson.edu	Thomas Jefferson Univ Ortho
Fryhofer	George	fryhofer@upenn.edu	Penn Ortho
Galarraga	Jonathan	jgala@seas.upenn.edu	Penn Bioengineering
Ganley	Theodore	ganley@email.chop.edu	CHOP Ortho
Gittings	Daniel	daniel.gittings@uphs.upenn.edu	Penn Ortho
Goel	Peeyush	pgoel@upenn.edu	Penn Ortho
Gong	Yanqing	gongy@mail.med.upenn.edu	Penn Medicine
Gravare Silbernagel	Karin	kgsilbernagel@gmail.com	Univ of Delaware Physical Therapy
Gui	Jianman	asdmxwin@gmail.com	Penn Ortho
Gullbrand	Sarah	selinley516@gmail.com	Penn Ortho
Hamilton	Amber	amber@sas.upenn.edu	Penn Ortho
Han	Biao	bh462@drexel.edu	Drexel Univ Biomedical Engineering
Han	Lin	lh535@drexel.edu	Drexel Univ Biomedical Engineering
Hast	Michael	hast@upenn.edu	Penn Ortho
Hebb	John	johnhebb@mail.med.upenn.edu	Penn Ortho
Henning	Elizabeth	ehenning@mail.med.upenn.edu	Penn Ortho
Heo	Su Chin	heosc@mail.med.upenn.edu	Penn Ortho
Huegel	Julianne	jhuegel08@gmail.com	Penn Ortho
Hullfish	Todd	Todd.Hullfish@uphs.upenn.edu	Penn Ortho
Hume	Eric	eric.hume@uphs.upenn.edu	Penn Ortho

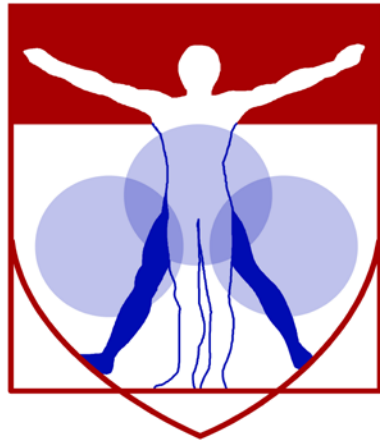
Ita	Meagan	meita@seas.upenn.edu	Penn Bioengineering
Iwamoto	Masahiro	iwamotom@email.chop.edu	CHOP Ortho
Izumi	Sohtaroh	rousai12330472@yahoo.co.jp	CHOP Surgery
Jacenko	Olena	jacenko@vet.upenn.edu	Penn Biomedical Sciences
Jadhav	Gaurav	jgaurav@upenn.edu	Penn Dental Anatomy & Cell Biology
Jiang	Xi	jiangxi@mail.med.upenn.edu	Penn Ortho
Johncola	Alyssa	johncola@sas.upenn.edu	Penn Radiology
Kandel	Shital	shitalkandel@gmail.com	Temple Univ Bioengineering
Kaplan	Fred	Frederick.Kaplan@uphs.upenn.edu	Penn Ortho
Karchner	James	james.karchner@temple.edu	Temple Univ Bioengineering
Karnawat	Vishakha	vishakha.karnawat@gmail.com	Penn Physiology
Kartha	Sonia	skartha@seas.upenn.edu	Penn Bioengineering
Kelly	John	john.kelly@uphs.upenn.edu	Penn Ortho
Khoury	Viviane	viviane.khoury@hotmail.com	Penn Radiology
Khurana	Tejvir	tsk@mail.med.upenn.edu	Penn Physiology
Kim	Minwook	kimminw@mail.med.upenn.edu	Penn Ortho
Kim	Dong Hwa	kimd1@mail.med.upenn.edu	Penn Ortho
Klyne	David	d.klyne@uq.edu.au	The University of Queensland
Kneeland	John	bruce.kneeland@uphs.upenn.edu	Penn Radiology
Knight	M. Noelle	mkni@vet.upenn.edu	Penn Vet Ortho
Kobe	Elizabeth	ekobe@seas.upenn.edu	Penn Bioengineering
Koyama	Eiki	koyamae@email.chop.edu	CHOP Orthopaedic Research
Krach	Michelle	Michelle.Krach@uphs.upenn.edu	Penn Ortho
Kuntz	Andrew	andrew.kuntz@uphs.upenn.edu	Penn Ortho
Kwon	Mi	mi.michelle.kwon@gmail.com	Penn Bioengineering
Lawrence	John	lawrencej@email.chop.edu	CHOP Ortho
Lazar	Sophie	sophie.lazar@temple.edu	Temple Univ Medicine
Lei	Hong	hong.lei@jefferson.edu	Thomas Jefferson University
Leiphart	Ryan	rleip@seas.upenn.edu	Penn Bioengineering
Levin	L. Scott	scott.levin@uphs.upenn.edu	Penn Ortho
Lewis	Gregory	glewis1@hmc.psu.edu	Pennsylvania State Univ Ortho & Rehabilitation
Li	Yihan	yiharl@seas.upenn.edu	Penn Bioengineering
Li	Qing	ql55@drexel.edu	Drexel Univ Biomedical Science
Lim	Jormay	jormay@upenn.edu	Penn Dental Anatomy & Cell Biology
Linardi	Renata	rlinardi@upenn.edu	Penn Vet Clinical Studies

Liu	Min	lium4@email.chop.edu	CHOP Ortho
Liu	Yang	liuyang2@upenn.edu	Penn Ortho
Liu	Sherry	xiaowei@mail.med.upenn.edu	Penn Ortho
Loebel	Claudia	loebelcl@seas.upenn.edu	Penn Ortho
Loro	Emanuele	eloro@mail.med.upenn.edu	Penn Physiology
Lounev	Vitali	vlounev@mail.med.upenn.edu	Penn Ortho
Lu	Ming	luming.chop.upenn@gmail.com	CHOP Ortho
Ma	Xiaoyuan	asd-maxiaoyuan@163.com	Penn Ortho
Mandalapu	Sai	saiman@sas.upenn.edu	Penn Ortho
Mao	Qin	maoqin@upenn.edu	Penn Dental Oral Surgery
Martin	Viviane	martinv@upenn.edu	Penn Center for Innovation
Martinez	Jerahme	jerahme@udel.edu	Univ of Delaware Mechanical Engineering
Mascareno	Rachel	mascarenor@email.chop.edu	CHOP Ortho
Matalon	Dena	matalond@email.chop.edu	CHOP Genetics
Matsuoka	Masatake	MATSUOKAM@email.chop.edu	CHOP Ortho
Mauck	Robert	lemauck@mail.med.upenn.edu	Penn Ortho
McCarrick-Walmsley	Ruth	rwalmsle@mail.med.upenn.edu	Penn Ortho
McGinnis	Kelly	Kellymm@upenn.edu	Penn Ortho
McHugh	Christian	ctmhugh@udel.edu	Penn Radiology
McLeod	Claire	cm.mcleod@gmail.com	Penn Ortho
Mellor	Xochitl	mellorx@email.chop.edu	CHOP Ortho
Millar	Sarah	millars@mail.med.upenn.edu	Penn Dermatology
Minnig	Molly	mminnig@sas.upenn.edu	Penn Ortho
Mohanraj	Bhavana	mohanraj.bhavana@gmail.com	Penn Bioengineering
Mourkioti	Faye	fmour@mail.med.upenn.edu	Penn Ortho
Mundy	Christina	matticolac@email.chop.edu	CHOP Ortho
Newton	Joseph	Josebr@seas.upenn.edu	Penn Bioengineering
Nguyen	Vu	vunguyen@mail.med.upenn.edu	Penn Rheumatology
Nuss	Courtney	cnuss@mail.med.upenn.edu	Penn Ortho
Oeckenpöhler	Simon	simon.oeckenpoehler@ukmuenster.de	University Münster
Offemaria	Arlene	Ago24@drexel.edu	Thomas Jefferson University
Olson	John	olsonjc@email.chop.edu	CHOP Ortho
Ortved	Kyla	kortved@vet.upenn.edu	Penn Vet Clinical Studies
Pacifici	Maurizio	pacificim@email.chop.edu	CHOP Ortho
Pan	Ding	panding08@126.com	Penn Ortho

Parajuli	Ashutosh	parajuli.ashutosh@GMAIL.COM	Univ of Delaware Mechanical Engineering
Pardes	Adam	apardes@seas.upenn.edu	Penn Ortho
Paschos	Nikolaos	nikolaos.paschos@uphs.upenn.edu	Penn Ortho
Pasha	Saba	pasha.saba@gmail.com	CHOP Ortho Surgery
Patel	Pavan	pdp35@drexel.edu	Drexel Univ Biomedical Engineering
Peck	Sun	sunchung@mail.med.upenn.edu	Penn Ortho
Pei	Shaopeng	shaopeng@udel.edu	Univ of Delaware Mechanical Engineering
Piazza	Matthew	matthew.piazza@uphs.upenn.edu	Penn Neurosurgery
Pleshko	Nancy	npleshko@temple.edu	Temple Univ Bioengineering
Prosser	Benjamin	bpros@upenn.edu	Penn Physiology
Qin	Ling	qinling@mail.med.upenn.edu	Penn Ortho
Qu	Feini	Feini@upenn.edu	Penn Vet
Raffiani	Greg	raffiani@princeton.edu	Princeton Univ Athletics
Raja	Harina	harina.a.raja@gmail.com	Penn Ortho
Rajapakse	Chamith	chamith@mail.med.upenn.edu	Penn Radiology & Ortho
Rajaratnam	Anjali	anjalir@seas.upenn.edu	Penn Bioengineering
Ramaswamy	Girish	rgirish@mail.med.upenn.edu	Penn Ortho
Richardson	Dean	dwr@vet.upenn.edu	Penn Vet Clinical Studies
Riggin	Corinne	criggin@seas.upenn.edu	Penn Ortho
Risbud	Makarand	makarand.risbud@jefferson.edu	Thomas Jefferson Univ Ortho
Roberts	Douglas	Douglas2@vet.upenn.edu	Penn Vet Biomedical Sciences
Robinson	Kelsey	Kelseyr@upenn.edu	Penn Ortho
Rodriguez	Ashley	ashley.b.rodriguez0391@gmail.com	Penn Ortho
Rous	Clarissa	rousc@mail.med.upenn.edu	Penn Cell & Molecular Biology
Salvadeo	Danielle	tuf50863@temple.edu	Temple Univ Anatomy & Cell Biology
Sambamurthy	Nisha	nishasam@mail.med.upenn.edu	Penn Rheumatology
Scanzello	Carla	cscanz@upenn.edu	Penn Rheumatology
Sebro	Ronnie	ronnie.sebro@uphs.upenn.edu	Penn Radiology
Seiber	Breanna	Breanna.n.seiber@gmail.com	Penn Ortho
Sennett	Mackenzie	sennett@mail.med.upenn.edu	Penn Ortho
Seravello	Donna	donnaser@exchange.upenn.edu	Penn Ortho
Shanahan	Maureen	shanm@upenn.edu	Penn Ortho
Shapiro	Irving	irving.shapiro@jefferson.edu	Thomas Jefferson Univ Ortho
Sharifi-Sanjani	Maryam	msharif@upenn.edu	Penn Ortho

Shetye	Snehal	shetye@upenn.edu	Penn Ortho
Shi	Shihong	shihongs@upenn.edu	Penn Dental Oral Surgery
Shore	Eileen	shore@mail.med.upenn.edu	Penn Ortho
Sidibe	David	dsidibe@upenn.edu	Penn Ortho
Sinha	Sayantani	sinhas@email.chop.edu	CHOP Pediatrics Ortho
Smalley	Ryan	rynsmalley@gmail.com	VA TMRC Ortho
Smith	Gail	smithgk@vet.upenn.edu	Penn Vet Clinical Studies
Smith	Lachlan	lachlans@mail.med.upenn.edu	Penn Ortho
Smith	Harvey	harvey.smith@uphs.upenn.edu	Penn Ortho
Soslowsky	Lou	soslowsk@upenn.edu	Penn Ortho
Sperry	Megan	sperrym@seas.upenn.edu	Penn Bioengineering
Spiro	Robert	Bob.spiro@aesculap.com	Aesculap, Inc.
Stanley	Alexandra	astanle@mail.med.upenn.edu	Penn Ortho
Stedman	Hansell	Hstedman@mail.med.upenn.edu	Penn Surgery
Stoeckl	Brendan	bdstoeckl@gmail.com	Penn Ortho
Szczesny	Spencer	esy@mail.med.upenn.edu	Penn Ortho
Tamsen	Shereen	tamsens@mail.med.upenn.edu	Penn Ortho
Tarr	Joseph	tue57207@temple.edu	Temple Univ Anatomy & Cell Biology
Taylor	Brittany	b.taylor1888@gmail.com	Penn Ortho
Thomas	William	William.Thomas@uphs.upenn.edu	HUP ENT
Thornton	Angelique	thorntona1@email.chop.edu	CHOP Ortho
Tichy	Elisia	etichy@mail.med.upenn.edu	University of Pennsylvania
Tomlinson	Ryan	ryan.tomlinson@jefferson.edu	Thomas Jefferson Univ Ortho
Tong	Wei	tongwei312@gmail.com	Penn Ortho
Tower	Robert	robert.tower@kuleuven.be	Penn Ortho
Towler	Will	owtowler@gmail.com	Penn Ortho
Trujillo Munoz	Sara	s.trujillo-munoz.1@research.gla.ac.uk	University of Glasgow
Tseng	Wei-Ju	weits@mail.med.upenn.edu	Penn Ortho
Tsinman	Tonia	ttsinman@seas.upenn.edu	Penn Bioengineering
Tucker	Scott	smt46@cornell.edu	Penn State Hershey Ortho
Vega	Sebastian	sebv@seas.upenn.edu	Penn Bioengineering
Volk	Susan	swvolk@vet.upenn.edu	Penn Vet Clinical Studies
Waldorff	Erik	erikwaldorff@orthofix.com	Orthofix, Inc.
Wang	Chao	cw583@drexel.edu	Drexel Univ Biomedical Engineering
Wang	Luqiang	luqiang@mail.med.upenn.edu	Penn Ortho

Wang	Liyun	lywang@udel.edu	Univ of Delaware Mechanical Engineering
Wang	Bin	bin.wang@jefferson.edu	Thomas Jefferson Univ Medicine
Wang	Haitao	whaitao@mail.med.upenn.edu	Penn Ortho
Warman	Matthew	donnaser@exchange.upenn.edu	Boston Children's Hospital
Wehrli	Felix	wehrli@mail.med.upenn.edu	Penn Radiology
Weiss	Stephanie	weisssn@gmail.com	Penn Ortho
Weisshaar	Christine	weissha@seas.upenn.edu	Penn Bioengineering
White	Richard	richard.white4@uphs.upenn.edu	Penn Rheumatology
Whitney	Daniel	dwhitney@udel.edu	Applied Physiology
Wu	Lily	wul4@email.chop.edu	CHOP Ortho
Xu	Qilin	xuqilin@upenn.edu	University of Pennsylvania
Xu	Cheng	chengxu@upenn.edu	Penn Dental Anatomy & Cell Biology
Xu	Meiqi	mqx@mail.med.upenn.edu	Penn Ortho
Yang	Feiukun	feikun@vet.upenn.edu	Penn Vet Clinical Studies
Yang	Shuying	shuyingy@upenn.edu	Penn Dental Anatomy & Cell Biology
Yang	Yanmei	yanmei.yang@jefferson.edu	Thomas Jefferson University
Yousefi	Farzad	farzad.yousefi@temple.edu	Temple Univ Bioengineering
Yuh	Da-Yo	Yuhda@upenn.edu	Penn Dental Periodontics
Zellers	Jennifer	jzellers@udel.edu	Univ of Delaware Physical Therapy
Zemel	Babette	zemel@email.chop.edu	CHOP Pediatrics
Zhang	Qunzhou	zqunzhou@upenn.edu	Penn Dental
Zhang	Yejia	yejia.zhang@uphs.upenn.edu	Penn Ortho & PM&R
Zhang	Sijia	sijiaz@seas.upenn.edu	University of Pennsylvania
Zhang	Yueling	yuelingz@upenn.edu	Penn Dental Oral Surgery
Zhang	Deyu	deyz@mail.med.upenn.edu	Penn Ortho
Zhang	Hongtao	zhanghon@mail.med.upenn.edu	Penn Ortho
Zhao	Hongbo	zhongbo@mail.med.upenn.edu	Penn Ortho



PENN  
—  
CENTER for  
MUSCULOSKELETAL  
DISORDERS

## Speaker Abstracts

**Sex Hormones and ACL Injury**  
Ellen Casey, MD  
Assistant Professor  
Physical Medicine and Rehabilitation  
University of Pennsylvania Perelman School of Medicine

The rate of musculoskeletal injury differs substantially between men and women, with the incidence of anterior cruciate ligament (ACL) injuries 2-5 times higher in female athletes<sup>1</sup>. These injuries cause short- and long-term health problems, including time lost from school or work, psychological distress, and post-traumatic osteoarthritis<sup>2</sup>. Sex hormones may make a significant contribution to this injury disparity: differences in injury rate are not evident until puberty, and injuries occur disproportionately in the first half of the menstrual cycle<sup>3-6</sup>. While most research has focused on passive components of the musculoskeletal system, arguing that female fluctuating hormone concentrations may change mechanical properties of the ligament itself, a direct link between ligament laxity and ACL injury has not been proven<sup>7-8</sup>. Our central hypothesis that changes in sex hormone concentration result in changes to the basic elements of motor control – at multiple levels, from the musculotendinous unit to motor control circuitry. In our preliminary data, at the muscle level, we have shown that the muscle reflex response is lowest when estradiol concentrations are highest, with no change in anterior knee laxity<sup>9</sup>. At the spinal circuitry level, we have shown that while day-to-day changes in hormone concentration do not modulate spinal motor neuronal excitability, a lower overall level of excitability exists in women who take oral contraceptives<sup>10</sup>. Finally, at the level of the brain, we have shown the excitability of intra-cortical interneuronal circuits is increased when estradiol concentrations are highest. Our findings have the potential to guide future research in injury prevention strategies, including targeted neuromuscular training. This knowledge will enable clinicians to educate female patients on neuromuscular effects of sex hormones during times of high fluctuations, including puberty, pregnancy, and menopause.

1. Agel J, Arendt EA, Bershadsky B. Anterior cruciate ligament injury in national collegiate athletic association basketball and soccer: a 13-year review. *Am. J. Sports Med.* 2005;33(4):524-530.
2. von Porat A, Roos EM, Roos H. High prevalence of osteoarthritis 14 years after an anterior cruciate ligament tear in male soccer players: a study of radiographic and patient relevant outcomes. *Ann. Rheum. Dis.* 2004;63(3):269-273.
3. Shea KG, Pfeiffer R, Wang JH, Curtin M, Apel PJ. Anterior cruciate ligament injury in pediatric and adolescent soccer players: an analysis of insurance data. *J. Pediatr. Orthop.* 2004;24(6):623-628.
4. Sigward SM, Pollard CD, Havens KL, Powers CM. Influence of sex and maturation on knee mechanics during side-step cutting. *Med. Sci. Sports Exerc.* 2012;44(8):1497-1503.
5. Slauterbeck JR, Fuzie SF, Smith MP, et al. The menstrual cycle, sex hormones, and anterior cruciate ligament injury. *Journal of athletic training.* 2002;37(3):275.
6. Arendt EA, Bershadsky B, Agel J. Periodicity of noncontact anterior cruciate ligament injuries during the menstrual cycle. *J. Gend. Specif. Med.* 2002;5(2):19-26
7. Yu WD, Panossian V, Hatch JD, Liu SH, Finerman GA. Combined effects of estrogen and progesterone on the anterior cruciate ligament. *Clin. Orthop. Relat. Res.* 2001(383):268-281.
8. Romani W, Patrie J, Curl LA, Flaws JA. The correlations between estradiol, estrone, estriol, progesterone, and sex hormone-binding globulin and anterior cruciate ligament stiffness in healthy, active females. *Journal of Women's Health.* 2003;12(3):287-298
9. Casey E, Hameed F, Dhaher YY. The muscle stretch reflex throughout the menstrual cycle. *Med. Sci. Sports Exerc.* 2014;46(3):600-609
10. Casey E, Reese M, Okafor E, Chun D, Nigl F, Gagnon C, Dhaher Y.: Influence of Menstrual and Contraceptive Phase on Spinal Excitability. *Physical Medicine and Rehabilitation* 2016; Epub (ahead of print).

## **Statistical considerations on the diagnosis of osteoporosis – implications for disease prevalence**

Ronnie Sebro, M.D.  
Assistant Professor of Radiology

**Aim:** The current World Health Organization (WHO) guidelines for the diagnosis of osteoporosis and osteopenia, utilize bone mineral density (BMD) T-scores estimated using dual-energy x-ray absorptiometry (DEXA) at the femoral neck, hip or lumbar spine, but fail to consider the intra-individual correlation between bone mineral densities at these sites. The goal of this study is to assess estimate how the proportion of individuals diagnosed with osteoporosis and osteopenia change while accounting for the intra-individual correlations.

**Methods:** Multivariate statistical theory is used to derive the joint distribution of bone mineral densities (BMD) at the femoral neck, hip and lumbar spine. We simulated a cohort of 3 million European-American women aged 65 years with varying degrees of correlation between each of the BMD measurements ( $r = 0, 0.3, 0.5$  and  $0.8$  respectively). Multivariate scores for BMD measurements are calculated and the diagnoses made (% normal, % osteopenia, % osteoporosis) were compared to the diagnoses made using the conventional univariate T-scores and WHO guidelines.

**Results:** Simulation studies – simulating the proportion of 65 year-old European-American women biannually screened in a population of the size of the United States and show that accounting for the intra-individual correlation in BMD scores results in a larger proportion of individuals diagnosed as osteopenic and osteoporotic compared to the WHO guidelines.

**Conclusions:** This study shows that the WHO guidelines are anti-conservative and that statistically, the proportion of post-menopausal females with osteoporosis and osteopenia may be higher than currently appreciated in clinical practice. There is substantial increased morbidity and mortality associated with osteoporosis related fractures; therefore further research needs to be done to re-assess criteria for diagnosing osteoporosis and osteopenia.

## **“Microtubule Mechanics in Contracting Myocytes”**

Benjamin Prosser, Ph.D.  
Assistant Professor of Physiology

### **Abstract:**

Microtubules have long been implicated in the regulation of the heart beat, yet their precise contribution to cardiac mechanics, and how it changes in disease, has remained obscure. One barrier to progress has been a lack of observation of microtubules in the living, beating myocyte. Recent advances utilizing Airyscan point spread function imaging have allowed us to capture microtubule behavior in contracting and stretching myocytes (Robison et al., Science 2016). Microtubules deform dramatically during the heart beat, forming buckled sinusoids that resemble spring like elements. These microtubule “springs” increase the internal mechanical resistance to contraction, as well as provide a passive resistance to myocyte stretch. We further identify two key components that mediate microtubule mechanics; 1) post-translational “detyrosination” of cardiac microtubules and 2) desmin intermediate filaments. Detyrosinated microtubules associate with desmin at the sarcomeric Z-disk, thus cross-linking microtubules to the force generating structures of the heart cell, and inserting them as resistance elements. Finally, we provide correlative evidence that such cytoskeletal resistance may limit cardiac function in human heart disease.

## **“Patients’ recovery after tendon injury”**

Karin Grävare Silbernagel PT, ATC, PhD  
Assistant Professor  
Department of Physical Therapy  
University of Delaware

Chronic tendon injuries have been estimated to account for 50% of occupational injuries and the prevalence of tendinopathy in recreational athletes has been reported to be as high as 45%. Injuries to the tendon include both painful overuse injuries (tendinitis/tendinopathy) and acute injuries such as ruptures. The challenge for the medical community treating tendon injuries is that tendons heal slowly, and frequently the original structure and mechanical properties are not achieved. Of interest is to understand how the tendon injury affects the patients’ symptoms, function and ability to return to work and physical activity. This presentation will review how patients’ recover after an Achilles tendon rupture and how this relates to the recovery of tendon structure and mechanical properties.

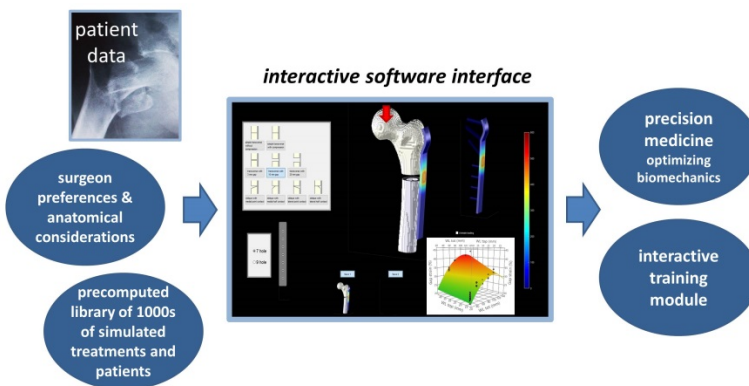
## “Simulation-Based Design for Orthopaedic Surgical Procedures”

Gregory S. Lewis PhD & J. Spence Reid MD

Department of Orthopaedics & Rehabilitation, Penn State College of Medicine, Hershey PA

Orthopaedic surgeons treating difficult fractures often need to choose a fixation construct and postoperative weightbearing strategy for a patient which provides proper biomechanical stability (stresses and strains) to the fracture site. Fracture stability affects fracture healing, and inadequate constructs and rehabilitation plans can lead to fracture nonunion, residual deformity, implant failure, and revision surgery. Poor treatment of fractures involving joints can also lead to posttraumatic arthritis. For complex fracture cases these three-dimensional biomechanics can defy simpler rules-of-thumb and are difficult to predict. Surgeons currently have a large number of choices for implant types, sizes, materials, and construct configurations. Patient variables include fracture geometry and bone quality, which we and others have shown to substantially affect mechanics. Surgeon experience level has been correlated with clinical outcomes and safety, pointing to the importance of clinical decision making in the treatment of patients. Recently the Editor-in-Chief of *J Bone & Joint Surg* wrote: “as is often said with fracture reduction, the surgeon is responsible for 80% of the outcome...surgical technique and surgeon experience/judgment are the major determinants.”

Our approach is inspired by precision medicine and an emerging paradigm in engineering, simulation based design, in which complex systems are designed with assistance from automated computer simulations. Simulations are capable of predicting deterministic behavior of complex systems, and humans are uniquely able to account for qualitative factors and make final design decisions with competing objectives. Applying this concept to orthopaedic procedures, the designer is the surgeon, and the design project is the treatment for a particular patient. We have been developing an interactive human-computer flatscreen interface that enables a surgeon to visualize the 3D biomechanics associated with surgical variations in fracture fixation procedures. Powered by novel automated modeling methods,<sup>1-2</sup> the interface enables the surgeon to adjust the construct design and immediately see the resulting stresses and strains displayed on a 3D-rotatable model. We are investigating two parallel applications of this type of interface: (1) as a novel decision support and preoperative planning tool for identifying optimal personalized treatment; and (2) as a training and educational tool, fed real cases from the decision support tool. We have developed surrogate mathematical models<sup>1</sup> and multivariate visualization and optimization tools<sup>2</sup> based on precomputed libraries of 1000s of simulated treatments and patient characteristics. Our working hypothesis is that interactive human-computer interfaces based on biomechanical simulation and systematic optimization of many surgical variations can assist and train surgeons in reducing surgical errors, complications, and recovery time.



[1] Wee H, Reid JS, Chinchilli VM & Lewis GS. Finite Element-Derived Surrogate Models of Locked Plate Fracture Fixation Biomechanics. *Ann. Biomed. Eng.*. (In Press).

[2] Wee H, Reid JS & Lewis GS. Parametric and Surrogate Modeling of Internal Fixation of Femur Fractures Demonstrate Influence of Surgical and Patient Variables. *Ann. Biomed. Eng.*. (In Press).

Acknowledgements: Hwabok Wee, April Armstrong, Scott Tucker; Funding: AO Foundation & Pennsylvania Dept. Health

**“Substance P Increases Collagen Type I via TGF- $\beta$ -Dependent and -Independent Pathways in Rat Tenocytes”**

Mary Barbe, Ph.D.  
Professor, Anatomy and Cell Biology  
Professor, Department of Physical Therapy  
Lewis Katz School of Medicine, Temple

TGFB-1 and CCN2 are important mediators of fibrosis by their stimulatory effect on extracellular matrix deposition, with CCN2 functioning as a downstream mediator of TGFB-1. Substance P (SP), a neuropeptide, has also been linked to tissue fibrosis and collagen production in tenocytes. We sought to determine if SP induces tenocyte proliferation, CCN2 or collagen production via TGFB-1 signaling or independently *in vitro* using primary tenocytes isolated from rat tendons. We observed that primary tenocytes expressing proteins characteristic of tenocytes (vimentin and tenomodulin) underwent increased proliferation in a dose-dependent manner after SP and TGFB-1 treatments alone, or their combination (with highest proliferation when combined). SP induced TGFB-1 expression in tenocytes in a dose- and time-dependent manner (after 48 hours, but not 24 hours of stimulation). SP and TGFB-1, both alone or combined, stimulated CCN2 expression in dose-dependent manners in tenocytes and their supernatants after both 24 and 48 hours of stimulation; effects blocked with addition of a TGFB-1 receptor inhibitor (TGFB-RI). In contrast, TGFB-1 promoted collagen type I expression after 48 hours only, whereas SP promoted its expression in tenocyte supernatants at both time points. At the 24 hour time points, collagen type I expression was not reduced when SP was combined with a TGFB-RI. Our findings suggest that both SP and TGFB-1 are involved in tenocyte fibrogenic processes, albeit differently. Both increased tenocyte proliferation and CCN2 production, the latter via TGFB-1 signaling. In contrast, SP induced collagen production independently of TGFB-1 signaling at 24 hours prior to the onset of signaling dependently.

## **"Intramuscular Fat Accumulation in Rheumatoid Arthritis: A New Perspective on Cachexia"**

Joshua Baker, M.D., M.S.C.E.  
Assistant Professor, Rheumatology & Epidemiology  
University of Pennsylvania

Rheumatoid arthritis is associated with a loss of muscle mass. This has recently been shown to be compounded by a loss of muscle quality in the form of intramuscular fat accumulation resulting in low muscle density. We previously showed that patients who have undergone muscle loss also experience loss of muscle density and muscle-specific force. This has implications for long-term outcomes related to adverse body composition including physical functioning, bone health, cardiometabolic health. Intramuscular fat accumulation can occur in both the intra- and extra-cellular compartments. Since muscle is responsible for removing 40% of post-prandial glucose from the circulation, accumulation of intramyocellular fat has been strongly associated with insulin resistance. In our PCMD-funded pilot project, we aimed to quantify intramyocellular fat content among patients with rheumatoid arthritis compared to matched controls and to assess relationships with muscle density, physical function, and other evidence of cachexia.

## **“Stem Cell Molecular Mechanisms in Chronic Skeletal Muscle Injury”**

Foteini Mourkioti

Department of Orthopaedic Surgery, Cell and Developmental Biology  
Perelman School of Medicine, University of Pennsylvania

Acknowledgement: Elisia Tichy, Nicholas Oyster

Skeletal muscle diseases or myopathies result in loss of muscle mass, degeneration and functional weakness. Duchenne muscular dystrophy (DMD) is the most common recessive chronic muscle disorder that results from lack of dystrophin, a cytoskeletal protein that is essential for the stability of the skeletal muscle membrane. A conundrum has been that dystrophy knockout mice (*mdx*), which share the same dystrophin deficiency as DMD patients, exhibit only mild muscle weakness in contrast to patients. We reasoned that the ~8-fold difference in telomere length between mice and humans could account for this discrepancy and developed a new *mdx* mouse model with shortened telomeres (*mdx/mTR*). This dystrophic model exhibits all the pathological hallmarks of human DMD (Sacco, Mourkioti, *Cell*, 2010, Mourkioti, *Nat. Cell Biol.* 2013) and offers a useful tool to unravel the molecular mechanisms associated with injury in dystrophic muscles. Here, we demonstrate that muscle stem cell (MuSC) exhaustion is responsible for the failure to sustain the damage-repair cycle during regeneration. These data support the notion that modulation or maintenance of MuSCs function might prevent or diminish destructive muscle processes in dystrophic muscles. By analyzing signaling dynamics in muscle stem cells, we identified that NF- $\kappa$ B signaling pathway is contributing to stem cell exhaustion and telomere shortening during the progression of the disease. By analyzing human MuSCs from healthy and DMD young patient, we demonstrated the relevance of our mouse findings for the human DMD disease. To investigate the therapeutic potential of NF- $\kappa$ B inhibition in muscle stem cells, we performed transplantation experiments into dystrophic muscles and showed that MuSC-specific NF- $\kappa$ B inhibition improves regeneration in diseased muscles. All together, our studies suggest that NF- $\kappa$ B activation is a direct potential molecular pathway affected in DMD MuSCs that can be therapeutically manipulated for better management of the disease.

## **“Defining the Roles of Esrp1 Regulated Alternative Splicing in Craniofacial Development”**

**Russell P. Carstens, M.D.**  
**Associate Professor of Medicine**

Cleft lip with or without cleft palate (CL/P) is among the most highly prevalent birth defects in human patients. In contrast to isolated CP, CL/P is more common in human patients and yet there are few mouse models for CL/P available to define mechanisms that give rise to CL/P. An improved understanding of the genes and molecular pathways involved in craniofacial development is needed in order to better understand CL/P and CP pathogenesis. It is well established that crosstalk between epithelial and mesenchymal cells underlies formation of the face and palate, yet the basic molecular events underlying this crosstalk are poorly understood. While a number of key transcription factors and signaling pathways involved in craniofacial development have been identified, the role of alternative splicing is largely unexplored. My lab studied alternative splicing of fibroblast growth factor receptor 2 (FGFR2), a gene associated with craniofacial abnormalities. We discovered two paralogous epithelial-cell-type-specific splicing factors, Esrp1 and Esrp2, which are required for expression of the epithelial Fgfr2-IIIb isoform and a broader epithelial program of alternative splicing. We generated mice with knockout (KO) of the *Esrp* genes and the primary defect in *Esrp1* KO mice is 100% penetrant CL/P. Mice with combined KO of both *Esrp1* and *Esrp2* had more severe abnormalities in craniofacial development and also defects in forelimb formation. These *Esrp* KO mice provide a new tool we can leverage to probe the epithelial-mesenchymal interactions that underlie craniofacial development. We hypothesize that *Esrp1* KO causes cell autonomous defects in epithelial cells as well as cell-non-autonomous defects in underlying mesenchyme that lead to CL/P. We further hypothesize that Esrp1 target transcripts encode epithelial-specific protein isoforms that are essential for maintenance of signaling events that regulate epithelial-mesenchymal interactions. We are therefore carrying out a more detailed characterization of the stages and mechanisms through which *Esrp1* ablation leads to CL/P. In recent studies we have determined that conditional ablation of early embryonic surface ectoderm using *Crect* transgenic mice recapitulates the CL/P phenotype indicating that splicing disruptions in this cell population underpins the defects in craniofacial development seen with *Esrp1* KO. We are therefore dissecting early ectoderm and underlying mesenchyme for RNA isolation to profile alterations in splicing and total transcript expression in each cell compartment with loss of Esrp1. Further characterization of the genes and pathways that are impacted by the loss of Esrp1 in these cells will provide further insights into epithelial-mesenchymal crosstalk during craniofacial development and how disruptions in key genes and signaling can lead to CL/P and other craniofacial abnormalities.

## **Strategies for Improving Bone Properties in Patients with Osteogenesis Imperfecta**

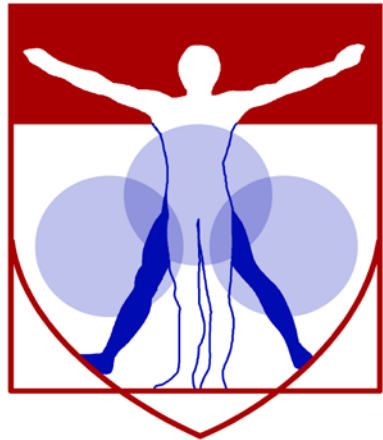
Matthew L. Warman, M.D.

Howard Hughes Medical Institute

Orthopaedic Research Laboratories, Boston Children's Hospital

Department of Genetics, Harvard Medical School

Osteogenesis Imperfecta (OI) is a skeletal fragility disorder that most often results from mutations that affect type I collagen synthesis, assembly, or secretion. There is currently no fully satisfactory therapy for patients with OI. We are determining whether the Wnt-LRP5/6 signaling pathway, which has important roles during skeletal development and homeostasis, can be modulated to benefit patients with OI. This knowledge is important, since therapies that modulate Wnt-LRP5/6 signaling are in phase III clinical trials for adult osteopenia and could be considered for patients with OI. This lecture will provide a clinical overview of human OI and summarize prior work that revealed how Wnt-LRP5/6 signaling affects bone mass accrual and homeostasis. Ongoing experiments in which Wnt-LRP5/6 signaling is genetically or pharmacologically modulated in mouse models of OI will then be discussed.



PENN  
—  
CENTER for  
MUSCULOSKELETAL  
DISORDERS

# Biomechanics Abstracts

# Tensile Mechanical Properties and Dynamic Collagen Fiber Re-Alignment of the Murine Cervix are Dramatically Altered Throughout Pregnancy

Carrie E. Barnum<sup>1</sup>, Jennifer L. Fey<sup>1</sup>, Stephanie N. Weiss<sup>1</sup>, Guillermo Barila<sup>3</sup>, Amy G. Brown<sup>3</sup>, Brianne K. Connizzo<sup>1, 2</sup>, Snehal S. Shetye<sup>1</sup>, Michal A. Elovitz<sup>3</sup>, and Louis J. Soslowsky<sup>1</sup>

<sup>1</sup>McKay Orthopedic Research Laboratory, University of Pennsylvania, Philadelphia, PA

<sup>2</sup>Department of Biological Engineering, Massachusetts Institute of Technology, Cambridge, MA

<sup>3</sup>Maternal and Child Health Research Program; Department of Obstetrics and Gynecology Perelman School of Medicine, University of Pennsylvania, Philadelphia, PA

The cervix is a unique organ able to dramatically change its shape and function by serving as a physical barrier for the growing fetus and then undergoing dramatic dilation allowing for delivery of a term infant. As a result, the cervix endures changing mechanical forces from the growing fetus. There is an emerging concept that the cervix may change or remodel “early” in many cases of spontaneous preterm birth. However, the mechanical role of the cervix in both normal and preterm birth remains unclear. Therefore, the primary objective of this study was to determine the mechanical and structural response of murine cervical tissue throughout a normal gestational time course. In this study, both tissue structural and material properties were determined via a quasi-static tensile load-to-failure test while simultaneously obtaining dynamic collagen fiber re-alignment via cross-polarization imaging. This study demonstrated that the majority of the mechanical properties evaluated decreased at mid-gestation and not just at term, while collagen fiber re-alignment occurred earlier in the loading curve for cervices at term. This suggests that although structural changes in the cervix occur throughout gestation, the differences in material properties function in combination with collagen fiber re-alignment as mechanical precursors to regulate term gestation. This work lays a foundation for investigating cervical biomechanics and the role of the cervix in preterm birth.

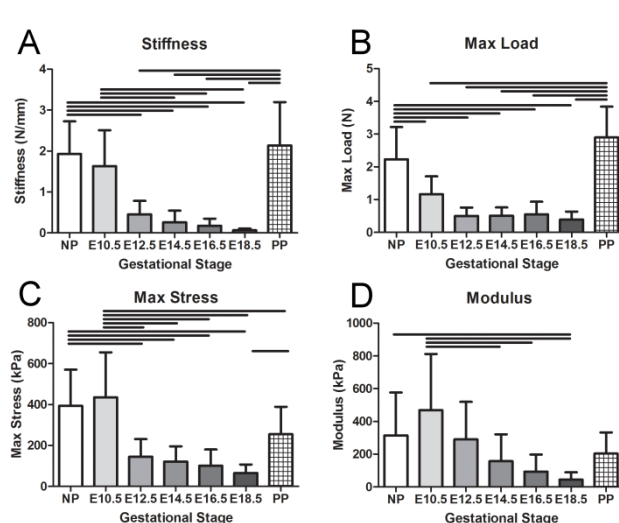


**Figure 1:** Mechanical properties, such as maximum load (A), ultimate stress (B), stiffness (C) and modulus (D), for NP and gestational ages (n=10-19 for all samples) are presented. Data is represented as mean±standard deviation and significance denoted by a bar spanning two comparison groups ( $p$ -value < 0.05).

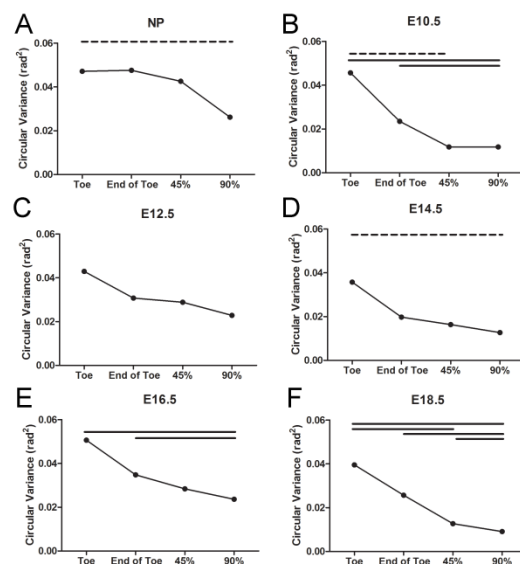


**Figure 2:** Collagen re-alignment of non-pregnant and pregnant cervix during tensile loading, comparing circular variance of fiber alignment distributions at Toe, End of Toe, 45% of Max Load, and 90% of Max Load for NP (A), E10.5 (B), E12.5 (C), E14.5 (D), E16.5 (E) E18.5 (F) cervix. Each graph is a representative image of the data, while each point signifies alignment at each part of the mechanical test. Data is presented with significance denoted by a bar spanning two comparison groups ( $p$ -value < 0.05) dashed lines represent trends ( $p$  < 0.1).

Supported in part by the March of Dimes Prematurity Research Center and the Penn Center for Musculoskeletal Disorders (P30 AR069619) at the University of Pennsylvania

## Effects of Autologous Tenocyte-Seeded Nanofibrous Scaffolds in Rotator Cuff Repair are Age-Dependent

Huegel J, Kim DH, Cirone JM, Pardes AM, Morris TR, Nuss CA, Mauck RL, Soslowsky LJ, Kuntz AF

McKay Orthopaedic Research Laboratory, University of Pennsylvania, Philadelphia, PA

[andrew.kuntz@uphs.upenn.edu](mailto:andrew.kuntz@uphs.upenn.edu)

Disclosures: Huegel J (N), Kim DH (N), Cirone JA (N), Pardes AM (N), Morris TH (N), Nuss CA (N), Mauck RL (N), Soslowsky LJ (N), Kuntz AF (N)

**Introduction:** Rotator cuff tears affect millions of individuals each year, with an increased prevalence in the elderly population. Although advancements in surgical methods and rehabilitation protocols have improved clinical results, rotator cuff repair failure remains common [1]. To further improve surgical outcomes, rotator cuff repair augmentation has been studied, wherein scaffolds are used to aid in mechanical support at the time of surgery, and/or to deliver cells and/or biologic factors to the repair site. For example, local delivery of mesenchymal stem cells or tenocytes can increase collagen content and decrease inflammation at the repair site [2-4]. However, whether the success of such therapies is age-dependent is unknown. Therefore, the objective of this study was to determine the effects and mechanisms of action of autologous juvenile, adult, and aged tenocytes delivered using aligned nanofibrous scaffolds on healing tissue properties in our novel rat model of augmented rotator cuff repair [5]. Our hypotheses were: 1) Tenocyte-seeded scaffolds will increase collagen and cell organization at the repair site compared to scaffold only controls, resulting in enhanced tendon-bone healing with improved mechanical properties. 2) Tenocytes from juvenile rats will result in greater improvement of functional outcomes in cuff healing compared to adult or aged rats.

**Methods:** A total of 57 Fisher (F-344) rats were divided into three age groups: juvenile (4 weeks), adult (8 months) and aged animals (16 months). Animals underwent bilateral transection of their supraspinatus tendons and simultaneous harvest of the intra-articular biceps tendons. Biceps tendon cells were harvested by morselizing explant tissue and allowing cell migration onto tissue culture surfaces over 1 week. Cells were expanded in culture and split at confluence. At P2, cells from each donor were seeded onto an electrospun poly(L-caprolactone) (PCL) nanofibrous scaffold (3x5x0.5 mm) at  $2 \times 10^5$  cells/scaffold. Three weeks later, augmented supraspinatus repair was performed in which the right shoulder received a tenocyte-seeded scaffold while the left shoulder received an acellular scaffold as a control. Animals were sacrificed 8 weeks after the second surgery and frozen (for mechanical analysis, n=12) or fixed in formalin (for histologic analysis, n=6). One additional animal from each age group received Qtracker labeled cells bilaterally for cell tracking and was sacrificed at 1 week. Tissues were cryosectioned and processed for fluorescent imaging. *Tendon Mechanical Testing.* For testing, animals were thawed and the humerus was dissected with the supraspinatus intact. For local optical strain measurement, stain lines were placed on the tendon. Cross sectional area was measured using a custom laser device. Tensile testing was performed as: preload, preconditioning, stress relaxation, and ramp to failure. Stress was calculated as force divided by initial area and 2D Lagrangian strain was determined. *Histology:* Tendons were processed using paraffin procedures. Sagittal sections (7  $\mu$ m) were collected and stained with Hematoxylin-Eosin (H&E) or Safranin O-Fast Green (SafO). Cell density and cell shape were graded by three blinded investigators, using a scale of 1-3 (1=low, 2=moderate, 3=high) for cellularity and 1-3 (1=spindle shaped, 2=mixed, 3=rounded) for cell shape. SafO staining was quantified using ImageJ. Polarized light images were used to quantitate tendon organization as described [6]. Tissue mechanics, SafO quantification, and polarized light analysis were assessed using t-tests, comparing scaffold control and cell-seeded scaffold treatment within age groups. Histology scores were evaluated using a Mann-Whitney test. Significance was set at p<0.05 (\*) and trends at p<0.1 (†); \*\* denotes p<0.01.

**Results:** The presence of delivered tenocytes in the shoulder one week after surgery was confirmed via fluorescent imaging of Qtracker-labeled tenocytes. Concurrent *in vitro* culture of labeled cells demonstrated that tenocytes readily adhered to and colonized the PCL scaffolds (data not shown). Elastic and viscoelastic mechanical properties improved with cell-seeded scaffolds in both juvenile and aged animals when compared to scaffold-only controls. Specifically, in cell-seeded groups, stiffness and midsubstance modulus increased in juvenile animals, and midsubstance modulus increased in aged animals, with a trend toward an increase in stiffness (Fig 1A-B). Similar improvements in insertion modulus were also noted (data not shown). Stress relaxation decreased in juvenile animals (Fig 1C), while maximum stress increased in aged animals (Fig 1D) relative to controls. Implantation of cell-seeded scaffolds also improved histological parameters. Specifically, cells were significantly more spindle-shaped in juvenile animals (insertion only, data not shown) and in aged animals (trend, midsubstance only, data not shown), while cellularity increased at the insertion in both juvenile and aged groups (Fig 2). Cell delivery decreased SafO staining in aged animals (data not shown), and increased collagen organization (decreased circular standard deviation) in both the insertion and midsubstance of aged animals, and in the insertion of juvenile animals (Fig 3). No changes were seen in any parameter in adult animals.

**Discussion:** Results demonstrate that delivery of autologous tenocytes to the healing supraspinatus is beneficial in juvenile and aged animals, with no effect in adult animals. As aged animals exhibit deteriorated tendon mechanical properties and healing potential [7], a 44% increase in maximum stress with cell augmentation denotes a substantial improvement. Coupled with up to three-fold increases in tendon modulus and stiffness, the improvements in tendon mechanical strength for both aged and juvenile animals were striking. Increased numbers of cells at the insertion of treated animals demonstrates a more robust repair response, reflected in significant increases in collagen organization. These data support earlier matrix remodeling and increased collagen production after cell-augmented repair. While these findings support our first hypothesis, our second hypothesis was not substantiated. Surprisingly, both young and old animals benefitted similarly, yet no changes were seen in adult animals. Adult tendons are in relative "equilibrium" with regards to catabolic and anabolic processes, so additional tenocytes likely only sustain regular repair mechanisms. Conversely, juvenile tendons are actively growing whereas aged tendons exhibit diminished cell activity and matrix turnover. In these "imbalanced" states, the addition of a supplemental cell population contributes substantially to the healing process. Further research will investigate precise mechanisms of action by which these cell populations improve tissue healing.

**Significance:** This research addresses regenerative medicine and musculoskeletal repair by using bioengineered scaffolds *in vivo* to improve tendon repair in a clinically relevant and well-established animal model. As this approach uses FDA approved materials and minimally manipulated autologous cell populations, it has the potential for rapid translation to clinical practice to address this important clinical problem. We have demonstrated the potential for autologous cell-seeded scaffolds to improve repairs in both the juvenile and aged population.

**Acknowledgements:** This study was supported by the UPenn Institute on Aging and the Penn Center for Musculoskeletal Disorders (P30 AR0069619).

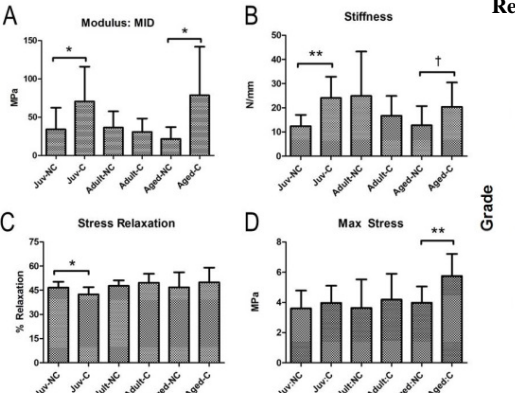


Figure 1: Augmenting repair with autologous cells caused (A) increased midsubstance modulus and (B) increased stiffness in both juvenile and aged animals, (C) decreased stress relaxation in juvenile animals, and (D) increased max stress in aged animals. (NC=Scaffold only, C=Cells)

**References:** [1] Galatz LM et al. J Bone Joint Surg Am, 2004. [2] Hernigou P et al. Int Orthop, 2014. [3] Chen JM et al. Tissue Eng, 2007. [4] Longo UG et al. Br Med Bull, 2010. [5] Beason DP et al. J Shoulder Elbow Surg, 2012. [6] Gimbel JA, J Biomech, 2004. [7] Plate JF et al. Am J Sports Med, 2014.

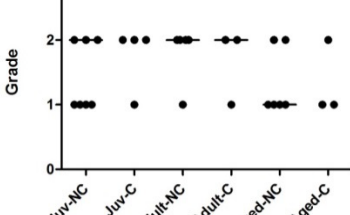


Figure 2: There was a significant increase in cellularity at the insertion of juvenile and aged tendons treated with cell-seeded scaffolds compared to scaffold-only controls.

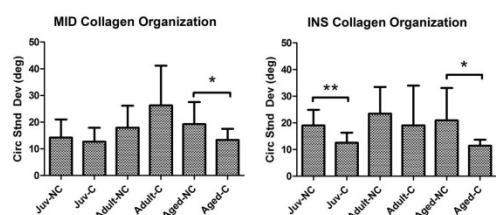


Figure 3: When comparing groups treated with cells to those without cells, collagen fiber organization was increased at the both the midsubstance and insertion in aged animals, and at the insertion in juvenile animals.

## Achilles tendon structural and mechanical properties relate to clinical outcomes following rupture

Jennifer A. Zellers<sup>1</sup>, Laura Pontiggia<sup>2</sup>, Daniel H. Cortes<sup>3</sup>, Karin Grävare Silbernagel<sup>1</sup>

<sup>1</sup>University of Delaware, Newark, DE, <sup>2</sup>University of the Sciences, Philadelphia, PA, <sup>3</sup>Penn State University, State College, PA

**INTRODUCTION:** Following Achilles tendon rupture, early elastic modulus has been reported to relate to functional performance later in recovery [Schepull]. Quantification of tendon viscoelastic properties is challenging in this population, however, as non-invasive techniques used to measure Achilles tendon elastic modulus via ultrasound imaging require measurement of plantar flexor isometric force. This is particularly limiting early post-rupture. Shear wave elastography, has been adapted for use in the Achilles tendon rupture population and was found to relate to a commonly used foot and ankle appearance and function clinical scoring system, the American Orthopedic Foot and Ankle Society (AOFAS) score [Zhang]. The relationship between viscoelastic properties measured by shear wave elastography and functional performance using Achilles tendon-specific outcomes has not been described.

Continuous shear wave elastography (cSWE) is a non-invasive technique, allowing for quantitative assessment of shear modulus and viscosity. The purpose of this study was to apply cSWE to the Achilles tendon rupture population post-rupture and examine the relationship of tendon viscoelastic properties on Achilles tendon-specific functional outcomes.

**METHODS:** Individuals within 8 months post-Achilles tendon rupture were included in this cross-sectional study. Exclusion criteria were bilateral Achilles tendon rupture, delayed treatment, or condition significantly limiting calf function on the non-rupture side (ex. severe spinal radiculopathy). Tendon length to the gastrocnemius was measured using B mode ultrasound imaging [Silbernagel, 2016]. A modification of the Achilles tendon resting angle was used to measure passive tension on the Achilles tendon [Carmont, 2015]. Tendon shear modulus and viscosity were measured using continuous shear wave elastography (cSWE) [Suydam, Cortes]. Plantar flexor performance was measured using the heel-rise test to determine number of repetitions, maximum heel-rise height, and total work (total linear displacement \* body weight) [Silbernagel, 2006]. Participant self-reported function was measured using the Achilles tendon total rupture score (ATRS).

**RESULTS:** Fourteen individuals (Mean(SD) age 43.5(15.2) years) following acute, unilateral Achilles tendon rupture were included in the study. The Median(IQR) time since rupture was 3(2-6) months with 10 subjects treated via surgical repair and 4 subjects treated non-surgically. Participants scored a Median(IQR) of 43(28-59) on the ATRS.

Participants demonstrated elongation of the tendon on the ruptured side, with a Median(IQR) length of 22.2(21.3-23.1) cm on ruptured and 21.2(19.7-22.7) cm on non-ruptured sides ( $p < 0.01$ ). The Median(IQR) side-to-side difference in Achilles tendon length was 1.4(0.6-2.4) cm. Participants performed less total work ( $p < 0.01$ ), with less heel-rise height ( $p < 0.01$ ) on the heel-rise test on the ruptured side ( $n = 10$ ). Viscosity was significantly lower on the rupture side, with a Median(IQR) limb symmetry index (rupture/non-rupture) of 0.60(0.46-0.65) ( $p = 0.001$ ). Shear modulus was not significantly different between sides, with a Median(IQR) limb symmetry index of 0.92(0.75-1.17) ( $p = 0.64$ ). Total work on the heel-rise test related to shear modulus ( $p = 0.642$ ,  $p < 0.05$ ) on the ruptured side ( $n=10$ ). Maximum heel-rise height was not related to shear modulus or viscosity ( $n=10$ ). Shear modulus related to ATRS score (Image 1). Both shear modulus and viscosity were found to relate to Achilles tendon resting angle (Image 2).

**DISCUSSION:** Similar to previous studies which have reported lower elastic modulus in Achilles tendons post-rupture, viscosity was significantly lower in ruptured tendons compared to the non-ruptured side. Shear modulus was not found to be significantly lower on the ruptured side, but was found to relate to both functional performance on the heel-rise test as well as participant self-reported symptoms and function on the ATRS. These findings suggest that viscosity may be indicative of presence or absence of pathology, whereas shear modulus is more associated with functional capacity. Additional longitudinal studies are required to see whether these relationships change over the course of healing.

### REFERENCES:

- Carmont et al., *Asia-Pacific J of Sports Med, Arthrosc, Rehabil and Technology* 2(2):49-55, 2015.  
Cortes et al., *Ultra. Med & Biol* 41(6):1518-29, 2015.  
Schepull et al., *Scand J Med Sci Sports* 22:18-23, 2012.  
Silbernagel et al., *Knee Surg Sport Traumatol* 14:1207-17, 2006.  
Silbernagel et al., *Muscles Ligaments Tendons J* 6(1): 104-10, 2016.  
Suydam et al., *J Orthop Res* 33(6): 926-31, 2015.  
Zhang et al., *Med Sci Mon* 22:1186-91, 2016.

**ACKNOWLEDGEMENTS:** Research reported in this abstract was supported by the National Institute of Arthritis and Musculoskeletal and Skin Diseases of the National Institutes of Health under award number R21AR067390, the University of Delaware Research Foundation, and the Foundation for Physical Therapy.

### IMAGES AND TABLES:

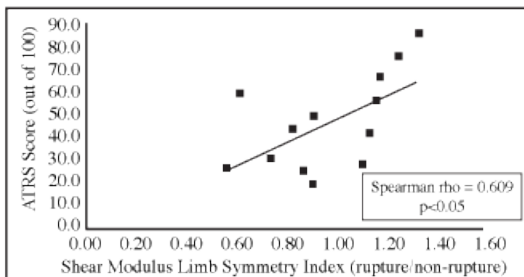


Image 1: Shear modulus limb symmetry index relates to Achilles tendon total rupture score (ATRS)

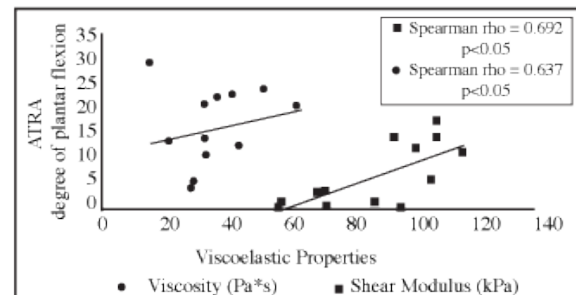


Image 2: Viscoelastic properties relate to Achilles tendon resting angle (ATRA)

## Type III Collagen is Critical to the Proper Functioning of Knee Cartilage and Meniscus

Chao Wang<sup>1</sup>, Becky K. Brisson<sup>2</sup>, Qing Li<sup>1</sup>, Kevt'her Hoxha<sup>1</sup>, Motomi Enomoto-Iwamoto<sup>3</sup>, Susan W. Volk<sup>2</sup>, Lin Han<sup>1</sup>

<sup>1</sup>Drexel University, Philadelphia, PA; <sup>2</sup>University of Pennsylvania, Philadelphia, PA; <sup>3</sup>The Children's Hospital of Philadelphia, Philadelphia, PA.

**Disclosures:** Chao Wang (N), Becky K. Brisson (N), Qing Li (N), Kevt'her Hoxha (N), Motomi Enomoto-Iwamoto (N), Susan W. Volk (N), Lin Han (N).

**INTRODUCTION:** It has long been recognized that the collagen network of cartilage extracellular matrix (ECM) is dominated by the heterotypic fibrils of type II, IX and XI collagens [1]. However, recent studies suggested that type III collagen is also present, and can make up for ~ 10% total collagen in mature human cartilage [2] and osteoarthritis (OA) cartilage [3]. In fact, in human genetic diseases associated with type III collagen (COL3A1) deficiency, such as vascular Ehlers-Danlos syndrome (EDS) [4], premature OA is a common symptom [5]. Additionally, recent biochemical analyses indicated that type III collagen can bind to type II collagen fibril surface and facilitate inter-fibril cross-linking [6]. These evidences suggest that type III collagen could be an important structural constituent of cartilage ECM. However, the exact roles of type III collagen in cartilage structure and mechanical properties are unclear. To this end, to test whether type III collagen has essential roles in joint functioning, this study examined the structural and mechanical phenotype of articular cartilage, as well as its direct loading counterpart, the meniscus, in *Col3a1* heterozygous mice (*Col3a1*<sup>+/−</sup>).

**METHODS:** Articular cartilage and meniscus were harvested from 2-month old wild-type (WT) and *Col3a1*<sup>+/−</sup> BALB/c male mice. The null mice (*Col3a1*<sup>−/−</sup>) were not included because they are perinatal lethal [7]. For histology and immunohistochemistry (IHC), whole joints of both knees were harvested, fixed in 4% paraformaldehyde, decalcified in 10% EDTA, and embedded in paraffin. Serial 4-μm-thick sagittal sections were cut, and one every consecutive six sections was used for staining of type III collagen by its primary IHC antibody (ab7778, Abcam), joint and cell morphology by Hematoxylin and Eosin (H&E), as well as sulfated glycoaminoglycans (sGAGs) by Safranin-O/Fast Green. AFM-nanoindentation was performed in PBS using a microspherical tip ( $R \approx 5\text{ }\mu\text{m}$ ,  $k \approx 5.4\text{ N/m}$ ,  $\mu\text{Masch}$ ) and a Dimension Icon AFM, following established procedures [8,9]. For each condyle and meniscus, at least 20 locations were tested on the intact surface to account for spatial heterogeneity. The effective indentation modulus,  $E_{ind}$ , was calculated for every location via Hertz model [8]. For SEM imaging, cartilage was treated with hyaluronidase and trypsin overnight to remove proteoglycans, fixed with Karnovsky's fixative for 3 hours in room temperature, then dehydrated in graded ethanol and hexamethyldisilazane [10]. Collagen fibrils on cartilage surfaces were then visualized by SEM (Zeiss Supra 50 VP). Two sample student's *t*-test was used to detect the structural and mechanical differences between WT and *Col3a1*<sup>+/−</sup> mice at a significance level of 0.05.

**RESULTS:** In comparison of the *Col3a1*<sup>+/−</sup> mice against the WT control, IHC showed the deposition of type III collagen in cartilage and meniscus was greatly reduced, while histology did not detect appreciable differences in articular cartilage organization or proteoglycan content (Fig. 1). Both cartilage and meniscus of *Col3a1*<sup>+/−</sup> mice showed significantly lower  $E_{ind}$  compared to WT (cartilage:  $p < 0.001$ ,  $n \geq 7$ ; meniscus:  $p < 0.05$ ,  $n \geq 8$ ) (Fig. 2). Furthermore, cartilage collagen fibril diameter of *Col3a1*<sup>+/−</sup> was significantly larger than WT ( $p < 0.0001$ ,  $n \geq 200$  fibrils from 3 animals) (Fig. 3).

**DISCUSSION:** Immunohistochemistry (Fig. 1) confirmed that type III collagen is not only present in murine cartilage, but also is substantially reduced in *Col3a1*<sup>+/−</sup> mice, ascertaining these mice as an *in vivo* model for examining the roles of type III collagen. In *Col3a1*<sup>+/−</sup> mice, the thickening of collagen fibrils (Fig. 3) highlights the active roles of type III collagen in the fibrillar network structure. Such observation is consistent with previous hypothesis that type III collagen co-polymerizes with type II collagen on fibril surfaces [6], in which, it may contribute to limiting the lateral growth of type II/IX/XI collagen fibrils. On the other hand, the absence of phenotype in sGAG staining or gross-level histology (Fig. 1) suggests that type III collagen's roles could be limited to the collagen content, at least at the tissue-level. The reduction in cartilage  $E_{ind}$  (Fig. 3a) can thus be mainly attributed to the altered collagen structure. In cartilage ECM, the collagen network functions as the scaffold that holds aggrecan aggregates up to ~ 50% compressive molecular strain, even in unloaded cartilage [11], changes in collagen structure can affect not only the modulus of collagen network itself, but also the molecular strain and apparent stiffness of aggrecan, which cannot be detected by histology. In addition, it is also possible that given type III collagen's potential roles in inter-fibrillar cross-linking [6], its reduction can result in decreased collagen network cross-linking density.

Besides cartilage, we also observed the modulus reduction in type I collagen-dominated meniscus (Fig. 2b). This observation suggests that type III collagen is involved in the formation of type I collagen-based synovial tissues. Therefore, its impact in joint functioning is likely not limited to articular cartilage, but other fibrous synovial tissues, such as the meniscus, anterior cruciate ligament (ACL) and synovium. It is therefore necessary to examine multiple synovial tissues simultaneously to fully understand the roles of type III collagen in the knee function and OA. On the other hand, while our current study clearly illustrated the importance of type III collagen in the knee, it does not reveal the exact mechanisms, which can be tissue-specific and age-specific. Since the study of adult *Col3a1*<sup>+/−</sup> mice is not feasible, our ongoing studies are developing joint-specific targeted inducible knockout of *Col3a1* using the aggrecan-CreER mice [12], which will allow for uncovering the specific roles of type III collagen in each synovial tissue with temporal specificity.

**SIGNIFICANCE:** This study is the first to discover the importance of type III collagen in the structure and mechanics of articular cartilage and meniscus. It provides a basis for future studies to reveal the exact roles of type III collagen in joint function and OA.

**REFERENCES:** [1] Eyre, D, *Arthritis Res.* 4:30-35, 2002. [2] Eyre, DR et al., *Eur. Cell. Mater.* 12:57-63, 2006. [3] Hosseiniinia, S et al., *Osteoarthr. Cartilage* 24:1029-1035, 2016. [4] Pepin, M et al., *N. Engl. J. Med.* 342:673-680, 2000. [5] Castori, M, *ISRN Dermatol.* 2012:751768, 2012. [6] Wu, JJ et al., *J. Biol. Chem.* 285:18537-18544, 2010. [7] Brisson, BK et al., *Am. J. Pathol.* 185:1471-1486, 2015. [8] Batista, MA et al., *Matrix Biol.* 38:84-90, 2014. [9] Li, Q et al., *J. Biomech.* 48:1364-1370, 2015. [10] Bray, DF et al., *Microsc. Res. Tech.* 26:489-495, 1993. [11] Wight, TN et al. 1991. In *Cell Biology of the Extracellular Matrix*. 45-78. [12] Henry, SP et al., *Genesis* 47:805-814, 2009.

**ACKNOWLEDGEMENTS:** This work was supported by the National Institutes of Health (R21AR066824) and the Penn Center for Musculoskeletal Diseases (PCMD) (NIH P30AR069619).

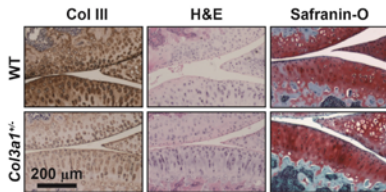


Fig. 1 Immunohistochemistry of collagen III and H&E, Safranin-O/FastGreen histology of WT and *Col3a1*<sup>+/−</sup> mouse knees.

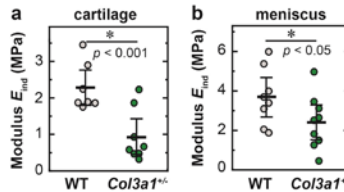


Fig. 2 Comparison of modulus,  $E_{ind}$ , between WT and *Col3a1*<sup>+/−</sup> mice: a) cartilage, b) meniscus ( $n \geq 7$ , mean  $\pm$  95% CI). Each data point represents average of  $\geq 20$  positions from one animal.

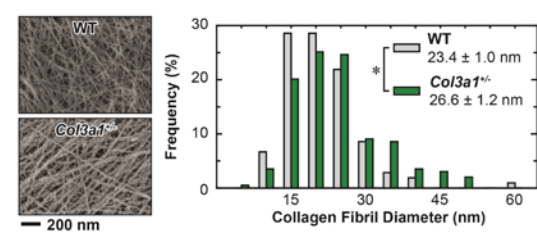


Fig. 3 Comparison of collagen fibril diameter between WT and *Col3a1*<sup>+/−</sup> cartilage (\*:  $p < 0.0001$ , mean  $\pm$  95% CI,  $n \geq 200$  fibrils for each genotype).

## Aging leads to inferior Achilles tendon mechanics and altered ankle function in rodents

Pardes AM, Rodriguez AB, Freedman BR, Fryhofer GW, Soslowsky LJ  
 McKay Orthopaedic Laboratory, University of Pennsylvania, Philadelphia, PA  
 soslowsky@upenn.edu

**Disclosures:** Pardes AM (N), Rodriguez AB (N), Freedman BR (N), Fryhofer GW (N), Soslowsky LJ (N)

**Introduction:** Achilles tendon injuries are most common in middle-aged men, especially those involved in recreational sports. Increased tendon stiffness, decreased blood flow, and lack of regular physical activity have been suggested as potential causes for the high incidence of ruptures in this age group, although clinical evidence is conflicting [1-3]. Animal models offer a highly controlled system to study Achilles tendon biomechanics, and have demonstrated a potential explanation for the disparate incidence in Achilles tendon rupture across sex [4]. However, it is unknown if aging also alters Achilles tendon mechanical behavior that could help explain the particularly high frequency of Achilles tendon ruptures in middle-aged men. Therefore, the objective of this study was to identify functional, mechanical, and structural differences among Achilles tendons from young, middle aged, and old male rats. We hypothesized that middle aged and old rats would exhibit increased joint stiffness and decreased Achilles tendon material quality compared to young rats.

**Methods:** *Design:* Young (7 mo), middle aged (18 mo), and old (27 mo) male F344XBN rats, approximating respective human ages of 18, 41, and 60 years, were acquired from the National Institute of Aging (n=16/group) (IACUC approved) and euthanized three weeks after arriving [5]. *Gait analysis:* Animals (n=12-16/group) were acclimated to an instrumented walkway, and spatial, temporal, and kinetic parameters were quantified during autonomous locomotion [6]. *Passive joint function:* Ankle range of motion (ROM) and stiffness were measured using a custom device while animals (n=16/group) were anesthetized [6]. *Sample preparation:* Following euthanasia, Achilles tendon-foot units were harvested and either processed for histological assays or frozen until preparation for structural and mechanical analysis. *High frequency ultrasound (HFUS):* B-mode images of tendons (n=11-12/group) were captured and analyzed to determine tendon matrix alignment and density [6]. *Mechanical testing:* Samples (n=11-12/group/protocol) were tested to evaluate failure properties (ramp to failure with optical strain tracking) or viscoelastic and fatigue properties (stress relaxation, frequency-sweep, fatigue testing). *Statistics:* One-way ANOVAs were used to compare groups, and significant relationships ( $p<0.05$ ) were further evaluated using post hoc Student's t-tests with Bonferroni corrections, except for cycles completed (where non-parametric Kruskal-Wallis test with Dunn's post hoc tests were used).

**Results:** Gait analysis revealed that propulsion force decreased and lateral force increased with increasing age (Fig. 1A-B). Animals also took slower, wider, and shorter steps as they aged (not shown). Aging resulted in increased plantarflexion stiffness and decreased range of motion (Fig. 1C-D). HFUS analysis showed no differences in tendon organization or density (not shown). Although tendon area was significantly increased in middle aged and old compared to young animals (Fig. 2A), stiffness and max load were not different between groups (not shown). Conversely, Achilles tendon max stress and modulus were superior in young animals (Fig. 2B-C). Dynamic modulus was greater in the young group compared to middle aged and old animals at all frequencies tested (not shown). Viscoelastic properties (percent relaxation,  $\tan(\delta)$ ) were not different between groups, as well as most fatigue properties (peak strain, laxity, secant stiffness) (not shown). Young animals exhibited decreased fatigue life, but increased hysteresis (trend, 1500 cycles) and secant modulus (50 cycles) (Fig. 2D-F).

**Discussion:** This study identified numerous functional and mechanical differences in the Achilles tendons of young, middle aged, and old rats. Most notably, the young tendons exhibited the greatest material quality (max stress, modulus), which could help explain why younger individuals experience fewer Achilles tendon ruptures than middle aged adults. Interestingly, older rats demonstrated impairments in ankle joint function similar to those observed in humans [7-8]. Increased calf muscle activation and metabolic cost of walking during gait in the elderly may be a compensatory mechanism to overcome passive plantarflexion stiffness and could potentially lead to overtraining and subsequent injury of an already mechanically inferior tendon [9-11]. However, this requires further investigation in a more clinically relevant age group and during more challenging physical activity. We did not detect age-related differences in tendon low-strain viscoelastic properties, although such differences may be present in the entire Achilles tendon-muscle unit [5]. The similar tendon macrostructure observed by HFUS in the current study indicates that age-specific mechanical differences may primarily be the result of altered composition or microstructure, rather than matrix degeneration as a result of increased MMP activity as has been previously suggested [12]. Lastly, the decreased fatigue life of the younger tendons is likely explained by their decreased cross-sectional area, as they consequently experienced greater peak cyclical stress during load-controlled fatigue testing. We are currently investigating Achilles tendon histological properties and muscle composition in this aging model.

**Significance:** This study supports a potential explanation of the increased incidence of Achilles tendon rupture in the active middle-aged population. Additionally, our results provide a foundation for future studies on potential age-specific responses of the Achilles tendon-muscle unit to loading or injury.

**Acknowledgements:** The authors thank C Hillin, C Riggan, and Z Beach for their contributions and the NIH/NIAMS (R01AR064216S2, P30AR069619), NIH/NCATS (TL1TR000138), and NSF GRFP for funding support.

**References:** [1] Hess GW. *Foot Ankle Spec*, 2010;3(1). [2] Langberg H. *Eur J Appl Physiol*, 2001;84(3). [3] Lenskjold A, et al. *Scand J Med Sci Sports*, 2015;25(1). [4] Pardes A, et al. *Ann Biomed Eng*, in press, 2016. [5] Plate JF, et al. *J Biomech*, 2013;46(3). [6] Freedman BR, et al. *J Orthop Res*, in press, 2016. [7] Devita P, et al. *Med Sci Sports Exerc*, 2016;48(1). [8] Menz HB. *Gerontology*, 2015;61(4). [9] Schmitz A, *J Electromyog Kinesiol*, 2009;19(6). [10] Mian OS, et al. *Acta Physiol*, 2006;186(2). [11] Mian OS, et al. *Acta Physiol*, 2007;189(1). [12] Yu TY et al. *BMC Musculoskelet Disord*, 2013;14(2).

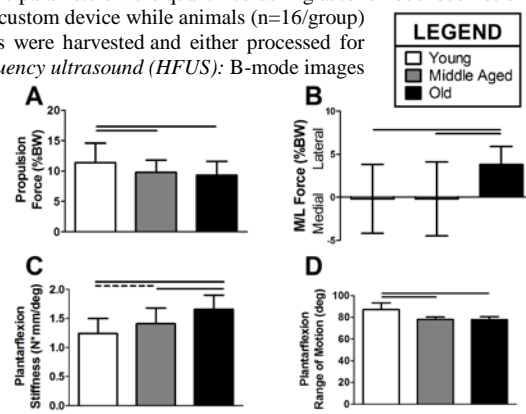


**Figure 1 – Ankle function.** (A) Propulsion force decreased and (B) lateral force increased with increasing age during gait. Passive motion analysis revealed greater ankle joint (C) stiffness and inferior (D) range of motion in middle-aged and old rats. Data presented as mean and standard deviation. Solid lines indicate significant differences ( $p<0.017$ ), dashed lines indicate trends ( $p<0.10$ ).

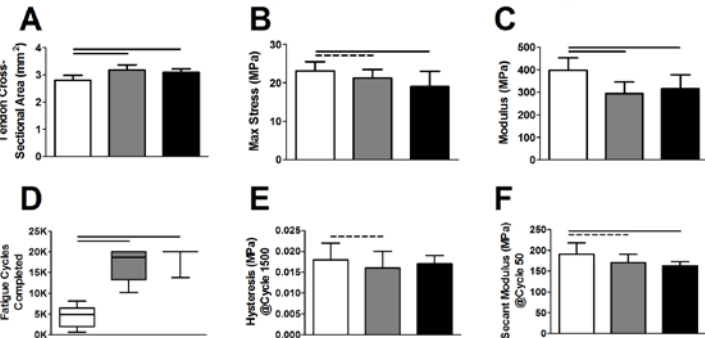


**Figure 2 – Achilles tendon mechanical properties.** Young animals had the smallest (A) tendon area and greatest (B-C) quasi-static material properties, though they also had the shortest (D) fatigue life. Tendons from the young group increased (E) hysteresis after 1500 cycles and (F) secant modulus after 50 cycles. Data presented as mean and standard deviation, except fatigue cycles completed (five number summary box plot). Solid lines indicate significant differences ( $p<0.017$ ), dashed lines indicate trends ( $p<0.10$ ).

P5

## **Post-Injury Biomechanics of Achilles Tendon Vary By Sex and Hormone Status**

**Authors:** George W. Fryhofer<sup>1</sup>, Benjamin R. Freedman<sup>1</sup>, Cody D. Hillin<sup>1</sup>, Nabeel S. Salka<sup>1</sup>, Adam M. Pardes<sup>1</sup>, Stephanie N. Weiss<sup>1</sup>, Daniel C. Farber<sup>2</sup>, Louis J. Soslowsky<sup>1</sup>

**Affiliation:** <sup>1</sup> McKay Orthopaedic Laboratory, University of Pennsylvania, Philadelphia, Pennsylvania

<sup>2</sup> Department of Orthopaedic Surgery, University of Pennsylvania, Philadelphia, Pennsylvania

**Study approved by:** University of Pennsylvania IACUC.

**Grants:** This study was funded by NIH/NIAMS R01AR064216S1, the NIH/NIAMS supported Penn Center for Musculoskeletal Disorders (P30 AR069619), the NIH/NCATS (TL1TR000138), the NIH/NIAMS T32AR007132, and NSF GRFP.

### **ABSTRACT**

Achilles tendon ruptures are common injuries. Sex differences are present in mechanical properties of uninjured Achilles tendon, but it remains unknown if these differences extend to tendon healing. We hypothesized that ovariectomized females (OVX) and males would exhibit inferior post-injury tendon properties compared to females. Male, female, and OVX Sprague-Dawley rats ( $n = 32/\text{group}$ ) underwent acclimation and treadmill training prior to blunt transection of the Achilles tendon mid-substance. Injured hindlimbs were immobilized for 1 week, followed by gradual return to activity and assessment of active and passive hindlimb function. Animals were euthanized at 3 or 6 weeks post-injury to assess tendon structure, mechanics, and composition. Passive ankle stiffness and range of motion were superior in females at 3 weeks; however, by 6 weeks, passive and active function were similar in males and females but remained inferior in OVX. At 6 weeks, female tendons had greater normalized secant modulus, viscoelastic behavior, and laxity compared to males. Normalized secant modulus, cross-sectional area and tendon glycosaminoglycan composition were inferior in OVX compared to females at 6 weeks. Total fatigue cycles until tendon failure were similar among groups. Post-injury muscle fiber size was better preserved in females compared to males, and females had greater collagen-III at the tendon injury site compared to males at 6 weeks. Despite male and female Achilles tendons withstanding similar durations of fatigue loading, early passive hindlimb function and tendon mechanical properties, including secant modulus, suggest superior healing in females. Ovarian hormone loss was associated with inferior Achilles tendon healing.

## Direct Investigation of the Roles of Decorin in Cartilage Pericellular Matrix via Immunofluorescence-guided AFM

Daphney R. Chery<sup>1</sup>, Samuel J. Rozans<sup>1</sup>, Biao Han<sup>1</sup>, Ling Qin<sup>2</sup>, David E. Birk<sup>3</sup>, Renato V. Iozzo<sup>4</sup>, Motomi Enomoto-Iwamoto<sup>5</sup>, Lin Han<sup>1</sup>

<sup>1</sup>Drexel University, Philadelphia, PA; <sup>2</sup>University of Pennsylvania, Philadelphia, PA; <sup>3</sup>University of South Florida, Morsani College of Medicine, Tampa, FL; <sup>4</sup>Thomas Jefferson University, Philadelphia, PA; <sup>5</sup>The Children's Hospital of Philadelphia, Philadelphia, PA.

**Disclosures:** Daphney R. Chery (N), Samuel J. Rozans (N), Biao Han (N), Ling Qin (N), David E. Birk (N), Renato V. Iozzo (N), Motomi Enomoto-Iwamoto (N), Lin Han (N).

**INTRODUCTION:** The pericellular matrix (PCM) of cartilage is a  $\approx 5 \mu\text{m}$ -thick layer surrounding each chondrocyte, which regulates the biomechanical microenvironment of chondrocytes [1] and protects chondrocytes from overloading [2], while the territorial and interterritorial extracellular matrices (T/IT-ECM) between cell lacunae are directly responsible for overall mechanical functions [3]. The PCM is composed of localized collagen VI in the form of beaded filaments [4] and perlecan [5], as well as other non-fibrillar proteins [6]. Currently, the exact contribution of each molecular constituent to the PCM properties is unclear. Recently, the role of collagen VI in the PCM was studied by the application of immunofluorescence (IF)-guided AFM [7] to cross-sections of collagen VI-deficient (*Col6a1*<sup>-/-</sup>) murine cartilage [8]. In this seminal work, the PCM of *Col6a1*<sup>-/-</sup> cartilage showed much reduced modulus, despite that the T/IT-ECM appeared to be normal [8]. Our recent studies discovered the indispensable roles of decorin, a class I small leucine rich proteoglycan (SLRP), in the properties of articular cartilage ECM [9]. To this end, we hypothesize that decorin also exerts an important role to the PCM properties. By combining tape-assisted cryo-sectioning that is applicable to mineralized tissues [10] and IF-guided AFM, we developed a new method to directly measure the mechanical properties of murine knee cartilage PCM and examined the impacts of decorin deficiency on the PCM properties.

**METHODS:** Femoral condyles were harvested from male wild-type (WT) and decorin-null (*Dcn*<sup>-/-</sup>) mice at both immature (2-week old) and mature (3-month old) ages ( $n = 3$  from each genotype and age). The condyle was then embedded in OCT. Kawamoto's tape-assisted cryo-sectioning [10] was applied to obtain  $\approx 5\text{-}\mu\text{m}$ -thick, unfixed sagittal sections containing both untreated cartilage and subchondral bone. Following established procedures [7], the cryo-sections were stained by immunofluorescent antibodies specific for collagen VI. Using the Total Internal Reflection Fluorescence (TIRF)-AFM (MFP-3D, Asylum Research), we performed nanoindentation ( $R \approx 2.5 \mu\text{m}$ ,  $k \approx 5.4 \text{ N/m}$ ,  $15 \mu\text{m/s}$  rate) in PBS with the guidance of type VI collagen fluorescence imaging to distinguish the PCM versus T/IT-ECM (Fig. 1a). Within each region of interest, nanoindentation was performed as a  $40 \times 40$  grid (1,600 indents) over a  $20 \times 20 \mu\text{m}^2$  region containing both the PCM and the T/IT-ECM of the middle/deep zone uncalcified cartilage. From each indentation curve, effective indentation modulus,  $E_{\text{ind}}$ , was calculated via the finite thickness-corrected Hertz model [11].

**RESULTS:** IF images detected distinctive rings of collagen VI -concentrated PCM surrounding each chondrocyte in both WT and *Dcn*<sup>-/-</sup> murine cartilage (Fig. 1a). Guided by the IF-imaging, from each nanoindentation modulus map, the regions corresponding to the T/IT-ECM versus PCM were registered via our custom Matlab program, and each region was analyzed separately (Fig. 1b). Within each genotype and age, modulus of the PCM was found to be significantly lower than that of the T/IT-ECM. When compared across genotypes, both the PCM and T/IT-ECM of *Dcn*<sup>-/-</sup> cartilage had significantly lower moduli than WT at both ages (Fig. 1c). In addition, in WT cartilage, the impacts of maturation were apparent in the modulus increase from 2 weeks to 3 months of age in both the PCM and the T/IT-ECM. For *Dcn*<sup>-/-</sup> mice, however, while a significant increase was observed in the T/IT-ECM, the modulus of PCM was similar between the two ages (Fig. 1c).

**DISCUSSION:** This study discovered a critical role for decorin in the normal functioning of cartilage PCM. The involvement of decorin in PCM organization is indicated by its binding activities. It can connect collagen VI with collagen II and aggrecan core protein through matrilins [12,13]. To this end, this study provides direct evidence supporting that a loss of decorin leads to significantly weakened mechanical properties of the PCM, in addition to its impacts on the T/IT-ECM. Furthermore, in *Dcn*<sup>-/-</sup> mice, the lack of an increase in PCM modulus during maturation is also distinctive from the WT PCM. This suggests that decorin's influence on PCM is not only at the early stage of skeletal development, but also throughout maturation. It is possible that decorin can influence the PCM properties through both its binding activities in the matrix, and through regulating chondrocytes synthesis activities. Our ongoing studies aim to reveal the exact mechanism of decorin's roles in the PCM. However, these observations clearly suggest that decorin is an essential component of cartilage matrix, responsible for both direct mechanical function in the cartilage ECMs, as well as specific regional cell biomechanical differences in the PCM.

The combination of tape-assisted cryo-sectioning and IF-guided AFM offers a new method to study cartilage PCM in mice. Importantly, applicability of this test to mature murine knee cartilage enables future studies of PCM not only in uncalcified cartilage, but also in calcified cartilage. For example, knee cartilage is the focus of studies on post-traumatic OA [14], this new approach enables direct examination of injury-induced changes in the PCM of hypertrophic chondrocytes, which could yield new targets for early OA detection and rescue.

**SIGNIFICANCE:** This study discovered an important role of decorin in cartilage PCM mechanical properties. The new nanomechanical method holds great potential in studying PCM changes in various murine models of cartilage development and OA.

**REFERENCES:** [1] Guilak, F et al., *J. Biomech.* 33:1663-1673, 2000. [2] Poole, CA et al., *J. Orthop. Res.* 5:509-522, 1987. [3] Maroudas, A. 1979. In *Adult Articular Cartilage*. 215-290. [4] Soder, S et al., *Osteoarthr. Cartilage* 10:464-470, 2002. [5] Melrose, J et al., *J. Biol. Chem.* 281:36905-36914, 2006. [6] Wilusz, RE et al., *Matrix Biol.* 39:25-32, 2014. [7] Wilusz, RE et al., *J. Royal Soc. Interface* 9:2997-3007, 2012. [8] Zelenski, NA et al., *Arthritis Rheum.* 67:1286-1294, 2015. [9] Doyran, B et al., *Trans. ORS* 62:491, 2016. [10] Kawamoto, T et al., *Methods Mol. Biol.* 1130:149-164, 2014. [11] Dimitriadis, EK et al., *Biophys. J.* 82:2798-2810, 2002. [12] Wiberg, C et al., *J. Biol. Chem.* 276:18947-18952, 2001. [13] Wiberg, C et al., *J. Biol. Chem.* 278:37698-37704, 2003. [14] Anderson, DD et al., *J. Orthop. Res.* 29:802-809, 2011.

**ACKNOWLEDGEMENTS:** This work was supported by the National Institutes of Health (AR066824), and the U.S. Department of Education iCare for Healthcare Fellowship (DRC).

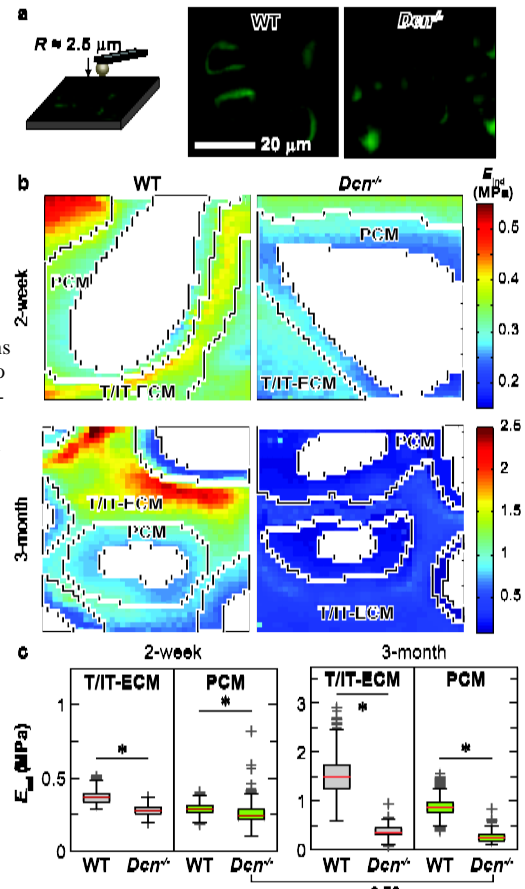


**Fig. 1** **a)** Immunofluorescence Images of type VI collagen identifies cartilage pericellular matrix (PCM) in both WT and *Dcn*<sup>-/-</sup> mice (shown for 2-week old murine cartilage). **b)** Typical Indentation modulus maps ( $20 \times 20 \mu\text{m}^2$ ) of 2-week and 3-month old WT and *Dcn*<sup>-/-</sup> murine cartilage cross-sections prepared via tape-assisting cryo-sectioning. The T/IT-ECM and PCM regions were distinguished by IF-images. **c)** Box-and-whisker plot of all Indentation modulus measured ( $n = 3$  each genotype and age). \*:  $p < 0.0001$  for WT versus *Dcn*<sup>-/-</sup>. In addition, modulus of the PCM was significantly lower than T/IT-ECM in all mice, and significant age-dependence was found in all tested regions, except for the PCM in *Dcn*<sup>-/-</sup> mice.  $p = 0.78$

## Temporal healing response of Achilles tendons in rodents following injury depends on surgical treatment and return to activity time

Benjamin R. Freedman, Tyler R. Morris, Nabeel S. Salka, Joshua A. Gordon, Adam M. Pardes, Corinne N. Riggan, Courtney A. Nuss, Jennica J. Tucker, Pankti R. Bhatt, George W. Fryhofer, Daniel C. Farber, Louis J. Soslowsky  
McKay Orthopaedic Laboratory, University of Pennsylvania, Philadelphia, PA

**Disclosures:** Benjamin R. Freedman (N), Tyler M. Morris (N), Courtney N. Nuss (N), Corinne N. Riggan (N), Nabeel S. Salka (N), Joshua A. Gordon (N), Aricia Shen (N), Daniel C. Farber (N), Louis J. Soslowsky (Funding from Orthofix and DJO)

**INTRODUCTION:** Achilles tendon ruptures are devastating injuries that affect 8.3 in 100,000 people yearly [1]. Despite the higher risk for complications and increased costs, operative treatment has historically been believed to provide superior outcomes compared to non-operative treatment in terms of function and re-rupture rates [2]. However, recent studies have suggested that surgical treatment for Achilles ruptures is not necessarily superior [3, 4]. To elucidate the basic mechanical and structural mechanisms governing these clinical outcomes, it is necessary to evaluate the role of various surgical and rehabilitation strategies on tendon quality and function in a controlled model system. Therefore, the objective of this study was to investigate the effects of surgical repair and limb immobilization on Achilles healing and ankle joint function following complete tendon transection in a rat model. We hypothesized that surgical treatment and aggressive rehabilitation would result in superior Achilles tendon mechanical, structural, and functional properties following injury.

**METHODS:** Study Design: Sprague Dawley rats (n=108) received 2 weeks of treadmill exercise training (up to 60 minutes at 10m/min) [5] (IACUC approved) prior to surgical removal of the right central plantaris longus tendon and blunt mid-substance transection of the right Achilles tendon. Animals were then randomized into repaired (R) (Modified Kessler approach) (n=54) or non-repaired (NR) (n=54) groups, and all hind limbs were immobilized in plantar flexion. These groups were further divided into aggressive (Agg), moderate (Mod), or conservative (Con) rehabilitation (**Fig.1**). Functional evaluation (n=18/group) of passive ankle joint range of motion (ROM) and stiffness was completed using a custom torque cell and accelerometer-based device on anesthetized animals [5]. All assays were performed after 6 weeks of healing. Ex vivo Assays: After sacrifice, the Achilles tendon-foot complex was carefully removed *en bloc*, fine dissected, measured for cross sectional area, and secured in fixtures. Tendons were then loaded at 1N in a PBS bath while a series of sagittal B-mode high frequency ultrasound images (HFUS) were acquired using a 40MHz scanner (Vevo 2100, MS550D; VisualSonics) (n=10-11/group) [6]. Tendons were then mechanically tested and imaged (n=10-11/group) with a protocol consisting of stress relaxation (6% strain), a low-load dynamic frequency sweep (0.1 to 10 Hz), and fatigue testing (~10-75% of ultimate failure load) at 2Hz using a sinusoidal waveform until failure (Instron Electropuls 3000). Analysis: Functional ankle joint properties (i.e., ankle ROM and stiffness) for both dorsiflexion and plantar flexion were evaluated. Achilles tendon percent relaxation, dynamic modulus, tan $\delta$ , toe and linear modulus, hysteresis, cycles to failure, and laxity were computed from mechanical and optical testing data. Echogenicity and collagen fiber alignment were evaluated from the HFUS images for the injury region [6]. Two-way ANOVAs with post hoc Fisher's tests were used to evaluate the effects of surgical treatment and rehabilitation on mechanical, functional, and structural properties.

**RESULTS:** After 6 weeks of healing, the plantar- (data not shown) and dorsi-flexion ROM was superior in aggressively rehabilitated animals, closer to pre-injury values (**Fig.2**). Aggressively rehabilitated animals had dorsiflexion toe stiffness values closer to pre-injury values compared to the moderate rehabilitation group. No changes in plantarflexion toe or linear stiffness, or dorsiflexion linear stiffness were observed. Tendon cross sectional area was higher in repaired tendons, and this effect was exacerbated in animals with aggressive rehabilitation. Mechanical property evaluation revealed an increase in the toe modulus in non-repaired aggressively rehabilitated tendons, but no changes in the percent relaxation or dynamic properties. Marked differences in quasi-static linear modulus and fatigue properties were observed (**Fig.3**) ( $p<0.05$ ). Specifically, non-repaired tendons with aggressive and moderate rehabilitation had an increased linear modulus and number of cycles to failure (**Fig.3**) ( $p<0.05$ ). Additionally, the number of cycles to failure was greatest in the aggressively rehabilitated group. Non-repaired tendons experienced more laxity through 5% fatigue life compared to repaired tendons in aggressive and moderate rehabilitation, and transitioned to the secondary phase of fatigue life earlier ( $p<0.05$ ) (data not shown). Ultrasound evaluation revealed an effect of rehabilitation, but not surgical treatment type, on increased matrix echogenicity, a surrogate measure of fiber density, and alignment ( $p<0.05$ ) (data not shown).

**DISCUSSION:** Achilles tendon healing following a variety of common clinical treatment methods was evaluated after 6 weeks of healing in a rat model. We discovered a mechanism whereby non-repaired tendon fatigue properties had marked improvements in the number of cycles to failure. This work suggests the functional and mechanical benefits of aggressive rehabilitation on Achilles tendon healing following a variety of treatment paradigms [7]. Ultrasound evaluation showed promise to detect changes in healing capacity between groups with different rehabilitation strategies. Although the conservative rehabilitated tendons had higher echogenicity and alignment compared to other groups, they also had lower cross sectional area, which likely limited the capacity of the more aligned tendon to withstand fatigue loading. Future work will relate organizational measures from HFUS to tendon fatigue mechanical properties. Additional ongoing studies will evaluate the long-term effects of these treatment and rehabilitation paradigms.

**SIGNIFICANCE:** This study demonstrates that aggressive rehabilitation with nonsurgical management leads to improved tendon fatigue mechanics and ankle function after 6 weeks of healing in this rat Achilles tendon injury model. Ultrasound evaluation showed promise to detect changes in healing capacity between groups.

**ACKNOWLEDGEMENTS:** We acknowledge financial support from NIH/NIAMS R01AR064216, NIH/NIAMS P30AR069619, and the NSF GRFP. We thank Adam Pardes, Jennica Tucker, Bob Zanes, James Cirone, and Joanna Fried for assistance.

**REFERENCES:** [1] Suchak AA et al., 2005. *FAI*, 26(11) 932-6. [2] Freedman BR et al., 2014. *MLTJ*, 4(2) 245-255. [3] AAOS Guidelines for Achilles Tendon Repair, 2009. [4] Soroceanu et al., 2012. *JBJS* 94(23):2136-43. [5] Peltz CD et al., 2010. *JOR* 28(7): 841-5. [6] Riggan CN et al., 2014. *JBiomech Eng*, 136(2):21-29. [7] Olsson N, et al., 2013. *AJSM*, 41(12):2867-76.

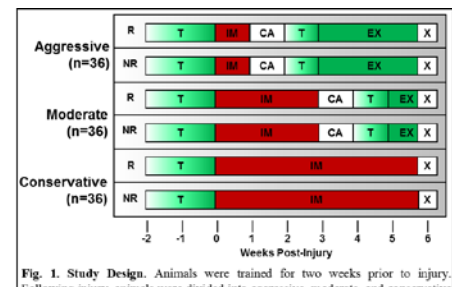


**Fig. 1. Study Design.** Animals were trained for two weeks prior to injury. Following injury, animals were divided into aggressive, moderate, and conservative rehabilitation groups. Definitions: CA- cage activity; T- treadmill training; IM- immobilization; EX- exercise; R- repaired, NR-non-repaired, X-sacrifice.

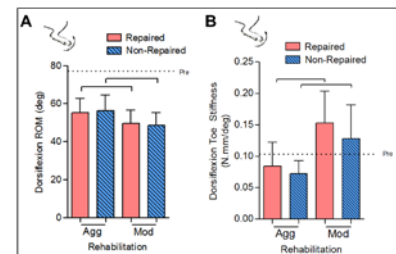


**Fig. 2. Ankle joint range of motion (ROM) and stiffness functional outcomes.** Rehabilitation was a significant factor ( $p<0.05$ ) on dorsiflexion ROM (A) and toe-stiffness (B) after 6-weeks of healing. Data shown as mean  $\pm$  standard deviation. Lines indicate significant differences ( $p<0.05$ ). Pre-presurgery values.

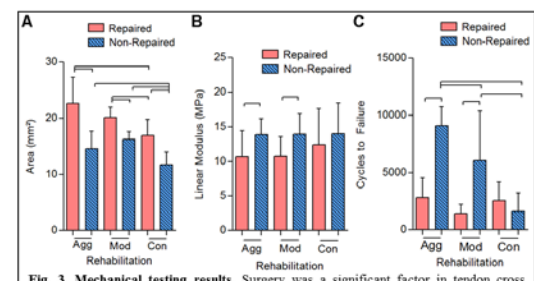


**Fig. 3. Mechanical testing results.** Surgery was a significant factor in tendon cross sectional area (A), linear modulus (B), and cycles to failure (C) ( $p<0.05$ ). Rehabilitation was a significant factor in tendon cross sectional area and cycles to failure (A,C) ( $p<0.05$ ). Data shown as mean  $\pm$  standard deviation. Lines indicate significant differences ( $p<0.05$ ).

## Engineered Endplates Enhance the *In Vivo* Performance of a Replacement Disc-Like Angle Ply Structure (DAPS)

Sarah E. Gullbrand,<sup>1</sup> John T. Martin,<sup>1</sup> Beth G. Ashinsky,<sup>1</sup> Dong Hwa Kim,<sup>1</sup> Lachlan J. Smith,<sup>1</sup> Dawn M. Elliott,<sup>2</sup> Harvey E. Smith,<sup>1</sup> Robert L. Mauck<sup>1</sup>

<sup>1</sup>University of Pennsylvania, Philadelphia, PA and Philadelphia VA Medical Center, Philadelphia, PA, <sup>2</sup>University of Delaware, Newark, DE

**Disclosures:** None

**Introduction:** Intervertebral disc degeneration involves a progressive cascade of cellular, compositional and structural changes.<sup>1</sup> Surgical treatment of disc degeneration is most commonly achieved via fusion of the degenerated motion segment, which does not restore native disc structure or function, and may exacerbate degeneration of adjacent discs.<sup>2</sup> For the treatment of advanced degeneration, total disc arthroplasty with a cellular, engineered replacement is a promising alternative to fusion; a viable, functional substitute may restore normal mechanics to the degenerated spine. To that end, our lab has created disc-like angle ply structures (DAPS) that mimic the structure and function of the native disc by combining an electrospun nanofibrous annulus fibrosus (AF) with a hydrogel nucleus pulposus (NP).<sup>3</sup> We have previously shown that while the DAPS are mechanically functional following *in vivo* implantation in the rat caudal disc space, the constructs do not integrate with the adjacent vertebral bodies and exhibit progressive reductions in MRI T2 signal and NP proteoglycan content.<sup>4</sup> Here, we report on the *in vivo* performance of an endplate DAPS (eDAPS) implant that was designed to improve construct integration and promote retention of implant composition via the addition of acellular porous polymer endplates.

**Methods:** *eDAPS Fabrication and Culture:* DAPS sized for the rat caudal disc space were fabricated by concentrically wrapping aligned, angled strips of electrospun poly( $\epsilon$ -caprolactone) (PCL) nanofibers to form the AF region, and filling the center with a hyaluronic acid hydrogel to form the NP region. Both regions were seeded with bovine disc cells ( $2 \times 10^6$  cells/AF and  $6 \times 10^5$  cells/NP) and cultured separately for two weeks in chemically defined media containing TGF- $\beta$ 3. After two weeks of culture, the AF and NP regions were combined, and acellular porous PCL endplates, (4 mm diameter, 1.5 mm high) fabricated via salt leaching, were apposed to each side of the DAPS to form the eDAPS construct (acellular construct viewed by  $\mu$ CT, Figure 1A). The eDAPS were cultured for an additional three weeks for a total of 5 weeks preculture. *Implantation Surgery:* Athymic male retired breeder rats were anesthetized, and kirschner wires were passed through the C8 and C9 caudal vertebral bodies allowing the placement of a ring-type external fixator.<sup>3</sup> eDAPS were implanted following removal of the C8-C9 disc and a partial corpectomy of the adjacent vertebral bodies. Rats were euthanized at 7 (n=3), 17 (n=3) and 35 (n=7) days. *Magnetic Resonance Imaging:* T2 mapping of the eDAPS was performed at 4.7T (16 echoes, TE/TR = 7.84 ms/2,000 ms, FOV = 15x15 mm<sup>2</sup>). Average T2 maps were generated for each time point using a custom MATLAB code.<sup>5</sup> Significant differences in eDAPS T2 values at each time point compared to native discs were assessed via a one-way ANOVA, with Tukey's posthoc test. *Mechanical Testing and Biochemistry:* Four vertebra-eDAPS-vertebra motion segments 35 days post-implantation, and four native rat tail motion segments, were subjected to mechanical testing (20 cycles, 0 to -3N/-0.3 MPa, 0.05 Hz). Displacement was tracked optically using a high resolution digital camera and a custom texture tracking MATLAB code. The 20<sup>th</sup> cycle of the force-displacement curve was used to calculate the toe and linear region compressive moduli, and transition and maximum strains via a bilinear fit. Significant differences in biomechanical parameters between native and eDAPS implanted motion segments were assessed via a Student's t-test. Following mechanical testing, the eDAPS were dissected from the motion segment, separated into NP, AF and EP regions, and digested with proteinase-K. Glycosaminoglycan (GAG) content was quantified via the DMMB assay. *Histology:* Vertebra-eDAPS-vertebra motion segments were fixed, decalcified and processed through paraffin. Sections were stained with Alcian blue (proteoglycans) and picrosirius red (collagen), and the cell nuclei stained with DAPI.

**Results:** The NP and AF T2 relaxation times of the eDAPS were superphysiologic 7 days after implantation into the rat caudal disc space; the T2 values decreased from 7 to 17 days post-implantation. AF T2 values remained superphysiologic up to 35 days *in vivo* (data not shown), while NP T2 values at 17 and 35 days *in vivo* were not different from the NP T2 of native rat tail discs (Fig 1B). The maintenance of NP T2 signal corresponded with robust Alcian blue staining in the NP region of the eDAPS at 35 days post-implantation. DAPI staining illustrated infiltration of the acellular PCL foam endplate from the AF and NP regions of the eDAPS, in addition to infiltration of native cells from the adjacent vertebral body (Fig 1D). DAPI staining also indicated sustained cellularity of the AF and NP regions of the eDAPS from 7 days to 35 days *in vivo*. After 35 days *in vivo*, GAG content was highest in the NP region of the eDAPS ( $0.27\% \pm 0.14\%$  ww), followed by the AF region ( $0.11\% \pm 0.01\%$  ww) and EP region ( $0.03\% \pm 0.006\%$  ww). The toe and linear region moduli of the eDAPS implanted motion segments were not significantly different from native discs. However, the transition and maximal strains were significantly higher in the eDAPS implanted motion segments compared to native (Fig 1C).

**Discussion:** Overall, the addition of engineered endplates improved integration and maintenance of DAPS matrix composition *in vivo*. This is in contrast with our previous findings, in which DAPS implanted without endplates were characterized by a lack of integration with adjacent vertebral bodies and progressive loss of NP T2 signal and proteoglycan content.<sup>4</sup> The improved *in vivo* performance of the eDAPS may be due in part to the PCL endplates serving as a barrier to the harsh native environment. eDAPS toe and linear region moduli were similar to that of native tissue, indicating the potential of this engineered implant for functional restoration of motion segment mechanics. Ongoing work will investigate longer durations of *in vivo* implantation, as well as remobilization strategies to further enhance integration and *in vivo* maintenance.

**Significance:** Current surgical strategies for disc degeneration do not restore native structure and function to the spine. A biologic total disc replacement that better integrates with surrounding tissue (while maintaining composition and mechanical function in the native environment) will significantly improve the standard of care for patients with low back pain.

**References:** <sup>1</sup>CDC. MMWR, 2009 <sup>2</sup>Ghisselli+ JBJS, 2004 <sup>3</sup>Martin+ Acta Biomater, 2014 <sup>4</sup>Martin+ ORS Proceedings, 2016. <sup>5</sup>Martin+ JOR, 2015

**Acknowledgments:** This work was supported by the Department of Veterans' Affairs and the Penn Center for Musculoskeletal Disorders (P30 AR069619).

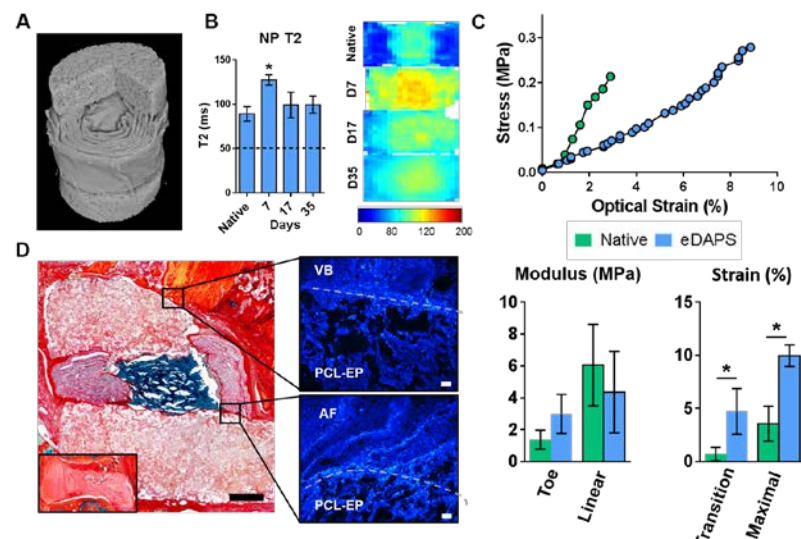


**Figure 1.** (A) 3D  $\mu$ CT reconstruction of an acellular eDAPS, with cut-away illustrating the lamellar AF structure and porous EP. (B) NP T2 values for native rat tail discs and eDAPS from 7 to 35 days *in vivo*, compared to the NP T2 of DAPS alone (dashed line) at 5 weeks. (\* = significantly different from all groups,  $p < 0.05$ ). (C) Stress-strain behavior of native rat tail and eDAPS implanted motion segments. (D) Representative Alcian blue and picrosirius red stained histology of eDAPS implanted for 35 days; DAPI staining illustrates the cellularity of the vertebral body (VB) and EP interface and the AF and EP interface. Inset illustrates the appearance of the DAPS alone at 5 weeks *in vivo*.

# Engineered Nanofiber Crimp Alters Scaffold Mechanics and Mesenchymal Stem Cell Mechanotransduction

Spencer E. Szczesny<sup>1</sup>, Pang-Ching Liu<sup>2</sup>, Tristan P. Driscoll<sup>3</sup>, Robert L. Mauck<sup>1</sup>, Pen-Hsiu G. Chao<sup>2</sup>  
<sup>1</sup>University of Pennsylvania, PA, <sup>2</sup>National Taiwan University, Taipei, Taiwan, <sup>3</sup>Yale University, CT

**Disclosures:** SE Szczesny (N), P Liu (N), TP Driscoll (N), RL Mauck (N), PG Chao (N)

**INTRODUCTION:** Tendons and ligaments are composed of highly aligned collagen fibers that, at the micron-scale, have an intrinsically crimped micro-architecture [1]. This crimping results in a non-linear mechanical response, which provides low-force deformation at small strains (in the so-called ‘toe’ region) and resists excessive deformation via the higher ‘linear region’ modulus that follows [2]. While existing biomaterials can reproduce features of this non-linear response [3], these materials fail to provide the micro-scale topography that cells within these tissues encounter, which may be important for proper mechanobiological signaling. Recently, we developed electrospun nanofibrous scaffolds that exhibit non-linear mechanics and mimic the native crimped fibrous tissue environment [4]. In this study, we used a fiber-reinforced structural constitutive model to characterize the mechanics of these scaffolds as a function of fiber crimp and investigated the effect of crimping on mesenchymal stem cell (MSC) mechanotransduction.

**METHODS:** Composite aligned nanofibrous scaffolds were generated by co-electrospinning poly-L-lactide (PLLA, 8.5% w/v in HFP) and poly(ethylene oxide) (PEO, 10% w/v in 90% EtOH) onto a common rotating mandrel. Composite PLLA/PEO scaffolds were washed (to remove the PEO fiber fraction) or washed and heated to 65° between two glass plates (to induce fiber crimp). Scaffolds were separated into three groups: washed (DW), heated and then washed (DHW), or washed and then heated (DWH). Scanning electron microscopy (SEM) was used to calculate the ratio between the fiber contour and end-to-end lengths, which defines the strain required to uncrimp the fibers. Scaffolds (40x10 mm<sup>2</sup>) were tested in uniaxial tension using a Bose 5500 (n=3-4/grp) either parallel or perpendicular to the fiber direction. The linear modulus was calculated using a bilinear fit and the mechanical data prior to sample yield was fit with a hyperelastic constitutive model incorporating crimped fibers embedded in a neo-Hookean matrix [5,6]. Additional scaffolds (70x5mm<sup>2</sup>) were coated with fibronectin (20ug/ml), seeded with passage 1 bovine MSCs (100k cells), and cultured for 2 days in chemically defined media. Scaffolds were stained with Hoechst (nuclei) in DMEM (20 min; 37° C) and then stretched (n=4/grp) in 1% increments to 8% strain using a microscope-mounted tensile device. Microscale Lagrangian strains were calculated from nuclear triads and a Poisson’s ratio was calculated for each triad. In parallel unstained samples, stretch was applied as above and protein was collected for Western blotting with p44/p42 MAPK (ERK) or phospho-p44/p42 MAPK (pERK) antibodies to determine MAPK/ERK activation. Differences were evaluated via one-way ANOVA and Bonferroni post-hoc tests with p<0.05.

**RESULTS:** Scaffolds that were heat-processed to induce crimp (DHW and DWH) exhibited markedly different mechanical properties compared to the non-heated DW group, with the greatest change observed for the DWH samples (Fig. 1A). The model successfully fit all scaffold groups; however, a non-zero matrix term was required to fit only the DWH samples, given their extensive toe-region (Fig. 1B). Conversely, the DW and DHW groups could also be fit by the crimped fibers alone (data not shown). While SEM measurements showed that fiber crimping increased for the DHW and DWH scaffolds, the fiber uncrimping indicated by the model fits increased only for the DWH group (Fig. 1C). The fiber modulus predicted by the model agreed with the measured linear modulus, which significantly decreased for both heat-processed groups (Fig. 1D). The matrix modulus determined from testing perpendicular to the fiber direction was similar across all groups; however, the matrix modulus determined from testing parallel to the fibers in the DWH group was significantly higher (Fig. 1E). Finally, the Poisson’s ratio was generally comparable between scaffold types (Fig. 1 F). Cells stretched on these scaffolds showed increased ERK phosphorylation with tensile stretch on both the DHW and DWH samples, but not on the DW scaffolds (Fig. 2).

**DISCUSSION:** This study aimed to determine whether the micron-scale crimping produced in nanofibrous scaffolds via heat-processing produced commensurate changes in scaffold mechanics and altered cell mechanotransduction with applied uniaxial stretch. We found that the greatest amount of fiber crimping was generated in the DWH scaffolds, which also exhibited the greatest changes in tensile mechanics, with a large toe-region and significantly reduced fiber modulus. Interestingly, this was the only scaffold group whose mechanical behavior included resistance generated within the non-fibrous matrix (e.g., fiber-fiber interactions). In contrast, the DHW scaffolds, which also exhibited crimped fibers under SEM, had a minimal toe-region and mechanical contribution from the matrix term. This suggests that washing and then heating the scaffolds not only generates greater fiber crimping, but also more fiber-fiber interactions that influence the uncrimping process in response to load. Despite these differences in mechanics with scaffold treatment, cell mechanosensing appeared to be more dependent on local fiber topology and interaction than bulk scaffold mechanics, as increased ERK activation was evident for both the DHW and DWH scaffolds in response to applied stretch. Future work will investigate additional mechanotransduction mechanisms that may lead to functional changes in scaffold maturation during culture as a result of this crimped micro-architecture.

**SIGNIFICANCE:** Micron-scale crimp produced within nanofibrous electrospun scaffolds successfully reproduced the non-linear mechanics of native tissue and provided topological cues that influence cell mechanotransduction. As such, these engineered materials may provide better replication of native tissue structure and biological function.

**REFERENCES:** [1] Rigby+ J Gen Phys (1959); [2] Hansen+ J Biomech Eng (2002); [3] Sahoo+ Biomed Mat (2007); [4] Chao+ Biofabrication. (2014); [5] Szczesny+ J Biomech Eng (2012); [6] Nerurkar+ Spine (2008).

**ACKNOWLEDGMENTS:** This work was supported by the National Institutes of Health (T32 053461 and R01 EB02425).

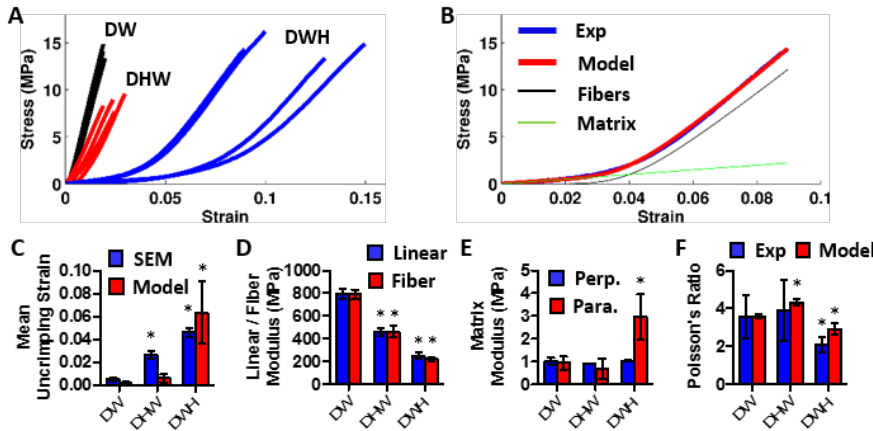


**Fig. 1:** A) Stress-strain response for each scaffold. B) Representative model fit of DWH sample ( $R^2=0.999$ ). C) Mean uncrimping strain increased with heat treatment. D) Linear-region modulus and model fiber modulus decreased with treatment. E) Testing perpendicular to fibers produced similar matrix moduli across all groups but the DWH group exhibited a higher value when tested parallel to fibers. F) Poisson's ratios were consistent between model and experiments. Mean  $\pm$  SD. \*  $p < 0.05$  compared to DW.

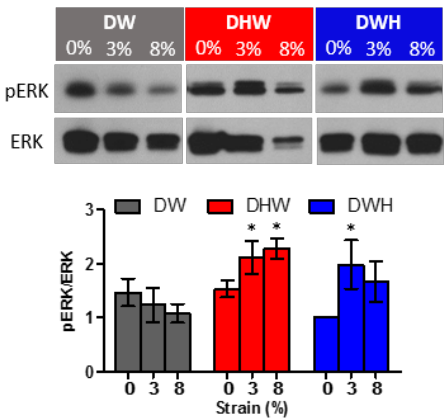


**Fig. 2:** The level of phosphorylated ERK (normalized to total ERK) did not change with strain for the DW group. However, strain applied to both DHW and DWH scaffolds increased ERK activation. Mean  $\pm$  SD. \*  $p < 0.05$  compared to 0%.

# Nuclear Softening Enhances Meniscus Cell Migration into Dense Fiber Networks and Native Tissue

Su Chin Heo<sup>1</sup>, Kwang Hoon Song<sup>1</sup>, Breanna N. Seiber<sup>1</sup>, Feini Qu<sup>1</sup>, Jason A. Burdick<sup>1</sup>, Robert L. Mauck<sup>1</sup>

<sup>1</sup>University of Pennsylvania, Philadelphia, PA

**Disclosures:** Su-Jin Heo (N), Kwang Hoon Song (N), Breanna N. Seiber (N), Feini Qu (N), Jason A. Burdick (N), Robert L. Mauck (N)

**INTRODUCTION:** Cell migration is essential for healing of dense connective tissues [1]. However, the cell nucleus, which is the stiffest organelle in mammalian cells, is an obstacle to efficient migration due to its inability to squeeze through the small pores that typify the dense extracellular matrices (ECM) of these tissues [2]. Modulation of nuclear stiffness is therefore a potential target for enhancing cell mobility. Nuclear mechanics are established in part by the proteins that make up the nuclear lamina, and in part by the packed DNA (chromatin) within [3]. Trichostatin A (TSA) is a histone deacetylase (HDAC) inhibitor that induces hyperacetylation and chromatin relaxation, decreasing nuclear stiffness [3]. We hypothesized that treatment of meniscus cells with TSA would result in more deformable nuclei and thus increase their mobility through both dense fiber networks and the dense ECM of the native tissue. To test these hypotheses, we first developed a novel PDMS/nanofiber membrane cell migration chamber and evaluated whether nuclear softening by TSA pre-treatment improved meniscus cell migration. Next, using sections of adult meniscus, we evaluated whether this same approach could improve meniscus cell migration into native tissue.

**METHODS:** Adult bovine meniscal fibrochondrocytes (MFCs) were seeded on aligned (AL) or non-aligned (NAL) nanofibrous scaffolds ( $2 \times 10^5$  cells, Passage 1) in basal media (BM: DMEM + 10 % FBS) [3]. A subset of scaffolds was treated with TSA (400 nM) for 3 hours. An image-based edge detection algorithm was used to determine the degree of chromatin condensation (the CCP) in individual DAPI stained nuclei [3] with and without TSA treatment. Additionally, constructs were stretched from 0 to 15% grip-to-grip strain on a custom tensile device and the change in nuclear aspect ratio (NAR) was measured with and without TSA pre-treatment [3]. As an initial assessment of MFC migration, a 96-well transwell migration assay was employed, with pore diameters of 3 or 5  $\mu\text{m}$  (Millipore) [4]. To assess cell contractility with and without TSA pre-treatment, MFCs were seeded onto 10 kPa polyacrylamide gels and traction force was measured [5]. To assess cell migration through dense nanofiber networks, a custom-PDMS ‘migration assay chamber’ was implemented. The device consisted of a top reservoir containing BM and a bottom reservoir containing BM + 200 ng/mL PDGF as a chemoattractant (Fig. 2A). Fluorescently labeled (Cell Tracker Red) aligned (AL) or non-aligned (NAL) nanofibrous PCL scaffolds (thickness: ~ 150  $\mu\text{m}$ ) were interposed between the reservoirs, and MFCs (1000 cells, passage 1) were seeded onto the top of each scaffold and cultured in BM with/without TSA for 3 days. At the end of three days, cells were fixed and visualized by actin/DAPI staining. Confocal z-stacks were obtained at 40 $\times$  magnification and maximum z-stack projections were used to assess cellular morphology. The % of infiltrated cells was quantified, with cells located beneath fibers categorized as ‘infiltrated’. To evaluate meniscus cell migration in native tissue, adult meniscus tissue was cryosectioned onto glass slides (~35  $\mu\text{m}$  thick) [4]. To visualize cell invasion, additional living adult meniscal explants (5 mm  $\phi$ ) were incubated in Cell Tracker™ Green for 1 hour and then placed atop the tissue sections to allow for cell egress onto and invasion into the section [4]. These samples were cultured in BM with/without TSA for 48 hours, at which point maximum z-stack projections were acquired and cell infiltration depth was measured as the distance between the apical tissue surface and the basal cell surface [4]. Statistical analysis was performed using ANOVA (with Tukey’s post hoc) or with a Student’s t-test ( $p < 0.05$ ).

**RESULTS:** TSA treatment decreased in the number of visible edges in MFC nuclei (decreased the CCP), indicating efficient relaxation of the chromatin (Fig. 1A, B). When TSA-treated cells were deformed, their nuclei increased in NAR to a greater extent than control cells, indicating a softer nucleus (Fig. 1C). Treatment with TSA also significantly increased MFC migration through both 3 and 5  $\mu\text{m}$  pores in the transwell assay (Fig. 1D). TSA treatment did not, however, alter traction force generation in these cells (data not shown). When MFCs were placed atop scaffolds, the % of cells that had infiltrated was higher in the NAL group than the AL group, and infiltration increased in both groups with TSA treatment (Fig. 2B, C). Of note, compared to control MFCs, TSA treated-cells had more elongated nuclei with higher nuclear aspect ratios (NAR, data not shown). When placed on tissue sections, untreated MFCs (Ctrl) remained primarily on the tissue surface, whereas TSA treated MFCs were found below the tissue surface (Fig. 3A). Quantification showed that MFC infiltration depth was significantly greater with TSA treatment compared to controls (Fig. 3B).

**DISCUSSION:** Endogenous cell recruitment is required for healing of injured dense connective tissues. In this study, we demonstrated that nuclear softening via pharmacological decondensation of chromatin in MFCs enhanced their migration through dense fibrous networks and through native tissue. In a previous study, we had shown that partial enzymatic digestion of the ECM also expedites interstitial cell migration [4]. Together, these findings suggest that decreasing the physical impediments to migration (i.e., the properties of the cells themselves and/or the matrix through which they are traveling) can enhance interstitial cell mobility and foster repair.

**SIGNIFICANCE:** Nuclear softening of meniscus cells increased their interstitial migration in dense fiber networks and in native tissue. This approach may improve dense connective tissue repair by enabling more cells to migrate to and colonize the wound site after injury.

**REFERENCES:** [1] Scarpa+ 2016 J Cell Biol, [2] Davidson+ 2014 Cell Mol Bioeng, [3] Heo+ 2015 Sci Rep, [4] Qu+ 2016 ORS, [5] Driscoll+ 2015 Biophys J.

**ACKNOWLEDGEMENTS:** This work was supported by the National Institutes of Health (AR056624 and EB02425).

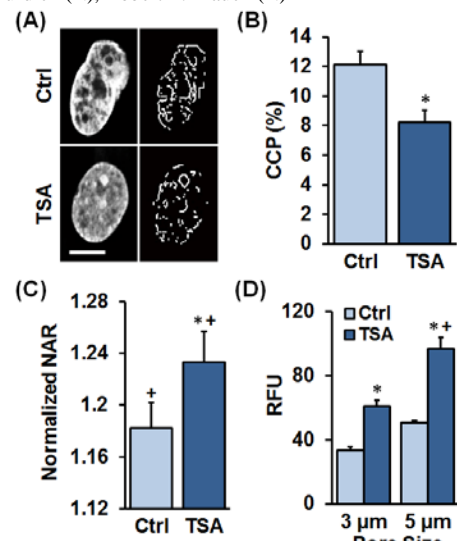


**Fig. 1:** (A) DAPI stained nuclei (left) and corresponding edge detection (right) with/without TSA treatment (Ctrl/TSA, bar = 3  $\mu\text{m}$ ), and quantification of chromatin condensation parameter (CCP, right). (B) Quantification of nuclear deformation (NAR) with 15% scaffold stretch ( $n = -48$ , \* $p < 0.05$  vs. Ctrl, + $p < 0.05$  vs. 0%, normalized 0%). (D) Fluorescence intensity of migrated MFCs in a traditional transwell assay with TSA treatment ( $n = 5$ , \* $p < 0.05$  vs. Ctrl, + $p < 0.05$  vs. 3  $\mu\text{m}$  pore).

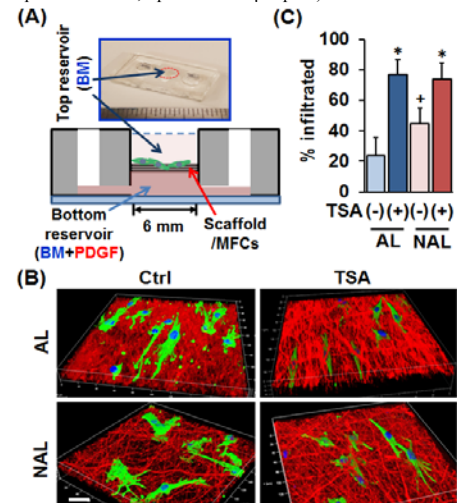


**Fig. 2:** (A) Schematic of PDMS/nanofiber migration chamber. (B) Fluorescent images of cells (green), nuclei (blue), and nanofiber scaffolds (red) with/without TSA treatment (Ctrl/TSA, bar = 20  $\mu\text{m}$ ). (C) Quantification of % infiltrated cells [\* $p < 0.05$  vs. no TSA (-), + $p < 0.05$  vs. aligned scaffold (AL),  $n = -35$ ].

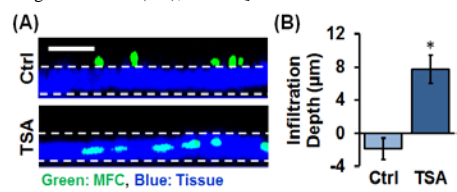


**Fig. 3:** (A) Cross-section view of confocal reconstruction of MFCs (green) migrating through tissue substrates (blue); bar = 50  $\mu\text{m}$ , dashed lines: tissue borders. (B) Quantification of cell infiltration depth ( $n = 45\text{--}70$  cells, \* $p < 0.05$  vs. Ctrl).

## Local discontinuities in aligned fibrous networks reduce tissue-to-nuclear strain transmission

Tonia K. Tsinman,<sup>1</sup> Spencer E. Szczesny,<sup>1</sup> Su-Jin Heo,<sup>1</sup> Dawn M. Elliott,<sup>2</sup> Robert L. Mauck<sup>1</sup>

<sup>1</sup>University of Pennsylvania, Philadelphia, PA; <sup>2</sup>University of Delaware, Newark, DE.

**Disclosures:** none.

**Introduction:** Tensile load bearing soft tissues, such as the knee meniscus, tendon, and the annulus fibrosus of the intervertebral disc, have an anisotropic and hierarchical organization. The extracellular matrix (ECM) of these tissues is comprised of aligned type I collagen whose organization is crucial for proper transmission of loads and strains across the ECM-to-cell length scale and subsequent normal mechanical signaling and homeostasis. During aging and pathologic remodeling, however, the ordered structure of these tissues is often lost. For instance, we recently reported that microscopic proteoglycan-rich domains emerge within the otherwise ordered collagenous ECM of the knee meniscus [1]. These micro-domains, with differing composition and mechanical properties, altered local strain transmission and created heterogeneous mechano-signaling patterns [1]. While the origin of these micro-domains remains to be determined, one hypothesis is that local interruptions of the fibrous architecture (i.e., local micro-damage) change the mechano-biologic stimuli received by resident cell populations, resulting in altered differentiation and matrix accumulation. To begin testing this hypothesis, this study developed an aligned polymer scaffold inclusive of local interruptions in the fibrous architecture in order to probe their impact on both macroscopic and cell scale strain transmission and signaling.

**Methods:** Aligned poly ( $\epsilon$ -caprolactone) (PCL) scaffolds were fabricated by electrospinning 14.3% w/v PCL solution onto a rotating mandrel (as in [2]). Generated scaffolds were segmented into 1 x 6.5cm strips with the prevailing fiber direction oriented in the long axis of the scaffold. Small interruptions in the fibrous architecture were created by introducing two 0.4 cm incisions (oriented perpendicular to the fibers) spaced 2cm apart (Fig. 1a). To map strain at the macro-scale, strips were speckle coated, and grip-to-grip strain was applied in the fiber direction at a rate of 0.5%/s to 25%. Images were acquired during the test (at 15fps) and analyzed using Vic-2D (Correlated Solutions) to determine  $E_{11}$  Lagrangian strain across the sample. At least 200 points per sample were tracked. To determine Lagrangian strain at the cell scale (as well as to measure subcellular deformations), mesenchymal stem cells (MSCs)—isolated from juvenile bovine bone marrow and expanded through passage 1—were seeded onto scaffolds at a density of  $10^5$  cells/scaffold. Prior to seeding, scaffolds were hydrated through an ethanol gradient and coated overnight with 20 $\mu$ g/mL fibronectin. Seeded constructs were cultured for two days in a chemically defined medium to allow for cell attachment. To measure nuclear deformation (denoted as the change in nuclear aspect ratio, NAR, relative to baseline), cell-seeded scaffolds (with and without local incisions) were stained with Hoechst 33342 and uniaxial strain was applied in 3% grip-to-grip strain increments using a custom micromechanical test device mounted on top of an inverted fluorescent microscope [3], and nuclei of selected cells were imaged at 3, 6, 9, 12, and 15% strain steps using a 20X objective. The NAR was defined as the ratio of the long to short axis of the nucleus at each strain step, and was quantified using a custom MATLAB code (n>50 for each group). The same software was used to calculate Lagrangian strains at the cellular level, based on the original and deformed positions of nuclear triads. Statistical differences were established using a two-way ANOVA with Bonferroni post-hoc testing to make comparisons between groups (significance threshold: p<0.05).

**Results:** Strain mapping of intact speckle coated PCL scaffolds demonstrated relatively uniform ‘global’  $E_{11}$  strain distributions that largely matched the magnitude of the applied grip-to-grip strain. As expected, introduction of discontinuities in the aligned fiber network resulted in non-uniform strain fields; most evident at 15% applied strain, where measured  $E_{11}$  strains were substantially diminished in the region located between the two incisions as compared to the outside edges of the scaffold (Fig. 1a). These ECM-level strain field alterations held true at the cellular level as well. Determination of ‘local’ Lagrangian strains through cell nuclei tracking showed similarity between locally and globally measured  $E_{11}$  strains of control and cut scaffolds (Fig. 1b), thus validating nuclear tracking as a method for Lagrangian strain mapping in this experimental system. Significant strain attenuation at the cellular level in the  $E_{11}$  and  $E_{22}$  directions was observed in the middle of the cut region compared to all other locations at all applied grip-to-grip strains (Fig. 2a). Importantly, local strain field perturbations were reflected in differences in nuclear deformation. Cells positioned along fully continuous fibers (uncut scaffolds, edge of cut scaffolds) showed a monotonic increase in NAR up to 23%. In contrast, the NAR of cells seeded in areas containing a fiber discontinuity (middle of cut scaffolds) did not change with the applied strain (Fig. 2b).

**Discussion:** This study shows that local interruptions in scaffolds composed of aligned nanofibers result in localized strain attenuation at the macroscopic (Fig. 1) and microscopic (Fig. 2) level. Diminished strain transfer was particularly evident at length scales relevant to the cellular mechanoresponse. Similar trends in NAR and local strain fields confirmed that strains in the principle directions influence the magnitude of nuclear deformation. Importantly, the local fiber discontinuities effected nuclear deformation *only* in regions within the defect, while cells residing in regions of uninterrupted fibers experienced similar deformations as those of uncut control samples. These data illustrate how local fiber disruption can generate distinct mechanical microenvironments within the same scaffold, with neighboring cells experiencing markedly different mechanical inputs based on local boundary conditions. Based on these data and our previous findings in native and engineered tissues [1], these micro-scale perturbations also likely result in different mechano-response. Future studies will focus on differential cellular mechano-signaling within the heterogeneous regions of these scaffolds.

**Significance:** This work developed an *in vitro* system in which cells within the same material framework can be exposed to markedly different micromechanical conditions. This platform will enable the exploration of how localized changes in the mechanical environment influence cellular response. In particular, future work using this system will query how perturbed local mechanics of native tissues due to micro-damage influences the development of differential cell-mediated ECM deposition and remodeling, potentially shedding light on the mechanism of formation of micro-domains in the meniscus.

**References:** [1] Han+ 2016. [2] Baker+ 2012. [3] Driscoll+2015.

**Acknowledgements:** This work was supported by the National Institutes of Health (R01 EB02425) and the Penn Center for Musculoskeletal Disorders (P30 AR069619).

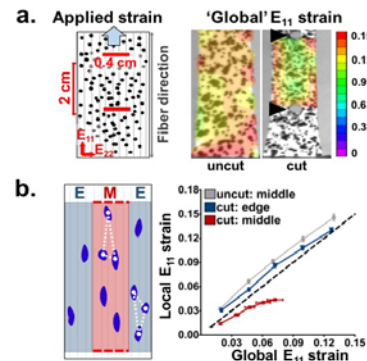


**Figure 1.** a) Schematic of the Vic-2D analysis set-up (left) and generated  $E_{11}$  Lagrangian strain maps for control and defected scaffolds at 15% applied strain (right). b) ‘Local strain’ calculation using cell-nuclei tracking.  $E_{11}$  strains in the middle of uncut scaffolds and middle and edge of cut scaffolds were compared to Vic-2D measurements (‘global strain’). Black dashed line = a 1:1 relation (slope of 1).

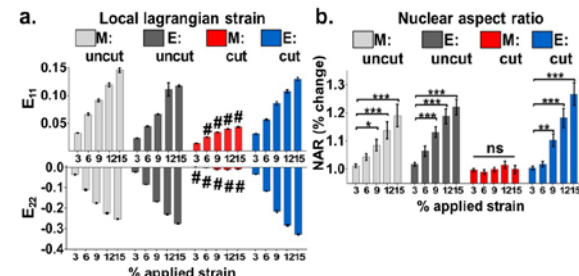


**Figure 2.** a)  $E_{11}$  and  $E_{22}$  measured through nuclear tracking (‘local strain’) at denoted applied strains. ‘M’=middle, ‘E’=edge, as in Fig. 1b. ‘Middle: cut’ cohort compared to all other groups at each strain. (#: p<0.001) b) NAR (normalized to 0%) as a function of applied strain. ns: not significant, \*p<0.05, \*\*p<0.01, \*\*\*p<0.001.

These ECM-level strain field alterations held true at the cellular level as well. Determination of ‘local’ Lagrangian strains through cell nuclei tracking showed similarity between locally and globally measured  $E_{11}$  strains of control and cut scaffolds (Fig. 1b), thus validating nuclear tracking as a method for Lagrangian strain mapping in this experimental system. Significant strain attenuation at the cellular level in the  $E_{11}$  and  $E_{22}$  directions was observed in the middle of the cut region compared to all other locations at all applied grip-to-grip strains (Fig. 2a). Importantly, local strain field perturbations were reflected in differences in nuclear deformation. Cells positioned along fully continuous fibers (uncut scaffolds, edge of cut scaffolds) showed a monotonic increase in NAR up to 23%. In contrast, the NAR of cells seeded in areas containing a fiber discontinuity (middle of cut scaffolds) did not change with the applied strain (Fig. 2b).

This study shows that local interruptions in scaffolds composed of aligned nanofibers result in localized strain attenuation at the macroscopic (Fig. 1) and microscopic (Fig. 2) level. Diminished strain transfer was particularly evident at length scales relevant to the cellular mechanoresponse. Similar trends in NAR and local strain fields confirmed that strains in the principle directions influence the magnitude of nuclear deformation. Importantly, the local fiber discontinuities effected nuclear deformation *only* in regions within the defect, while cells residing in regions of uninterrupted fibers experienced similar deformations as those of uncut control samples. These data illustrate how local fiber disruption can generate distinct mechanical microenvironments within the same scaffold, with neighboring cells experiencing markedly different mechanical inputs based on local boundary conditions. Based on these data and our previous findings in native and engineered tissues [1], these micro-scale perturbations also likely result in different mechano-response. Future studies will focus on differential cellular mechano-signaling within the heterogeneous regions of these scaffolds.

## **Cannulated Cancellous Screws vs. Solid Cortical Screws for Fixation of Lisfranc Injuries: Does it matter?**

Joshua C. Rozell, MD, Matthew Chin, BS, Derek J. Donegan, MD, Michael W. Hast, PhD

**Introduction:** Lisfranc injuries are a frequent cause of patient morbidity, and if not treated with anatomic reduction and fixation, may lead to substantial pain, chronic instability, and arthritis. The use of cannulated screws provide the surgeon with the unique ability to visualize screw vectors with Kirschner wires prior to final implantation; however, no biomechanical studies have compared the strength and stability of cannulated cancellous screws to solid cortical screws in a Lisfranc application. The purpose of this study was to evaluate potential differences in stability provided by the two screw constructs using a cadaveric model subjected to controlled loads.

**Methods:** Ten matched pairs of fresh frozen mid-tibia to toe tip cadaver specimens were used in this experiment. Each specimen was dissected to expose the dorsal midfoot. The tibiotalar joint was fused in 30 degrees of plantarflexion and the tibia was securely potted in polycarbonate tubing. Potted specimens were mounted to a universal testing frame and retroreflective marker clusters were fixed to the first metatarsal, second metatarsal, medial cuneiform, and middle cuneiform. Healthy specimens were slowly loaded to 343N and the 3-D motions of marker clusters were recorded during the static loaded pose. This process was repeated after sectioning of the Lisfranc ligament, and again after a three screw repair (Figure 1) with either solid 3.5mm cortical (Depuy Synthes) or cannulated 4.0mm cancellous screws (Depuy Synthes). Finally, specimens were cycled 100 times between 10-343N at a rate of 1Hz before being returned to 343N and held in a static pose. Upon the completion of testing, 3-D relative displacements between the first and second metatarsals, and the medial and middle cuneiform were calculated with a virtual marker transformation technique for all trials.

**Results:** Due to variations in anatomy across specimen pairs, relative displacements between bones of healthy specimens were normalized to a unitless value of 1. The mean normalized distance between cuneiforms after repair was 1.16 and 1.06 for solid and cannulated screws respectively, while cycled specimens had mean values of 1.10 and 1.08 (Figure 2A). Similarly, mean normalized distance between metatarsals after repair was 1.02 and 1.05 for solid and cannulated screws, while cycled specimens had mean values of 1.05 and 1.15 (Figure 2B). There were no significant differences between groups in any comparison.

**Discussion/Conclusion:** The results of this experiment suggest that fully threaded solid cortical screws and partially threaded cannulated cancellous provide similar immediate construct strengths when used for Lisfranc injury repair. By using the cannulated cancellous screw insertion technique over a Kirschner wire, the surgeon may appreciate the theoretical advantage of fewer passes with the drill and potentially limited articular damage to the midfoot joints, as well as ease of hardware removal.



Figure 1. Anteroposterior radiograph illustrating the 3-screw fixation construct used to repair the Lisfranc injury.

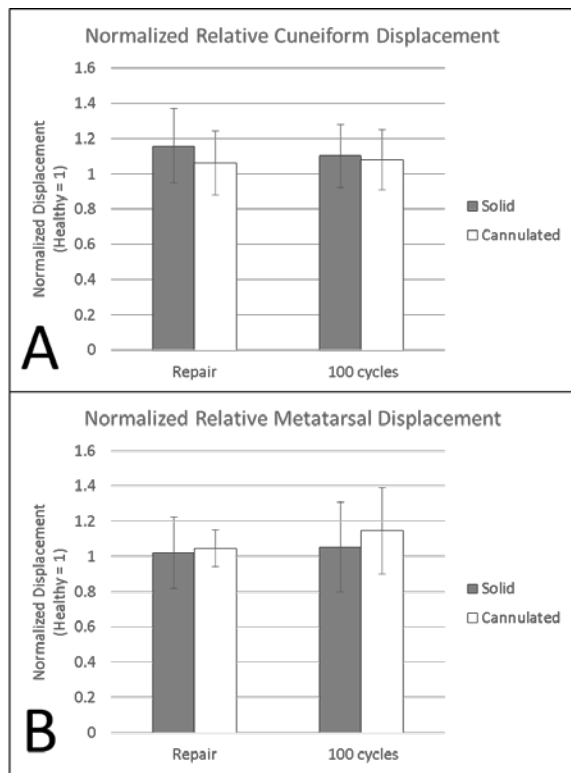


Figure 2: Normalized relative displacement of the A) cuneiforms and B) metatarsals after the Lisfranc injury has been repaired and after 100 cycles of 343N loads have been applied to the repaired foot. All results were normalized, so a value of 1 represents the distance between bones for healthy specimens and values exceeding 1 represent increased spacing between bones. Error bars are  $\pm 1$  standard deviation.

## Effects of Reproduction and Lactation on Maternal Bone Tissue Mechanical Properties at Different Length Scales

Yihan Li<sup>1</sup>, Guo Peng<sup>1</sup>, Wei-Ju Tseng<sup>1</sup>, Chantal de Bakker<sup>1</sup>, Prashant Chandrasekaran<sup>2</sup>, Yonghoon Jeong<sup>3</sup>, Do-Gyo Kim<sup>3</sup>, Lin Han<sup>2</sup>, X. Sherry Liu<sup>1</sup>

<sup>1</sup> University of Pennsylvania, PA; <sup>2</sup> Drexel University, PA; <sup>3</sup> The Ohio State University, OH.

**Disclosures:** None

**Introduction:** The fetal/infant bone growth that occurs during pregnancy and lactation exert remarkable pressure on maternal calcium homeostasis, resulting in substantial loss of bone mineral density. Although bone formation dramatically increases following weaning, bone mass nevertheless cannot be fully recovered. This partial recovery has been demonstrated in the rat skeleton. Our previous studies show that compared to age-matched virgin rats, post-weaning rats had 60% lower trabecular bone volume fraction (BV/TV) in the proximal tibia and 10% lower cortical bone area in the femur midshaft. However, multiple studies indicate that the number of pregnancies and the duration of lactation have a neutral or even positive effect on long-term fracture risk [1-3]. This paradox implies that reproduction and lactation may lead to a functional adaption of maternal skeleton in bone's structure and mechanosensitivity, generating balanced skeletal responses to improve bone quality beyond bone quantity across different length scales. A few recent studies suggest that osteocytes can actively remodel their peri-lacunar matrix during lactation [4], which may alter material properties of peri-lacunar bone matrix thus affecting skeletal mechanosensitivity. Therefore, we hypothesize that bone tissue mechanical properties could be modulated by osteocyte peri-lacunar remodeling during female reproduction. The first objective of this study was to compare both short-term and long-term changes in mechanical properties of bone tissue at different length scales in response to reproduction and lactation. The second objective was to investigate the roles of osteocytes in modulating these changes and define changes in osteocyte micro-mechanical environment during different reproductive stages.

**Methods:** All animal experiments were approved by IACUC. **6-Month Old Rats:** Female, SD rats were assigned to 3 groups: Virgin (n=5), Lactation (n=5, euthanized 2-week post lactation), and Recovery (n=5, euthanized 2-week post weaning). All animals were sacrificed at age 6 months. **14-Month Old Rats:** Female, SD rats were assigned to 2 groups: Virgin (n=3), and Reproduction (n=3). Reproductive rats underwent 3 repeated cycles of pregnancy, lactation, and weaning. All animals were sacrificed at age 14 months.  **$\mu$ CT Scan:** Femurs were harvested from each rat at euthanasia and subjected to *ex vivo*  $\mu$ CT scanning (vivaCT40, Scanco, 10.5  $\mu$ m voxel size) to assess cortical bone area (Ct.Area) at the midshaft. **3-Point Bending Test:** was performed at the femur midshaft region (Instron 5542). Load-displacement curve was used to calculate whole bone stiffness. **Nanoindentation Test:** The midshaft of bended femur was cut along transverse plane, and manually polished until grain size 0.06  $\mu$ m in wet condition. Indentation tests were performed using a nanoindenter (Nano-XP, MTS) in a wet chamber with Berkovich tips (speed 10nm/s; indentation depth 500nm; 30-second holding time). The elastic modulus (E) were calculated based on the unloading portion of the load-displacement curve by Oliver-Pharr method. 8-10 osteocyte lacunae were chosen for each specimen. 2 indents were applied at 10- $\mu$ m and 2 at 25- $\mu$ m distance to the center of each osteocyte lacuna (Fig 1). **Statistic:** 2-way ANOVA with Bonferroni corrections was applied to compare groups and indentation distances in both 6-month rats and 14-month rats. Differences were considered significant when p<0.05.

**Results:** **6-Month-Old Rats:** Ct.Area was 13% and 10% lower in the Lactation and Recovery groups, respectively, compared to the Virgin group (Fig 2A), indicating that the femoral cortical bone volume was significantly reduced by reproduction. However, 3-point bending tests indicated no reproductive effect on the whole bone stiffness between Virgin, Lactation, and Recovery rats (Fig 2B). Interestingly, nano-indentation tests revealed that bone matrix tissue modulus in the Lactation group was 5% and 10% higher than Virgin and Recovery groups, respectively (Fig 2C). By stratifying indentation modulus based on their distance to the center of lacunae, we found that elastic moduli at 10  $\mu$ m ( $E_{10\mu m}$ , within peri-lacunar space) and 25  $\mu$ m ( $E_{25\mu m}$ , interstitial bone region) had no difference in the virgin group. In contrast,  $E_{10\mu m}$  was 3% lower than  $E_{25\mu m}$  in the lactation group, while in the recovery group,  $E_{10\mu m}$  was 7% greater than  $E_{25\mu m}$ . Furthermore, the ratio of  $E_{10\mu m}:E_{25\mu m}$  in the recovery group were significantly greater than those in the Virgin and Lactation groups (Fig 2D). **14-Month-Old Rats:** No difference was found in the femoral Ct.Area and whole bone stiffness between the virgin rats and rats with reproduction history (Fig 2A-B). However, average indentation modulus was 4% higher in the Reproduction group than the Virgin group (Fig 2C). No difference between  $E_{10\mu m}$  and  $E_{25\mu m}$  was found in Virgin or Reproduction group. Furthermore, the ratio of  $E_{10\mu m}:E_{25\mu m}$  was not different between two groups (Fig 2D).

**Discussion:** This study investigated both short-term and long-term changes in bone mechanical properties in response to reproduction and lactation. Lactation dramatically reduced cortical bone area in rat femur, and this reduction persisted after weaning. However, whole bone stiffness was preserved in both lactating and post-weaning rats, likely through altered material properties of bone tissue. Further tests by nanoindentation suggested that nano-scale bone tissue modulus and significantly increased during lactation, which may compensate for the reduced bone area to preserve whole bone mechanical properties. Despite smaller bone area and lower nano-scale elastic modulus, whole bone stiffness of post-weaning rats was not different from that of the virgin rats. Therefore, further tests at different length scales, such as microindentation tests, may be necessary to elucidate tissue level mechanisms to preserve whole bone mechanical properties in post-weaning bone. Moreover, our study also demonstrated significant tissue-level changes in rats with multiple reproduction cycles, suggesting reproduction history may exert long-term effect on bone tissue composition and mechanics. Additionally, the decrease of  $E_{10\mu m}/E_{25\mu m}$  over the course of lactation and the increase of  $E_{10\mu m}/E_{25\mu m}$  over the course of recovery suggest that the osteocyte may have the ability to directly remodel its local surrounding bone tissue to generate positive or negative gradient of material properties during different stages of a reproductive cycle. This alteration may influence the tissue deformation and strain distribution in the peri-lacunar bone region [5], thus affecting osteocyte signaling. However, even though osteocyte remodeling has important influence on the heterogeneity of bone tissue properties, this local mediation itself cannot account for the overall changes in tissue-level mechanical properties, e.g., increased elastic modulus during lactation. Further explorations are required to uncover the mechanism behind bone tissue adaptation to reproduction and lactation.

**Acknowledgements:** This study is supported by NIH/NIAMS P30-AR069619, R03-AR065145, and NSF Graduate Student Research Fellowship.

**References:** [1] Paton, LM et al., *Am J Clin Nutr*, 2003; [2] Kovacs, CS and Ralston, SH., *Osteoporos Int*, 2015; [3] Melton, LJ et al., *Osteoporos Int*, 1993; [4] Qing, H et al., *J Bone Miner Res*, 2012; [5] Bonivtch, AR et al., *J Biomech*, 2007.

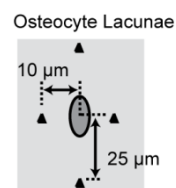


**Fig 1.** Indentations at 10 $\mu$ m vs. 25 $\mu$ m from the center of osteocyte lacunae.

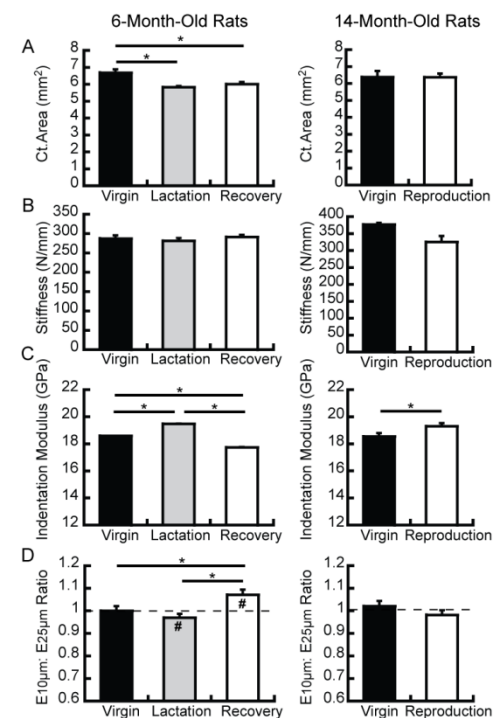


**Fig 2.** (A) Ct.Area, (B) Whole bone stiffness, (C) Nano-scale elastic modulus, and (D) Ratio of  $E_{10\mu m}:E_{25\mu m}$  of (Left) 6-month-old rats and (Right) 14-month-old rats. \* difference between groups; # difference between  $E_{10\mu m}$  and  $E_{25\mu m}$ .

## UNINJURED SUPRASPINATUS TENDONS IN RODENTS DO NOT EXHIBIT DIFFERENT MATERIAL PROPERTIES ACROSS SEX

Kelsey A. Robinson, Adam M. Pardes, Benjamin R. Freedman, Louis J. Soslowsky  
McKay Orthopaedic Research Laboratory University of Pennsylvania Philadelphia, PA, USA

**INTRODUCTION:** Injuries to the rotator cuff are common causes of disability among otherwise healthy individuals, especially in an aging population [1]. Although the exact prevalence of rotator cuff tears has not been established, known risk factors include increasing age [2], hypercholesterolemia [3], smoking [4], and family history [5]. While the relationship between sex and rotator cuff tears is debated [6, 7, 8, 9], gender is known to be a risk factor for other soft tissue injuries. For example, 84% of Achilles ruptures occur in men [10], while ACL injuries are more common in women [11]. Previously, we demonstrated that uninjured male and female Achilles tendons in rodents have different mechanical properties, which may partially explain the disproportionate clinical incidence of spontaneous Achilles ruptures in men [12]. Unfortunately, this mechanical property information has yet to be established for the supraspinatus tendon. Therefore, the objective of this study was to determine the mechanical properties of uninjured supraspinatus tendons in male, female, and ovariectomized (OVX) rats. We hypothesized that the supraspinatus tendon of female and OVX rats would exhibit decreased cross-sectional area but equal mechanical properties to male supraspinatus tendons.

**METHODS:** Shoulders were harvested from 36 age-matched adult male (n=12), female (n=12), and OVX (6-weeks after OVX) (n=12) Sprague-Dawley rats. The supraspinatus tendon and humerus were fine dissected and Verhoeff's stain lines were placed at the bony insertion site and 8 mm proximally. Tendon cross-sectional area was measured with a custom laser device [13]. Humeri were then secured in PMMA, and cyanoacrylate was used to secure the tendon between two pieces of sandpaper leaving an 8mm gage length. A custom fixture was used to secure the samples in an Instron ElectroPuls E3000 affixed with a 250 N load cell. Tendons were submerged in a 1x 37°C PBS bath and underwent ramp to failure testing at 0.1% strain/sec. Comparisons between groups were made with one-way ANOVAs and significant relationships were evaluated with post-hoc t-tests with Bonferroni corrections ( $\alpha=0.05/3$ ). Data represented as mean and standard deviation. Significance bars indicate  $p<0.017$ .

**RESULTS:** The cross-sectional area of male supraspinatus tendons was significantly larger (30%) than female and OVX tendons (Figure 1). The maximum loads of male tendons were significantly larger (50%) than female and OVX tendons (Figure 2A). Stiffness in the linear region of the load-displacement curve was significantly larger (40%) in male tendons compared to female and OVX tendons (Figure 2C). The modulus of the toe region of the stress-strain curve was significantly smaller (30%) in male tendons compared to female and OVX tendons (Figure 2D). While changes in cross-sectional area and maximum loads were dramatic and expected, there were no significant differences in maximum stress, linear modulus, toe stiffness or transitional strain among groups (Figures 2B-E).

**DISCUSSION:** The objective of this study was to evaluate differences in the mechanical properties of supraspinatus tendons in male, female, and ovariectomized rats. In accordance with our first hypothesis, male tendons had increased cross-sectional area compared to female and OVX tendons, which likely contributed to the greater maximum load in the male supraspinatus tendons. The increased linear stiffness in male tendons was also expected given the increased size of these tendons and maximum load. These results are in contrast to findings in the Achilles tendon, where there was no difference in linear stiffness across sex (Figure 3). The greater modulus of the toe region, but not the linear region, of female supraspinatus tendons suggests that sex may impact collagen fibril uncrimping [14]. Interestingly, this data is also in contrast to our previous results in the Achilles tendon, where the modulus of both the toe and linear regions of female tendons were greater than in male tendons (Figure 3). The similar maximum stress, transitional strain, and linear modulus of the supraspinatus tendon among groups suggests that the mechanical properties of male tendons are generally similar to that of female and OVX tendons. Unlike the Achilles tendon, which ruptures spontaneously clinically, supraspinatus injuries are typically degenerative [14, 15]. Therefore, it is possible that the similar supraspinatus tendon mechanical properties observed between sexes may result in degeneration occurring at a similar rate regardless of sex. This would support the lack of a clear relationship between gender and incidence of tears reported in the literature. One potential limitation of this study is the age of the animals, as differences in mechanical properties may be more prominent in aged animals, given that rotator cuff tears are most common in older adults. Future work will investigate dynamic properties of the supraspinatus tendon and muscle in order to further compare and contrast the mechanisms underlying tissue-specific sex differences.

**ACKNOWLEDGEMENTS:** This study was supported supported Penn Center for Musculoskeletal Disorders (P30AR069619), the NIH/NCATS (TL1TR000138), and the authors thank M. Hast for his contributions.

**REFERENCES:** [1] Chakravarty, K et al. *J Rheum*, 1993. [2] Yamaguchi, K et al., *JBJS*, 2006. [3] Abboud, J et al. *Clin Orthop Relat Res*, 2010. [4] Baumgartner, K et al., *Clin Orthop Relat Res*, 2010. [5] Tashjian, R et al., *JBJS*. 2009. [6] Keener, et al. *J Shoulder Elbow Surg*, 2010. [7] Milgrom, C, et al., *JBJS Br*, 1995. [8] da Rocha Motta, G, et al., *J Shoulder Elbow Surg* 23:227-235, 2014. [9] Yamamoto, A, et al., *J Shoulder Elbow Surg*, 19:116-120, 2010. [10] Vosseller, J, et al. *Foot Ankle Int*, 34:49-53, 2013. [11] Wojtys, E, et al., *Am J Sports Med*, 2002. [12] Pardes, A, et al., *Ann Biomed Eng*, in press, 2016. [13] Favata, M, Dissertations available from ProQuest, Paper AAI3246156, 2001. [14] Miller, K, et al, *J Biomech*, 2012. [15] Tashjian, R., *Clin Sports Med*, 2012. [16] Clayton, R, *Injury*, 2008.

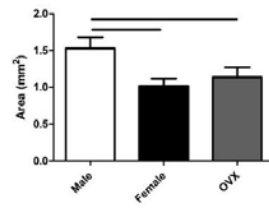


**Figure 1:** Cross-sectional area of male supraspinatus tendons is greater than that of female or OVX tendons.

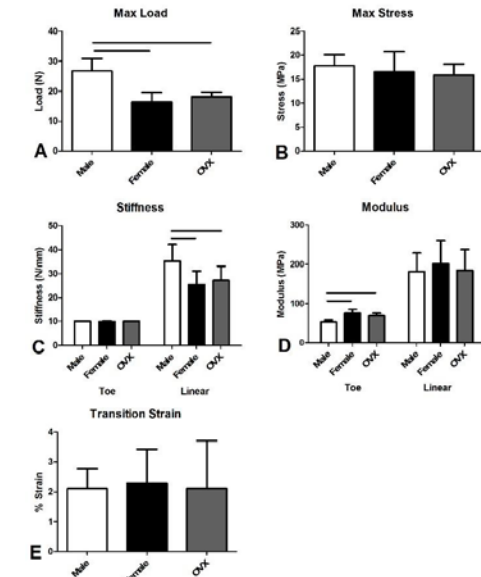


**Figure 2:** Mechanical properties of supraspinatus tendons. A. maximum load, B. maximum stress, C. stiffness, D. modulus, E. transition strain (between toe and linear regions of the force-displacement curve). Maximum load and stiffness in the linear region of the force displacement curve were significantly greater in male tendons, while toe modulus was significantly smaller than female and OVX tendons.

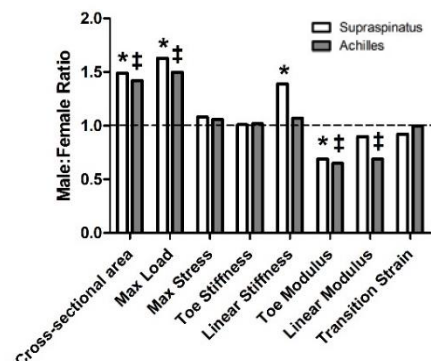


**Figure 3:** Tendon-specific sex differences in mechanical properties for supraspinatus and Achilles. Ratio of male to female means were taken for each parameter. Data that is significantly different between male and female supraspinatus or Achilles tendons are indicated by \* and ‡, respectively. There were significant sex differences in cross-sectional area, maximum load, and toe modulus in both supraspinatus and Achilles tendons. Male supraspinatus tendons had increased linear stiffness and male Achilles tendons had decreased linear modulus compared to female tendons. No direct comparisons were made between supraspinatus and Achilles tendon property male:female ratio. Dotted line is a ratio of 1.0.

# **Increased force sensing and aberrant muscle tissue repair by mutant ACVR1/ALK2 FOP progenitor cells – implications for heterotopic ossification**

Alexandra Stanley,<sup>1,3</sup> Julia Haupt,<sup>1,3</sup> Brian Cosgrove,<sup>1,4,6</sup>  
Robert L. Mauck,<sup>1,4,5,6</sup>, Eileen M. Shore<sup>1,2,3</sup>

Departments of <sup>1</sup>Orthopaedics and <sup>2</sup>Genetics, and the <sup>3</sup>Center for Research in FOP and Related Disorders, Perelman School of Medicine, University of Pennsylvania

Departments of <sup>4</sup>Bioengineering and <sup>5</sup>Mechanical Engineering and Applied Mechanics, School of Engineering and Applied Science, University of Pennsylvania

<sup>6</sup>Translational Musculoskeletal Research Center, Philadelphia VA Medical Center

In the rare genetic disease fibrodysplasia ossificans progressiva (FOP), progenitor cells are misregulated to differentiate to heterotopic bone in connective tissues. Rigidity of the microenvironment is a key modulator of lineage specification and sufficient to direct cell fate decisions. Soft substrates induce mesenchymal progenitors towards neuro-/adipogenic lineages while stiff substrates promote chondro-/osteogenesis. Pathologic stiffening of the microenvironment occurs in fibrotic diseases when damaged tissue aberrantly acquires increased rigidity during wound healing. Injury-induced early-to-intermediate stage FOP lesions similarly exhibit excessive fibroproliferation, with impaired regeneration of damaged muscle tissue at later stages. Gain-of-function mutations in the BMP type I receptor ACVR1/ALK2 cause FOP, with the R206H mutation as the most prevalent. Since BMP signaling regulates and is regulated by cell tensional force (with low signaling activity on soft vs. high activity on stiff substrates), altered ACVR1 signaling could influence mechanotransduction pathways. In addition to a role in misdirecting mesenchymal progenitor cells, the cell environment plays a large role in regulating endogenous muscle stem cells (MuSCs), the cells responsible for skeletal muscle regeneration after injury. Injury to FOP muscle tissue does not repair as fast or as efficiently as injured WT muscle tissue. We hypothesized that elevated BMP signaling by the *Acvr1*<sup>R206H/+</sup> mutation alters cell perception of physical environment, leading to abnormal cell fate decisions by MSCs and impaired ability of MuSCs to repair muscle. We used immortalized mouse embryonic fibroblasts (iMEFs) from an *Acvr1*<sup>R206H/+</sup> knock-in embryos and WT littermates on varied matrix elasticity (soft: 5kPa; moderate: 15kPa, stiff: 55kPa) and analyzed morphological parameters (cell size, aspect ratio (AR), circularity, solidity) at low cell density. WT iMEFs responded to increasing stiffness as expected with increased cell size and AR, and decreased circularity and solidity. However, FOP iMEF response to soft substrates was similar to WT on stiff substrates, and FOP iMEFs were less responsive to substrate rigidity. The response of FOP iMEFs to substrate rigidity was rescued when BMP signaling through the Alk2 receptor was inhibited. Furthermore, activation of mechanotransductive effectors such as RhoA/ROCK, pMLC2, pCofilin, and Yap/Taz were all increased in FOP iMEFs as measured by Western blot and immunofluorescence. These data support that the combination of increased BMP signaling, misinterpretation of soft substrates, and overall reduced sensitivity to mechanical stimuli in FOP cells lowers their threshold for commitment to chondro-/osteogenic lineages, resulting in an aberrant tissue repair response that leads to ectopic bone formation. To examine the effect of the *Acvr1*<sup>R206H/+</sup> mutation on MuSCs specifically, cells were isolated based on their expression of the cell surface markers  $\alpha$ 7-integrin and CD34 using fluorescent activated cell sorting (FACS). Isolated MuSCs were analyzed for proliferation based on BrdU incorporation, and there appeared to be no significant differences between proliferation of muscle stem cells from WT and FOP injured muscles or WT and FOP uninjured muscles at day 3, day 5, and day 7 post-cardiotoxin (CTX) injury in 2 month-old mice. This indicates that that MuSCs are present in FOP muscle tissue at normal levels, confirming that the *Acvr1*<sup>R206H/+</sup> mutation does not impact the production of MuSCs, nor impair their activation. Future experiments will be to assess the ability of the *Acvr1*<sup>R206H/+</sup> mutation to influence differentiation of MuSCs into mature myoblasts and efficiently repair damaged muscle tissue.

# Decorin Plays an Indispensable Role in Cartilage Poroelasticity at the Nanoscale

Biao Han<sup>1</sup>, Qing Li<sup>1</sup>, Mei Sun<sup>2</sup>, Hadi T. Nia<sup>3</sup>, Ramin Oftadeh<sup>4</sup>, Basak Doyran<sup>1</sup>, Ling Qin<sup>5</sup>, Renato V. Iozzo<sup>6</sup>, David E. Birk<sup>2</sup>, Lin Han<sup>1</sup>

<sup>1</sup>Drexel University, Philadelphia, PA; <sup>2</sup>University of South Florida, Morsani College of Medicine, Tampa, FL; <sup>3</sup>Harvard Medical School, Boston, MA; <sup>4</sup>Massachusetts Institute of Technology, Cambridge, MA; <sup>5</sup>University of Pennsylvania, Philadelphia, PA; <sup>6</sup>Thomas Jefferson University, Philadelphia, PA.

**Disclosures:** Biao Han (N), Qing Li (N), Mei Sun (N), Hadi T. Nia (N), Ramin Oftadeh (N), Basak Doyran (N), Ling Qin (N), Renato V. Iozzo (N), David E. Birk (N), Lin Han (N).

**INTRODUCTION:** Poroelasticity is the dominant mechanism for energy dissipation and impact force protection in articular cartilage during high frequency activities, such as jumping and impactful loading [1,2]. In cartilage, poroelastic mechanics is governed by the interactions between water molecules and glycosaminoglycan (GAG) side chains of aggrecan [3] (mainly chondroitin sulfate (CS)-GAGs) [4]. The collagen fibrillar network serves as a scaffold that holds aggrecan aggregates at  $\approx 50\%$  compressive molecular strain that is critical for tissue hydraulic permeability [5]. To this day, while the roles of aggrecan and collagen are well understood, it remains unclear how quantitatively minor molecules, such as small leucine rich proteoglycans (SLRPs), contribute to cartilage poroelasticity [6]. Such knowledge is critical, as SLRPs can play key roles in directing the assembly of cartilage extracellular matrix (ECM) [7], thereby influencing both elastic and poroviscoelastic characteristics. To this end, this study examined the role of decorin, the most abundant SLRP in cartilage [8], in the poroelastic mechanical properties of cartilage. AFM-based nanorheometric test [9] was applied to study the time-dependent nanomechanics of wild-type (WT) and decorin-null ( $Dcn^{-/-}$ ) murine cartilage in both intact and CS-GAG-depleted forms.

**METHODS:** Femoral condyle cartilage (Fig. 1) was harvested from 3-month old male  $Dcn^{-/-}$  and WT C57BL/6 mice, and stored in PBS at 4°C with protease inhibitors for < 48 h prior to mechanical testing. **AFM-nanorheometric test** [9] was applied to the surface of medial condyle cartilage using microspherical tips ( $R \approx 5 \mu\text{m}$ ,  $k \approx 16 \text{ N/m}$ ) via a Dimension Icon AFM (Bruker) and our custom-built nanorheometer. A 2-3 nm random binary sequence displacement was superimposed onto the  $\sim 1 \mu\text{m}$  static depth during a 90-sec ramp-and-hold. The dynamic force,  $F^*$ , and depth,  $D^*$ , as a function of frequency (1-1000Hz) were extracted via discrete Fourier transform. The complex dynamic modulus magnitude,  $|E^*$ , and phase angle,  $\delta$ , were derived via the Taylor expansion of Hertz model [10]. The self-stiffening ratio was calculated as the ratio of  $|E^*$  at high (800-1000 Hz,  $E_H$ ) versus low (1-3 Hz,  $E_L$ ) frequencies. **Finite element modeling:** Previous studies have shown the dominance of poroelasticity in the frequency-domain mechanics of murine cartilage [9]. Fiber-reinforced poroelasticity model [11] was applied to extract the fluid pressure and hydraulic permeability,  $k$ . To reveal the roles of CS-GAGs, additional condyles were incubated in 0.1U/ml chondroitinase-ABC for 48hr for CS-GAG removal, and subjected to the same nanorheometric tests. **Collagen nanostructure:** Additional joints ( $n = 5$ ) were used for imaging the collagen network structure via SEM and TEM, following established procedures [12,13].

**RESULTS:** We found that WT and  $Dcn^{-/-}$  cartilage had significant differences in the frequency-dependent spectra of  $|E^*$  and  $\delta$ , indicating their distinctive poroelastic characteristics (Fig. 2). In comparison to the WT control, besides having a lower elastic modulus [14],  $Dcn^{-/-}$  cartilage showed a significantly weaker increase in  $|E^*$  with frequency, and a smaller maximum phase angle,  $\delta_m$  (Fig. 2a). Such results correspond to a  $1.8 \pm 0.6$ -fold (mean  $\pm$  95% CI) lower self-stiffening ratio,  $E_H/E_L$ , as well as a  $7.5 \pm 2.5$ -fold higher hydraulic permeability,  $k$ , as calculated from the fiber-reinforced FEM (Fig. 2b). In addition, the fiber-reinforced FEM extracted significantly lower pore pressure in  $Dcn^{-/-}$  cartilage (Fig. 2c). On the other hand, as expected, for each genotype, CS-GAG-depletion resulted in significant decreases in  $E_H/E_L$  and  $\delta_m$ , as well as increases in  $k$ . Without CS-GAGs, these properties are similar for WT and  $Dcn^{-/-}$  cartilage collagen networks. Despite the similarities in poroelastic mechanical properties, SEM and TEM imaging detected significant variations in the collagen structure, where  $Dcn^{-/-}$  cartilage showed larger collagen fibril diameters both on the surface (Fig. 3a) and in middle/deep zones (Fig. 3b).

**DISCUSSION:** This study highlights indispensable, critical role of decorin in the energy dissipation function of cartilage, as evidenced by the significantly impaired poroelastic mechanical properties of  $Dcn^{-/-}$  cartilage (Fig. 2). While this effect could be due to structural defects of both aggrecan (Fig. 1) and collagen (Fig. 3), the lack of a poroelastic phenotype in  $Dcn^{-/-}$  compared to WT CS-GAG-depleted cartilage suggests that it is the GAG reduction, instead of collagen, the dominating factor. In cartilage, poroelastic mechanics is determined by the 2-3 nm “effective pore size” between GAGs [5]. The regulation of decorin on poroelasticity is thus mainly manifested through its governing of aggrecan content, and therefore, the packing density of GAG chains. The collagen network alone has several orders of magnitude larger pore size ( $\sim 100 \text{ nm}$ ) [15], and at this length scale, structural changes likely do not have marked impacts on the fluid-solid interactions. Since time-dependent mechanics is a key function of cartilage in load bearing and energy dissipation [16], understanding the role of decorin can provide a new path for documenting osteoarthritis-induced cartilage dysfunction and for evaluating tissue repair products. Our ongoing studies aim to uncover the molecular mechanism whereby decorin influences cartilage ECM structure and mechanics.

**SIGNIFICANCE:** This study discovered the critical role of decorin in the energy dissipative, poroelastic mechanical functions of cartilage. It provides a basis for decorin to serve as a potential target in detecting cartilage degradation and improving cartilage repair.

**REFERENCES:** [1] Cross, R. *Am. J. Physiol.* 67:304-309, 1999. [2] Hoshino, A et al., *J. Bone Joint Surg. Br.* 69:807-811, 1987. [3] Nia, HT et al., *ACS Nano* 9:2614-2625, 2015. [4] Lee, H-Y et al., *J. Struct. Biol.* 181:264-273, 2013. [5] Wight, TN et al. 1991. In *Cell Biology of the Extracellular Matrix*. 45-78. [6] Heinegård, D. *Int. J. Exp. Pathol.* 90:575-586, 2009. [7] Chen, S et al., *FEBS J.* 280:2120-2137, 2013. [8] Poole, AR et al., *J. Orthop. Res.* 14:681-689, 1996. [9] Nia, HT et al., *J. Biomech.* 48:162-165, 2015. [10] Mahaffy, RE et al., *Biophys. J.* 86:1777-1793, 2004. [11] Soulhat, J et al., *J. Biomech. Eng.* 121:340-347, 1999. [12] Batista, MA et al., *Matrix Biol.* 38:84-90, 2014. [13] Birk, DE et al., *Dev. Dyn.* 208:291-298, 1997. [14] Doyran, B et al., *Trans. ORS* 62:491, 2016. [15] Clark, IC. *J. Bone Joint Surg. Br.* 53B:732-749, 1971. [16] Setton, LA et al., *J. Biomech.* 26:581-592, 1993.

**ACKNOWLEDGEMENTS:** This work was supported by the National Institutes of Health (AR066824).

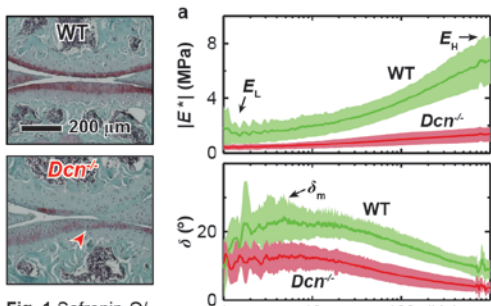


**Fig. 1** Safranin-O/Fast Green histology showed marked reduction of CS-GAGs in 3-month old  $Dcn^{-/-}$  murine cartilage (red arrowhead).

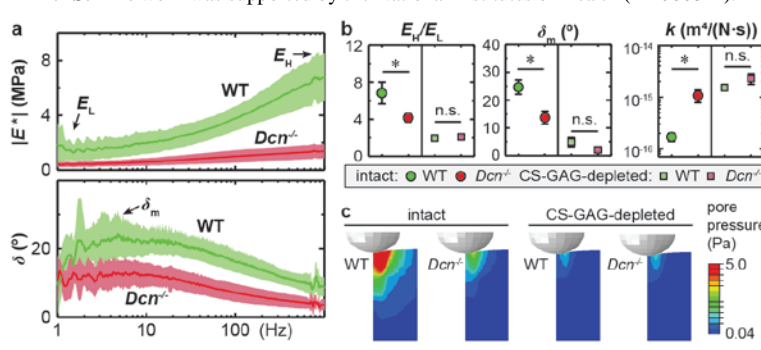


**Fig. 2** Poroelastic nanomechanical properties via AFM-nanorheometric test. **a)** Frequency spectra of dynamic modulus  $|E^*$  and phase angle  $\delta$ , from intact WT and  $Dcn^{-/-}$  cartilage (mean  $\pm$  95% CI of  $\geq 5$  animals). **b)** Poroelastic mechanical properties of both intact and CS-GAG-depleted cartilage: self-stiffening coefficient  $E_H/E_L$ , maximum phase angle  $\delta_m$  and hydraulic permeability,  $k$  (mean  $\pm$  SEM,  $n \geq 4$  animals, \*:  $p < 0.05$  via Mann-Whitney U test). **c)** Maximum pore pressure calculated from the fiber-reinforced poroelastic finite element model.

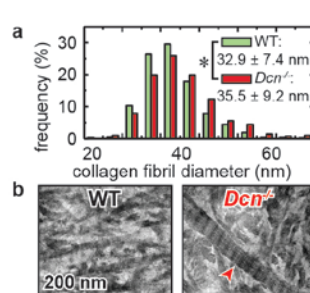


**Fig. 3** **a)** Distribution of cartilage surface fibrils measured by SEM (images not shown) suggested increased average ( $p < 0.0001$ ) and std ( $p < 0.0001$ ) of collagen fibril diameters in  $Dcn^{-/-}$  cartilage. **b)** TEM on cartilage matrix cross-sections showed the presence of thickened fibrils (red arrowhead).

## **“Spine and pelvic alignment impacts the rate of vertebral growth in adolescent idiopathic scoliosis”**

Saba Pasha

**Introduction:** Longer anterior vertebral column in adolescent idiopathic scoliosis (AIS) has been observed. However the relationship between the anterior-posterior vertebral height (APVH) in patients with different lumbopelvic alignment and how it affect the derotation of the lumbar has not been discussed.

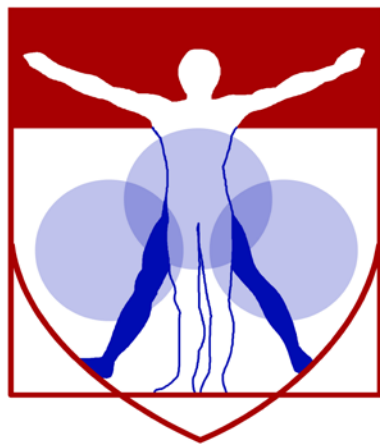
**Objective** to compare the APVH differences between AIS patients with main thoracic, thoracolumbar/lumbar, and controls and relate it to lumbo-pelvic alignment.

**Method** a total number of 30 AIS with main right thoracic (MT), 27 AIS with left thoracolumbar/lumbar (TLL) and 14 asymptomatic controls (Control) were selected retrospectively. The 3D reconstruction of the spinal vertebrae was generated and the APVH differences were calculated in the local coordinate system of each vertebra. The differences between the APVH were compared between the three groups. Two cluster of patients in each group were determined based on the pelvic incidence (PI) and the APVH differences were compared between the high a low PI groups. Lumbar lordosis was calculated the sagittal view and the true plane of rotation of the lumbar curve.

**Results** The patterns of the APVH differences were significantly different in the three groups in lumbar spine (Fig.1). Patients with higher PI (average of 57 versus 48 in MT and 55 versus 46 in TLL) had significantly higher APVH differences in lumbar spine in both AIS groups however these differences were not significant in the control group (average of 55 versus 47 for high and low PIs). The mean absolute difference between the sagittal lumbar lordosis and derotated lumbar lordosis was 16° and 32° in MT and TLL groups respectively.

**Discussion** PI was an important factor associated with increased lumbar anterior vertebral height with respect the posterior height in the AIS group. Considering the differences between the anterior height of the vertebrae as appears on X-rays images and the true anterior height in the local coordinate system of each vertebra is required to determine the lordosis particularly in patients with high PI.

**Clinical significance** considering the APVH differences can be an important factor in planning for adequate lordosis while derotating the lumbar vertebra to avoid excessive pressure on the disk. This quantitative consideration can provide guideline for preforming an anterior release in lumbar spine, especially in patient with high PI.



PENN  
CENTER for  
MUSCULOSKELETAL  
DISORDERS

# Histology Abstracts

# Electrospun PLGA Nanofiber Scaffolds Release Ibuprofen Faster and Degrade Slower after *In Vivo* Implantation

Corinne N Riggan<sup>1</sup>, Feini Qu<sup>1</sup>, Dong Hwa Kim<sup>1</sup>, Julianne Huegel<sup>1</sup>, David R Steinberg<sup>1,2</sup>, Louis J Soslowsky<sup>1</sup>, Robert L Mauck<sup>1,2</sup>, Joseph Bernstein<sup>1,2</sup>

<sup>1</sup> McKay Orthopaedic Research Lab, University of Pennsylvania, PA, <sup>2</sup> Translational Musculoskeletal Research Center, Philadelphia VA Medical Center, PA

**Disclosures:** CN Riggan (N), F Qu (N), DH Kim (N), J Huegel (N), DR Steinberg (N), LJ Soslowsky (5;Orthofix, DJO), RL Mauck (N), J Bernstein (7;CORR)

**INTRODUCTION:** Non-steroidal anti-inflammatory drugs (NSAIDs) are often prescribed, and are effective, for pain relief following tendon repairs. While improved healing after delayed delivery of NSAIDs has been demonstrated [1], these drugs have also been shown to impair healing in early stages of tendon repair by inhibiting inflammatory responses [1,2]. Therefore, to support the use of NSAIDs after tendon repair, it is imperative to identify a dose, timing, and mode of delivery that provides pain relief but does not impede tendon healing. Recent tissue engineering work has demonstrated that nanofibrous electrospun scaffolds may be useful in this realm [3]. Release of factors that are directly incorporated into nanofibers can be modulated by selecting polymers with appropriate degradation properties [3]. Therefore, the objective of this study was to develop a scaffold that would allow for local controlled release of NSAIDs during tendon healing. We further aimed to characterize the release profile and scaffold degradation properties both *in vitro* and *in vivo*.

**METHODS:** Scaffold Fabrication: Poly(lactic-co-glycolic acid) (PLGA) scaffolds were fabricated with and without the incorporation of ibuprofen (IBP) using standard electrospinning techniques [4]. Solutions of 35% w/v 75:25 PLGA, with 5% w/w ibuprofen (IBP) or without IBP (blank), were dissolved in 1:1 tetrahydrofuran and N,N-dimethylformamide and then electrospun on a rotating mandrel to create aligned nanofibrous scaffolds. In Vitro IBP Release in PBS: IBP scaffolds were placed in phosphate buffered saline (PBS) at 37°C on a shaker. At designated time points, the PBS solution was removed and centrifuged and the IBP concentration in the supernatant quantified by measuring optical absorbance and normalized to scaffold weight. In Vivo IBP Release: With IACUC approval, 8mm diameter PLGA scaffolds were implanted subcutaneously in Sprague Dawley rats (4/animal). Rats were sacrificed at 0.5, 3, 7, and 14 days after implantation, and scaffolds harvested for subsequent ibuprofen quantification, continued *in vitro* release in PBS, histological analysis, and SEM imaging. IBP remaining within the scaffolds was determined by dissolving them in dimethyl sulfoxide (DMSO) and measuring absorbance. In Vitro Release in Serum: To more accurately replicate *in vivo* conditions *in vitro*, 10 IBP-containing and 5 blank scaffolds per time point were incubated in either PBS or rat serum for 0.5, 3, 7, 14, and 21 days at 37°C on a shaker. Scaffolds were removed after these incubation times for SEM (n=1), mechanics (n=3, retained for future analysis), and IBP quantification (n=3, IBP only). For three IBP and one blank scaffold, the serum was replaced with PBS for continued release and analysis of degradation. Histology: Scaffolds explanted from rats were immediately placed in formalin, soaked in sucrose, flash frozen in embedding compound, cryosectioned at 10 µm, and stained with hematoxylin and eosin. SEM: Samples were flash frozen immediately after *in vitro* or *in vivo* incubation, lyophilized, mounted, and imaged at 1000x (not shown) and 5000x. Mechanical Testing: As-spun IBP and blank scaffolds (day 0) were cut into 60 x 5 mm strips with the fibers oriented along the long axis and mechanically evaluated using a ramp to failure test (0.5%/second).

**RESULTS:** In Vitro Response in PBS: A distinct and reproducible release profile of IBP was observed in PBS: a burst phase over the first 3 days (releasing ~10% of the total IBP), followed by a lag phase from days 3-10, and then a linear phase during which roughly 1 µg/mg scaffold/day was released (Fig 1 – green plot). Macroscopically, the scaffold began to degrade and lose its shape after ~20 days (Fig 2A). SEM demonstrated that the fibers swelled immediately upon hydration, coalesced by day 14, and then disintegrated by day 21 (Fig 2A). In Vivo Response: After removal from subcutaneous implantation for 0.5, 3, 7, and 14 days, all scaffolds retained only 10-20% of the original IBP load (Fig 1 – red plot). Macroscopically, there was no degradation apparent and little to no tissue adherence. Histologically, there was only scant cellular infiltration into the scaffold by day 14 (Fig 2D). After further incubation in PBS, the scaffold showed a rapid but small burst release of the remaining 10% of IBP, and failed to degrade even after nearly 3 months of incubation in PBS (data not shown). SEM demonstrated the maintenance of a fibrous structure throughout, with minimal fiber swelling compared to the PBS incubated scaffolds (Fig 2C). In Vitro Response in Serum: Scaffolds placed in serum for 0.5, 3, 7, 14, and 21 days demonstrated a pattern of release similar to those implanted *in vivo*, namely, an immediate burst release of nearly 100% of the IBP (Fig 1A – blue plots). Macroscopically, the scaffolds did not show any signs of degradation, even after almost 2 months of incubation in PBS (Fig 2B). SEM demonstrated that the scaffolds maintained their fibrous structure with very little fiber swelling over 21 days (Fig 2B). Blank vs. IBP Scaffolds: Incubation in PBS steadily degraded both the IBP and blank scaffolds, though the IBP scaffold degraded at a faster rate (data not shown). Interestingly, neither scaffold showed signs of degradation when incubated in serum for up to 40 days (data not shown). Additionally, mechanical testing demonstrated that as-spun IBP scaffolds had no change in stiffness, failure load, and yield strain properties (data not shown) compared to blank scaffolds. However, the IBP scaffolds showed a decreased modulus (Fig 3B), yield load, yield stress, and failure stress (data not shown), as well as an increased failure strain (Fig 3B) compared to blank scaffolds (p<0.01).

**DISCUSSION:** This study demonstrated that a controlled linear release profile of IBP can be created using PLGA nanofiber scaffolds when maintained *in vitro* in PBS. Although this release profile is highly desirable for our clinical application, the release profile of scaffolds placed in serum or *in vivo* was not (i.e., we observed a burst release). This may be due to IBP's tendency to bind to serum albumin, as it does within the vascular system [5]. Additionally, serum and *in vivo* conditions seem to inhibit degradation of the scaffold, the reason for which remains unknown. It is known that biomaterials perform differently *in vitro* vs. *in vivo*, as these data confirm, and this study demonstrates the necessity to fully evaluate biomaterials in environments similar to the intended application. Additionally, this study supports a method for more accurately mimicking the *in vivo* environment, allowing a more thorough *in vitro* investigation prior to progressing to *in vivo* animal studies. Ongoing work is focused on determining the polymer molecular weight and dispersion, and evaluating the mechanical properties of these scaffolds during *in vitro*, *in vivo*, and simulated-*in vivo* degradation. Additionally, we are working to create a scaffold whose release profile following *in vivo* implantation better mirrors the more desirable *in vitro* results.

**SIGNIFICANCE:** This work demonstrates that electrospun nanofibrous scaffolds can deliver NSAIDs, though the *in vivo* release profile has not yet matched the more desirable *in vitro* behavior. Additionally, this study supports the use of serum over saline for *in vitro* evaluation, to more accurately represent *in vivo* conditions, and thereby, reduce the number of animal subjects.

**REFERENCES:** [1] Virchenko O, et al., 2004, AJSM, 32:1743-47. [2] Connizzo BK, et al., 2014, CORR, 472:2433-9. [3] Ionescu LC, et al., 2010, Biomat, 31:4113-20. [4] Li WJ, et al., 2007, J Biomech, 40:1686-93. [5] Davies NM, 1998, Clin Pharm, 34:101-54.

**ACKNOWLEDGMENTS:** We acknowledge financial support from VA Medical Center Merit Grant (O0979-R) and the NSF GRFP.

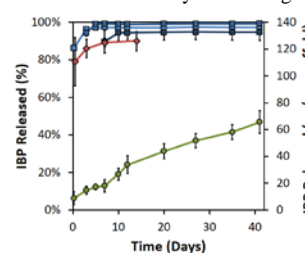


Figure 1: IBP release data represented as % release from the total (left y-axis) and ug/mg scaffold (right y-axis) after incubations in serum (blue) for 0.5, 3, and 7 days and PBS (green), as well as *in vivo* subcutaneous incubation (red).

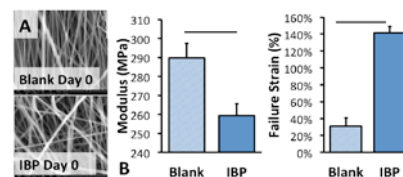


Figure 2: SEM (5000x) and macroscopic images of IBP scaffolds at 0.5, 14, and 21 days of incubation in (A) PBS, (B) rat serum, and (C) *in vivo* subcutaneous implantation. The macroscopic view at 14 days includes surrounding tissue, with the scaffold location outlined. (D) Histological image demonstrating sparse cellular infiltration into the scaffold at 14 days.

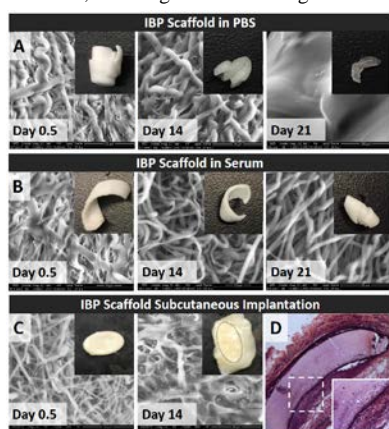


Figure 3: (A) SEM images of blank and IBP scaffolds prior to incubation. (B) Modulus and failure strain of IBP and blank scaffolds prior to incubation (p<0.01).

## Fabrication, Maturation, and Implantation of a Composite Tissue-Engineered Total Disc Replacement

Dong Hwa Kim<sup>1,2</sup>, John T. Martin<sup>1,2</sup>, Sarah E. Gullbrand<sup>1,2</sup>, Christian G. Pfeifer<sup>1,2</sup>, Dawn M. Elliott<sup>3</sup>, Lachlan J. Smith<sup>1,2</sup>, Harvey E. Smith<sup>1,2</sup>  
and Robert L. Mauck<sup>1,2\*</sup>

<sup>1</sup>University of Pennsylvania, Philadelphia, PA, <sup>2</sup>Philadelphia VA Medical Center, Philadelphia, PA, <sup>3</sup>University of Delaware, Newark, DE

Disclosures: DH Kim (N), JT Martin (N), SE Gullbrand (N), CG Pfeifer (N), DM Elliott (N), LJ Smith (N), HE Smith (N), RL Mauck (N)

**INTRODUCTION:** Low back pain arising from disc degeneration is one of the most common causes of limited function in adults [1]. Current treatment options are limited, favoring either physical therapy and pain management or surgical methods to fuse the motion segment. Neither approach restores native tissue structure and function, and so a number of tissue engineering strategies have emerged that are focused on the creation of a composite tissue engineered total disc replacement [2,3], with some recent studies showing promise *in vivo* [4,5]. To further this line of inquiry, we fabricated a simple composite engineered disc based on the combination of a porous polymer foam annulus fibrosus (AF) and a hyaluronic acid (HA) gel nucleus pulposus (NP). We used these constructs to determine whether the combination of native AF/NP cells or mesenchymal stem cells (MSCs) would mature to a greater extent *in vitro* and which cell type would best retain their phenotype after *in vivo* implantation in a rat tail model of disc replacement [6].

**METHODS:** Porous polycaprolactone (PCL) foams were fabricated by salt-leaching to form the AF regions of the engineered discs. PCL was dissolved in chloroform at a 20% (w/v) concentration and NaCl particles were sieved to yield particulate of ~106 µm that was loaded and mixed into the PCL solution with a PCL/NaCl mass ratio of 1:4 (% w/w). The resultant solidified PCL sheet with entrapped salt particles was 1.5 mm in height and individual plugs were extracted using 4 mm biopsy punch for the outer diameter and 2 mm for the inner diameter; this geometry approximates that of the rat caudal disc. To form the NP regions of the engineered discs, 1% methacrylated HA (MeHA) hydrogels were produced as in [7]. AF cells (AFCs) or MSCs were seeded onto the PCL foam at a density of 2×10<sup>6</sup> cells/construct, whereas NP cells (NPCs) or MSCs were encapsulated in HA at a density of 20×10<sup>6</sup> cells/ml. AF and NP regions were cultured separately in chemically defined media and combined at 2 weeks. At regular intervals over 9 weeks, compressive mechanical, biochemical, and histologic properties were evaluated. Additionally, AF/NP cell and MSC/MSC cell-seeded constructs were implanted into the rat caudal disc space after 5 weeks of pre-culture, as in [6]. After 5 weeks *in vivo*, disc height, hydration of the nucleus pulposus, and structure were assessed by µCT, fluoroscopy, and quantitative T2 MRI, and structure was evaluated via histological analyses with alcian blue/picosirius red and collagen type II staining.

**RESULTS:** By 3 weeks, the NP region of all the groups stained intensely for proteoglycans, while collagen staining in the NP increased with further culture time. In the AF region, staining gradually increased with time, though to a lesser extent than in the NP (Fig. 1). There were no significant changes in compressive modulus over 8 weeks for either group (not shown). After 5 weeks of pre-culture and 5 weeks of implantation, disc height index (DHI) for implanted constructs was significantly greater than pre-operative levels, with only small differences between groups. Implanted discs did not result in intervertebral fusion (Fig. 2A). Alcian blue/picosirius red staining showed abundant collagen in the disc, but little proteoglycan in the NP region in either group. However, collagen type II staining was intense and localized to the NP at this time point (Fig. 2B). MRI showed that implanted discs had a similar structure to native discs (Fig. 3A, B). T2 mapping showed reduced signal in the NP for both groups compared to native discs. However, there was no significant difference between AF/NP group and native discs (Fig. 3C).

**DISCUSSION:** This study demonstrated that a tissue engineered disc composed of a PCL foam AF region and a hydrogel NP region could be fabricated, matured *in vitro*, and implanted and maintained in the rat caudal spine. Engineered discs comprised of AF/NP cells and MSCs performed similarly, maintaining their structure after 5 weeks *in vivo*, though loss of proteoglycan was evident in the NP region for both groups. This suggests that, following 5 weeks of implantation, water and proteoglycan content are less than in the native disc, perhaps reflecting the inflammatory nature of the operative site and unwanted remodeling post-implantation.

**SIGNIFICANCE:** This work demonstrates the successful fabrication, maturation, and *in vivo* function of a composite engineered disc composed of a PCL foam AF and a hydrogel NP using both native disc cells or MSCs.

**REFERENCES:** [1] Whatley+ 2012 Mater. Sci. Eng. [2] Mizuno+ 2004 Spine [3] Mizuno+ 2006 Biomaterials [4] Martin+ 2014 Acta Biomat. [5] Bowles+ 2011 PNAS [6] Martin+ 2015 SB3C [7] Kim+ 2015 Acta Biomat.

**ACKNOWLEDGEMENTS:** This work was supported by the Department of Veterans' Affairs (I01 RX001321 and IK2 RX001476) and the Penn Center for Musculoskeletal Disorders (P30 AR069619).

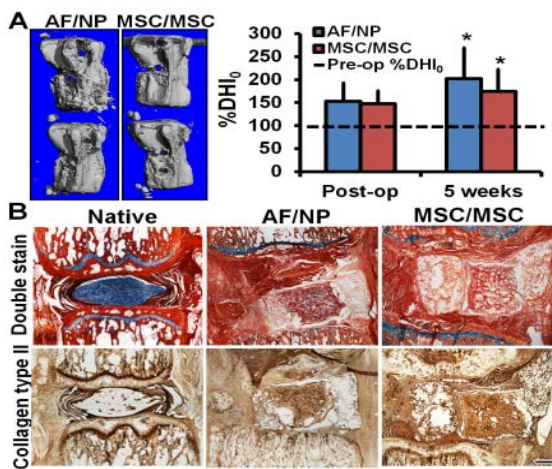


Fig. 2 (A) µCT and fluoroscopic analysis of %DHI for implanted AF/NP and MSC/MSC engineered disc and (B) histology and immunostaining at 5 weeks after implantation. (\*:p<0.05 vs. pre-op) (bar = 500 µm)

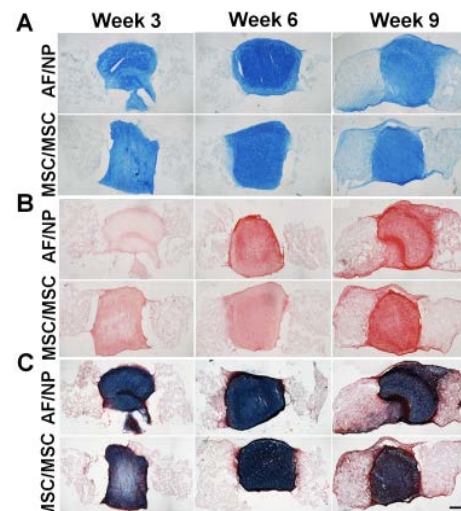


Fig. 1 (A) Alcian blue, (B) picosirius red, and (C) Alcian blue/picosirius red staining of AF/NP and MSC/MSC engineered disc with time in *in-vitro* culture. (bar = 500 µm)

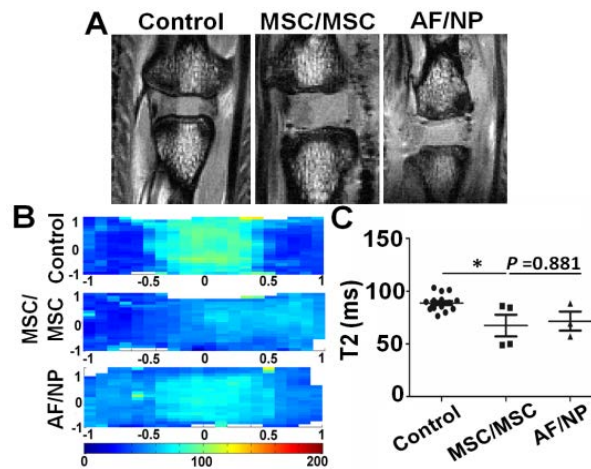


Fig. 3 (A) T2 MRI images and (B) T2 maps with (C) quantification at 5 weeks after implantation (\*:p=0.009 vs. control).

## **CD14 deficiency delays progression of cartilage degeneration and protects against early deficits in functional outcomes in a murine osteoarthritis model**

Nisha Sambamurthy, Vu Nguyen, Ryan Smalley, George R. Dodge, Carla R. Scanzello

**Purpose:** CD14, though expressed by multiple cell types, is highly expressed by monocytes and macrophages. It functions to bind LPS-LPS binding protein and complexes with Toll-like receptors (TLRs), particularly TLR-2 and TLR-4, to facilitate innate host defense mechanisms. Elevated CD14 expression has been associated with joint space narrowing and symptoms in patients with OA (Daghestani et al. 2015). Previous work from our lab has shown that soluble CD14 in synovial fluid from patients with knee OA sensitizes fibroblast like synoviocytes (FLS) to respond to multiple TLR ligands. In the current study, we investigate the involvement of CD14 in the development of structural and functional features of disease in a murine knee OA model.

**Methods:** CD14 deficient mice ( $CD14^{-/-}$ ) and C57BL/6J congenic controls (WT) were obtained through Jackson Laboratory. 10-12 week old male mice from both strains were subjected to destabilization of medial meniscus (DMM), sham surgery or left unoperated. Six and nineteen weeks post-surgery were chosen as early and advanced time points in this model, groups of 5-9 mice were sacrificed and knee joint histopathology evaluated using the modified OARSI score (Miller RE et al. 2016). As a surrogate for joint pain, changes in spontaneous activity were investigated longitudinally (every 4 weeks, up to 16 weeks) after DMM surgery in the two strains, using the LABORAS® Laboratory animal behavior observation registration and analysis system (Metris B.V., Hoofdorp, The Netherlands).

**Results:** Six weeks after DMM surgery,  $CD14^{-/-}$  mice showed similar degrees of cartilage erosion (Mean score  $\pm$ SEM,  $4.667 \pm 1.38$ ) as WT controls ( $4.6 \pm 0.6$ ,  $p > 0.9999$ ). However, by 19 weeks post-DMM, cartilage erosion was significantly reduced in  $CD14^{-/-}$  mice ( $6.0 \pm 0.46$ ) in contrast to their WT counterparts ( $13.44 \pm 2.5$ ,  $p < 0.0001$ ). Medial osteophytes were slightly larger in the WTs (mean measure ( $\mu\text{m}$ ) $\pm$  SEM:  $162 \pm 21.54$ ) compared to the  $CD14^{-/-}$  mice ( $101.7 \pm 38.51$ ,  $p = 0.03$ ) early on. By contrast at 19 weeks post-DMM, both strains displayed similar osteophytosis (WT:  $104.4 \pm 23.16$ ;  $CD14^{-/-}$ :  $138.8 \pm 22.48$ ,  $p = 0.15$ ). Analysis of spontaneous activity indicated significant decreases in climbing activity by WT mice at 4 weeks post-DMM; with maximal differences at 8 weeks (~84% lesser than baseline).  $CD14^{-/-}$  mice in contrast had maintained climbing activity through the course of 16 weeks post-DMM surgery. Furthermore,  $CD14^{-/-}$  mice climbed significantly greater number of times each hour at 8, 12 and 16 weeks post-DMM as compared to baseline ( $p \leq 0.004$ ), In contrast to WT mice, which display only mild increases compared to their baseline ( $p \geq 0.11$ ). **Conclusion:** Deficiency of CD14 expression significantly diminished medial cartilage erosion in the advanced phase of OA, while protecting the mice from early climbing deficits described in this model. Subsequently, an opposite time trend was observed in terms of osteophytosis. These findings indicate that loss of CD14 may affect structural and functional outcomes in this model through different mechanisms over different timelines. Further studies are needed to characterize the different immune cell types involved and the mechanism of action for suitable therapeutic targeting of OA progression.

## **Regulation of digit and joint development by *ACVR1* and its role in fibrodysplasia ossificans progressiva**

O Will Towler, Fred S Kaplan, Eileen M Shore

**Abstract:** Joint development during embryogenesis requires the coordination of multiple signaling pathways to ensure differentiation of cells in the joint space into synovium, tendons, and articular cartilage. Humans with fibrodysplasia ossificans progressiva (FOP) present with heterotopic ossification and digit joint malformation caused by a heterozygous gain-of-function mutation (R206H) in the bone morphogenetic protein (BMP) type 1 receptor ACVR1/ALK2. A mouse model expressing *Acvr1<sup>R206H</sup>* faithfully recapitulates these two phenotypes. Using this model, we demonstrate that the distal skeleton of the limbs experiences developmental delay of the joints and delayed ossification of skeletal elements. We show that *Acvr1<sup>R206H</sup>* aberrantly activates the canonical BMP signaling pathway early in development, leading to delayed separation of the phalanges and eventual joint malformation. We are investigating how this aberrant activation affects the activity of pathways necessary for articular cartilage differentiation such as TGF $\beta$  and Wnt. We are investigating the contributions of joint cell population, the developing growth plate, and apoptosis within the joint space that lead to perturbations in joint development and to the FOP phenotype. We hypothesize *Acvr1<sup>R206H</sup>* causes decreased contribution of joint cells to articular cartilage, delayed chondrocyte maturation in the growth plate, and increased apoptosis of joint interzone cells.

## Subchondral bone plate sclerosis during late osteoarthritis is mediated by loading-induced decrease in Sclerostin amount

Xiaoyuan Ma<sup>1</sup>, Haoruo Jia<sup>1</sup>, Wei Tong<sup>1</sup>, Zhaochun Yang<sup>2</sup>, Zeyang Sun<sup>3</sup>, Abhishek Chandra<sup>1</sup>, Lin Han<sup>4</sup>, Kairui Zhang<sup>5</sup>, James H-C Wang<sup>2</sup>, Motomi Enomoto-Iwamoto<sup>5</sup>, and Ling Qin<sup>1</sup>

<sup>1</sup> Department of Orthopaedic Surgery, School of Medicine, University of Pennsylvania, Philadelphia, Pennsylvania, USA; <sup>2</sup> Department of Orthopaedic Surgery, University of Pittsburgh School of Medicine, Pittsburgh, Pennsylvania, USA; <sup>3</sup> School of Engineering and Applied Science, University of Pennsylvania, Philadelphia, Pennsylvania, USA <sup>4</sup> School of Biomedical Engineering, Science and Health Systems, Drexel University, Philadelphia, Pennsylvania, USA; <sup>5</sup> Department of Surgery, The Children's Hospital of Philadelphia, Pennsylvania, USA

**Disclosures:** None

**INTRODUCTION:** Osteoarthritis (OA) is not only a cartilage disease but also accompanied by pathologic changes in bone beneath the articular cartilage. Subchondral sclerosis is a hallmark of late OA and previous studies attribute it to a high bone turnover<sup>(1)</sup>. In late stage disease, the subchondral bone plate (SBP) thickens, but subchondral trabecular bone undergoes bone loss. The exact mechanism is still largely unknown. Using a unique genetic mouse model that we recently established for OA study and a computational finite element analysis (FEA), we discovered a novel mechanical and cellular mechanism to explain how cartilage depletion causes local subchondral sclerosis.

**METHODS:** All animal work was approved by IACUC at the University of Pennsylvania. **Animals and surgery-** Cartilage-specific *Egfr CKO* (*Col2-Cre Egfr<sup>Wa5f</sup>*) mice and their *Wa5* (*Egfr<sup>Wa5f</sup>*) and wild-type (WT, *Col2-Cre Egfr<sup>f/+</sup>* and *Egfr<sup>f/+</sup>*) siblings were generated by breeding *Col2a1-Cre*, *Egfr<sup>Wa5/+</sup>*, and *Egfr<sup>f/f</sup>* mice as described previously<sup>(2)</sup>. *Egfr<sup>Wa5</sup>* codes for a kinase-dead, dominant negative receptor. To induce OA, male mice at 3 months of age were subjected to destabilization of the medial meniscus (DMM) surgery at the right knees and sham surgery at the left knees. Another OA mouse model was DMM and hemisection of the meniscus (DMMH) surgery on the right knees of WT mice. **μCT-** Distal femurs and proximal tibiae from mouse knee joints harvested after surgery were scanned by μCT 35 (Scanco Medical AG) at a resolution of 6 μm to calculate trabecular bone structural parameters. **Histology and immunohistochemistry (IHC)-** A serial of 6 μm-thick sagittal paraffin sections were cut across the entire joint followed by histology and IHC staining. **FEA analysis-** We constructed three knee models (Sham, early OA, and late OA) with effective modulus values obtained from nanoindentation tests for FEA using ANSYS160 by PLANE182 under axisymmetrical conditions. The top surface of femur was loaded with  $1 \times 10^4$  Pa to simulate loading on mouse knee joints, while the bottom surface of tibia was fixed. **Statistics-** Data are expressed as means±SEM and analyzed by Student's t-test.

**RESULTS:** At 2-3 months after DMM, while WT and *Wa5* mice developed mild to moderate OA with no changes in the SBP, *Egfr CKO* mice exhibited the most severe OA with a complete loss of articular cartilage layer at the medial site (Fig. 1A) and mild cartilage degeneration at the lateral site. Interestingly, these mice had a substantial 2.0-fold thickening in SBP restricted only at the medial site (Fig. 1B), implicating that this localized SBP response is likely due to the alteration of overlaying articular cartilage. IHC revealed a 6.6-fold increase in the number of osteoblasts lining the SBP at the medial site (Fig. 1C). This enhanced bone formation was accompanied by increased length of blood vessels aligning SBP surface to support new bone formation. Wnts are potent signals for osteoblastic bone formation. Strikingly, staining of Sclerostin, a Wnt antagonist, in osteocytic cell bodies and dendritic processes, was remarkably attenuated in SBP at the medial site of *CKO DMM* joint (Fig. 1D). The amount of Sclerostin at the lateral site was similar to those at sham sites of three types of mice, as well as those at WT and *Wa5* DMM sites. Aged *Egfr CKO* mice developed spontaneous OA at both medial and lateral sites, resulting in a similar level of SBP sclerosis across the entire knee (Fig. 2A, B). Interestingly, this was also accompanied by an elevation of osteoblasts at the bone marrow site of SBP (Fig. 2C) and a drastic reduction of osteocytic Sclerostin within SBP (Fig. 2D). Diminished Sclerostin amount at late OA is not limited to *CKO* mice only. At 16 weeks post DMMH, WT joints developed late OA symptoms at medial site. Similarly, DMMH knees had a significant decrease of sclerostin within SBP only at medial site but not at lateral site (Fig. 3). Mechanical loading is a major regulator of Sclerostin in the cortical bone. Using computational FEA to simulate mouse OA knees, we demonstrated that the highest focal stress on SBP at late OA stage (without cartilage) drastically increased to 14.6-fold of early OA joints (with cartilage), indicating that SBP at late OA experiences very high mechanical stress.

**DISCUSSION:** Our data demonstrated that increased mechanical loading on SBP after cartilage depletion at late OA attenuates osteocytic Sclerostin amount within SBP, resulting in increased bone formation at the bone marrow site of SBP and subsequent SBP sclerosis. One potential concern of using *Egfr CKO* mice to study SBP sclerosis is that this model might target bone forming cells so this model is not chondrocyte-specific. Since our previous studies have demonstrated an important regulatory role of EGFR signaling on bone marrow mesenchymal progenitors<sup>(3,4)</sup>, it is possible that SBP sclerosis in *Egfr CKO* mice might be partially resulted from changes in bone remodeling. However, trabecular bone structure in the secondary spongiosa analyzed by μCT and serum bone formation and resorption markers were not altered in these mice, proving that SBP changes in *CKO* mice must be due to late OA progression. The similar mechanism observed in WT mice after DMMH further substantiates our conclusion.

**SIGNIFICANCE:** Subchondral bone plays a crucial role in the initiation and progression of OA and therefore is recognized as therapeutic target for OA treatment. Our study elucidates the important role of mechanical loading and Sclerostin in regulating the response of SBP toward cartilage degeneration at the late OA stage.

**REFERENCES:** 1. Castaneda S et al. Biochem Pharmacol. 2012;83(3):315-23; 2. Zhang X et al. J Bone Miner Res. 2011;26(11):2622-33; 3. Chandra A et al. J Biol Chem. 2013;288(45):32229-40; 4. Zhang X et al. J Bone Miner Res. 2011;26(5):1022-34.

**ACKNOWLEDGEMENT:** This work was supported by ASBMR Research Career Enhancement Award (to LQ), NIH grants AR060991 (to LQ), AR062908 (to ME-I), and AR066824 (to LH) and Penn Center for Musculoskeletal Disorders P30AR069619 (NIAMS/NIH)

**Fig. 1**

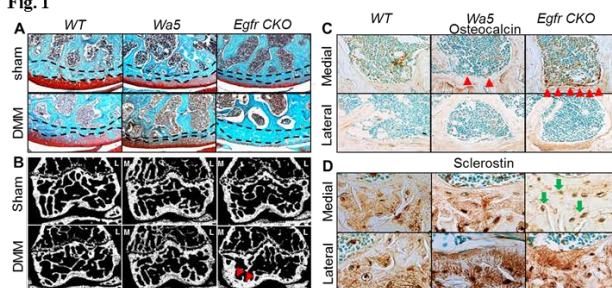


**Fig. 2**

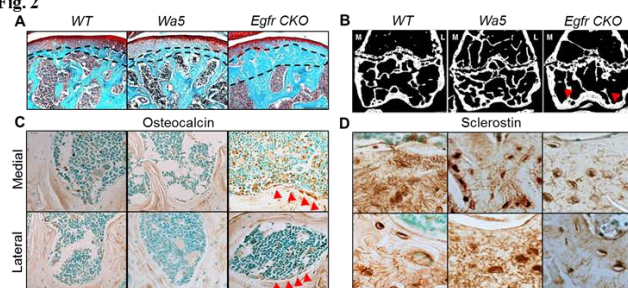
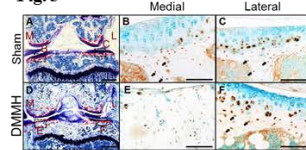


Fig. 1. *Egfr CKO* mice develop local SBP sclerosis underneath the severely damaged cartilage area after OA surgery. (A) Safranin O staining of WT, *Wa5*, and *CKO* mouse sham and DMM joints at medial site 2 months post surgery. Dashed lines depict SBP. (B) μCT images of femoral epiphysial region. M: medial site; L: lateral site. Red arrows point to thickened SBP at the medial site of *CKO* joint after DMM. (C) IHC of osteocalcin to identify osteoblasts (red arrowheads) beneath SBP in DMM joints. (D) IHC of Sclerostin in SBP in DMM joints. Green arrows point to reduced Sclerostin staining at medial site of *CKO* DMM knees. n=4-10/genotype.

Fig. 2. SBP sclerosis in aging *Egfr CKO* knees are caused by increased bone formation along SBP surface and suppressed Sclerostin expression in SBP. (A) Safranin O staining of femoral epiphysial region in 12-month-old WT, *Wa5*, and *CKO* mice. Dashed lines: SBP. (B) μCT images of femoral epiphysial region. Red arrows point to thickened SBP in *CKO* joints. (C) IHC of osteocalcin to identify osteoblasts (red arrowheads) beneath SBP. (D) IHC of Sclerostin in SBP. n=4/genotype.

Fig. 3. Late OA symptoms after DMMH include thickened SBP and its associated reduction in osteocytic sclerostin amount. H&E staining (A,D) showed obvious SBP thickening (depicted by red lines) at the medial site (M) only. Sclerostin staining (B,C,E,F) on neighboring sections revealed reduced staining in medial site of DMMH knees (E). Black squares in A and D depict the corresponding areas for B,C,E,F. n=3 mice.

**Fig. 3**



## RAR $\gamma$ Agonist Promotes Functional Restoration of Severely Injured Skeletal Muscle in Mouse

Min Liu<sup>1</sup>, Agnese Di Rocco<sup>2</sup>, Lily Wu<sup>1</sup>, Masaoka<sup>1</sup>, Suzu Deie<sup>3</sup>, Motomi-Enomoto-Iwamoto<sup>1</sup>, Iwamoto Masahiro<sup>1</sup>  
<sup>1</sup>Division of Orthopedics Surgery, Children Hospital of Philadelphia, Philadelphia, <sup>2</sup>Dept of Cancer Biology, Thomas Jefferson University, Philadelphia, and <sup>3</sup>Hiroshima University Medical School, Hiroshima

**INTRODUCTION:** Skeletal muscles can be damaged or injured by multiple causes including overuse, trauma, infections, or loss of blood circulation. When the damage is not severe, skeletal muscles repair themselves efficiently with major contribution from satellite cells that surround the muscle fibers. In contrast, repair of severely damaged muscles is much more challenging. It takes a long time, and often results in decrease of muscle functionality due to scar formation. We recently showed in mice that selective agonists for nuclear retinoic acid receptor  $\gamma$  (RAR $\gamma$ ) blocks genetic or rhBMP-induced forms of heterotopic ossification, a pathology involving ectopic bone formation at the expense of skeletal muscles. Furthermore; muscle injury repair was remarkably delayed in RAR $\gamma$  null mice. These observations suggest that activation of RAR $\gamma$  prevents muscle degeneration and/or promotes muscle repair. To follow up this intriguing observation, we investigated the effect of RAR $\gamma$  agonists on functional restoration of experimentally generated critical defect in TA muscle in mice.

**METHODS:** Animals and Drug treatment: CD1 mice were randomly divided into four groups: 1 month control, 1 month treated, 2 month control and 2 month treated groups (n=5). Control mice received vehicle corn oil and the treated mice received oral gavage of palovarotene, a selective RAR $\gamma$  agonist (4 mg/kg) every other day during 2-4 weeks after surgery. Surgery: Critical muscle defect injury was generated by thermal cautery (Figure 1). In situ assessment of TA muscle function: TA muscles were individually attached to the lever arm of a 305B dual-mode servomotor transducer. The sciatic nerve was exposed and all its branches cut except for the common peroneal nerve, which innervates the TA and EDL muscles. TA muscle contractions were then elicited by stimulating the distal part of the deep peroneal nerve via bipolar electrodes. Maximum isometric tetanic force of TA was determined at 150Hz for 500ms duration. The TA specific forces (N/cm<sup>2</sup>) were calculated by dividing Po by muscle cross-sectional area. Transplantation of mesenchymal stem cells: Muscle derived local mesenchymal cell like population (M-MSC) was obtained by digesting minced muscle tissue of P1-P5 mice with 0.1% collagenase. Bone marrow stroma cells (BMSCs) were isolated as described (Nat Med 2011, 17:454e460). Cells were treated with 300 nM NRX204647 (RAR $\gamma$  agonists) or vehicle for three days before transplantation. Cells (1-2 x10<sup>4</sup> cells per site) were then transplanted into the muscle defect. Tissue was collected 2 weeks after operation and subjected to histological analyses.

**RESULTS:** Histomorphometric analysis revealed that palovarotene (R667) treatment significantly increased muscle content and decrease adipose tissue at 1 month after surgery (Figure 1). By 2 months post-surgery, we observed a time-dependent increase in number of the neuromuscular junctions in healing muscle. Mechanical tests of TA muscles revealed that TA muscles of the drug treatment group showed 15-24% higher peak twitch tension, peak tetanic force and muscle specific force. To investigate RAR $\gamma$  target cells during muscle repair, we stained intact and experimentally injured muscle tissue by the antibodies against RAR $\gamma$  and TGM2 (a retinoid target). Interestingly, over 75% cells showed positive to the staining in the interstitial space, but few cells in the muscle fibers, suggesting that the targets of RAR $\gamma$  agonists are resident or circulating MSCs. To test this, we treated MSCs derived from muscle, bone marrow and adipose tissues for 3 days with RAR $\gamma$  agonists or vehicle in culture and transplanted into the muscle injury sites. Transplantation of the RAR $\gamma$ -pretreated BMSCs induced superior muscle healing compared to the non-treated BMSCs transplantation. The pre-treated cells were retained within or around the muscle defect even 2 weeks after transplantation, and some BMSCs were positive to myosin heavy chain. In contrast, the control BMSCs were barely detectable in the transplanted region (Figure 2).

**DISCUSSION:** Present study shows that the injury model is indeed non-repairable at least for 2 months and that RAR $\gamma$  treatment significantly promoted functional restoration of injured TA-muscle. Histomorphometric and mechanical analysis revealed that functional restoration of the critically injured muscle requires 1 month of regeneration phase and at least 1 month of the remodeling phase. Cell transplantation study suggests that RAR $\gamma$  signaling promotes muscle repair at least indirectly through MSC like cells in the damaged muscle tissue. Thus RAR $\gamma$  agonist might be useful in drug and MSC-based therapies for severely damaged skeletal muscles.

**SIGNIFICANCE:** The research is conducted to explore an effective, easy to employ, and cost-effective therapy for severe muscle injury.

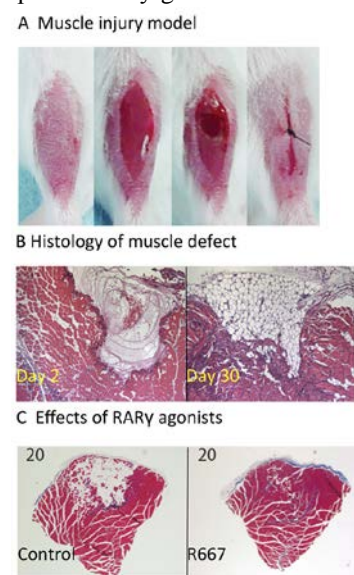


Figure 1: TA muscle injury model. Panel A shows four muscle samples with increasing red staining. Panel B shows histology at Day 2 and Day 30. Panel C compares Control and R667 groups.

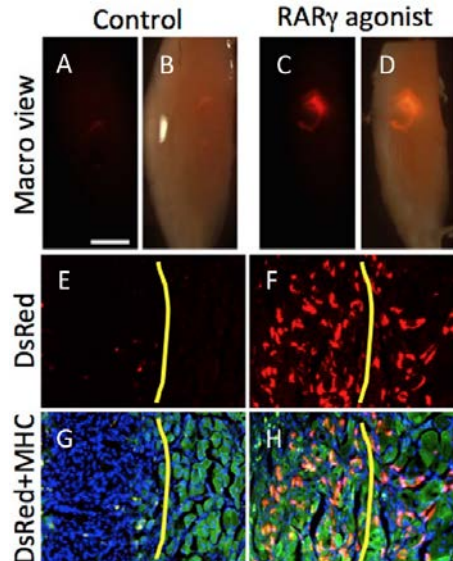


Figure 2: RAR $\gamma$  agonist treated BMSC retains and promotes repair.

# A GMSC/SIS-ECM Construct Promotes Myomucosal Regeneration of the Tongue

Qilin Xu<sup>1#</sup>, Rabie M. Shanti<sup>1, 2, 3#</sup>, Qunzhou Zhang<sup>1</sup>, Steven B. Cannady<sup>2</sup>, Bert W. O'Malley Jr.<sup>2\*</sup>, and Anh D. Le<sup>1, 3\*</sup>

<sup>1</sup>Department of Oral and Maxillofacial Surgery and Pharmacology, University of Pennsylvania School of Dental Medicine, Philadelphia, Pennsylvania; <sup>2</sup>Department of Otorhinolaryngology-Head and Neck Surgery, University of Pennsylvania Perelman School of Medicine, Philadelphia, Pennsylvania; <sup>3</sup>Department of Oral & Maxillofacial Surgery, Penn Medicine Hospital of the University of Pennsylvania, Philadelphia, Pennsylvania.

**Abstract:** In the oral cavity, the tongue is the anatomic subsite most commonly involved by invasive squamous cell carcinoma. Current treatment protocols often require significant tissue resection to achieve adequate negative margins and optimal local tumor control. Reconstruction of the tongue while preserving and/or restoring its critical vocal, chewing, and swallowing functions remains one of the major challenges in head and neck oncologic surgery. The objective of the current study is to explore the feasibility of fabricating a novel combinatorial construct using porcine small intestinal submucosa extracellular matrix (SIS-ECM) and human gingival mesenchymal stem cells (GMSCs) as a GMSC/SIS-ECM tissue graft for the reconstruction of tongue defects. A combinatorial construct was generated by seeding human gingiva-originated mesenchymal stem cells (GMSCs) onto an FDA-approved decellularized porcine small intestinal submucosa extracellular matrix (SIS-ECM 2.0), which was generously provided by Cook Biotech, Inc. (West Lafayette, IN, USA). A critical-sized (~6mm diameter) myomucosal defect of the tongue of rats was created and patched with SIS-ECM or GMSC/SIS-ECM constructs with the cell-seeded side oriented toward the wounded muscle layers. The therapeutic effects of the transplanted constructs on the repair and regeneration of the tongue defect was evaluated by histological and immunofluorescence studies. We showed that the GMSC/SIS-ECM construct engrafted at the host recipient site, promoted soft tissue healing, and regenerated the muscular layer, as compared to the SIS-ECM alone or non-treated defect controls. Furthermore, our results revealed that transplantation of the GMSC/SIS-ECM construct significantly increased the expression of several myogenic transcriptional factors, including PAX7, MYOD and MYF5, and simultaneously suppressed the expression of type I collagen at the wounded area of the tongue. These compelling findings suggest that, unlike the tongue contracture and fibrosis of the non-treated groups, transplantation of the combinatorial GMSC/SIS-ECM constructs accelerates wound healing and muscle regeneration, and maintains the overall tongue shape, possibly by both enhancing the function of endogenous skeletal progenitor cells and suppressing scar formation. Together, our findings indicate That GMSC/SIS-ECM serve a potential myomucosal graft for post-surgery tongue reconstruction for head and neck cancer patients.

**Key Words:** Gingiva-derived MSCs, SIS-ECM, Combinatorial construct, Wound healing, Tongue Regeneration, Skeletal progenitor cells

*This work was supported by National Institute of Health Research Grant, R01DE 019932, Oral and Maxillofacial Surgery Foundation (OMSF) Research Grant, OsteoScience Foundation, and the Schoenleber funding support.*

## Intraflagella Transport Protein 20 is Indispensable for Ciliogenesis and Bone Formation

Saif Abdul Majeed<sup>1</sup>, Xue Yuan<sup>2</sup>, Shuying Yang<sup>1,2,3</sup>

<sup>1</sup> Department of Anatomy & Cell Biology, School of Dental Medicine, University of Pennsylvania, PA, <sup>2</sup> Department of Oral Biology, School of Dental Medicine, University of Buffalo, State University of New York, Buffalo, NY

<sup>3</sup> Developmental Genomics Group, New York State Center of Excellence in Bioinformatics and Life Sciences, University of Buffalo, The State University of New York, Buffalo, NY, United States

\*Corresponding author: Dr. Shuying Yang, shuyingy@upenn.edu

Intraflagellar transport proteins (IFTs) play a pivotal role in cilia formation and function. Disruption of IFTs function can cause multiple diseases such as skeletal dysplasia. IFT20 is the smallest IFT protein in the IFT-B complex. However, the function and mechanism of IFT20 in bone formation remain elusive. In this study we generated osteoblast (OB)-targeted IFT20 knockout mice ( $\text{IFT20}^{\text{d/d}}$ ) by crossing the  $\text{IFT20}^{\text{flox/flox}}$  ( $\text{IFT20}^{\text{ff}}$ ) mice with OSX-Cre transgenic mice. Here we show that deletion of ciliary IFT20 in osteoblast precursor cells (OPC) in mice compromised ciliogenesis. Deletion of IFT20 *in vivo* lead to growth retardation, and markedly decreased bone mass, trabecular number, trabecular thickness as well as increased trabecular separation. Moreover, IFT20 loss impaired osteoblast differentiation and bone mineralization as reflected by alkaline phosphatase assay (ALP) and Alizarin red staining respectively. Gene expression of osteoblast markers such as osterix, ALP and osteocalcin were significantly decreased following IFT20 deletion. IFT20 loss significantly brought down the expression of bone formation genes such as BMP2, BMP4 and Runx2. Furthermore, deletion of IFT20 significantly decreased osteoblast proliferation and migration. In conclusion, our findings show that IFT20 is indispensable for regulating not only ciliogenesis but also for osteoblastogenesis and bone formation. Hence, IFT20 could be a therapeutic target for bone metabolic disorders.

Keywords: IFT20, ciliogenesis, bone formation, osteoblast differentiation, osteoblast proliferation.

## RGS12 cooperates with IFT20 to regulate cilia formation and osteoblast differentiation

Jormay Lim<sup>1</sup>, Changdong Wang<sup>2</sup>, Xue Yuan<sup>2</sup>, Saif Abdul Majeed<sup>1</sup> and Shuying Yang<sup>1,2,3\*</sup>

<sup>1</sup>Department of Anatomy and Cell Biology, School of Dental Medicine, University of Pennsylvania; <sup>2</sup>Department of Oral Biology, School of Dental Medicine, University of Buffalo, State University of New York, Buffalo, NY, United States; <sup>3</sup>Developmental Genomics Group, New York State Center of Excellence in Bioinformatics and Life Sciences, University of Buffalo, The State University of New York, Buffalo, NY, United States.

\*Corresponding author: Dr. Shuying Yang, shuyingy@upenn.edu

Intact ciliary structure and the dynamics of ciliary transport mediated by Intraflagellar transport proteins (IFTs) are important for many G protein coupled receptor (GPCR) signaling in particular Hedgehog signaling. Our previous data demonstrated that IFT80 is essential for cilia formation and Hedgehog signaling pathways. How GPCR transports in and out of cilia and whether this is mediated by Regulator of G protein signaling (RGS) such as RGS12 remain intriguing. To address the question, we generated the osteoblast specific conditional knockout mice of the RGS12, IFT20 and combination of both genes by using osteorix-cre transgenic mice. Primary osteoblasts (POB) were isolated from calvaria bones and treated with Adenovirus Cre or Adenovirus GFP. The effects of the deletions are quantified in comparison to non-deleted controls. ALP assay and Alizarin Red staining of differentiated osteoblasts showed that RGS12 and IFT20 and double deletion all reduced osteoblast differentiation. The reduction was enhanced in double deletions. In addition, IFT20 deletion led to loss of cilia, whereas RGS12 deletion caused a shortened cilium in POB. Moreover, overexpression of RGS12 results in a lengthened and thickened cilium. Preliminary data of mouse phenotypes showed that the anterior posterior length of the skull in the double deletion mouse was reduced in comparison to wildtype or IFT20 deletion alone. The histological analysis and micro-CT data also showed that RGS12 deletion or IFT20 deletion caused the decreased bone mass compared to Osterix-cre control and the double deletion deteriorates the effects. Thus, our collated data suggest that RGS12 is involved in IFT20 ciliary maintenance in osteoblast differentiation. Further studies are carried out to delineate the molecular mechanism by which RGS12 and IFT20 regulate cilia formation and bone formation.

## **Bortezomib rescues radiation-induced osteoporosis by promoting DNA repair and cell survival in osteoblasts**

Abhishek Chandra, Luqiang Wang, Tiffany Young and Ling Qin

Department of Orthopaedic Surgery Perelman School of Medicine, University of Pennsylvania,  
Philadelphia, Pennsylvania, 19104, USA

The maximum benefit of clinical radiotherapy is limited by its damage to tumor neighboring tissues. Bone atrophy and its related fragility fractures are frequent late side effects of radiotherapy in cancer survivors and have detrimental impact on their quality of life. We previously showed that PTH1-34 anabolic injections has the ability to block radiation-induced bone damage by accelerating DNA repair in osteoblasts after radiation. DNA damage responses are tightly regulated by the ubiquitin proteasome pathway. In this study, we examined whether proteasome inhibitors (PSI) have the similar bone protective effects again radiation damage. *In vitro*, MG132 treatment greatly attenuated apoptosis in irradiated primary osteoprogenitors, osteoblastic UMR106 cells, and osteoblasts in calvarial cultures. This survival effect of MG132 was accompanied by decreases in the number of DNA double-stranded breaks and overall DNA damage, as revealed by  $\gamma$ H2AX foci and comet assays, respectively, and up-regulation of amounts of Ku70 and DNA-PKc, two essential DNA repair proteins in the non-homologous end joining pathway. *In vivo*, we tested the efficacy of Bortezomib (Bzb), the first PSI approved for cancer treatment, in restoring bone quality after radiation. Two-month-old mice were focally irradiated at the distal metaphyseal region of right femurs by a unique SARRP irradiator that replicates clinical focal radiotherapy with a clinically relevant dosage (8Gy at day 1 and 3). Mice were administered twice weekly with saline or Bzb (1mg/kg) for 4weeks. MicroCT scans revealed a significant 63.7% decrease in trabecular bone volume fraction (BV/TV) in irradiated tibiae compared to the contralateral tibiae in the vehicle group. Strikingly, Bzb completely reversed the effects of radiation on bone ablation with a 4.6-fold increase in BV/TV together with an 86.7% increase in trabecular number and a 52% decrease in trabecular separation compared to vehicle-treated radiated femurs. Histomorphometry demonstrated that Bzb significantly increased osteoblast number (34.5%) and activity (11.5-fold in MS and 13-fold in BFR) and meanwhile suppressed osteoclasts number (67%). In addition, Bzb treatment drastically reduced the percentage of TUNEL+ osteoblast cells and bone marrow adiposity. Taken together, our data demonstrate a novel role of proteasome inhibitors in attenuating radiation-induced osteoblast apoptosis and identify Bzb as a potential therapy for radiotherapy-related osteoporosis.

## Growth Factor and Extracellular Matrix Expression and Localization during Nucleus Pulposus Formation

Sun H. Peck<sup>1</sup>, Kendra K. McKee<sup>2</sup>, Neil R. Malhotra<sup>1</sup>, Brian D. Harfe<sup>2</sup>, Lachlan J. Smith<sup>1</sup>

<sup>1</sup>University of Pennsylvania, Philadelphia, PA; <sup>2</sup>University of Florida, Gainesville, FL

**Disclosures:** SHP (N), KKM (N), NRM (N), BDH (N), LJS (N)

**Introduction:** Intervertebral disc degeneration is implicated as a major cause of low back pain [1]. Current available treatment options primarily focus on relieving pain rather than regenerating disc tissue, and thus, there is a need for new therapeutic strategies that alleviate symptoms as well as restore disc structure and mechanical function. The earliest degenerative changes occur in the central nucleus pulposus (NP), where altered composition initiates a cascade that compromises mechanical function and culminates in structural failure. An impediment to the development of cell-based strategies for NP repair is the unique developmental origin of the NP, as NP cells are derived from the notochord and not the mesenchyme [2-4]. Improved understanding of embryonic NP formation may enable recapitulation of developmental signals that might drive therapeutic cell types, such as mesenchymal stem cells, towards an NP cell-like phenotype to optimize adult disc regeneration. Previously, we established changes in global mRNA expression profiles of resident cells as the notochord transforms into the NP using whole-transcriptome sequencing (RNA-Seq), and found that key signaling pathway elements that regulate patterning, growth, differentiation, as well as structural extracellular matrix (ECM) molecules, showed significant differential gene expression across this embryonic developmental window [5]. In this study, our objectives were to build on these findings by examining protein expression of growth factors and ECM molecules identified in our RNA-Seq results at key developmental stages as the notochord transforms into the NP.

**Methods:** For these IACUC approved studies, we used the Shh-cre;ROSA:YFP mouse model [3], where all Sonic Hedgehog (Shh) expressing notochord-derived cells express YFP throughout the life of the mouse (i.e. creates a fate map). We examined two key developmental stages representing the immediate, opposite ends of the notochord to NP transformation: E12.5 (fully formed, intact notochord) and P0 (fully formed spine with distinct disc space). Whole embryos (E12.5) or isolated spines (P0) were fixed in formalin, and processed into paraffin. Midsagittal, 8 µm thick sections were stained with Alcian blue/picosirius red (ABPR) for GAG and collagen respectively, hematoxylin and eosin (H&E) for cellularity, or immunostained with antibodies specific to proteins-of-interest (ECM: Collagens I, II and VI, and aggrecan; growth factors: Shh, transforming growth factor β1 (TGF-β1), and insulin-like growth factor 1 (IGF-1)) and counterstained with hematoxylin. Staining intensity in the notochord/NP and associated tissues was semi-quantitatively assessed.

**Results:** At E12.5, there was a discrete notochordal structure with a GAG-rich inner core and outer sheath, both of which were relatively acellular compared to the rest of the notochord (Fig 1). GAG-rich mesenchymal condensations in regions that will form future vertebral bodies were clearly present (Fig 1). At P0, the spine was fully formed with distinct vertebral bodies and disc spaces, including clear boundaries between the annulus fibrosus and the NP (Fig 1). Extracellular matrix components collagens I, II, and VI, and aggrecan showed diffuse staining in non-cellular regions (core and sheath) of the E12.5 notochord (Fig 2). At P0, these molecules exhibited intense staining at the outer boundary of the NP. SHH, TGF-β1, and IGF-1 all showed cellular expression in the E12.5 notochord. At P0, expression of TGF-β1 and IGF-1 by NP cells was heterogeneous (strongly by some cells, weakly by others). SHH expression in the NP was weaker at P0 than at E12.5. In both the E12.5 and P0 samples, positive immunostaining of non-notochord/NP tissues for many of these molecules was also observed. Semi-quantitative scoring of protein localization is presented in Tables 1 and 2.

**Discussion:** In our previous whole-transcriptomic profiling study, we found a large number of differentially expressed growth factor and ECM genes at P0 compared to E12.5 [5], which are largely reflected on the protein level in our current results. We demonstrated marked changes in protein localization and expression levels between E12.5 and P0. As mRNA and protein levels do not always directly correlate in expression, ongoing work is focused on elucidating regulatory and functional roles of these genes on both the transcriptional and translational levels. The changes observed most likely reflect a switch from patterning (decreased Shh signaling) to growth (increased TGF-β1, IGF-1, and ECM structural genes) as the NP develops into a functional, load-bearing tissue. Heterogeneous expression within the NP at P0 suggests that resident cells may be undergoing progressive phenotypic changes to accommodate evolving functional requirements. Interestingly, we also observed staining of non-notochord derived tissue in our studies, which will help to inform future studies exploring the roles of these molecules in embryonic spine development as a whole. Overall, these data support our long-term goal to establish and recapitulate the specific developmental signals required for embryonic NP formation in order to improve cell-based therapeutic strategies for disc regeneration.

**Significance:** Low back pain associated with intervertebral disc degeneration is a significant global health and economic burden. The results from this study further our knowledge and understanding of NP development and serves to inform development of improved cell-based therapeutics for disc regeneration.

**References:** [1] Andersson. Lancet, 1999. [2] Smith+ Dis Model Mech, 2011. [3] Choi+ Dev Dyn, 2008. [4] McCann+ Dis Model Mech, 2012. [5] Peck+ ORS Trans, 2016.

**Acknowledgements:** NIH, University of Pennsylvania Institute on Aging, Penn Center for Musculoskeletal Disorders (P30 AR09619).

Molecule	Developmental Stage and Region					
	E12.5			P0		
N	DC	VC	NP	IAF	OAF	E
SHH	**	-	-	*	-	-
TGFβ1	**	**	*	**	*	*
IGF1	**	**	*	*	-	**

Molecule	Developmental Stage and Region					
	E12.5			P0		
N	DC	VC	NP	IAF	OAF	E
Aggrecan	**	*	*	***	*	*
Collagen I	*	***	*	**	*	***
Collagen II	*	*	*	*	**	*
Collagen VI	*	***	-	***	-	**

**Summary tables of immunostaining patterns. Table 1.** ECM. **Table 2.** Growth factors. N: notochord, DC: disc condensations, VC: vertebral condensations, NP: nucleus pulposus, IAF: inner AF, OAF: outer AF, E: epiphysis/growth plate. - : absent; \* : weak; \*\* : moderate; \*\*\* : strong.

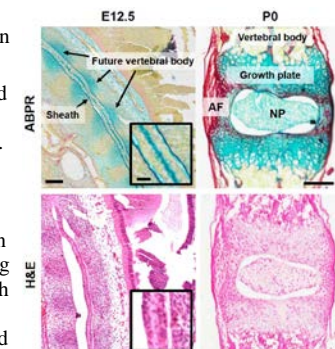


**Figure 1. Overall morphology at E12.5 (notochord) and P0 (disc).** AF: annulus fibrosus; NP: nucleus pulposus. Scale bar = 100 µm; inset scale bar = 20 µm.

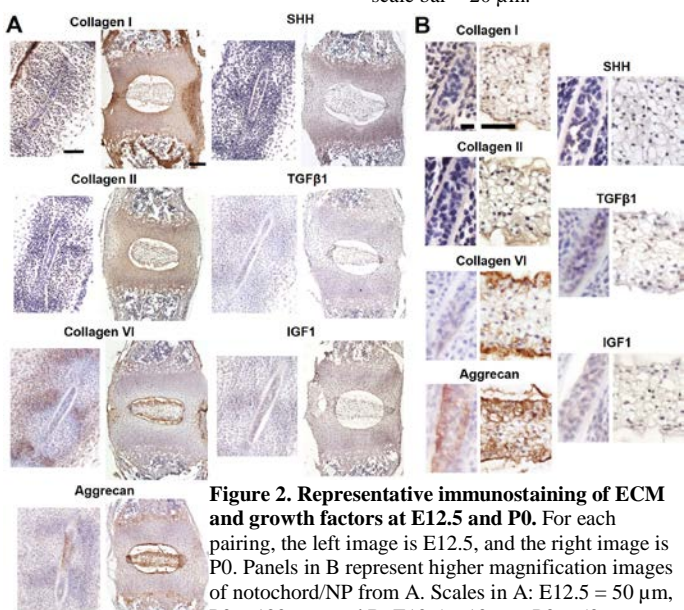


**Figure 2. Representative immunostaining of ECM and growth factors at E12.5 and P0.** For each pairing, the left image is E12.5, and the right image is P0. Panels in B represent higher magnification images of notochord/NP from A. Scales in A: E12.5 = 50 µm, P0 = 100 µm, and B: E12.5 = 10 µm, P0 = 50 µm.

# Visualizing osteocyte lacuna-canaliculi system and collagen network in bone

Shaopeng Pei<sup>1</sup>, Michael Moore<sup>2</sup>, Sherry X. Liu<sup>3</sup>, Liyun Wang<sup>1</sup>

1. Mechanical Engineering, University of Delaware; 2. Delaware Biotechnology Institute; 3. McKay Orthopaedic Research Lab, University of Pennsylvania

**Introduction:** Bone is a porous structure with osteocytes residing in elliptical spaces called lacunae and connected with long tube channels referred as canaliculi. Previous methods for staining the lacunar-canaliculi system (LCS), such as basic fuchsin bulk staining [1], usually involve plastic embedding and it takes more than one week to complete the process. In this study, we use an easier, quicker and higher quality staining technique, which shows good morphology of the LCS and provides a way of quantifying canaliculi density and porosity [2][3][4].

**Method:** Femur mid-shafts from mouse and rat were dissected and sectioned into 0.3 mm thick segments, fixed in 10% formaldehyde for 24hrs, polished to 0.05-0.1mm, dehydrated in ascending graded ethanol (70%,90%,100%), stained in sodium fluorescein solution for 4hrs and mounted on a glass slide with cover glass. High-resolution 3D stacks were captured using 63x oil objective in a Zeiss LSM 510 and 780 confocal microscopes (Carl Zeiss Microscopy, LLC, Peabody, MA, USA). Image segmentation process is carried out in Volocity software (PerkinElmer, Tempe, AZ, USA).

## Results:

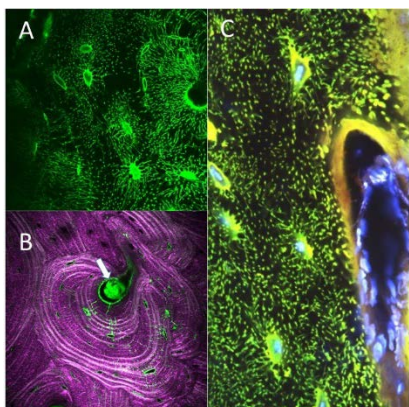


Fig.1 (A) Sodium fluorescein staining of LCS, showing osteon; (B) Alignment of collagen network (purple) with LCS (green), white arrow indicates the blood vessel; (C) Combined staining of longitudinal section of mouse femur, blue is nuclear staining, green is LCS staining.

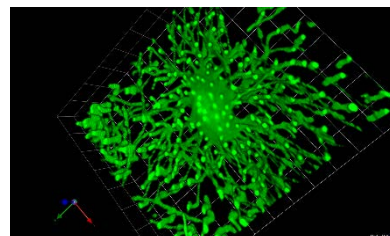


Fig. 2 3D view of segmented LCS in Volocity

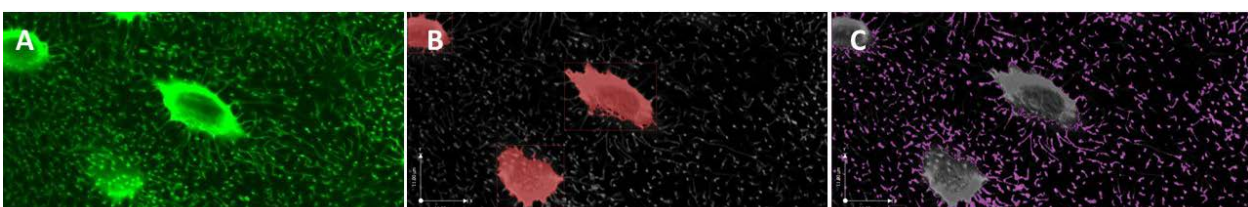


Fig. 3 (A) Sodium fluorescein staining of LCS; (B) Segmented lacuna; (C) Segmented canaliculi

**Discussion:** The proposed staining and visualization process provides an easy and quick way of visualizing the LCS and collagen network in bone. And the high quality images provides a way of analyzing osteocyte process density and overall porosity[3][4].

## Reference:

- [1] L. Wang, Y. Wang, Y. Han, S. C. Henderson, R. J. Majeska, S. Weinbaum, and M. B. Schaffler, "In situ measurement of solute transport in the bone lacunar-canalicular system," *Proc. Natl. Acad. Sci. U. S. A.*, vol. 102, no. 33, pp. 11911–6, Aug. 2005.
- [2] C. Ciani, S. B. Doty, and S. P. Fritton, "An effective histological staining process to visualize bone interstitial fluid space using confocal microscopy," *Bone*, vol. 44, no. 5, pp. 1015–1017, 2009.
- [3] L. Fan, S. Pei, X. Lucas Lu, and L. Wang, "A multiscale 3D finite element analysis of fluid/solute transport in mechanically loaded bone.," *Bone Res.*, vol. 4, no. August, p. 16032, 2016.
- [4] X. Lai, C. Price, S. Modla, W. R. Thompson, J. Caplan, C. B. Kirn-Safran, and L. Wang, "The dependences of osteocyte network on bone compartment, age, and disease.," *Bone Res.*, vol. 3, 2015.

## Meniscus Maturation is Accompanied by Marked Compositional and Structural Reorganization

Sonia Bansal<sup>1,2</sup>, Niobra M. Keah<sup>1,2</sup>, Olivia C. O'Reilly<sup>1</sup>, Feini Qu<sup>1,2</sup>, Robert L. Mauck<sup>1,2</sup>, Miltiadis H. Zgonis<sup>1,2</sup>

<sup>1</sup> McKay Orthopaedic Research Laboratory, University of Pennsylvania, Philadelphia, PA

<sup>2</sup> Translational Musculoskeletal Research Center, Philadelphia VA Medical Center, Philadelphia, PA

**Disclosures:** No disclosures to report.

**INTRODUCTION:** The menisci are semi-lunar shaped fibrocartilaginous wedges located between the femur and the tibial plateau and support the structure and mechanical function of the knee joint<sup>1,2</sup>. Understanding meniscus structure and function is particularly important given the high incidence of meniscal pathology<sup>3,4</sup>, and its association with progressive joint degeneration<sup>5</sup>. In the adult, the menisci are comprised primarily of circumferentially aligned type 1 collagen bundles, which function to convert compressive forces into tensile hoop stresses<sup>6,7</sup>. In addition to circumferential fibers, the meniscus contains “radial tie fibers” that originate at the meniscus periphery and interdigitate amongst the circumferential fiber population<sup>1,2,6-8</sup>. These radial tie fibers (RTFs) vary in size, spatial distribution, and in their degree of arborization<sup>8</sup>, and are thought to bind circumferential fibers together and protect against longitudinal splitting of the circumferentially-aligned collagen bundles<sup>6,9,10</sup>. Interestingly, a recent study suggested that radial tears that interrupt circumferential fibers do not increase contact stresses until they reach ~90% of the meniscus width<sup>11</sup>. This suggests alternative methods for strain transmission in the meniscus, a potential role of the RTFs. However, the morphology and composition of these structures during tissue formation and maturation has not yet been elucidated. To further this understanding, we quantified RTF area fraction and thickness as a function of tissue location and developmental state.

**METHODS:** Medial menisci (n=6/age) were harvested from fetal (mid-gestation), juvenile (6 month) and adult (skeletally mature) cows. Fetal menisci were divided into anterior and posterior regions. Juvenile and adult menisci were divided into four equal regions: anterior horn, anterior body (Body-A), posterior body (Body-P), and posterior horn. Each region was then cryosectioned into 10 µm thick slices spanning the entire cross section and fixed in 4% PFA. For each cross section, three zones were examined at high power: the outer (O), middle (M), and inner (I) zones. First, sections were stained with Safranin O/Fast Green for proteoglycans and fibrous tissue, respectively, as well as with Picosirius Red and a modified Masson's Trichrome with Verhoff stain to visualize collagen and elastin fibers. Next, unstained sections were imaged at 10X magnification via second harmonic generation (SHG, 840 nm excitation). Maximum projections spanning 4.8 ± 1.2 microns of the tissue depth were generated in each zone and the area fraction with positive SHG signal was computed as a measure of RTF area fraction. Additionally, RTF fiber thickness was estimated using the FIJI plugin BoneJ. Fiber area fraction and thickness were compared across regions, zones, and developmental states using ANOVA ( $p \leq 0.05$ ) with Tukey's post-hoc tests; data are presented graphically as the mean value in each region and zone.

**RESULTS:** As expected, meniscal tissue size increased with age. Histological analysis showed increased proteoglycan content from the inner to the outer zone with increasing age, via Safranin O staining (Figure 1). Likewise, Masson's Trichrome revealed increasing collagen staining throughout the entire meniscus with increasing age. SHG imaging revealed that RTF fiber area ranged from 8% to 43%, with both age and region being significant factors ( $p < 0.0001$ ). Adult menisci showed significant differences in RTF fiber area between zones, whereas juvenile and fetal menisci did not show significant differences ( $p = 0.135$  and 0.143, respectively). In the adult, central body regions had a lower RTF fiber area than the anterior or posterior horns (Figure 2). The thickness of RTFs also varied significantly with age ( $p < 0.0001$ ). Juvenile and fetal menisci showed no significant differences in RTF thickness with respect to regions or zones, while adult menisci had significant differences in RTF thickness as a function of region ( $p < 0.02$ ) and zone ( $p < 0.005$ ) (Figure 2).

**DISCUSSION:** This study provides evidence for marked compositional and structural changes in the knee meniscus as a function of maturation. Fetal menisci were characterized by lower levels of collagen (Masson's Trichrome) and proteoglycan (Safranin O/Fast Green) compared to both juvenile and adult tissue. Additionally, radial tie fibers in fetal tissue are poorly developed compared to adult specimens. Specifically, we observed an increase in RTF thickness as well as emergent heterogeneity in RTF fiber area in the adult. The higher RTF fiber area and size in the outer region of the mature posterior horn may underlie the reported higher stiffness in this region<sup>6</sup>. This specialization in meniscus structure was concentrated in the horns of the tissue, potentially reflecting the more complicated mechanical loading environment of the meniscus insertion site. Future work will determine the structure-function implications<sup>12</sup> of these findings, as well as the mechanisms governing RTF development during maturation. This improved understanding will inform engineering design towards the fabrication of functional meniscus replacements.

**SIGNIFICANCE:** This study demonstrates that radial tie fibers in the meniscus show spatially varying and age-dependent patterns, and will inform tissue engineering strategies to create functional and anatomically correct meniscal replacements.

**References:** [1] Kambic+, J. Orthop. Res. 2005. [2] Chevrier+, J. Orthop. Res. 2009. [3] Merriam+, J. Sports Med. 2015. [4] Mordecai+, World J. Orthop. 2014. [5] Fairbank+, J Bone Jt. Surg. 1948. [6] Skaggs+, J. Orthop. Res. 1994. [7] Makris+, Biomaterials 2011. [8] Andrews+, J Anat. 2014. [9] Mauck+, Tissue Eng. Part B. 2009. [10] Bullough+, J Bone Jt. Surg. 1970. [11] Bedi+, J. Bone Jt. Surg. 2010. [12] Li+, SB3C Conference. 2016.

**Acknowledgments:** This work was supported by an OREF New Investigator Grant, the NIH, and the Department of Veterans Affairs.

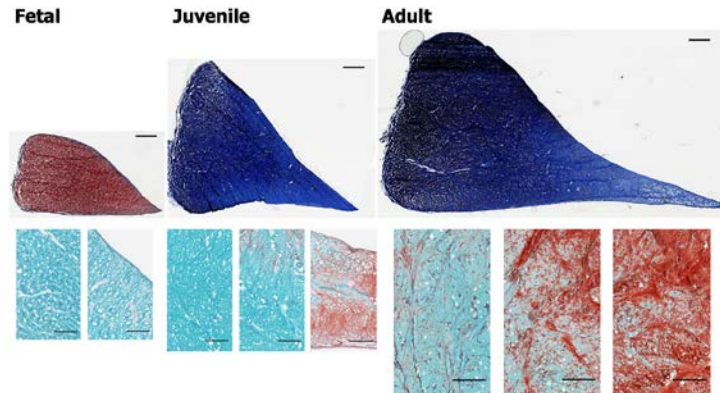


Figure 1 -- Histological staining of fetal, juvenile, and adult menisci. Top row: Masson's Trichrome, posterior sections, Scale bar = 2 mm. Bottom row: Safranin O/Fast Green, anterior sections, Scale bar = 500 µm.

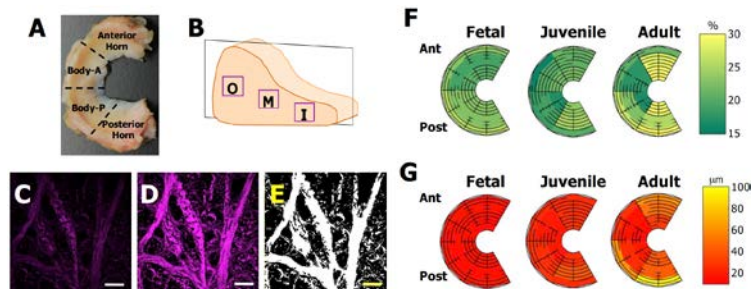
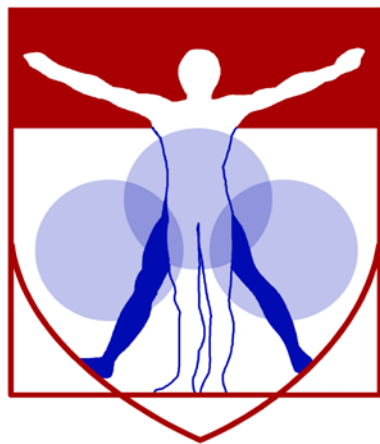


Figure 2 -- Schematic illustration of (A) meniscal regions and (B) outer (O) middle (M) and inner (I) zones with sectioning plane. Original SHG image (C), Maximum Projection (D), and binarized (E) images. Scale Bar = 200µm. Colors maps denoting RTF fiber area (F) ranging from 15% to 30% and mean fiber thickness (G) ranging from 10 to 100 µm.



PENN  
CENTER for  
MUSCULOSKELETAL  
DISORDERS

# MicroCT Abstracts

## Pulsed Electromagnetic Field Therapy Improves Tendon-to-Bone Healing in a Rat Rotator Cuff Repair Model

Jennica J Tucker<sup>1</sup>, James M. Cirone<sup>1</sup>, Tyler R. Morris<sup>1</sup>, Courtney A. Nuss<sup>1</sup>, Erik I. Waldorff<sup>2</sup>, Nianli Zhang<sup>2</sup>, James T. Ryaby<sup>2</sup>, Louis J. Soslowsky<sup>1</sup>

<sup>1</sup>McKay Orthopaedic Research Laboratory, Philadelphia, PA

<sup>2</sup>Orthofix Inc., Lewisville, TX

**DISCLOSURES:** JJ Tucker (N), JM Cirone (N), TR Morris (N), CA Nuss (N), EI Waldorff (3A- Orthofix, Inc), N Zhang (3A- Orthofix, Inc), JT Ryaby (3A- Orthofix, Inc), LJ Soslowsky (5- Orthofix, Inc)

**INTRODUCTION:** Rotator cuff tears are common musculoskeletal injuries which often require surgical intervention. Unfortunately, post-repair prognosis is poor, with surgical repairs that fail in up to 94% of cases<sup>1</sup>. In an effort to improve tendon-to-bone healing, non-invasive therapeutics have been utilized post-operatively including ultrasound and shock wave therapy. Of note, pulsed electromagnetic fields (PEMFs) have been shown to improve bone fracture healing<sup>2</sup>, but the effect on tendon-to-bone healing has not yet been elucidated. Therefore, the objective of this study was to investigate the effect of PEMF on rotator cuff healing using an established rat rotator cuff detachment and repair model<sup>3-8</sup>. We hypothesized that PEMF exposure post-repair would improve tendon-to-bone healing and joint function.

**METHODS:** 60 adult male Sprague-Dawley rats (400-450g) were used in this IACUC approved study. Animals received either: 1) acute injury and repair<sup>1</sup> followed by cage activity and PEMF (Physio-Stim<sup>®</sup>, Orthofix, Inc., Lewisville, TX; 3hrs daily) or 2) acute injury and repair<sup>4</sup> followed by cage activity only. Animals were sacrificed at 4, 8, and 16 weeks (n=10 per group per time point). Additionally, throughout the experiment prior to sacrifice, all animals in the 16 week group underwent longitudinal in vivo ambulatory<sup>9</sup> and passive shoulder joint mechanics assessments<sup>10</sup>. At sacrifice, right shoulders (n=7 per group per time point) were dissected and processed for histological analysis<sup>8; 11; 12</sup>. All contralateral limbs (n=10 per group per time point) were frozen at -20°C and thawed for dissection prior to tendon cross-sectional area measures and mechanical testing<sup>4; 12; 13</sup>.

Following mechanical testing, proximal humeri were subjected to µCT analysis (10.5 µm resolution). Statistical comparisons were made between the PEMF and non-PEMF groups at each time point. Mechanical testing, µCT, and collagen fiber organization comparisons were made using t-tests. Histological comparisons were made using Mann-Whitney U tests. Ambulatory assessment comparisons were made using a 2-way ANOVA with repeated measures on time with post-hoc tests at each time point. Multiple imputations were calculated for a repeated measures analysis for missing data (~10%). All significance was set at p≤0.05.

**RESULTS:** At 4 weeks, the PEMF group had a significantly smaller tendon cross-sectional area compared to the non-PEMF group (Fig. 1A), with no differences at 8 and 16 weeks. At 4 and 8 weeks, the PEMF group had a significantly increased tendon modulus (100% increased at 4 weeks, 60% at 8 weeks) compared to the non-PEMF group, with no differences detected at 16 weeks (Fig. 1C). At 4 weeks, the PEMF group had significantly increased maximum stress compared to the non-PEMF group, with no differences at 8 and 16 weeks (Fig. 1E). There were no differences in percent relaxation, stiffness, or maximum load at any time point (Fig. 1B, D, F). For histology, at the injury site, no differences were detected in both cell shape and cellularity at any time point between groups (data not shown). Additionally, no differences were observed in collagen fiber organization at the injury site (Fig. 2A). In the midsubstance at 8 weeks, the PEMF group had significantly more rounded cells (data not shown).

For collagen fiber organization, the PEMF group had trends towards decreased circular standard deviation (CSD) at both 8 and 16 weeks (Fig. 2B). No differences were found in ambulatory assessment or passive joint mechanics (data not shown). For µCT analysis at 4 weeks, trabecular thickness was significantly decreased and connectivity density was significantly increased in the PEMF group (Fig. 3E, H). At 8 weeks, no differences were observed in any parameter. At 16 weeks, the PEMF group had significantly increased bone volume fraction, trabecular thickness, and bone mineral density, and a trend toward increased bone mineral content (Fig. 3).

**DISCUSSION:** Overall, results suggest that PEMF has a positive effect on rat rotator cuff healing. Specifically, tendon mechanical properties were drastically improved in the PEMF group at both 4 and 8 weeks (100% and 60%, respectively) with a subsequent increase in bone properties at the tendon repair site. Histological analysis showed a more rounded cell shape in the PEMF group at 8 weeks in the midsubstance. This slight but significant finding might suggest inferior tissue, although this difference did not result in inferior mechanical properties. Additionally, collagen fiber organization in the midsubstance at 8 and 16 weeks showed the PEMF group trended toward decreased CSD, suggesting more organized tissue in the PEMF group, and perhaps later time points would further increase collagen organization. Overall, results demonstrate that PEMF improves tendon-to-bone healing in this animal model based on mechanical property measurements. Further studies can evaluate the mechanisms responsible for these changes.

**SIGNIFICANCE:** PEMF provides a non-invasive way to improve tendon-to-bone healing in an acute rat supraspinatus detachment and repair model and shows potential for use in a clinical scenario of rotator cuff tendon to bone healing following rotator cuff repair.

**REFERENCES:** [1] Galatz LM et al. J Bone Joint Surg Am, 2004. [2] Midura RJ et al. J Orthop Res, 2005. [3] Soslowsky LJ et al. J Shoulder Elbow Surg, 1996. [4] Beason DP et al. J Shoulder Elbow Surg, 2012. [5] Beason DP et al. J Shoulder Elbow Surg, 2014. [6] Caro AC et al. J Am Assoc Lab Anim, 2014. [7] Connizzo BK et al. Clin Orthop, 2014. [8] Gimbel JA et al. J Biomech Eng, 2007. [9] Sarver JJ et al. J Biomech 2010. [10] Sarver JJ et al. J Shoulder Elbow Surg, 2008. [11] Bey MJ et al. J Biomech Eng, 2002. [12] Thopopoulos S et al. J Orthop Res, 2003. [13] Gimbel JA et al. J Biomech, 2004.

**ACKNOWLEDGEMENTS:** Funding was provided by Orthofix, Inc. The authors thank XS Liu and WJ Tseng for assistance with µCT analysis.

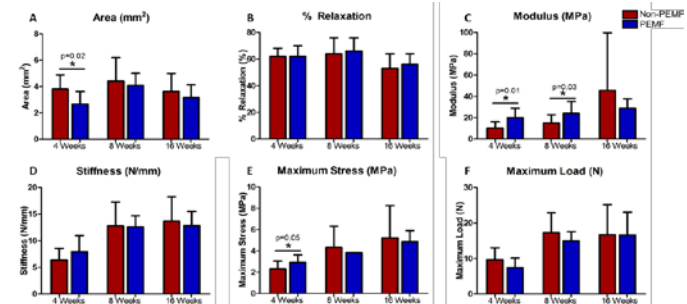


**Figure 1.** Tendon mechanical properties. (A) At 4 weeks, area was decreased in the PEMF group. (B) No differences were noted in % relaxation. (C) At 4 and 8 weeks, modulus was increased in the PEMF group. (D) No differences were noted in stiffness. (E) At 4 weeks, maximum stress was increased in the PEMF group. (F) No differences were noted in maximum load. Data as mean±SD.

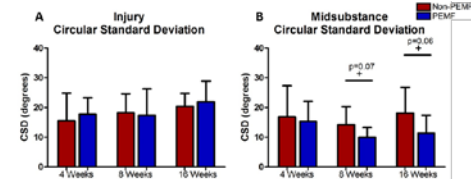


**Figure 2.** Collagen fiber alignment. (A) No differences were noted at the injury site. (B) At 8 and 16 weeks in the midsubstance the PEMF group had a trend toward decreased CSD. Data as mean±SD.

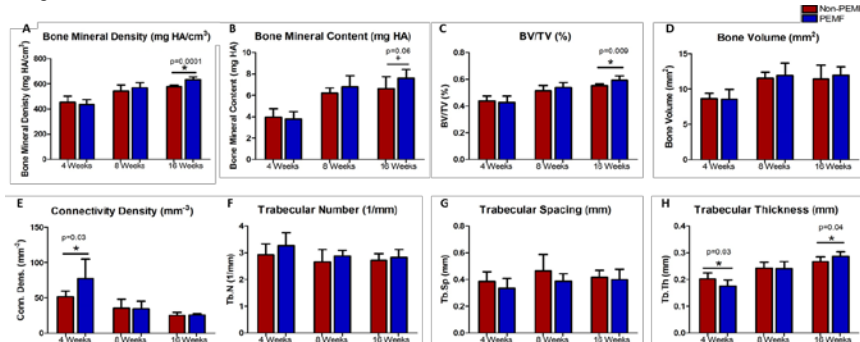


**Figure 3.** µCT analysis. (A) No differences were noted in bone mineral density at 4 and 8 weeks. At 16 weeks bone mineral density was increased in the PEMF group. (B) At 16 weeks bone mineral content trended toward increased in the PEMF group. (C) At 16 weeks bone volume fraction was increased in the PEMF group. (D) No differences were noted in bone volume. (E) At 4 weeks connectivity density was increased in the PEMF group. (F) No differences were noted in trabecular number. (G) No differences were noted in trabecular spacing. (H) At 4 weeks trabecular thickness was decreased in the PEMF group. At 16 weeks trabecular thickness was increased in the PEMF group. Data as mean±SD.

## Absence of Decorin Exacerbates DMM-induced Post-traumatic Osteoarthritis in Mice

Qing Li<sup>1</sup>, Liu Ouyang<sup>1</sup>, Basak Doyran<sup>1</sup>, Li Fan<sup>1</sup>, Wei Tong<sup>2</sup>, Wei-Ju Tseng<sup>2</sup>, X. Sherry Liu<sup>2</sup>, Renato V. Iozzo<sup>3</sup>, Ling Qin<sup>2</sup>, David E. Birk<sup>4</sup>, Lin Han<sup>1</sup>

<sup>1</sup>Drexel University, Philadelphia, PA; <sup>2</sup>University of Pennsylvania, Philadelphia, PA;

<sup>3</sup>Thomas Jefferson University, Philadelphia, PA; <sup>4</sup>University of South Florida, Morsani College of Medicine, Tampa, FL.

**Disclosures:** Qing Li (N), Liu Ouyang (N), Basak Doyran (N), Li Fan (N), Wei Tong (N), Wei-Ju Tseng (N), X. Sherry Liu (N), Renato V. Iozzo (N), Ling Qin (N), David E. Birk (N), Lin Han (N).

**INTRODUCTION:** Post-traumatic osteoarthritis (PTOA) is the prevalent OA form in young adults [1]. Currently, the pathogenesis of chondrocytes and extracellular matrix (ECM) molecules in PTOA is not well understood. This study aims to define the roles of decorin, a critical cartilage matrix regulatory molecule, in PTOA. In normal cartilage, decorin can bind to collagens II [2] and VI [3], aggrecan core protein [4] and transforming growth factor- $\beta$  (TGF- $\beta$ ) [5]. Our recent study showed that decorin-null ( $Dcn^{-/-}$ ) murine cartilage has substantially reduced glycosaminoglycan (GAG) content and weakened mechanical properties [6]. In early OA, decorin is markedly up-regulated [7], and in late OA, it becomes increasingly fragmented [8]. These evidences suggest that decorin plays an important role not only in the proper functioning of normal cartilage, but also in OA pathogenesis. To this end, we examined the progression of PTOA in wild-type (WT) and  $Dcn^{-/-}$  mice. The destabilization of the medial meniscus (DMM) surgery was performed to induce PTOA in mice, followed by an analysis of ECM morphology, nanostructure and the mechanical properties of cartilage. Here, the more severe cartilage degradation in  $Dcn^{-/-}$  compared to WT mice highlighted the critical roles of decorin in PTOA.

**METHODS:** *Surgery:* DMM surgery was performed on the right hind knees of skeletally mature, 12-week old, male C57BL/6 WT and  $Dcn^{-/-}$  mice, with the Sham control on contralateral left knees, following established procedures [9]. All animal work was approved by the IACUC. Mice were euthanized at 2 and 8 weeks post-surgery for mechanical and structural tests. *AFM-nanoindentation* was performed on the intact surface of medial condyle cartilage ( $n = 5$ ) at 10  $\mu\text{m}/\text{s}$  rate using a microspherical tip ( $R \approx 5 \mu\text{m}$ ,  $k \approx 8.9 \text{ N/m}$ ,  $\mu\text{Masch}$ ) and a Dimension Icon AFM [10]. For each condyle cartilage,  $\geq 15$  locations were tested to account for heterogeneity. Effective indentation modulus,  $E_{ind}$ , was calculated via the Hertz model. *Histology and immunohistochemistry (IHC)*: Whole joints of both knees were harvested from additional mice ( $n \geq 3$ ), fixed, decalcified, and embedded in paraffin. 6- $\mu\text{m}$ -thick sagittal sections were cut across the medial side and stained with Safranin-O/Fast Green for GAGs, and with decorin IHC antibodies. *SEM*: After indentation, samples were treated with Karnovsky's fixative, dehydrated in hexamethyldisilazane and imaged under Zeiss Supra 50VP SEM.  *$\mu\text{CT}$* : For joints used for histology, prior to decalcification, the fixed joints were scanned by ex vivo  $\mu\text{CT}$  (Scanco microCT 35) at 6  $\mu\text{m}$  resolution to characterize subchondral bone morphology.

**RESULTS:** In WT mice, IHC demonstrated an up-regulation of decorin after DMM, indicating the active involvement of decorin in OA (Fig. 1). Therefore, after DMM, WT and  $Dcn^{-/-}$  mice had distinctive structural and mechanical changes. On the Sham side,  $Dcn^{-/-}$  mice had lower  $E_{ind}$  than the WT (Fig. 2), which is associated with a marked reduction in sulfated GAGs in  $Dcn^{-/-}$  cartilage (Fig. 3a). During DMM-induced OA, the modulus decrease was significant at both 2 and 8 weeks post-DMM in WT mice. In contrast, it only became reduced at 8 weeks in  $Dcn^{-/-}$  mice (Fig. 2). Meanwhile, significant structural differences were observed between the two genotypes (Fig. 3): At early stage (2 weeks post-DMM),  $Dcn^{-/-}$  cartilage showed signs of collagen reorganization, where collagen fibrils became more aligned along the mediolateral orientation (Fig. 3b). This effect was absent in the WT mice. At late stage (8 weeks), more severe OA was observed in both genotypes, illustrated by the presence of chondrocyte hypertrophy. At this time,  $Dcn^{-/-}$  cartilage surface was depleted of GAGs and became completely dominated by highly aligned collagen fibrils (Fig. 3b), a clear sign of surface fibrillation. Furthermore,  $Dcn^{-/-}$  mice showed marked subchondral bone plate thickening (Fig. 3c), which was absent in the WT.

**DISCUSSION:** The surface fibrillation observed in  $Dcn^{-/-}$  cartilage is a typical OA-induced cartilage structural change [11], which is, however, absent in WT. This contrast suggests that during PTOA, decorin can inhibit collagen fibril aggregation and alignment, preventing the formation of fibrocartilage that is mechanically inferior to normal hyaline cartilage [7]. In  $Dcn^{-/-}$  mice, as a result of more severe fibrillation and cartilage degradation, subchondral bone thickening occurs at 8 weeks, a sign of advanced OA [11]. This evidence illustrates the active involvement of decorin in PTOA and its important role in preventing cartilage fibrillation and OA progression. In addition, the absence of modulus reduction in  $Dcn^{-/-}$  mice at 2 weeks post-DMM does not suggest that  $Dcn^{-/-}$  mice are more resistant to early OA (Fig. 2), as this could be a temporary artifact due to the initiation of surface fibrillation. It should be noted, however, that in  $Dcn^{-/-}$  mice, cartilage already has weakened properties before DMM [6]. In order to isolate decorin activities in skeletal development versus OA, our ongoing studies are using inducible decorin knockout mice to provide the temporal specificity of decorin gene ablation.

**SIGNIFICANCE:** For the first time, this study evidences the important roles of decorin in PTOA, especially in the inhibition of cartilage fibrillation. This finding could provide a basis for the use of decorin as a new molecular therapy target for attenuating PTOA.

**REFERENCES:** [1] Helmick, CG et al., *Arthritis Rheum.* 58:15-25, 2008. [2] Douglas, T et al., *Biomacromolecules* 7:2388-2393, 2006. [3] Wiberg, C et al., *J. Biol. Chem.* 276:18947-18952, 2001. [4] Wiberg, C et al., *J. Biol. Chem.* 278:37698-37704, 2003. [5] Hildebrand, A et al., *Biochem. J.* 302:527-534, 1994. [6] Doyran, B et al., *Trans. ORS* 62:491, 2016. [7] van der Kraan, PM et al., *J. Rheumatol.* 24:543-549, 1997. [8] Bock, HC et al., *Osteoarthr. Cartilage* 9:654-663, 2001. [9] Glasson, SS et al., *Osteoarthr. Cartilage* 15:1061-1069, 2007. [10] Batista, MA et al., *Matrix Biol.* 38:84-90, 2014. [11] Buckwalter, JA et al., *Instr. Course Lect.* 54:465-480, 2005.

**ACKNOWLEDGEMENTS:** This work was supported by the National Institutes of Health (AR066824).

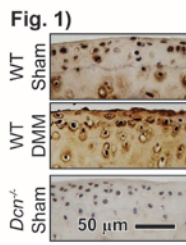


**Fig. 1** Immunohistochemistry of decorin shows decorin increase at 8 weeks after DMM.  $Dcn^{-/-}$ /Sham is shown as a negative control.

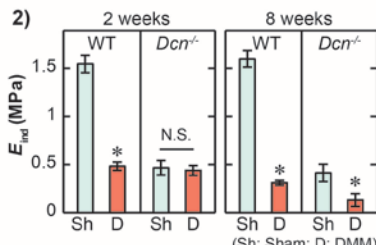


**Fig. 2** Effective indentation modulus  $E_{ind}$  of medial condyle cartilage at 2 and 8 weeks after surgery. (\*:  $p < 0.05$  of Sham versus DMM knees via Mann-Whitney U test, mean  $\pm$  95% CI,  $n \geq 5$  mice each).

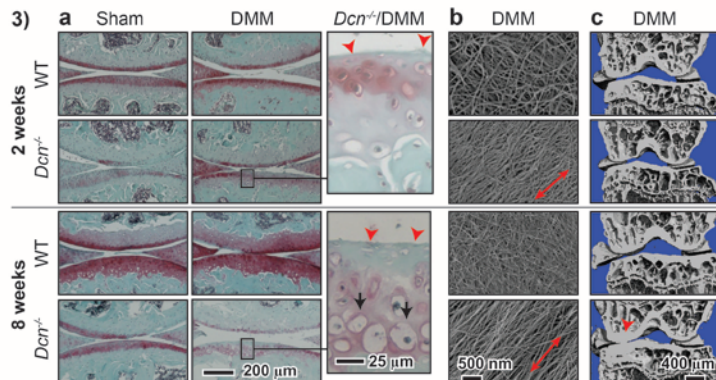


**Fig. 3** Structural and morphological changes of WT and  $Dcn^{-/-}$  mice at 2 and 8 weeks after surgery. a) Safranin-O/Fast Green histology (red arrowhead: GAG depletion, black arrow: chondrocyte hypertrophy in  $Dcn^{-/-}$  mice); b) Cartilage surface collagen fibril structure (red arrow: collagen alignment along mediolateral direction); c) Subchondral trabecular bone frontal plane image via  $\mu\text{CT}$  (red arrowhead: subchondral bone thickening and osteophyte formation).

## Murine Model for Developmental Dysplasia of Hip: Ablation of CX3CR1 Affects Gait and Acetabular Morphology

George Feldman<sup>1</sup>, Arlene Offemaria<sup>1</sup>, Jay Parvizi<sup>1,2</sup>, Theresa Freeman<sup>1</sup>

<sup>1</sup>Division of Orthopaedic Research, Thomas Jefferson University, Philadelphia, <sup>2</sup>Rothman Institute, Philadelphia

**Introduction:** Developmental Dysplasia of the Hip (DDH) is a debilitating condition whose distinguishing signs include incomplete formation of the acetabulum leading to dislocation of the femur, accelerated wear of the articular cartilage and joint laxity resulting in osteoarthritis. It is a complex disorder having environmental and genetic causes. Existing techniques fail to detect milder forms of DDH in newborns. It is this undetected sub-fraction of DDH patients that is the leading cause of hip osteoarthritis in young adults causing over 40% of cases in the 20-40 yo age group. A sensitive, specific and cost effective test would allow identification of newborns that could be non-invasively corrected by the use of a Pavlik harness. Previously, we identified a 2.5MB candidate region on human chromosome 3 by using linkage analysis of a 4 generation, 72 member family. Whole exome sequencing of the DNA of 4 severely affected members revealed a single nucleotide polymorphism variant, rs3732378 coinherited by all 11 affected family members. This variant causes a threonine to methionine amino acid change in the coding sequence of the CX3CR1 chemokine receptor and is predicted to be harmful to the function of the protein. Recently in a case-control study of 689 affected patients and an equal number of controls this chemokine variant was found to increase the risk of hip dislocation by a factor of 2.25 (OR=2.25, 95%CI 1.42-3.56) after adjustment for gender. To gain further insight into the potential function of this mutation we examined the effect of CX3CR1 ablation on the architecture of the mouse acetabulum and on the murine gait.

**Methods:** All experiments on mice were performed under conditions that conformed to standards set by TJU's IACUC guidelines. *Gait analysis:* DigiGait analysis was performed by Mouse Specifics, Inc (Boston) as previously described. Briefly, each mouse was placed on a motor-driven treadmill with a transparent treadmill belt and imaged from beneath with a high-speed digital video camera. 16/ 56 day old (8KO/8WT) were gait tested. *MicroCT:* Ten 35 day old females (5 KO/5WT) and 16/ 56 day old (8KO/8WT) female mice (the same mice that had been gait tested) were obtained from the NIAID transgenic repository at Taconic or from Jackson laboratory. WT mice were strain, sex and age matched. Carcasses were fixed and evaluated by microCT using Image-Pro Plus and Autovisualizer software to measure 11 parameters defining the shape and size of the space between the femur head and the acetabulum for each slice. The ratio of femur head to acetabular space was calculated for each slice. *Statistics:* Gait analysis: Statistical analyses were carried out using GraphPad Prism 5.01 for Windows (GraphPad Software, San Diego) statistical software. One-way t-tests to analyze effects of a single variable, (i.e. genotype on gait) were performed. uCT analysis: A two tail t-test was conducted between KO and WT measurement values to calculate the p value from each slice. Significant differences of the normalized area of the space between the femur head and the acetabulum are reported.

**Results:** *Gait Analysis:* Larger stance width ( $p=0.043$ ), step angle ( $p=0.010$ ), step angle variability ( $0=0.002$ ) and swing duration variability ( $p=0.002$ ) were seen in the KO mice. Gait symmetry significantly decreased in KO mice when they pulled a load ( $p=0.005$ ).

*MicroCT analysis:* The acetabula of 5 week old mice revealed that the left acetabulum of KO mice is 5.93-17.97% larger after normalization by femur head diameter. The size difference is significant over a range of tissue sections (6-31). Differences continued to be seen at 8 weeks. The normalized area of space between the femur head and acetabulum on the left side ranged from 38% ( $p=0.001$ ) to 21% ( $p=0.037$ ). No significant differences were found on the right side of either age.

**Discussion:** Evidence produced by the data outlined above provides insight into the mechanism by which the mutation found in the DNA of some patients with DDH could cause their disorder. Gait analysis shows several metrics consistent with impairment. A larger stance width in the KO mice indicates postural adjustment for stability. Swing duration variability increases such as that seen in the KO mouse are often seen in older human adults and individuals with osteoarthritis of the hip. Similarly, gait symmetry was significantly decreased in the KO mice and in humans with hip OA as was the percent stance stride (the percent of total stride duration that the paw is in any contact with the belt) measure ( $p=0.015$ ). This gait metric is known to decrease in the mono arthritic rat model 4 hours after intra-articular injection with carrageenan. The larger acetabulum relative to the femur head diameter at both 5 and 8 weeks in mice with the CX3CR1 gene ablated should produce greater joint laxity- one of the cardinal signs of DDH. The sequelae of this joint laxity over time produces detectable gait abnormalities in humans and we observed these in our murine model. In humans, DDH often manifests itself on one side and this observation is supported by this mouse model.

The effect of CX3CR1 deletion on murine acetabular study provides suggestive evidence of the causal role of the rs3732378 variant. We hypothesize that this chemokine and its receptor play a significant role in the progression of mesenchymal cells to chondrocytes and osteoblasts. A mutation in this receptor would serve to delay maturation of the acetabulum and lead to a mild but significant change in morphology. Further analysis of animal models with this and other susceptibility inducing mutations should provide insight into the mechanism of hip development and the pathogenesis of DDH.

## Skeletal Responses to the Discontinuation of Intermittent Parathyroid Hormone (PTH) Treatment in Intact and Ovariectomized Rats

<sup>1</sup>Tseng W-J; <sup>1</sup>Lee W; <sup>1</sup>Tong W; <sup>1</sup>Wang L; <sup>1</sup>Ma X; <sup>1</sup>Zhao H; <sup>1</sup>Li Y; <sup>1</sup>Chang C-C; <sup>1</sup>de Bakker C; <sup>1</sup>Qin L; <sup>+1</sup>Liu XS  
+<sup>1</sup> McKay Orthopaedic Research Laboratory, Department of Orthopaedic Surgery, University of Pennsylvania,  
Philadelphia, PA

Intermittent PTH treatment reduces the risk of fracture in postmenopausal women by improving bone mass. However, BMD rapidly decreases upon withdrawal from the treatment. To uncover the mechanisms behind this adverse phenomenon, we investigated the changes in bone microarchitecture in response to withdrawal of PTH in both intact and ovariectomized (OVX) rats.

23 female SD rats (4-5 month old) were assigned to four regimes: Intact Animals: PTH (n=9, PTH 40 $\mu$ g/kg 5x/wk for 3 wks followed by saline for 3wks); VEH (n=5, saline for 6wks). OVX Animals with 3-wk osteopenia development: PTH (n=6) and VEH (n=3) with the same treatment regime as intact rats. Sequential scans of proximal tibiae were performed by in vivo  $\mu$ CT (Scanco, 10.5  $\mu$ m) at week 0, 3, 4, 5 and 6.

Intact Animals: 3-wk PTH treatment caused a 31% and 33% increase in bone volume fraction (BV/TV) and trabecular thickness (Tb.Th), respectively, and a 49% decrease in structure model index (SMI, p<0.01). BV/TV and Tb.Th were 21% and 20% greater, and SMI was 42% lower in the PTH- vs. VEH-treated animals (p<0.01). Upon 3 wks of withdrawal, no changes were detected in BV/TV, Tb.Th, or SMI. The treatment benefits remained 3 wks after withdrawal (p<0.01, Fig 1). OVX Animals: 3-wk osteopenia development caused 52% and 13% decrease in BV/TV and Tb.Th, respectively, and a 157% increase in SMI (p<0.05). Bone loss continued in VEH rats for 6 wks. In contrast, 3-wk PTH treatment effectively slowed down the bone loss, causing no changes in BV/TV or SMI, and a 31% increase in Tb.Th. At wk3, BV/TV and Tb.Th were 74% and 26% greater, and SMI was 18% lower in the PTH- vs. VEH-treated rats (p<0.01). 1 wk after the withdrawal (wk4), BV/TV, Tb.Th, and SMI continued to show trends of improvement. Trends of bone deterioration appeared during the 2nd and 3rd wk of PTH withdrawal (wk 5 and 6), with a 28% decrease in BV/TV and a 15% increase in SMI (p<0.05) at wk6 vs. wk4. Nevertheless, the treatment benefit in BV/TV and Tb.Th remained 3 wks after PTH withdrawal (Fig 1).

Significant bone loss occurred in OVX rats in response to discontinuation of PTH treatment while no adverse effect was observed in intact rats, suggesting coupled effects between PTH withdrawal and the degree of bone remodeling dynamics. Intriguingly, there is a continuous anabolic window upon early withdrawal from PTH in OVX rats, which offers a new mechanism in support of the cyclic administration regime of PTH to maximize the treatment efficacy.

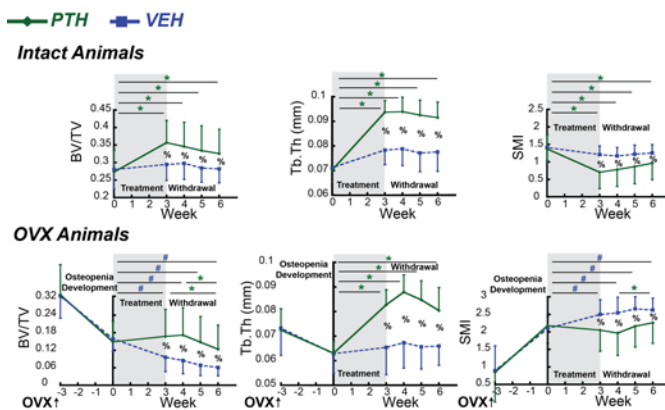


**Fig 1.** Mean  $\pm$  SD of BV/TV (Left), Tb.Th (Middle), and SMI (Right) in the tibial trabecular bone in response to PTH treatment and withdrawal in intact (Top) and OVX (Bottom) rats. \*: difference between time points in the PTH group; #: difference between time points in the VEH group; %: difference between PTH and VEH groups (p<0.05).

## Sensitivity of Imaging Biomarkers for Detecting Postmenopausal Bone Loss

Alyssa Johncola, Wenli Sun, Elizabeth Kobe, Chamith S. Rajapakse, Mona Al Mukaddam, Peter J. Snyder, and Felix W. Wehrli

Declined estrogen levels following menopause leads to rapid loss of bone mass, increasing the risk of developing osteoporosis. The rate of postmenopausal bone loss is a key determinant of bone fracture risk later in life. Early detection of greater than normal deterioration of bone in this population could assist pharmacological interventions which are known to be effective in reducing fractures. Besides DXA BMD, numerous imaging modalities and biomarkers are currently available for in-vivo assessment of bone, including density, structural, and strength measures. However, the sensitivity of these parameters in detecting early postmenopausal bone loss is not well established. The purpose of this study was to determine which image-based bone outcomes are most affected during the years following menopause.

This prospective study involved 90 postmenopausal women, aged 56-79 years (mean age=  $65.1 \pm 5.7$  years). Microstructural MRI of the distal tibia and radius was performed on a 3T scanner (Siemens Tim Trio, Erlangen, Germany) using 4-channel surface coil at  $0.137 \text{ mm} \times 0.137 \text{ mm} \times 0.410 \text{ mm}$  voxel size. Trabecular bone parameters (bone volume fraction, surface curve ratio, erosion index, number, separation, thickness, and stiffness) and stiffness of the whole section were computed on the basis of these images using digital topological and finite element analysis, respectively. Cortical and trabecular BMD was assessed at the diaphysis and metaphysis, respectively, in the tibia and radius by means of peripheral quantitative computed tomography (pQCT). Total hip and lumbar spine areal BMD were determined with DXA.

Out of all the parameters measured, only whole section stiffness and cortical BMD at tibia and radius significantly ( $p<0.05$ ) declined with age in this cohort representing a narrow age range (Figure 1). Loss of bone mass with age in the distal tibia and radius was visually evident from the MR images, as shown by the representative images in Figure 2. All parameters derived from the tibia were positively correlated with the corresponding parameters at the radius ( $p<0.05$ ), indicating the systemic nature of bone loss.

Measures focused on trabecular bone alone or 2D measures did not show any significant age effect in this cohort (age 55-78 years). Parameters that take cortical bone into account (e.g., MRI stiffness and pQCT cortical BMD) were significantly affected with increased age.

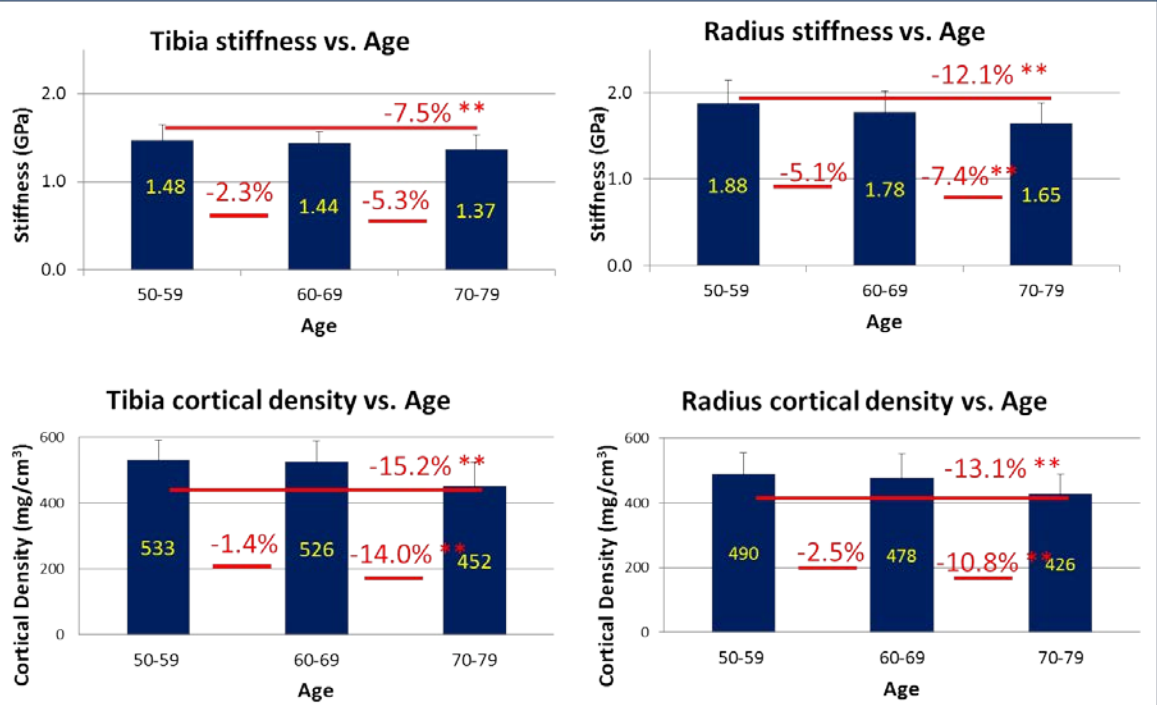


Figure 1: Boxplots of mean outcome versus age. \*\* indicates significant difference

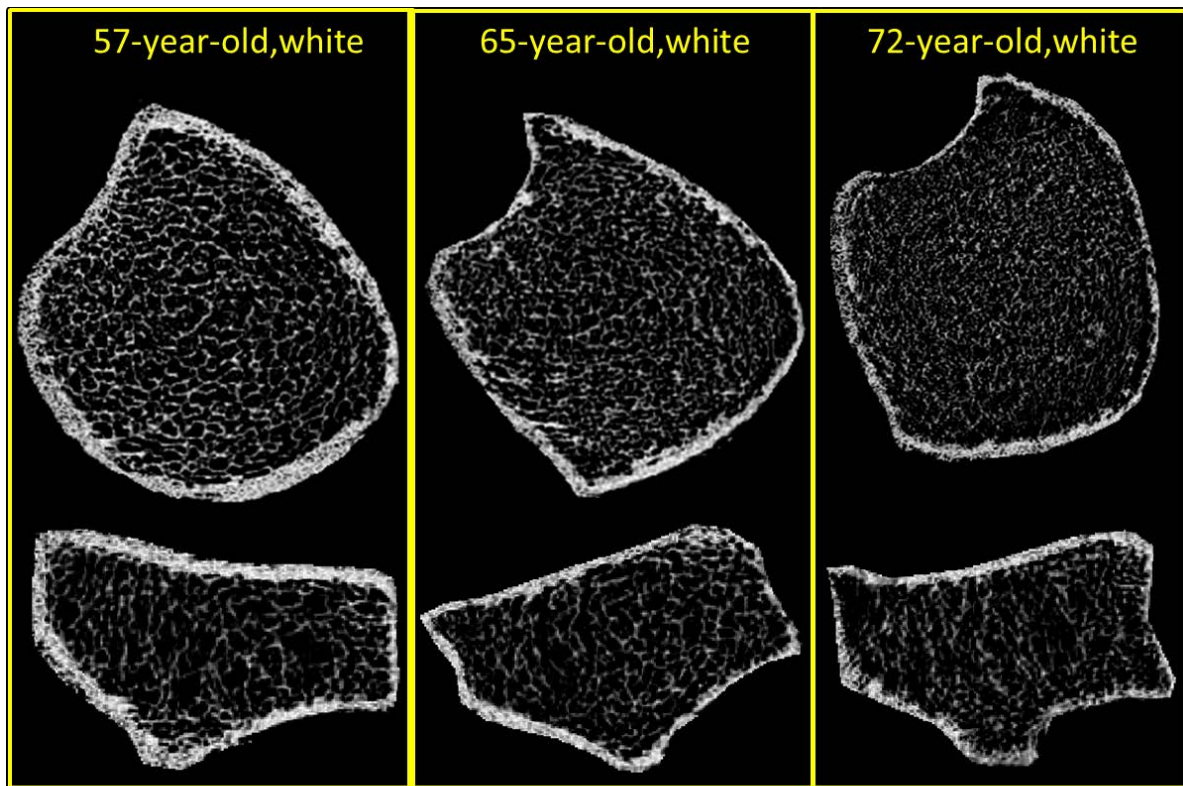


Figure 2: BVF maps of three post postmenopausal women.

## Reproductive History Significantly Alters Skeletal Responses to Estrogen Deficiency Induced by Ovariectomy in Rats

Chantal de Bakker, Laurel Leavitt, Wei-Ju Tseng, Allison Altman, Tiao Lin, Wei Tong, Ling Qin, X. Sherry Liu

Department of Orthopaedic Surgery, University of Pennsylvania, Philadelphia, PA, USA

**Disclosures:** C de Bakker: None, L Leavitt: None, W Tseng: None, A Altman: None, T Lin: None, W Tong: None, L Qin: None, XS Liu: None

**Introduction:** Due to increased calcium requirements during reproduction, pregnancy and lactation have long been known to result in significant maternal bone loss, which recovers at least partially following weaning [1]. However, recent studies indicate that even after a lengthy post-weaning recovery period, permanent deficits in maternal bone structure remain [2,3]. On the other hand, multiple clinical studies demonstrate that lactation and parity have no long-term adverse effects on future osteoporosis or fracture risk [1,4,5]. These conflicting results led us to hypothesize that, in order to compensate for differences in structure, reproductive and non-reproductive bone may undergo distinct patterns of post-menopausal bone loss. To investigate this hypothesis, we tracked the changes in bone structure at the proximal tibia following ovariectomy (OVX) in virgin rats and in rats that had undergone 3 cycles of pregnancy and lactation, and we also compared their trabecular and cortical bone quality at the L4 vertebra and femur midshaft at 3 months post-OVX.

**Methods:** All animal experiments were approved by IACUC. Female, SD rats were assigned to 4 groups: Virgin Control (n=10), Reproductive Control (n=7), Virgin OVX (n=4), and Reproductive OVX (n=4). Reproductive rats were mated and underwent 3 repeated cycles of pregnancy, lactation, and weaning starting at age 3 months. Virgin rats were housed in identical conditions. At age 12 months, virgin and reproductive OVX rats underwent OVX surgery to induce estrogen deficiency, and their proximal tibiae were scanned by *in vivo* μCT at 0, 4, 8, and 12 weeks post-OVX (10.5 μm resolution, vivaCT 40, Scanco Medical, Brüttisellen, Switzerland). All rats were sacrificed at age 14–19 months. L4 vertebrae and femurs were harvested and were μCT scanned at 10.5 μm resolution to allow for analysis of trabecular and cortical bone, respectively. Femurs were loaded to failure in 3-point bending to assess stiffness and peak load. Longitudinal comparisons of tibial microstructure were made using 2-way, repeated-measures ANOVA, adjusted for baseline values, and cross-sectional comparisons at the L4 vertebrae and femurs were made using 1-way ANOVA. Bonferroni corrections were applied to all *post hoc* tests, and significant differences were considered when p<0.05.

**Results:** Over the 12 weeks following OVX, the reproductive rats underwent a 51% decrease in bone volume fraction (BV/TV) at the tibia, but underwent no changes in trabecular number (Tb.N) or connectivity density (Conn.D) (Fig 1). In contrast, tibial BV/TV of virgin rats decreased by 76% over the 12 weeks post-OVX. Additionally, virgin rats also underwent 50% and 86% reductions in Tb.N and Conn.D, respectively (p<0.05), indicating significant deterioration of trabecular structural integrity following OVX. Cross-sectional comparisons of trabecular microstructure at L4 indicate that Virgin OVX rats had a 36% lower BV/TV and 23% lower trabecular thickness (Tb.Th) than did Virgin Control rats (p<0.05, Fig 2). In contrast, comparisons within the reproductive groups indicate no difference between Control and OVX rats in BV/TV, Tb.N, or Tb.Th. Non-ovariectomized reproductive rats did have a 31% and 24% lower BV/TV and Tb.N, respectively, than did virgin rats, indicating that reproductive bone loss resulted in baseline differences in the vertebral trabecular bone. However, these differences were abolished after OVX. Structural and mechanical properties of cortical bone at the femur midshaft showed minimal long-term effects of reproduction or OVX (Fig 3). Polar moment of inertia (pMOI), a measure of the bone structure's resistance to bending, showed no significant differences among groups, and similarly, there were no significant differences among groups in cortical area, thickness, or tissue mineral density. Mechanical properties of the femur midshaft indicated minimal differences in whole-bone stiffness, and no differences in peak load among the groups.

**Discussion:** Post-OVX bone loss was dramatically different between rats with previous pregnancy and lactation and those without. In particular, virgin rats underwent a larger drop in trabecular BV/TV at the proximal tibia than reproductive rats. Additionally, the tibial trabecular microarchitecture of virgin rats rapidly deteriorated following OVX surgery, while that of reproductive rats underwent minimal changes. As expected, cross-sectional comparisons at L4 indicate that OVX caused a significant deterioration of trabecular microstructure in virgin rats. Surprisingly, comparison within the reproductive groups indicated no significant change as a result of OVX in vertebral BV/TV and other microstructure parameters. Therefore, although reproduction and lactation resulted in inferior trabecular bone structure as compared to virgin rats, these differences were abolished after OVX in both tibial and vertebral trabecular bone. Effects of reproductive history or OVX surgery on cortical bone structure and mechanics at the femur midshaft appeared to be less substantial: post-OVX, no significant influence of reproductive history on changes in cortical structure or mechanical properties was observed. Results from the two trabecular sites studied indicate that while incomplete recovery following lactation causes a permanently altered trabecular microstructure, reproductive history-induced differences in post-OVX bone loss appear to compensate, resulting in a similar bone quality after menopause. This may help to explain the paradox that reproduction reduces bone mass without increasing fracture risk later in life [1,4,5].

**Significance:** The effects of reproduction on bone health remain controversial:

although pregnancy and lactation cause irreversible changes in bone structure, in the long-term, reproduction has been shown to have no detrimental effect on osteoporosis risk. This study addresses this unsolved clinical paradox by uncovering that reproduction and lactation history prepares the skeleton to be more resistant to estrogen deficiency-induced bone loss later in life.

**Acknowledgements:** Funding: NIH/NIAMS P30AR050950, NIH/NIAMS R03-AR065145, NSF Graduate Student Research Fellowship. Thanks to Haoruo Jia and Xiaoyuan Ma for assistance with animal experiments.

**References:** [1] Kovacs CS and Ralston SH., *Osteoporos Int*, 2015; [2] Liu XS et al., *J Bone Miner Res*, 2012; [3] Bowman BM and Miller SC, *Bone*, 1999; [4] Melton LJ et al., *Osteoporos Int*, 1993; [5] Paton LM et al., *Am J Clin Nutr*, 2003.

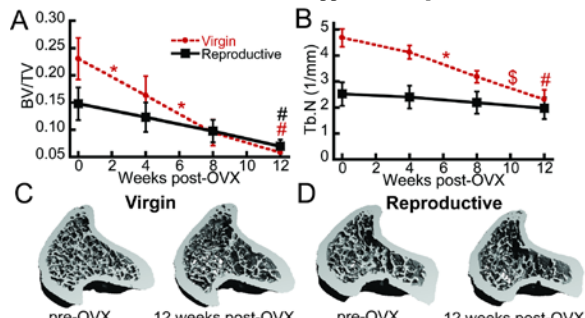


Fig 1. Longitudinal changes in (A) BV/TV and (B) Tb.N of trabecular bone at the tibia following OVX in virgin and reproductive rats.  
\*: difference between time-points (p<0.05), \$: trend towards difference between time-points (p<0.1), #: week12 ≠ week0 (p<0.05). Representative 3-D renderings of the proximal tibia of a (C) virgin and (D) reproductive rat are also shown pre- and post-OVX.

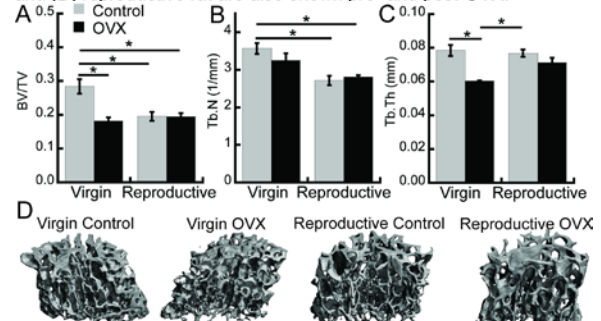


Fig 2. Effects of OVX on (A) BV/TV, (B) Tb.N, and (C) Tb.Th at the L4 vertebra in reproductive and control rats. \*: p<0.05.  
(D) Representative 3-D renderings from each group are also shown.

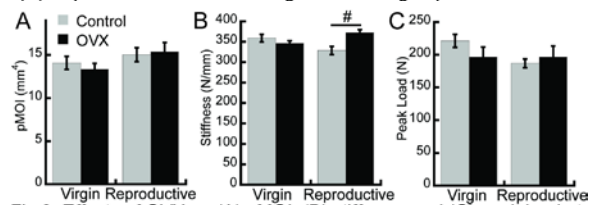


Fig 3. Effects of OVX on (A) pMOI, (B) stiffness, and (C) peak load at the femur midshaft in reproductive and control rats. #: p<0.1

## **Deletion of RGS12 causes osteopenia-like phenotype by inhibiting osteoblast differentiation through termination of Gai -cAMP-ERK signaling**

Cheng Xu<sup>1</sup>, Tongjun Liu<sup>2</sup>, Alyssa Gilmore<sup>2</sup>, Shuying Yang<sup>1,2,3</sup>

<sup>1</sup> Department of Anatomy & Cell Biology, School of Dental Medicine, University of Pennsylvania, PA,  
United States

<sup>2</sup> Department of Oral Biology, School of Dental Medicine, University of Buffalo, State University of  
New York, Buffalo, NY, United States

<sup>3</sup> Developmental Genomics Group, New York State Center of Excellence in Bioinformatics and Life  
Sciences, University of Buffalo, The State University of New York, Buffalo, NY, United States

\*Corresponding author: Dr. Shuying Yang, shuyingy@upenn.edu

### **Abstract:**

Regulators of G protein signaling (RGS) proteins play crucial roles in the regulation of G protein coupling receptors (GPCR), G proteins, and calcium signaling which are involved into bone development and remodeling. Our previous studies have shown that RGS12, the largest protein of RGS family, is essential for osteoclast differentiation. However, its function in osteoblasts is still unknown. Therefore, in this study, we generated osteoblast-specific *Rgs12* knockout mice (*Rgs12<sup>OSX</sup>*) by using *Osx-cre* transgenic mice. Compared with the control mice (*Osx-cre* mice), *Rgs12<sup>OSX</sup>* mice decreased the body weight. Micro-CT and histological studies showed a low bone mass phenotype due to the osteoblastic abnormality. To further understand the function of *Rgs12* in skeletal development, we performed the skeleton staining in newborn pups and observed the calvaria and rib deformity in *Rgs12<sup>OSX</sup>* mice. We also isolated the primary osteoblasts from calvarial bone of *Rgs12<sup>fl/fl</sup>* and used Adenovirus-cre to delete *Rgs12* *in vitro*. We found that deficiency of *Rgs12* in osteoblasts significantly decreased osteoblastic differentiation and mineralization by Alizarin Red and Von Kossa staining. In addition, the expression of osteoblast marker genes, *Col1*, *Ocn* and *Alp*, were significantly decreased by western blotting and real-time PCR. Moreover, the calcium oscillations were completely blocked in osteoblasts of *Rgs12<sup>OSX</sup>* mice. Deficiency of *Rgs12* in osteoblasts increased *Gai* expression whereas the tendencies in *Gnai1* and *Gnai3* were decreased after pertussis toxin (PTX) treatment. Meanwhile, Pi release was significantly decreased in *Rgs12<sup>OSX</sup>* mice, but restored after PTX treatment. Finally, the phosphorylation of ERK was attenuated in *Rgs12<sup>OSX</sup>* mice after PTX treatment, while the phosphorylation was increased in *Osx-cre* mice. Taken together, these data suggest that *Rgs12* plays an important role in osteoblast differentiation through regulating Gai -cAMP-ERK signaling.

# Interposition of a Cell-Seeded Slow-Degrading Membrane Generates a Stable Osteochondritis Dissecans-Like Lesion in a Large Animal Model

James M. Friedman MD<sup>1,2</sup>, Mackenzie L. Sennett BS<sup>1,2</sup>, Marcelo B. Bonadio MD<sup>1,3</sup>, Blair Ashley MD<sup>1,2</sup>, Robert L. Mauck PhD<sup>1,2</sup>, James L. Carey MD<sup>1,2</sup>  
<sup>1</sup>University of Pennsylvania, Philadelphia, PA, USA, <sup>2</sup>Philadelphia VA Medical Center, Philadelphia, PA, USA, <sup>3</sup> University of São Paulo, São Paulo Brazil

**Disclosures:** None

**Introduction:** Osteochondritis dissecans (OCD) is a rare but damaging disease that commonly affects skeletally immature individuals and is defined as the separation of an osteochondral fragment (progeny) from surrounding bone (parent bone). There is great interest in identifying the most effective treatment for this disease. However, the rarity and young patient population makes study in humans difficult. A recent pilot study by our group reported successful creation of OCD-like lesions in a porcine model at a two-week time point with the interposition of either collagen (CM) or fenestrated poly( $\epsilon$ -caprolactone) (fenPCL) membranes between a surgically created progeny fragment and parent bone [1]. The purpose of this study was to assess the durability of this non-union between the osteochondral fragment and surrounding subchondral bone at 5 and 10 weeks, as well as the impact of fibrous cell delivery on this process.

**Methods:** All animal procedures were approved by the Institutional Animal Care and Use Committee (IACUC) in accordance with NIH policy. Osteochondral fragments (progeny) were created bilaterally in the medial femoral condyles (parent bone) of 16 juvenile male Yucatan mini-pigs. Membranes were placed into the defect and the progeny fragment was secured with transchondral sutures (Fig 1). Membranes included CM (5wk: n=5; 10wk: n=3), fenPCL (5wk: n=5; 10wk: n=3), tenocyte-seeded CM (10wk: n=2), and tenocyte-seeded fenPCL (10wk: n=3). Prior to scaffold seeding, allogeneic porcine tenocytes were isolated from excised patellar tendon. Diced tendon fragments were placed in high glucose DMEM supplemented with 10% FBS and 1% Antibiotic-Antimycotic for 1 week before removal of tendon tissue. Isolated tenocytes were expanded through passage 2 before seeding on fenPCL or CM at a density of  $1.6 \times 10^5$  cells/cm<sup>2</sup>. Tenocyte-seeded membranes were cultured in chemically defined media with 10 ng/ml TGF- $\beta$ 3 for two weeks before implantation. Animals were sacrificed at 5 or 10 weeks after defect creation. Gross inspection, X-ray, micro-computed tomography ( $\mu$ CT), and histology were used to analyze each defect. Experimental groups were compared against control defects with no interposed membrane (5wk: n=3; 10wk: n=2). Three blinded scorers assessed the degree of union between the progeny fragment and parent bone on randomly selected  $\mu$ CT slices from all defects. Statistics were performed using one-way ANOVA with Tukey's post-hoc.

**Results:** Grossly, all defects were visible at the time of euthanasia with a clear demarcation between progeny fragment and parent bone cartilage. Blinded  $\mu$ CT scoring showed no significant difference in bone healing between acellular groups at 5 weeks, but had mostly healed by 10 weeks. Conversely, tenocyte-seeding of membranes significantly increased the degree of non-union at 10 weeks (Fig 2). Control groups showed nearly complete healing by 10 weeks (Fig 3). Histological analysis confirmed the  $\mu$ CT findings, with all acellular groups showing substantial bone healing and incomplete cartilage healing at 10 weeks (Fig 3). Tenocyte-seeded CM defects showed subsidence of the progeny fragment into the surrounding parent bone. In tenocyte-seeded fenPCL defects, a hypercellular, fibrous border was present around the edge of the progeny fragment.

**Discussion:** Tenocyte-seeded collagen and fenPCL membranes generated a higher degree of non-union at 10 weeks than acellular membranes. The addition of tenocytes may have resulted in the continuous generation of fibrous matrix that eventually replaced the degradable membranes, allowing for a more persistent fibrous non-union. While CM+teno and fenPCL+teno defects showed similar degrees of non-union, CM+teno progeny fragments subsided into the parent bone whereas fenPCL+teno progeny fragments remained flush with surrounding bone and cartilage. Clinically, OCD lesions are typically flush or slightly proud. The ability of fenPCL+teno membranes to generate non-union while keeping the progeny fragment flush at 10 weeks make it the best candidate for a clinically-relevant animal model of OCD. This animal model will provide a platform to evaluate interventional therapies in future studies.

**Significance:** This study demonstrates that a tenocyte-seeded fenPCL membrane is capable of generating a stable stage III OCD-like lesion in a Yucatan mini-pig. This animal model will provide a platform in which to evaluate interventional therapies for the treatment of OCD in future studies.

**Acknowledgements:** Funded by The University of Pennsylvania Department of Orthopaedic Surgery, Sports Medicine Division and the Penn Center for Musculoskeletal Disorders (P30 AR069619).

**References:** 1) Pfeifer+ Orthop Journal of Sports Med, 2015.

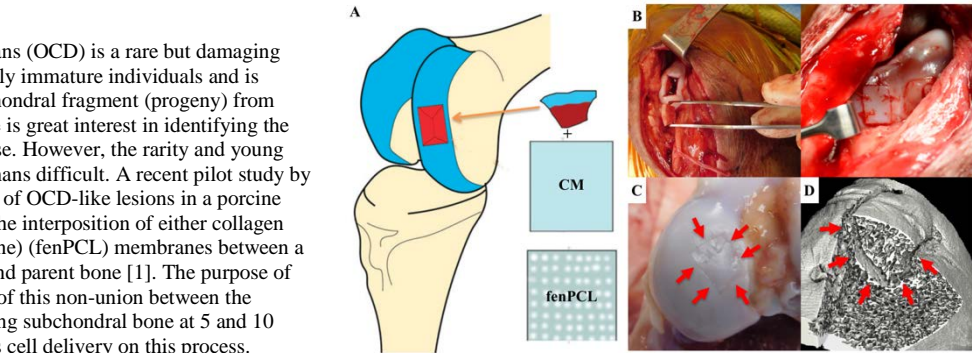


**Fig 1.** OCD-like lesion creation. (A) Schematic showing defect localization on medial femoral condyle as well as collagen and fenestrated PCL membranes. (B) Intraoperative views of progeny fragment removal and replacement with transchondral sutures after membrane placement. (C) Post-mortem gross view of OCD-like lesion (D) Cut-away view of  $\mu$ CT volume-rendering showing perilesional border within the condyle.

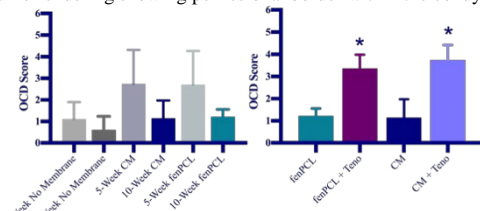


**Fig 2.** Blinded scoring of  $\mu$ CT images (mean  $\pm$  sd). Three random  $\mu$ CT slices per defect were assigned a score of 0 (complete bone healing) – 6 (complete non-union). No significant differences were found between acellular groups at 5 or 10 weeks (left), but seeded membranes resulted in significantly less healing at 10 weeks (right). (\*= $p<0.05$ ).

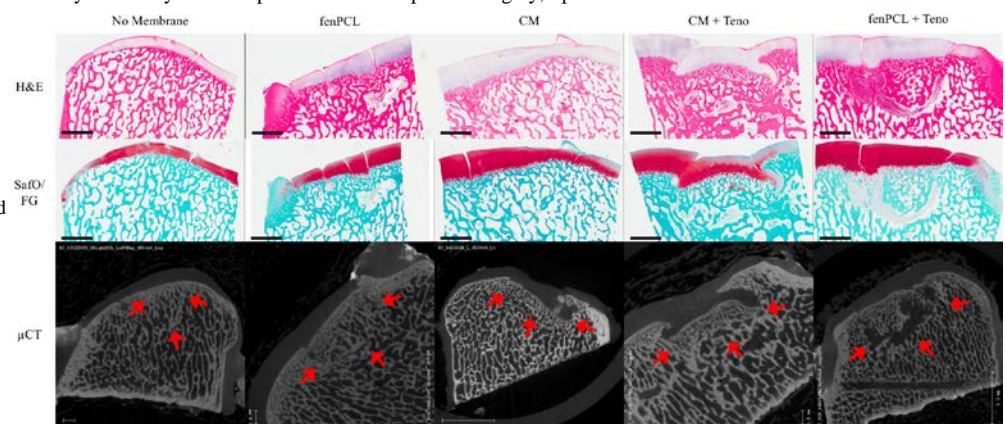


**Fig 3.** Hematoxylin & Eosin (H&E) and Safranin O/Fast Green (Saf O/FG) staining and  $\mu$ CT images of sections from all groups at 10-weeks post-surgery. Scale bar = 2 mm.

# Longitudinal Assessment Of Mouse Bone Microstructure By In Vivo $\mu$ Ct Imaging With Minimal Radiation Effects

Hongbo Zhao, Chih-Chiang Chang, Youwen Yang, Wei-Ju Tseng, Chantal M de Bakker, X Sherry Liu\*  
Department of Orthopaedic Surgery, University of Pennsylvania, Philadelphia, PA, USA

**Introduction:** In the last decade, development of the *in vivo* micro-computed tomography ( $\mu$ CT) imaging techniques has enabled assessment of longitudinal changes in bone mass and bone microstructure in small rodents, such as rats and mice [1]. However, there are concerns associated with *in vivo*  $\mu$ CT due to its exposure of tested animals to ionizing radiation. This side effect may cause damage to bone cells, thus affecting bone quality. Therefore, it is important to understand the radiation effects associated with *in vivo*  $\mu$ CT imaging protocols of different settings. However, to date only a limited number of studies have addressed this subject. Laperre *et al.* tested radiation effects of  $\mu$ CT protocols with a high (9 $\mu$ m) and low (18 $\mu$ m) image resolution on mouse tibia after 3 repeat scans with 2-week interval. They reported minor radiation effects for low image resolution protocol. However, the high resolution protocol caused significant bone loss in the irradiated tibia [2]. Another study by Klinck *et al.* tested radiation effects of a weekly scan protocol on multiple mouse strains and showed a significant decrease in bone volume fraction (BV/TV) in the irradiated tibia at 10.5  $\mu$ m voxel size [1]. The above studies suggested that different scan settings, such as image voxel size, scan frequency, and scan intervals, may have different effect on bone. The purpose of this study was to develop a low dose, *in vivo*  $\mu$ CT protocol for imaging mouse femur and vertebrae and to test the radiation effects of this protocol on bone quality and bone cell activities. The new protocol, in which mice are scanned at 10.5 $\mu$ m (femur) and 15 $\mu$ m (vertebra) with 3-week interval, was tested on both the tissue level and cellular level for the first time. We hypothesized that a well designed *in vivo* scanning protocol can assess longitudinal changes in mouse bone microstructure with minimized radiation effects.

**Methods:** All animal studies performed in this research were approved by the Institutional Animal Care and Use Committee (IACUC) at the University of Pennsylvania. Eight female C57BL/6J (BL6) mice were scanned at the right femur and the 4<sup>th</sup> lumbar vertebra (L4) by an *in vivo*  $\mu$ CT system (Viva CT40, Scanco Medical, Switzerland). For the distal femur, 212 slices were scanned at 10.5  $\mu$ m voxel size. For the L4, 212 slices at the center of L4 were scanned at 15 $\mu$ m voxel size. The scanner was operated at 55 kVp energy, 145  $\mu$ A intensity, and 200 ms integration time and the average time for each scan was about 10 minutes. This scan protocol induced a radiation dose of 639 mGy on femoral bone and 310 mGy on vertebral bone. Baseline scans occurred when mice reached age 12 weeks, and 2follow-up scans were performed at 3 and 6 weeks after the baseline scan. All animals were sacrificed 3 weeks after the last scan when they reached age of 21 weeks. Left (non-radiated) and right (radiated) femur, L3 (non-radiated) and L4 (radiated) vertebra were harvested from each mouse for further analysis.

All the harvested bone samples underwent *ex vivo* scans at 6  $\mu$ m isotropic voxel size in a  $\mu$ CT system (MicroCT35, Scanco Medical, Switzerland). In each scan, 227 slices in the region that was covered in the *in vivo*  $\mu$ CT scan were acquired. Images were smoothed using a Gaussian filter (sigma = 0.6, support = 1), followed by a segmentation threshold corresponding to 450.7 mgHA/cm<sup>3</sup> and semi-automatic contouring to extract the trabecular bone for microstructural analysis. Bone volume fraction (BV/TV), connectivity density (Conn.D), structure model index (SMI), trabecular number (Tb.N), trabecular thickness (Tb.Th), and trabecular spacing (Tb.Sp) were calculated by three dimensional (3D) standard microstructural analysis software provided by the manufacturer. Bone microstructure was also evaluated for all baseline scans. Percent changes over 9 weeks were quantified by comparisons between the baseline and endpoint scans.

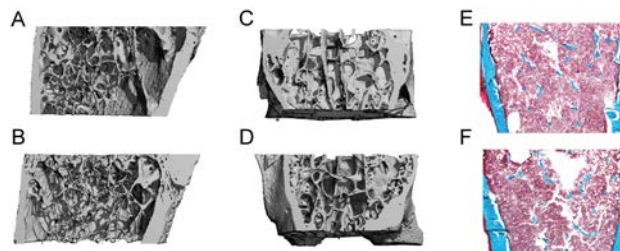
Both left and right femurs were processed for methylmethacrylate embedding. Five  $\mu$ m thick plastic sections were cut using a Polycut-S motorized microtome (Reichert, Heidelberg, Germany) and stained with Goldner's trichrome stain (Fig.1) [3]. Histomorphometric measurements were performed in the metaphyseal bone region that was scanned by *in vivo*  $\mu$ CT using Bioquant Osteo Software (Bioquant Image Analysis, Nashville, TN). Osteoblast number (Ob.N/BS), osteoclast number (Oc.N/BS), osteoblast surface (Ob.S/BS), and osteoclast surface (Oc.S/BS) were evaluated.

Paired Student's t-tests were performed to compare radiated and non-radiated bone microstructure and bone cell activities. A p value below 0.05 was considered to indicate significant radiation effect.

**Results:** Comparisons between radiated L4 and non-radiated L3 showed no significant difference in BV/TV, Tb.Th, SMI, or Conn.D. However, radiated L4 had 10.0% lower Tb.N and 14.1% greater Tb.Sp than non-radiated L3 (p<0.05). As for the femur, there was no difference in BV/TV, Tb.N, or Tb.Sp between radiated right femur and non-radiated left femur. However, radiated right femur had 28.8% lower Conn.D, 16.8% greater SMI, and 12.8% greater trabecular thickness (Tb.Th) than non-radiated left femur (Fig 2). Bone histomorphometry analysis showed no difference in Ob.N/BS, Oc.N/BS, Ob.S/BS or Oc.S/BS between the non-radiated and radiated femurs (Fig 2). Comparisons between the baseline and endpoint scans suggested significant bone loss in mice from age of 12 to 21 weeks, as shown in Table 1.

**Figure 1.** Representative  $\mu$ CT images of (A) non-radiated left femur vs. (B) radiated right femur; (C) non-radiated L3 vs. (D) radiated L4; and representative Goldner's trichrome staining images of (E) non-radiated left

**Table 1.** % change in bone microstructure in mice from age of 12 to 21 weeks. \* indicates significant change (p<0.05).



% change over time	Distal Femur	Lumbar Vertebra
BV/TV	-31.3± 22.6*	-12.4±10.6*
Tb.N	-21.7± 6.4*	-22.2± 8.9*
Tb.Th	2.3± 11.3	-19.6± 4.7*
Tb.Sp	31.9± 9.6*	29.6±14.5*
SMI	-3.7±12.1	-64.7± 8.9*
Conn.D	26.6±68.6	23.9±43.9

**Discussion:** In this study, we developed and tested a low dose, *in vivo*  $\mu$ CT scan protocol of the mouse femur and vertebra with image voxel size of 10.5 $\mu$ m and 15  $\mu$ m, respectively. Minimal radiation effects were found on trabecular bone mass and microstructure while no radiation effect was observed in number and surface of osteoblasts and osteoclasts.

Despite minimal radiation effect on BV/TV, significant differences found in Tb.N and Tb.Sp of the vertebra, and Conn.D, SMI, and Tb.Th of the femur suggested that radiation effect by *in vivo*  $\mu$ CT can lead to deteriorations in trabecular bone micro architecture. Nevertheless, aging also plays a significant role in trabecular bone loss. Results from our study is consistent with those reported by Glatt *et al.*, which showed that female mice had significant bone loss in the distal femur and vertebra from age of 3 to 5 months[4]. Comparing with aging effect, our study suggested that ionizing radiation associated with *in vivo*  $\mu$ CT exerted significant but negligible effect on some of trabecular bone microarchitecture parameters. Therefore, we conclude that the low dose *in vivo*  $\mu$ CT imaging protocols developed for the mouse femur and vertebra can assess longitudinal changes in bone mass and microstructure with minimal radiation effects.

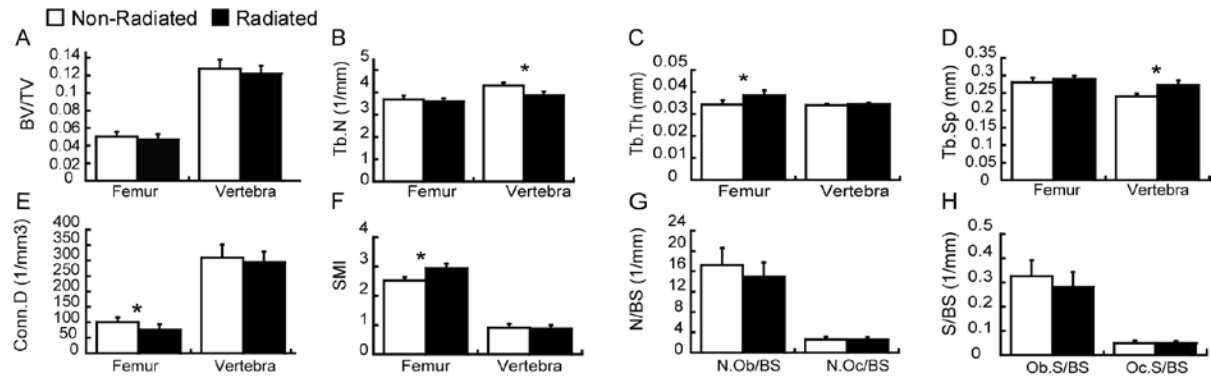


**Figure 2.** Differences of (A) BV/TV, (B) Tb.N, (C) Tb.Th, (D) Tb.Sp, (E) Conn.D, (F) SMI, (G) N.Ob/BS, N.Oc/BS and (H) Os.S/BS, Oc.S/BS between non-radiated and radiated bone.

**Acknowledgements:** This study is supported by NIH/NIAMS P30-AR050950, and NIH/NIAMS K01-AR069619.

**References:** [1] Klinck, R. J.*et al.*, Medical Engineering & Physics, 30(7):888-895, 2008; [2] Laperre, K*et al.*, Bone, 49(4): 613–622, 2011; [3] Chandra, A*et al.*, Bone, 55(2): 449–457, 2013; [4] Glatt, V*et al.*, Journal of Bone and Mineral Research, 22(8):1197–1207, 2007.

# Comparison of Quantitative Imaging Techniques for Detecting Degenerative Changes in a Mouse Caudal Intervertebral Disc Injury Model.

Matthew Piazza, Sun H. Peck, Sarah E. Gullbrand, Justin R. Bendigo, Harvey E. Smith, Neil R. Malhotra, Lachlan J. Smith

Departments of Neurosurgery and Orthopaedic Surgery, University of Pennsylvania

**Introduction:** Intervertebral disc (IVD) degeneration has been strongly implicated in the development of low back pain, a major cause of morbidity, health care expenditures, and lost productivity in the United States. As conservative management of low back pain secondary to disc degeneration is the mainstay of therapy and outcomes from surgical fusion are unimpressive, there is a strong need to develop novel therapies that restore disc structure and function. Developing animal models that recapitulate the pathological changes within the degenerating IVD is instrumental to studying novel cell based regenerative therapies. The objective of this study was to build on a previously reported mouse model of disc degeneration[1] and, specifically, to compare the sensitivity of two quantitative, high-resolution imaging techniques – magnetic resonance imaging (MRI) and microcomputed tomography ( $\mu$ CT) – for detecting disc degeneration induced by 3 different needle sizes.

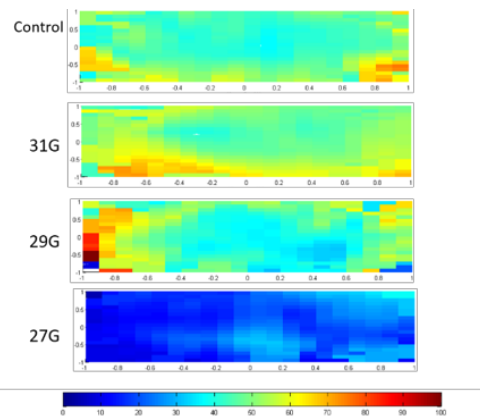


**Figure 2.** T2 relaxation population average color maps for control and disc injury levels.

post hoc tests. Significance and trend were defined as  $p<0.05$  and  $p<0.1$ , respectively. All statistical analyses were performed using SPSS.

**Results:** All six mice underwent the disc injury procedure without issue, survived the full four weeks post-operatively, and were subsequently euthanized. Post-mortem MRI revealed a significantly different T2 relaxation times within the nucleus pulposus overall ( $p=0.01$ ). Specifically, lower average T2 relaxation times in the 27G injury levels ( $19.7\pm8.7$ ms) compared with the intervening control ( $45.0\pm10.1$ ms,  $p=0.02$ ), 31G injury level ( $49.2\pm13.3$ ms,  $p=0.01$ ), and 29G injury level ( $43.1\pm9.1$ ms,  $p=0.05$ ).

**Figure 1** depicts T2 relaxation population average color maps for each experimental level. Differences in disc height index (**Figure 3**) trended towards significance across experimental groups ( $p=0.08$ ). The DHI for 27G injured discs ( $0.05\pm0.02$ ) was less than the intervening control, but this only approached significance ( $0.1\pm0.004$ ,  $p=0.08$ ). A similar trend was not observed when the 27G injured disc was compared with the 29G ( $0.1\pm0.002$ ,  $p=0.16$ ) or 31G injured discs ( $0.08\pm0.02$ ,  $p=0.54$ ). Neither the 29G or 31G injured discs differed from control with regards to DHI. **Figure 4** depicts example contour plots for disc height for 29G (A) and 27G (B) injured discs.

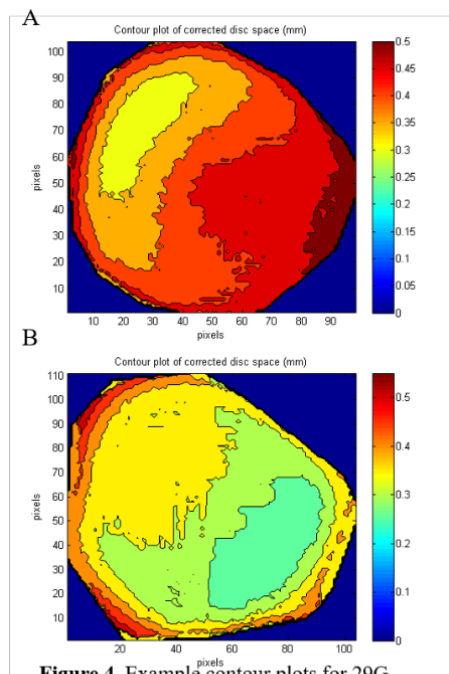


**Figure 4.** Example contour plots for 29G (A) and 27G (B) injured discs. Colorbars indicate disc height in mm.

**Methods:** Following approval by the institutional IACUC, six C57BL/6 retired breeder mice were anesthetized and in standard aseptic fashion underwent percutaneous, fluoroscopic guided needle puncture at approximately the C6/7 and C8/9 disc levels randomized to either 27G, 29G, or 31G needles ( $n=4$  for each group). The intervening C7/8 level served as a non-injury control ( $n=6$ ). At 4 weeks post injury, mice were euthanized for post-mortem analyses. Quantitative MRI was performed on mouse tails on a 9.4T scanner. T2 relaxation constant maps were constructed and average T2 relaxation times were calculated as a surrogate for disc composition [2]. One level (mouse 6, 27G injury) was excluded from this analysis due to substantial soft tissue inflammation/destruction that precluded delineating IVD from bone. Whole mouse tails were scanned on a  $\mu$ CT scanner ( $\mu$ CT35; Scanco, Switzerland) at 6  $\mu$ M resolution (up-scaled to 12  $\mu$ M for analysis). Volumetric measurements of mean disc height and mean vertebral body height were performed in MatLab. DHI was calculated as the mean disc height/mean vertebral body height [1]. One-way ANOVA was

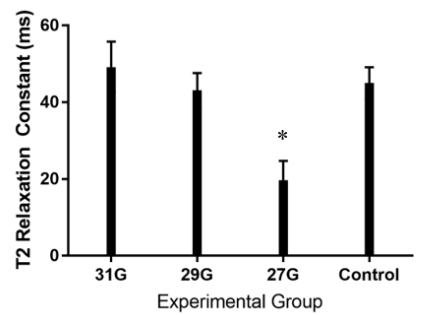


**Figure 1.** T2 relaxation constants for disc injury levels ( $n=4$ /needle size) and control ( $n=6$ ). Significant differences ( $p<0.05$ ) in T2 relaxation constants between 27G and 31G/controls indicated by (\*). Difference between T2 relaxation constant of 27G and 29G injured discs approached significance ( $p=0.05$ ).

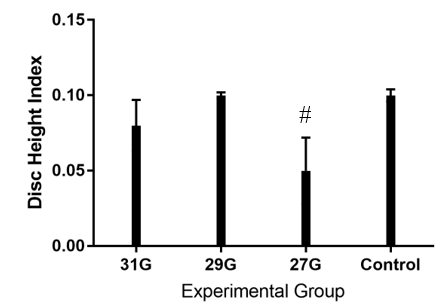


**Figure 3.** Average disc height index (DHI) for disc injury levels ( $n=4$ /needle size) and control ( $n=6$ ). DHI difference between 27G injured discs and controls approached significance (#,  $p=0.08$ ).

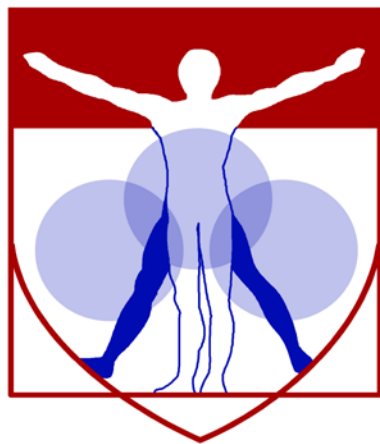
DHI for 27G injured discs ( $0.05\pm0.02$ ) was less than the intervening control, but this only approached significance ( $0.1\pm0.004$ ,  $p=0.08$ ). A similar trend was not observed when the 27G injured disc was compared with the 29G ( $0.1\pm0.002$ ,  $p=0.16$ ) or 31G injured discs ( $0.08\pm0.02$ ,  $p=0.54$ ).

Neither the 29G or 31G injured discs differed from control with regards to DHI.

**Conclusions:** The results of this study demonstrate that both quantitative MRI and  $\mu$ CT are able to detect degenerative changes in the mouse caudal disc injury model, but that MRI may be more sensitive than  $\mu$ CT. Both these imaging techniques detect clinically relevant changes (i.e. decreased T2 for MRI and loss of disc height for  $\mu$ CT) present in human disc degeneration. Results also suggest that 27G needle injury represents the threshold for detecting degenerative changes for both of these techniques, which is consistent with previous findings [1]. Needle sizes smaller than 27G may therefore be appropriate for cell delivery to the mouse disc in future therapeutic studies, without inducing significant damage. Ongoing work will correlate imaging findings with disc histopathology, and future studies will apply these imaging techniques to assess the response of the mouse disc to therapeutic intervention.

**References:** [1] Martin+ J Orthop Res 2013; [2] Martin+ J Orthop Res 2015

**Acknowledgements:** Funding received from the Penn Institute on Aging, the Penn Center for Musculoskeletal Disorders, and the Department of Neurosurgery at the University of Pennsylvania. Technical support received from Dr Stephen Pickup of the Penn Small Animal Imaging Facility.



PENN  
CENTER for  
MUSCULOSKELETAL  
DISORDERS

---

# Miscellaneous Abstracts

## **Imaging approaches to detect & monitor changes in joint architecture & brain networks in TMJ pain**

Megan M. Sperry<sup>1</sup>, Sonia Kartha<sup>1</sup>, Ya-Hsin Yu<sup>2</sup>, Eric J. Granquist<sup>3</sup>, Beth A. Winkelstein<sup>1,4</sup>

<sup>1</sup> Bioengineering, University of Pennsylvania, Philadelphia, PA, USA

<sup>2</sup> Dental Medicine, University of Pennsylvania, Philadelphia, PA, USA

<sup>3</sup> Oral & Maxillofacial Surgery, University of Pennsylvania, Philadelphia, PA, USA

<sup>4</sup> Neurosurgery, University of Pennsylvania, Philadelphia, PA, USA

**PURPOSE.** Temporomandibular joint (TMJ) osteoarthritis is a common, low-grade inflammatory condition that has a multifactorial etiology including pain. In most patients, pain resolves without needing further clinical action. However, for a subset of patients, chronic TMJ disorder develops, with long-lasting symptoms. Sustained neuronal hyperexcitability throughout the central nervous system is a major contributor to the development of chronic pain and can lead to changes in brain circuitry. This study investigates alterations in the TMJ and brain using quantitative *in vivo* imaging techniques to compare different pain states.

**METHODS.** All procedures were IACUC-approved. Repeated mouth-opening was imposed daily for one week in female Holtzman rats under isoflurane anesthesia to induce either resolving or persistent pain (n=7/group). Orofacial pain was assessed by measuring mechanical hyperalgesia. CT images of the TMJ were acquired before loading (baseline) and at day 14, to quantify joint structure. Image stacks were registered between days, automatically segmented, and reconstructed in 3D. Changes in joint architecture were evaluated using image subtraction between registered images. In addition, FDG-PET images of the brain were acquired at baseline and day 7 to evaluate metabolic activity when the pain responses diverge. Images were registered to Schwarz's rat brain template. Networks were created by representing each brain region as a node; edges connecting nodes were defined by the Pearson correlation coefficient between FDG uptake in two regions for all rats. Meso-scale structure of the network was evaluated by the Louvain algorithm.

**RESULTS.** Orofacial sensitivity is established during the loading period for both groups ( $p<0.001$ ), but only remains at day 14 in the persistent pain group ( $p<0.001$ ). Flattening of the TMJ condylar head is evident at day 14 only in the persistent painful group; this change in bone shape is not evident in the other group. Image subtraction reveals image intensity changes between day 14 and baseline that are larger in the painful group ( $1785\pm621$ ) compared to the group ( $1232\pm542$ ) with no pain at that time. In combining both groups, the modularity of the brain networks significantly decreases ( $p<0.0001$ ) at day 7 when pain is present. However, a change in community structure emerges in the sustained pain group at day 7 that is not evident in the resolving pain group.

**CONCLUSIONS.** Both peripheral tissue and brain are altered when TMJ pain persists. These findings suggest that these, and/or other imaging approaches, may have predictive value in diagnosing disease (i.e. pain) progression in TMJ osteoarthritis.

## Effect of Low Magnitude Mechanical Stimulation on Postmenopausal Bone Loss

C McHugh, CS Rajapakse, W Sun, K Sexton, B Newman, MM Al Mukaddam, PJ Snyder, FW Wehrli

Low bone mass is key risk factor for osteoporotic fractures and thus a major public health threat for older Americans, particularly for women after menopause. Data in animals have shown that low-magnitude mechanical stimulation (LMMS) treatment is strongly osteogenic [1] but less compelling in humans where the effect critically depends on subjects' adherence [2-5]. A clinical double-blinded, randomized, placebo-controlled study on early post-menopausal women is currently in progress in the authors' laboratory. The study subjects are randomly assigned to either an active or placebo device involving 10 minutes daily of standing on a platform resembling a bathroom scale. The active device vibrates at 30 Hz and 0.3g (an acceleration corresponding to a displacement of approximately 90  $\mu\text{m}$ ) whereas the placebo device merely emits an equal acoustic signal and thus is indistinguishable to the patient from the active device. Of the 26 subjects who have completed the study, the data suggests that the baseline MRI-derived bone volume fraction (BVF) of trabecular bone was inversely correlated with the fractional change from baseline; a subject whose baseline BVF is low will see a greater increase in BVF after the completion of a 12-month LMMS treatment than that of a subject whose baseline BVF is already high (Figure 1). This result is potentially significant since BVF is the single largest predictor of the bone's mechanical behavior estimated by computational biomechanics. Since the data has not yet been unblinded, approximately half the subjects are in the placebo group, and thus would not show an effect or bone loss as it is expected following menopause. At the present, no definitive conclusions can be drawn from this limited dataset, yet the effect observed is highly statistically significant.

1. Rubin C, Turner AS, Bain S, Mallinckrodt C, McLeod K. Anabolism. Low mechanical signals strengthen long bones. *Nature*. 2001 Aug 9;412(6847):603-4.
2. Gilsanz V, Wren TA, Sanchez M, Dorey F, Judex S, Rubin C. Low-level, high-frequency mechanical signals enhance musculoskeletal development of young women with low BMD. *J Bone Miner Res*. 2006 Sep;21(9):1464-74.
3. Rubin C, Recker R, Cullen D, Ryaby J, McCabe J, McLeod K. Prevention of postmenopausal bone loss by a low-magnitude, high-frequency mechanical stimuli: a clinical trial assessing compliance, efficacy, and safety. *J Bone Miner Res*. 2004 Mar;19(3):343-51.
4. Leonard MB, Shults J, Long J, Baldassano RN, Brown JK, Hommel K, Zemel BS, Mahboubi S, Howard Whitehead K, Herskovitz R, Lee D, Rausch J, Rubin CT. Effect of Low-Magnitude Mechanical Stimuli on Bone Density and Structure in Pediatric Crohn's Disease: A Randomized Placebo-Controlled Trial. *J Bone Miner Res*. 2016 Jun;31(6):1177-88.
5. Kiel DP, Hannan MT, Barton BA, Bouxsein ML, Sisson E, Lang T, Allaire B, Dewkett D, Carroll D, Magaziner J, Shane E, Leary ET, Zimmerman S, Rubin CT. Low-Magnitude Mechanical Stimulation to Improve Bone Density in Persons of Advanced Age: A Randomized, Placebo-Controlled Trial. *J Bone Miner Res*. 2015 Jul;30(7):1319-28.

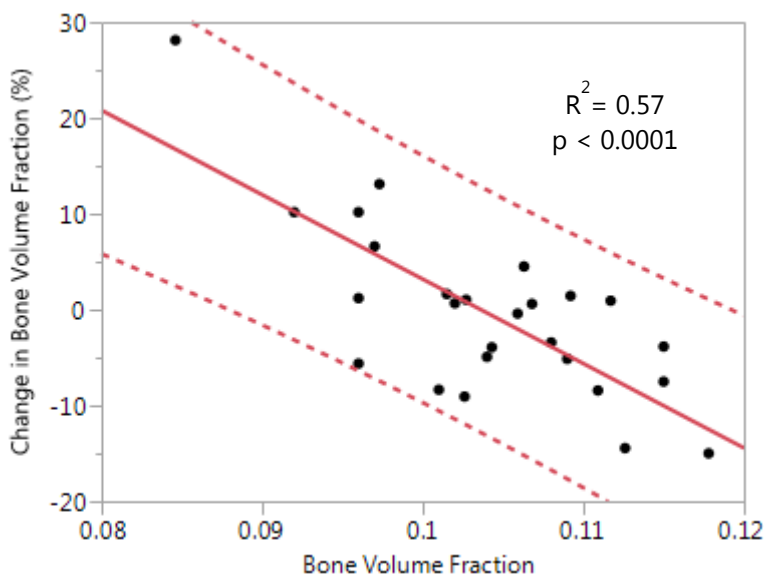


**Figure 1:** Fractional change (%) in bone volume fraction (BVF) of trabecular bone after one year of LMMS treatment. The data suggest that the treatment effect, if any, scales inversely with the baseline BVF. Notably, approximately half the subjects were in the placebo group, thus should not experience a treatment effect, if any, but rather experience bone loss as expected following menopause.

## Intercellular Communication in Chondrocyte/MSC Co-Cultures is Mediated by Extracellular Vesicles

Minwook Kim<sup>1,2</sup>, Jason A. Burdick<sup>2</sup>, Robert L. Mauck<sup>+1,2</sup>

+McKay Orthopaedic Research Laboratory, Departments of Orthopaedic Surgery<sup>1</sup> and Bioengineering<sup>2</sup>, University of Pennsylvania, Philadelphia, PA

**INTRODUCTION:** Co-culture systems have been introduced as a strategy to improve the use of progenitor cells for cartilage repair. Previous studies have demonstrated that a small fraction (~20%) of young/healthy chondrocytes (CH) mixed with aged/infirm mesenchymal stem cells (MSC) can restore the chondrogenic capacity of MSCs and suppress their hypertrophic conversion. These studies also suggested that molecular factors secreted from CHs induce and/or promote MSC chondrogenesis [1-3]. In our recent work, we noted that dye from CHs (red) appeared within co-cultured MSCs (that were initially green), forming a double positive (DP) population in which red speckles were present in the green cells [4]. Potentially explaining this observation, several studies have suggested that cell-derived extracellular vesicles (EVs; exosomes and microvesicles) that can carry proteins, enzymes, mRNAs, miRNAs, DNA are present in synovial fluid and the extracellular matrix (ECM), and that these EVs may play an important role in intercellular communication [5-7]. It is not yet clear, however, whether these EVs play a role in mediating cell-to-cell communication in co-cultures of MSCs and CHs. To address this question, we utilized fluorescent activated cell sorting along with microarray and pathway analysis to elucidate key signaling factors involved in the co-culture effect, and interrupted the mechanisms that enable EV formation and trafficking between cells to evaluate its role in this process.

**MATERIALS AND METHODS:** Adult MSCs and juvenile CHs were obtained from bone marrow and articular cartilage of bovine knees. Cells were isolated and expanded through passage 3. To enable sorting of distinct cell populations and tracing of vesicular exchange, MSCs (green) and CHs (red) were labeled using CellTracker (Molecular Probes). MSCs (MSC), CHs alone (CH) or mixed (CO) cell populations (MSC:CH ratio = 4:1) were encapsulated at 20×10<sup>6</sup> cells/mL (Ø4 × 0.75 mm; **Study 1**) or 60×10<sup>6</sup> (Ø4 × 2.25 mm; **Study 2**) in 1% w/v hyaluronic acid (HA) hydrogels (Lifecore Biomedical) [8]. **[Study 1]** To investigate potential molecular factors and/or signaling pathways regulated by co-culture, constructs (MSC alone or CO) were cultured in a defined medium without (CM-) or with TGF-β3 (CM+; 10ng/mL). On day 10, constructs were minced and digested with hyaluronidase (100U/mL) [8] to re-isolate cells from constructs. Isolated cells underwent FACS sorting according to their CellTracker labeling. RNA isolation (Qiagen) and microarray analysis were performed (Affymetrix), with a focus on the MSC populations sorted from each group (n = 3 replicates). Ingenuity software was used to identify pathways associated with the co-culture effect, using identified genes that were differentially regulated with a false discovery rate (q-value) of 0.25 and fold change of 1.5. Fold change was compared across four groups (CO+ vs. MSC+, MSC+ vs. MSC-, CO- vs. MSC- and CO+ vs. CO-). **[Study 2]** To identify whether intercellular communication occurs through EVs, constructs (MSC alone, CH alone or CO) were cultured in the presence of TGF-beta along with Pitstop 2 (0, 10, 25 or 50μM; Abcam; to inhibit clathrin mediated vesicle formation) or Dyngo 4a (50μM; Abcam; to inhibit dynamin and t-SNARE mediated vesicle fusion) for 6 weeks. Vesicular transfer was also examined via confocal microscopy. Bulk properties were assessed via unconfined compression [9], and glycosaminoglycan (GAG) and collagen contents were measured. Paraffin sections (8μm) were stained with Alcian Blue for proteoglycans and immunohistochemistry for type I and II collagen. Significance was determined by two-way ANOVA with Tukey's post hoc ( $p < 0.05$ ).

**RESULTS:** **[Study 1]** FACS analysis showed that some MSCs in the CO group retained their green signal (CO G) while others (40~50%) in the same group became DP (CO DP), indicating transfer of internal contents from the CH to the MSC population. PCA analysis showed that MSCs in the CO+ group had shifted in their expression profile compared to MSCs alone with TGF (MSC+). MSCs that were DP (CO+ DP) also differed from MSCs that remained green (CO+ G) (data not shown). Further analysis produced a set of genes with significant fold changes in MSCs that were DP (CO+ DP) compared to MSCs alone (MSC+) (CO+ DP vs. MSC+) and to MSCs in co-culture that remained green (CO+ G) (CO+ G vs. MSC+) (**Table 1**). Expression patterns in the CO+ DP MSCs were distinct from those induced by TGF alone (MSC+ group) and from MSCs co-cultured with chondrocytes in the absence of TGF (CO- MSC population). **[Study 2]** Inhibition of clathrin with a high dose of Pitstop 2 (50μM) completely suppressed GAG synthesis in both MSCs and CHs. Conversely, inhibition of t-SNARE/dynamin with Dyngo 4a (50μM) did not alter ECM accumulation (data not shown). Mild inhibition of clathrin (25μM) did not alter the equilibrium modulus ( $E_Y$ ) and GAG content of CH- (309kPa/3.52% WW GAG) and MSC-laden constructs (0kPa/0.4% WW) compared to controls (389kPa/4.3% WW and 34kPa/0.4% WW, respectively). However, co-cultured constructs (containing MSCs and CHs) showed a marked decrease in mechanical properties (43kPa/1.9% WW) compared to co-cultures maintained in the absence of inhibitors (195kPa/2.4% WW) (**Fig 1a**). Further, the number of green cells that became DP decreased with the addition of Pitstop (**Fig 1b**).

**DISCUSSION:** In this study, we queried the intercellular communication mechanisms that underlie the positive and synergistic effects seen in CH-MSC co-cultures. Over 3 days, red dye from CHs appeared within MSCs, suggesting that vesicular transfer had occurred between the two cell types. We found a distinct shift in the molecular profile of cells that had become DP versus those that had not. Moreover, the set of genes differentially regulated in these DP MSC populations was distinct from that caused by TGF or CHs alone. This suggests that, in the context of TGF, CH-derived EVs transform the molecular profile of recipient MSCs. Additional pathway analysis and target validation is now underway. On a mechanistic basis, we found that the modulus of co-cultured constructs decreased substantially with inhibition of clathrin by Pitstop, and confocal microscopy showed a reduction in the number of MSCs that had become DP. This supports the notion that shuttling of molecular factors from CHs to MSCs is mediated by EVs. Identifying the specific molecular factors secreted by young/healthy CHs to rejuvenate aged/infirm MSCs, as well as their mechanism of transfer, might lead to new therapeutics to improve functional tissue engineering using adult autologous MSCs, and may ultimately obviate the need for such co-cultures.

**SIGNIFICANCE:** Co-culture is a promising strategy in cartilage tissue engineering, especially given its potential to rescue function in aged MSCs. This work is of translational relevance, given the clinical availability of allogeneic juvenile CHs. Furthermore, identifying molecular factors mediating the co-culture effect, as well as their carriers and delivery mechanisms, may lead to the development of new therapeutic agents and effective delivery systems, eliminating the need for CHs and enabling functional cartilage tissue formation by adult autologous MSCs.

**REFERENCES:** [1] Aung+ Arthritis Rheum 2011 [2] Bian+ Tissue Eng 2011 [3] Kim+ ORS 2012 [4] Kim+ ORS 2015 [5] Gyorgy+ Cell Mol Life Sci 2011 [6] Raposo+ J Cell Sci 2013 [7] Malda+ Nat Rev 2016 [8] Burdick+ Biomacromol 2005 [9] Mauck+ J Biomech Eng 2000

**ACKNOWLEDGEMENTS:** This work was supported by the NIH (R01 EB008722) and the Penn Center for Musculoskeletal Disorders (P30 AR069619).

# Fabrication and Characterization of a Bilayer Delivery System for Localized and Sustained Therapeutic Release

Dong Hwa Kim<sup>1,2</sup>, Julianne Huegel<sup>1,2</sup>, Louis J. Soslowsky<sup>1,2</sup> Robert L. Mauck<sup>1,2</sup>, and Andrew F. Kuntz<sup>1,2</sup>

<sup>1</sup>University of Pennsylvania, Philadelphia, PA, <sup>2</sup>Philadelphia VA Medical Center, Philadelphia, PA

Disclosures: DH Kim (N), J Huegel (N), LJ Soslowsky (N), RL Mauck (N), AF Kuntz (N)

**INTRODUCTION:** Biodegradable micro-particle systems have attracted increasing interest for use as delivery vehicles for drugs, proteins, and other therapeutic agents for tissue repair and regeneration given their ease of fabrication [1-2]. Among the various methods, microencapsulation can improve protein stability and has the capacity to selectively entrap proteins in a biodegradable polymer matrix [3]. While these approaches provide an avenue for release, it is also important to be able to deliver and release agents in a localized environment and in a controlled manner over time *in vivo*. To address this need, this study used a water-in-oil-in-water (w/o/w) emulsion technique to prepare protein-loaded microspheres (MS) and developed a Bilayer Delivery System (BiLDS) to sequester these MS in a defined location while enabling release. Towards validation, we explored how sequestration within the BiLDS influenced MS release kinetics and degradation.

**METHODS:** Microspheres (MS) were produced by combining 75:25 PLGA (0.15 g/mL, Mw=70 kDa) with 145 mg of BSA (0.15 g/mL) in 2 mL of dichloromethane. The solution was further spiked with 5 mg of Alexa-labeled BSA (0.005 g/mL) to enable fluorescent tracking and quantification of release. The external phase of the emulsion consisted of 5 mL of aqueous 1% poly(vinyl alcohol). The emulsion was sonicated, added to distilled water, and stirred for 2 min. Formed microspheres were suspended in distilled water and stirred continuously for 4 hr.

Finally, microspheres were washed and lyophilized for 48 hr. To characterize release, MS (10 mg) were suspended in 1 mL of PBS or serum for 60 days followed by fluorescence and SEM imaging. To generate the bilayered delivery system (BiLDS), Alexa-BSA microspheres (10 mg) were suspended in 20  $\mu$ L of PBS and placed onto the center of an aligned poly( $\epsilon$ -caprolactone) nanofibrous scaffold (6 $\times$ 8 mm) [4]. A second layer was placed atop and the two layers were sealed together by heat-annealing in a circular pattern around the microspheres using a custom heating device (set at 60°C). Assembled BiLDS were lyophilized and stored at -20°C until use. To determine *in vitro* Alexa release from Alexa-BSA microspheres within the BiLDS, assembled constructs were suspended in 3 mL of serum at 37°C on a shaker for 30 days. The supernatant (80  $\mu$ L) was withdrawn (and replaced with fresh serum) at various time intervals throughout the experiment. Alexa-BSA in the supernatant was measured using a fluorescent microplate reader (Synergy HT; BioTek, VT) at an excitation wavelength of 530 nm and an emission wavelength of 590 nm.

**RESULTS:** Fluorescent imaging showed that Alexa-BSA was well distributed throughout the formed MS (**Fig. 1A**). SEM analysis demonstrated that MS were spherical with a smooth surface. MS ranged in diameter from 1.5-3  $\mu$ m (not shown) (**Fig. 1B**). With 60 days of incubation in PBS or serum, MS decreased in diameter and released their contents. MS in PBS for 60 days were 0.5-2  $\mu$ m in diameter while in serum they were 1.5-2.5  $\mu$ m in diameter (**Fig. 1C-D**). Upon BiLDS fabrication, SEM images showed that MS could be localized and retained in the central BiLDS formed during assembly (**Fig. 2A**) with a continuous seal formed along the margin (**Fig. 2B**). Cross-sectional views of the BiLDS showed large quantities of MS within the BiLDS (**Fig. 2C-D**). With long term incubation in serum, BiLDS remained intact (**Fig. 3A**), and SEM imaging of cross sections showed that MS remained entrapped after 30 days and showed evidence of degradation (**Fig. 3B-C**). Release from Alexa-BSA-loaded MS within the BiLDS reached 7% over the first day and continued to release over a 30 day period, with 16% released over this time period. This release was slightly attenuated compared to free MS incubated similarly, which had reached 31% release over this same time period (**Fig. 3D**).

**DISCUSSION:** In this study, we developed a bilayered delivery system (BiLDS) to localize MS release using a clinically relevant and previously validated scaffold system. We have previously established that such nanofiber systems can be used in an overlay fashion to support rotator cuff repair and to deliver cells in a small animal model [5]. Our data here show that MS entrapped within the BiLDS system showed a somewhat attenuated release profile compared to free microspheres, and that protein release was sustained and continuous for up to 30 days. Ongoing studies will determine whether the final amount of release matches that of free microspheres. These data establish the BiLDS technology as a sustained *in vivo* drug delivery device that can localize protein and other biofactor release to a surgical site. In future studies, we will explore the ability of this BiLDS technology to deliver growth factors relevant to rotator cuff repair in a small animal model. We will also explore inclusion of multiple MS formulations within the same BiLDS to enable differential timing and payload release in a controlled and localized fashion.

**SIGNIFICANCE:** This work establishes a novel bilayered delivery system (BiLDS) that can enable sustained release from biodegradable microspheres in a localized and clinically relevant fashion for tissue repair and regeneration.

**REFERENCES:** [1] Rafati+, 2012 *J Control Release* [2] Ambrosch+, 2012 *Acta Biomater* [3] Emma+, 2007 *Biomaterials* [4] Ionescu+, 2010 *Biomaterials* [5] Huegel+, 2016 *J Orthop Res*.

**ACKNOWLEDGEMENTS:** This work was supported by the Department of Veterans' Affairs (O0979-R and RX001764) and the Penn Center for Musculoskeletal Disorders (P30 AR069619).

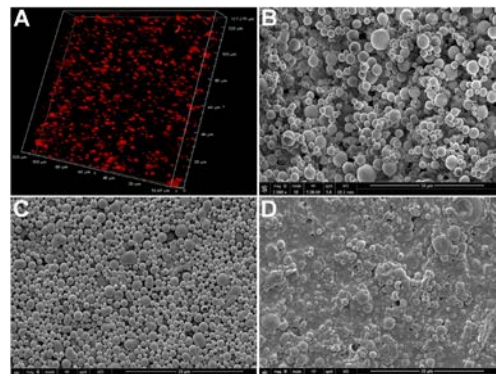


**Fig. 1** (A) 3D fluorescent image of Alexa-BSA microspheres (B) SEM image of Alexa-BSA microspheres, (C) SEM of MS after 60 days in PBS, and (D) SEM of MS after 60 days in serum (scale bar = 30  $\mu$ m,  $\times$ 2000).

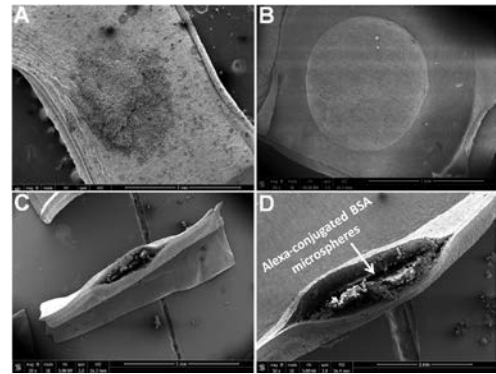


**Fig. 2** (A) Alexa-BSA-loaded microspheres on the PCL nanofiber scaffold. (B) Top view of sealed BiLDS. (C) Cross-view of BiLDS immediately after fabrication (scale bar = 3 mm). (D) High magnification image of BiLDS cross-section showing MS within BiLDS (scale bar = 1 mm).

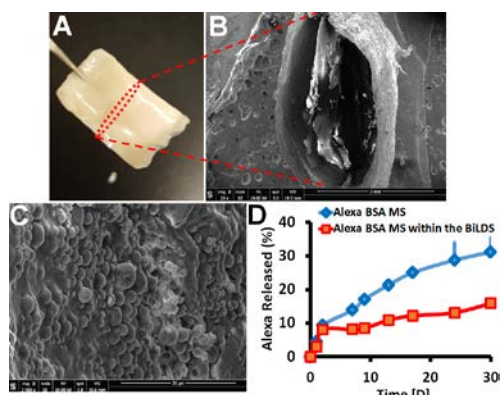


**Fig. 3** (A) Photo of BiLDS construct after 30 days in serum. (B) SEM image of cross-sectioned BiLDS after 30 days in serum (scale bar = 3 mm). (C) High magnification image of MS inside BiLDS after 30 days in serum (scale bar = 30  $\mu$ m). (D) Release profile from Alexa-BSA-loaded MS within the BiLDS compared to free Alexa-BSA-loaded MS over 30 days in serum demonstrating slower release with the BiLDS.

## Overexpression of Human Interleukin (IL)-8 in Mouse Intervertebral Disc Tissue to Model Patients with Back Pain

Tian Z, Enomoto-Iwamoto M, Xiu Y, Markova D, Anderson DG, Chen Y, Pacifici M, Huang J, Chen D and Zhang Y

**Introduction:** The etiology of axial back pain has been intensively investigated. We have previously shown that inflammatory mediators found in annulus fibrosus (AF) tissues from patients with discogenic back pain are likely produced by intervertebral disc (IVD) cells, and may play a key role in back pain. Among the chemokines identified, IL-8 is the most inducible in vitro: following IL-1 $\beta$  stimulation, IL-8 mRNA expression increased over 20,000 fold in NP and AF cells, while protein released increased by over 1,000 fold. To investigate the molecular mechanism of IL-8 signaling in the development of disc degeneration *in vivo*, we have generated a conditional IL-8 transgenic (Tg) mouse model. Our aim was to demonstrate that IVD cells produce interleukins that may, at least in part, be responsible for pain generation.

**Methods.** Tissue culture studies: IVDs from human spine segments (donor age range 21-75y), procured by the Gift of Hope Human Donor and Tissue Network of Illinois, were used with an approved IRB protocol. IVDs were dissected and AF and nucleus pulposus (NP) were separated. Cells were isolated by sequential enzymatic digestion of disc tissue and plated in 12- or 24-well plates. NP and AF cells were cultured in monolayer, with DMEM/F12 medium with 10% or 20% FBS, until they reached confluence. Cells were then serum-starved for 24 hours and subsequently stimulated with IL-1 $\beta$  (10 ng/mL) for 24 hours. IL-8 gene expression was analyzed using real-time PCR. IL-8 protein in the conditioned media was analyzed using enzyme-linked immunosorbent assay (ELISA). Cytokine array analysis: AF tissues were collected from patients undergoing spinal surgeries at Thomas Jefferson University, with an approved IRB protocol. Detailed discography scores and MRI grades were also recorded. Protein was extracted from the tissue and used to probe human cytokine array membranes. Cytokine profiles of painful and non-painful IVDs of the same MRI grades were compared. Transgenic mouse generation: pCALL2 plasmid was used to construct human IL-8 transgene. pCALL2-IL-8 mice were then bred with GDF5-Cre mouse (generously provided by David Kinsley, Stanford University) to conditionally express the transgene in cartilage and intervertebral disc tissues. Transgene expression was confirmed with PCR and IL-8 ELISA. Mouse behavioral testing was performed with Laboras (laboratory animal behavior observation, registration and analysis system, Metris®), a fully automatic and non-invasive system, to record more than 18 spontaneous behaviors.

**Results.** Following IL-1 $\beta$  stimulation, IL-8 gene expression increased 26,541 fold in NP cells (n=4, p=0.0083) and 22,429 fold in AF cells (n=4, p=0.0105). IL-8 protein released by the NP cells in response to IL-1 $\beta$  treatment also increased, from 31 pg/ml to 74,056 pg/ml, a 2,388 fold increase (n=4, p=0.0004). Similarly, IL-8 protein released by the AF cells increased, from 53 pg/ml to 94,540 pg/ml, a 1,784 fold increase (n=4, p=0.0055). IL-8 protein concentration in the AF tissues from patients with axial back pain is 1.8 fold of that in patients undergoing surgery for reasons other than back pain (e.g., scoliosis). But, due to the large individual variation, the difference is not statistically significant (p= 0.19). At 12 weeks of age, male Tg mice with IL-8 over-expression induced by breeding with GDF5-Cre mice showed a trend of decrease in ambulation and grooming (n=7, P=0.08), while female mouse behavior did not differ significantly.

**Conclusion.** We have shown that cultured IVD cells produce a massive amount of IL-8 in response to IL-1 $\beta$  stimulation, and generated a Tg mouse line to overexpress IL-8. We have preliminary evidence that male mice ambulate and groom less than negative controls. We will continue to characterize mouse behavior with a larger sample number, and will examine inflammatory cell infiltration and joint and spine tissue morphology.

## **Pathophysiological Role of ADAM8 (A Disintegrin And Metalloproteinase 8) in intervertebral disc degeneration**

Yejia Zhang, Miersalijiang Yasen, Robert Mauck, Maurizio Pacifici, Lachlan Smith, Motomi Enomoto-Iwamoto

### **INTRODUCTION:**

Chronic back pain related to intervertebral disc (IVD) degeneration is a significant problem, costing billions in the U.S. alone. Despite the staggering disease burden, there is no current effective treatment to retard IVD degeneration and reduce associated pain because the etiology of IVD degeneration remains unclear. IVD degeneration is characterized by increased extracellular matrix degradation and a variety of cellular responses. ADAM8 (A Disintegrin and Metalloproteinase 8) is a membrane-anchored proteinase and involved in cell-matrix and cell-cell interactions in physiological and pathological processes. Our results lead to the hypothesis that ADAM8 is a key enzyme in the degenerative cascade in IVD tissues and represents a major, novel and potentially far-reaching step ahead in understanding disease etiology.

### **METHODS:**

To examine expression and distribution of ADAM8 in IVD, degenerative annulus fibrosus and nucleus pulposus tissues were collected from patients undergoing surgery for back pain with appropriate institutional review board (IRB) approval. Degree of IVD degeneration was determined by MRI (grade V being the most degenerative). Distribution of ADAM8 in the IVD tissues was analyzed by immunostaining. ADAM8 and its specific proteolytic product, fibronectin fragments (FN-f (VRAA271), were quantified by Western blotting (n=3-4 each grade). To examine the role of ADAM8 in IVD degeneration, we performed gain-of-function experiments in mice. Mature human ADAM8 ectodomain was generated in HEK293T cell line (BioZyme, Apex, NC), labeled with the infrared dye (IRDye, Li-Cor Biosciences) and injected into the wild type mouse tail IVD. The ADAM8 or vehicle-injected IVD tissue was harvested 1-4 weeks after injection and subjected to histological inspection and immunostaining with an antibody to VDPIEN (neoepitope of cleaved aggrecan, a generous gift from Dr. J. Mort). We have also performed loss-of-function experiments in mice. The ADAM8 gene-inactivation mutant mice that harbor a point mutation, replacing the Glutamic acid at position 330 with a Glutamine (ADAM8E330Q/E330Q mice, generously provided by Dr. Anne Marie Malfait) was used to examine requirement of ADAM8 for IVD. We dissected IVDs from wild type and the ADAM8E330Q/E330Q mice at 9 months of age and examined the neoepitope of the fibronectin fragment (FN-f) (VRAA271) by Western blotting. Aggrecan cleavage was examined by immunostaining.

**Design:** To examine expression and distribution of ADAM8 in IVD, degenerative annulus fibrosus and nucleus pulposus tissues were collected from patients undergoing surgery for back pain with appropriate institutional review board approval. Degree of IVD degeneration was determined by MRI. Distribution of ADAM8 in the IVD tissues was analyzed by immunostaining. ADAM8 and its specific proteolytic product, fibronectin fragments (FN-f (VRAA271), were quantified by Western blotting. To examine the role of ADAM8 in IVD degeneration, we performed gain-of-function experiments in mice. Mature human ADAM8 ectodomain was labeled with the infrared dye and injected into the wild type mouse tail IVD. The ADAM8 or vehicle-injected IVD tissue was harvested 1-4 weeks after injection and subjected to histological inspection and immunostaining with an antibody to VDPIEN (neoepitope of cleaved aggrecan). We have also performed loss-of-function experiments in mice. The ADAM8 gene-inactivation mutant mice that harbor a point mutation, replacing the Glutamic acid at position 330 with a Glutamine (ADAM8E330Q/E330Q mice) was used to examine requirement of ADAM8 for IVD. We dissected IVDs from wild type and the ADAM8E330Q/E330Q mice at 9 months of age and examined the neoepitope of the fibronectin fragment (FN-f) (VRAA271) by Western blotting. Aggrecan cleavage was examined by immunostaining.

### **RESULTS:**

Immunostaining demonstrated that ADAM8 was expressed in human IVD tissues. Both ADAM8 and its proteolytic products (fibronectin fragments) were increased with IVD degeneration. These findings establish the clinical significance of ADAM8 in IVD degeneration. We observed that disorganized chondrocyte proliferation in IVDs was much more evident in the ADAM8-injected IVDs than in the PBS-injected IVDs in wild type mice. ADAM8-injected IVDs showed higher immunoreactivity to the antibody against the neoepitope of cleaved aggrecan, compared with the PBS-injected IVDs.

**Conclusion.** These findings suggest that the ADAM8 proteolytic domain stimulates IVD degeneration. Inhibition of ADAM8 may be a valid therapeutic option for IVD degeneration and related back pain.

## Stem Cell Seeded Injectable Hydrogels for Intervertebral Disc Regeneration in a Preclinical Animal Model

Sarah E. Gullbrand<sup>1,2</sup>, Thomas P. Schaer<sup>1</sup>, Justin R. Bendigo<sup>1,2</sup>, Prateek Agarwal<sup>1</sup>, Zosia Zawacki<sup>1</sup>, George R. Dodge<sup>1,2</sup>, Edward J. Vresilovic<sup>3</sup>, Dawn M. Elliott<sup>4</sup>, Robert L. Mauck<sup>1,2</sup>, Neil R. Malhotra<sup>1</sup>, Lachlan J. Smith<sup>1,2</sup>

<sup>1</sup>University of Pennsylvania, Philadelphia, PA, <sup>2</sup>Philadelphia VA Medical Center, Philadelphia, PA, <sup>3</sup>Penn State Hershey Bone and Joint Institute, Pennsylvania State University, Hershey, PA, <sup>4</sup>University of Delaware, Newark, DE

**Disclosures:** None

**Introduction:** Intervertebral disc degeneration is a progressive cascade that leads to structural and mechanical failure of the disc, and is frequently associated with low back pain. For early or mid-stage disc degeneration, there is considerable interest in employing biologic therapeutics – including stem cell, hydrogel, and/or growth factor injections – to stimulate tissue regeneration.<sup>1,2</sup> We previously developed a large animal model of disc degeneration in the goat lumbar spine, in which moderate degeneration is achieved 12 weeks following intradiscal injection of 1U chondroitinase ABC (ChABC).<sup>3</sup> Our group has also shown that a triple interpenetrating network hydrogel composed of dextran, chitosan and teleostean (DCT) mimics nucleus pulposus (NP) mechanical properties and acts as an effective carrier for mesenchymal stem cells (MSCs).<sup>4,5</sup> The purpose of this study was to undertake a clinically relevant investigation to establish the feasibility and efficacy of a combined stem cell and DCT hydrogel intradiscal injection to regenerate the disc and restore mechanical properties using a large animal model.

**Methods:** *Ex Vivo Studies:* Goat lumbar spine motion segments from a previous animal cohort were utilized to assess the capacity of the DCT hydrogel to normalize disc mechanics. *Ex vivo* motion segments (n=5) that had previously been degenerated via 1U ChABC *in vivo* for 12 weeks were mechanically tested in tension-compression (20 cycles, -230N to +115N) prior to, and then following, intradiscal injection of the DCT hydrogel. Force and optical displacement data were analyzed in MATLAB to quantify compressive and neutral zone (NZ) modulus, NZ range of motion (ROM) and total ROM;<sup>3</sup> differences between groups were assessed via one-way ANOVA and Tukey's post-hoc tests. *In Vivo Studies:* Surgery was performed on 3 male large frame goats to induce disc degeneration at four levels of the lumbar spine (n=12 discs total) via intradiscal injection of 1U ChABC.<sup>3</sup> Following progressive degeneration for 12 weeks, a second surgery was performed to deliver the combined cell and hydrogel therapeutic. Four therapeutic groups were randomized to the 12 degenerated lumbar discs: DCT hydrogel alone, allogeneic MSCs + hydrogel, allogeneic MSCs preconditioned in hypoxic culture (2% O<sub>2</sub> for 1 week in monolayer culture) + hydrogel, allogeneic NP cells + hydrogel. Cells were suspended in the hydrogel at a density of 10 million cells/mL, and injected into the disc via a 22G needle (200 - 600μL gel per level). The hydrogel was labelled with radiopaque zirconia nanoparticles (30 wt%).<sup>6</sup> Lateral lumbar spine radiographs were taken immediately before and after each surgical procedure, as well as every 4 weeks during degeneration, and weekly following therapeutic delivery. Disc height index (DHI) was quantified and normalized to pre-operative values. Two weeks following therapeutic delivery, animals were euthanized and the lumbar spines harvested. MRI scans were obtained at 3T for quantitative T2 and T1ρ mapping. DHI and MRI data were analyzed via two-way ANOVA. Following MRI, high resolution μCT was performed for each motion segment to assess the presence and distribution of the injected hydrogel in the disc. Samples were then fixed, decalcified, processed through paraffin and sectioned for histological analyses.

**Results:** *Ex Vivo Studies:* ROM was significantly increased and NZ modulus significantly decreased in degenerative discs compared to intact, healthy discs. Following injection of the DCT hydrogel, mechanical properties of the degenerated motion segments were not significantly different from controls (Figure 1). *In Vivo Studies:* The radiopaque gel was easily detectable in the disc space on post-op plain radiographs (Figure 2A). μCT analysis illustrated that the hydrogel was well-distributed throughout the disc, was present in both the NP and in between layers of the annulus fibrosus, and had not extruded from the disc (Figure 2B). Two-way ANOVA indicated no significant contribution of cell treatment to MRI or DHI outcome measures, thus, data were pooled for analysis. 12 weeks following delivery of 1U ChABC, disc height was reduced a mean 22.7% compared to pre-operative values, consistent with our previous data in this model. A partial recovery of DHI occurred immediately following cell and hydrogel delivery which was maintained at 89.9% of pre-operative DHI 2 weeks following treatment (Figure 3A). The mean NP MRI T2 and T1ρ values of cell and hydrogel treated discs were not different from healthy control discs, and were significantly higher than 1U ChABC degenerated, untreated discs at 12 weeks (data obtained from a prior animal cohort) (Figure 3B). Histological analyses of disc structure and composition, and the respective contributions of each cell therapy to regeneration, are ongoing.

**Discussion:** Results from this study illustrate the feasibility of stem cell and hydrogel delivery as a regenerative therapeutic approach using a pre-clinical animal model. These data illustrate that the hydrogel remains within the disc space over a 2 week period following delivery, and suggests that the DCT hydrogel and/or stem cell injections may acutely restore disc height and MRI signal of degenerate discs to near control levels. When tested *ex vivo*, the DCT hydrogel restored whole disc mechanics to within the normal range, consistent with our prior studies on human cadaveric discs following partial nucleotomy.<sup>7</sup> Ongoing work is assessing cell distribution and survival in the disc space, including the potential benefits of hypoxic MSC conditioning. Future work will explore the regenerative potential of combined cell and hydrogel therapies over longer durations in this preclinical animal model of disc degeneration.

**Significance:** Using a clinically relevant large animal model, this study illustrates the potential of stem cell-seeded injectable hydrogels as a regenerative therapeutic approach for the treatment of mild to moderate disc degeneration.

**References:** [1] Sakai+2015, [2] Mizuno+2006 [3] Gullbrand+2016 (in press) [4] Smith+2014 [5] Malhotra+2012 [6] Martin+2015 [7] Showalter+2014

**Acknowledgments:** This study was supported by the Department of Veteran's Affairs and the Penn Center for Musculoskeletal Disorders (P30 AR069619). The authors acknowledge Dr Weilam Chen for providing hydrogel components.

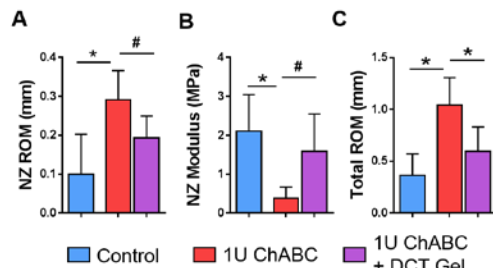


**Figure 1.** NZ ROM (A), NZ Modulus (B), and total ROM (C) in degenerative discs before and after hydrogel injection compared to control. [\*= $p<0.05$ , #= $p<0.1$ ].

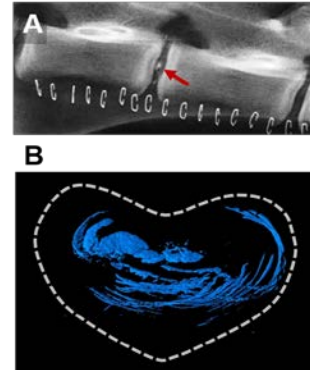


**Figure 2.** DCT hydrogel visualization via x-ray (A) and a 3D axial μCT reconstruction (B).

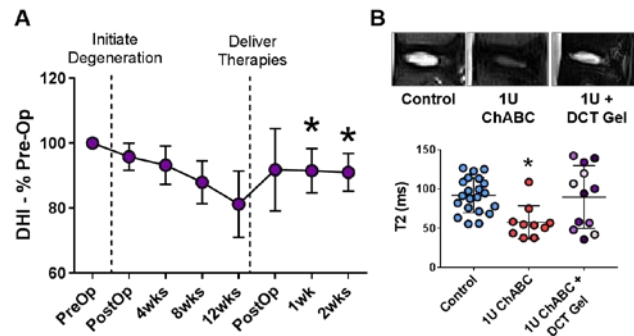


**Figure 3.** Average DHI for all treated levels over time [\* =  $p<0.05$  compared to 12 weeks] (A). Representative T2 MRI images from each group with quantitative T2 measurements [\* =  $p<0.05$  compared control and 1U + DCT gel injected] (B). Different color shades in the 1U + DCT gel group represent different cell treatments.

# **Neural Progenitor-like Cells Induced from Human Gingiva-derived Mesenchymal Stem Cells Promote Rat Sciatic Nerve Regeneration via Regulating Myelination of Schwann Cells**

Qunzhou Zhang<sup>a</sup>, Phuong Nguyen<sup>b</sup>, Qilin Xu<sup>a</sup>, Sumin Lee<sup>a</sup>, and Anh D. Le<sup>a, c\*</sup>

<sup>a</sup>*Department of Oral and Maxillofacial Surgery and Pharmacology, University of Pennsylvania School of Dental Medicine, Philadelphia, Pennsylvania*

<sup>b</sup>*Division of Plastic and Reconstructive Surgery, University of Pennsylvania Perelman School of Medicine, Philadelphia, Pennsylvania*

<sup>c</sup>*Department of Oral & Maxillofacial Surgery, Penn Medicine Hospital of the University of Pennsylvania, Philadelphia, Pennsylvania*

**Abstract:** Regeneration of peripheral nerve injury (PNI) remains a major clinical challenge. Fully functional recovery of injured nerve depends on new axonal outgrowth, myelination, and correct reinnervation of the end-organ target. Currently, autologous nerve grafts remain the gold standard for repairing injured nerves with a large gap, but have some major shortcomings, including the donor site morbidity, limited availability and mismatch of donor nerves. Stem cell-based therapy is emerging as a novel approach for peripheral nerve regeneration. Neural stem or progenitor cells (NSCs) are considered an ideal candidate seed cell source for nerve regeneration, but the difficulty to obtain enough number of NSCs has significantly impeded their potential application in clinic. Recently, mesenchymal stem cells (MSCs) are considered as potential candidate for peripheral nerve regeneration; however, the underlying mechanisms remain elusive. Here, we showed that human gingiva-derived mesenchymal stem cells (GMSCs) could be directly reprogrammed into multipotent neural progenitor-like cells (iNPCs) under defined culture conditions without the introduction of exogenous genes. Using a crush-injury model of rat sciatic nerve, we found that GMSC-derived NPCs transplanted to the injury site were capable of differentiating into both neuronal and Schwann cells, while parental GMSCs could only differentiate into neuronal cells. Meanwhile, iNPCs, in comparison to GMSCs, displayed enhanced therapeutic effects on axonal regeneration at both the injury site and the distal segment of the injured sciatic nerve. Mechanistically, transplantation of GMSCs, especially iNPCs, significantly attenuated injury-triggered increase in the expression of c-Jun, a transcription factor that functions as a major negative regulator of myelination and played a central role in dedifferentiation/reprogramming of Schwann cells into progenitor-like state. Meanwhile, transplantation of GMSCs and iNPCs consistently increased the expression of Krox-20/EGR2, a transcription factor that governed the expression of myelin proteins and facilitated myelination. These data suggest that transplantation of GMSCs and iNPCs facilitates peripheral nerve repair/regeneration possibly by promoting remyelination of Schwann cells mediated via the regulation of the antagonistic myelination regulators, c-Jun and Krox-20/EGR2. These findings support that human GMSCs represent a promising and easily accessible cell source for stem cell-based therapy of peripheral nerve injury.

**Key words:** Peripheral Nerve Regeneration; Gingiva-derived Mesenchymal Stem Cell; Induced Neural Progenitor Cells; Schwann Cells; Myelination

*This work was supported by National Institute of Health Research Grant, R01DE 019932, Oral and Maxillofacial Surgery Foundation (OMSF) Research Grant, OsteoScience Foundation, and the Schoenleber funding support.*

## **Considering the patient rotation with respect to the X-ray scanner improves the prediction of the 3D sagittal spinal measurements from radiographs**

**Xochitl Mellor, B.S. and Saba Pasha, Ph.D., M.S.**

**Purpose:** To estimate the 3D thoracic kyphosis and lumbar lordosis from 2D biplanar radiographical measurements.

**Methods:** 45 right thoracic AIS patients received biplanar radiographs. Using a dedicated software, 3D reconstructions of the spine were generated to provide 3D measurements of T1-T12, T4-T12 kyphosis, L1-S1 lordosis, and pelvic rotation. Using the same radiographs, 2D T1-T12, T4-T12 kyphosis, L1-S1 lordosis, and thoracic and lumbar Cobb angles were manually measured. Pelvic axial rotation was measured using the frontal and sagittal distances between the two femoral heads on the X-ray images. A multiple linear regression model was used to predict 3D kyphosis/lordosis from 2D kyphosis/lordosis, 2D frontal curve measurements of the thoracic and lumbar, and 2D pelvic rotation.

**Results:** 2D and 3D pelvic rotation were significantly correlated ( $r = 0.84, p < 0.05$ ). 3D T1-T12 kyphosis was predicted from 2D T1-T12 kyphosis, 2D pelvic rotation, and 2D thoracic Cobb ( $R^2 = 0.83, p < 0.05$ ). In the model wherein pelvic rotation was not included, 2D thoracic kyphosis and main thoracic Cobb significantly predicted 3D kyphosis ( $R^2 = 0.76, p < 0.05$ ). The 3D L1-S1 lordosis was significantly predicted by the 2D L1-S1 lordosis and 2D pelvic rotation ( $R^2 = 0.90, p < 0.05$ ). In the model without pelvic rotation, only 2D lordosis significantly predicted 3D lordosis ( $R^2 = 0.86, p < 0.05$ ). The mean absolute error was  $4.1^\circ$  between the predicted T1-T12 kyphosis and 3D kyphosis and  $3.5^\circ$  between the predicted lordosis and 3D lordosis. The segmental sagittal measurements of T4-T12 kyphosis was only predicted by 2D T4-T12 kyphosis ( $R^2 = 0.67, p < 0.05$ ). The corresponding measurements of the frontal thoracic Cobb and pelvic rotation did not appear significant  $p > 0.05$ .

**Conclusion:** The influence of pelvic rotation should be considered when evaluating a 3D deformity of the spine in scoliosis. Considering the pelvic rotation correction can significantly impact the prediction of the 3D kyphosis and lordosis measurements from the 2D radiographic measurements.

**Level of Evidence:** IV

## **Cardiomyocyte-specific Telomere Shortening is a Distinct Signature of Heart Failure in Human**

<sup>1</sup>Maryam Sharifi-Sanjani, <sup>1</sup>Nocholas Oyster, <sup>2</sup>Kenneth C. Bedi, <sup>2</sup>Kenneth B. Margulies, <sup>1,2,3</sup>Foteini Mourkioti

<sup>1</sup>Department of Orthopaedic Surgery, <sup>2</sup>Cardiovascular Institute University of Pennsylvania Perelman School of Medicine, <sup>3</sup>Department of Cell and Developmental Biology, Perelman School of Medicine, University of Pennsylvania

**Background:** Hypertrophic cardiomyopathy (HCM) is a clinically heterogeneous disorder with serious adverse outcomes. Despite efforts, current treatments entail only supportive strategies as detailed mechanisms behind HCM etiology are not fully uncovered. Extensive studies are carried out to link phenotype with genotype in patients. Our team recently recognized the role of distal ends of chromosomes, called telomeres, in unveiling cardiac disease phenotype. In proliferative cells, telomere shortening occurs with each cell division. Importantly, however, the role of telomere attrition in the setting of heart failure and specifically in human adult cardiomyocytes, as post-mitotic cells, is equivocal.

**Methods:** We prospectively studied cardiac tissues from healthy individuals (n=27) and HCM patients (n=37) by optimizing telomere quantitative fluorescence in situ hybridization (Q-FISH), a highly sensitive method with single-cell resolution.

**Results:** Our results demonstrate that patients with HCM have shorter telomeres compared with healthy individuals. In fact, the observed telomere shortening is specific to cardiomyocytes and not to other cell types within the same cardiac tissues, arguing against universal telomere shortening. Interestingly, longest cardiomyocyte telomere lengths were observed in patients with preserved ejection fraction and sustained hypertrophy, illustrating a strong correlation between telomere length and cardiac function. We further found that, in contrast to other reported cell types, no telomere shortening was evident with age in cardiomyocytes of healthy hearts. However, under disease condition, telomere attrition occurred regardless of age suggesting that the cardiac telomere defect is not age-dependent and it solely occurs under the disease state. We further demonstrate that females have longer telomeres regardless of the presence or absence of disease, which may contribute to the well-known lower prevalence of females with HCM.

**Conclusion:** Our data provide the first clear evidence that cardiomyocyte-specific telomere shortening is a hallmark of human heart failure and highlights its significance in aging and gender and suggest possible new therapeutic avenues important in cardiomyocyte function.

## **Genetic Analysis of Osteochondritis Dissecans**

Eileen P. Storey BA, Hakon Hakonarson, MD, PhD, Kevin G. Shea, MD, James L. Carey, MD,  
Theodore J. Ganley, MD

**Background/Purpose:** While repetitive microtrauma and athletic overuse patterns are most commonly associated with osteochondritis dissecans (OCD), emerging research has identified a potential underlying genetic predisposition to OCD. The purpose of this study is to review the results of a preliminary investigation of genetics and OCD at The Children's Hospital of Philadelphia (CHOP) and to lay out the plans for extending this investigation through the multicenter Research in Osteochondritis Dissecans of the Knee (ROCK) prospective cohort study.

**Methods:** In collaboration with the Center for Applied Genomics at CHOP, we conducted a prospective callback study on OCD familial inheritance patterns and a genome-wide association study (GWAS) to uncover candidate loci associated with OCD.

**Results:** In the cohort of 103 pediatric patients that responded to the OCD family history survey, 14% had a positive family history of OCD, which significantly exceeded the previously reported prevalence of OCD in the general population (0.01 – 4%). There was not a significant difference in rates of positive family history in patients with phenotypically potent lesions (bilateral and multiple) compared to those with less potent lesions (conservative and unilateral). GWAS analysis of 209 OCD case patients and 1855 population-matched controls identified multiple SNPs (35) at several loci with evidence of suggestive association with OCD ( $p < 5.0 \times 10^{-5}$ ).

**Conclusion:** The results of the preliminary investigation at CHOP are promising and encourage further research to determine the underlying genetic etiology of OCD. Large-scale, multicenter efforts are warranted to obtain sufficient sample sizes to conduct high-throughput genomic sequencing and to match genotypic and comprehensive phenotypic information.

**Future Directions:** Collect samples from OCD patients enrolled in the multicenter ROCK prospective cohort study to obtain enough cell lines to meta-analyze the GWAS data and identify common variants associated with OCD with effect sizes of 1.4 or greater. In addition, whole exome sequencing of multi-case families should be conducted to uncover private mutations, including copy number variants (CNVs), contributing to familial OCD.

## **Regulation of BMP Receptor Dynamics and Signaling by Cell Surface Heparan Sulfate Proteoglycans**

Christina Mundy, Paul C. Billings and Maurizio Pacifici

Division of Orthopaedic Surgery, The Children's Hospital of Philadelphia  
Philadelphia, PA

The bone morphogenetic protein (BMP) signaling pathway has critical roles in many processes including skeletal development and growth, and its perturbations can lead to diverse pathologies. A case in point is Hereditary Multiple Exostoses (HME), a pediatric musculoskeletal disorder caused by loss-of-function mutations in the heparan sulfate (HS)-synthesizing enzymes EXT1 and EXT2. HME is characterized by benign cartilaginous tumors (exostoses) that form next to the growth plates of long bones, vertebrae and ribs, causing multiple health problems. The HS chains, and the proteoglycans of which they are part (HSPGs), regulate signaling by key HS-binding proteins including hedgehogs and FGFs, but their roles in BMP signaling remain unclear. Previously we showed that interference with HS function by genetic or pharmacological means rapidly increases canonical BMP signaling, suggesting that HS normally limits BMP signaling by restricting ligand availability, BMP receptor (BMPR) dynamics and/or BMPR-ligand interactions. To analyze such possibilities, we transfected cell lines with constructs encoding Snap-BMPRII and/or Clip-BMPRIa fusion proteins. Co-transfected cells rapidly responded to rhBMP-2 treatment with major increases in pSMAD1/5/8 and p-P38 levels and interestingly, a similar response was observed following treatment with heparitinase or Surfen, an HS antagonist. To assess BMPR dynamics, we carried out fluorescence recovery after photobleaching (FRAP) assays and found that BMPRII mobility decreased significantly after treatment with rhBMP-2 or Surfen, suggesting the receptors had transitioned to lipid rafts and/or had undergone oligomerization. In contrast, we found that BMPRIa mobility was not affected after treatment with rhBMP-2 or Surfen, suggesting that type I receptors are confined to lipid rafts. Ongoing studies will verify the location of these receptors along the cell membrane and determine whether BMP receptors directly interact with HSPGs. Together, our data indicate that cell surface HSPGs are important regulators of both BMP signaling and BMPR dynamics. The HS deficiency in HME may alter these important basic physiologic mechanisms, causing unruly increases in local BMP signaling and promoting exostoses formation.

## **Regulation of cell fate decisions in heterotopic ossification**

Authors: Niambi Brewer, John Fong, Girish Ramaswamy, and Eileen Shore

**Abstract:** Progressive osseous heteroplasia (POH) is a disorder of extraskeletal bone formation, or heterotopic ossification (HO), in which bone forms within the skin, subcutaneous fat and muscle. POH first presents in childhood, with HO formation in the skin and subcutaneous fat that then progresses to deeper tissues resulting in severely impaired movement and growth retardation. POH is associated with paternally inherited, inactivating mutations of the *Gnas* locus. The major product of this locus, *Gnas*, encodes the alpha stimulatory subunit of the G protein complex, which transmits signals from G-protein coupled receptors (GPCRs) to activate cyclic-AMP (cAMP). Formation of bone within fat tissue in POH suggests that stem cells within adipose tissue are misdirected to an osteogenic cell fate through *Gnas* inactivation. Our lab has shown that decreased *Gnas* expression in adipose derived stromal cells (AdSCs) leads to an increased osteogenic potential and a decreased adipogenic potential *in vitro*, as well as a reduction in subcutaneous adipose tissue which is replaced by fibrotic-like tissue and HO *in vivo*. Cell fate decision is influenced in part by the stiffness of the surrounding extracellular matrix (ECM). Cells sense and interpret the physical cues exerted by ECM components through a process known as mechanotransduction. GPCR signaling can also regulate key mechanotransduction signaling factors, RhoA and transcription co-activators YAP/TAZ. This work seeks to investigate the influence of inactivation of *Gnas* on mechanotransduction in AdSCs and the ECM composition of adipose tissue. *I hypothesize that dysregulation of the Gnas locus leads to impaired mechanotransduction and maintenance of the adipose tissue microenvironment.* While POH is a rare disorder, HO is a common physiological response to severe tissue trauma such as combat blast injuries, forceful trauma and hip replacements. The investigation of rare disorders provides insight to the aberrant mechanisms that cause HO formation and can lead to identification of targets for pharmacological intervention in both genetic and non-genetic forms of HO. Additionally insights gained from this study will provide a better understanding of the process of cell fate decision within adult tissue.

## Stem Cell Regulation in Muscular Dystrophy

Elisia Tichy<sup>1</sup>, Nicholas Oyster<sup>1</sup> and Foteini Mourkioti<sup>1</sup>

<sup>1</sup>Department of Orthopaedic Surgery, Perelman School of Medicine, University of Pennsylvania,  
Philadelphia, PA 19104, USA.

**INTRODUCTION:** Skeletal muscle diseases or myopathies result in loss of muscle mass, degeneration and functional weakness. Duchenne muscular dystrophy (DMD) is the most common recessive chronic muscle disorder that results from lack of dystrophin, a cytoskeletal protein that is essential for the stability of the skeletal muscle membrane. A conundrum has been that dystrophy knockout mice (*mdx*), which share the same dystrophin deficiency as DMD patients, exhibit only mild muscle weakness in contrast to patients. We reasoned that the ~8-fold difference in telomere length between mice and humans could account for this discrepancy and developed a new *mdx* mouse model with shortened telomeres (*mdx/mTR*). This dystrophic model exhibits all the pathological hallmarks of human DMD and offers a useful tool to unravel the molecular mechanisms associated with injury in dystrophic muscles.

**METHODS:** In the current study, we use fluorescence-activated cell sorting (FACS) to prospectively isolate muscle stem cells to test whether during the progression of the dystrophic phenotype; the increased activity of a pleiotropic transcription factor contributes to the rapid muscle stem cell exhaustion and subsequent skeletal muscle defects. By prospectively isolating MuSCs from conditionally knockout and overexpressing animals and we test their ability to enhance tissue regeneration in dystrophic muscles.

**RESULTS:** Our *in vitro* and *in vivo* experiments demonstrated that muscle stem cell (MuSC) exhaustion and telomere shortening is responsible for the failure to sustain the damage-repair cycle during regeneration. To identify molecular defects in dystrophic MuSCs that could be targeted therapeutically to enhance their function, we isolated MuSCs and assayed several internal signaling pathways by flow cytometry. Our analysis showed that MuSCs from dystrophic mice exhibited increased p65 relative to those from control mice. To test whether mouse findings are relevant to DMD disease, we analyzed human MuSCs from healthy and DMD young patients and found a significant reduction (~40%) of DMD MuSCs in their telomere length compared to aged-matched controls. These data provide the first reported evidence, that similar to our mouse data, telomere shortening in MuSCs is also an unequivocal defect in DMD patients. To examine whether the degree of NF-κB involvement in DMD patients, we analyzed MuSCs derived from human patients and found increased p65 levels in diseased cells compared to the controls. To investigate the therapeutic potential of NF- κB inhibition in muscle stem cells, we performed transplantation experiments into dystrophic muscles and showed that MuSC-specific NF-κB inhibition improves regeneration in diseased muscles. All together, our studies suggest that NF-κB activation is a direct potential molecular pathway affected in mouse MuSCs during the advancement of DMD that can be therapeutically manipulated for better management of the disease.

**DISCUSSION:** In addition to uncovering the precise molecular signaling events in dystrophic muscle stem cells, our results indicate a stem cell therapy for better management of muscular dystrophies. By further analyzing the transcriptional profile of NF-κB inhibition in muscle stem cells, we have the potential to identify new muscle-specific targets for the treatment of DMD.

**SIGNIFICANCE:** The identification of specific signaling pathways that affect MuSC function in relation to their telomere length may have therapeutic value for treating muscular dystrophies. Moreover, our results open the door for broader applications in other muscle diseases with stem cell exhaustion, such as chronic injury in aging muscles.

## Osteochondroma formation in long bones and ribs is therapeutically blocked by treatment with a BMP antagonist in mice

Sayantani Sinha, Christina Mundy, Federica Sgariglia, Paul Billings, Eiki Koyama and Maurizio Pacifici

Division of Orthopaedic Surgery, The Children's Hospital of Philadelphia

Osteochondromas are benign cartilaginous tumors that characterize the rare musculoskeletal pediatric disorder Hereditary Multiple Exostoses (HME). These tumors form exclusively within perichondrium flanking the growth plates of long bones, ribs and other elements. Because of their size, large number and location, the osteochondromas can cause severe problems such as skeletal deformities, chronic pain and early onset osteoarthritis. Surgery is currently used to remove the most symptomatic osteochondromas, but because of their large number and difficult locations, most osteochondromas are left in place, causing life-long problems. Indeed, in 2-5% of patients, osteochondromas can transform into malignant and life-threatening chondrosarcoma. Thus, there is a great need to find more definitive therapeutic remedies. HME is caused by loss-of-function mutations in EXT1 or EXT2 that are Golgi-resident co-polymerases responsible for heparan sulfate (HS) synthesis. The HS chains are key components of cell-surface proteoglycans that interact with, and control the function of, essential signaling proteins such as bone-morphogenetic proteins (BMPs). In previous studies, we showed that conditional *Ext1* mouse mutants developed stereotypic osteochondromas and tumor formation was preceded by ectopic BMP signaling within perichondrium. Since BMP signaling has strong pro-chondrogenic activity, it is possible that ectopic signaling was a key causative factor in osteochondroma formation. Here, we asked whether it could also represent a therapeutic target. We created *Ext1<sup>ff</sup>;Col2CreER* mice and injected them with tamoxifen once at 5 weeks of age. In untreated controls, onset of osteochondroma formation was already appreciable by 2 weeks and included clear changes in arrangement and morphology of progenitor cells along the chondro-perichondrial border. By 4 to 5 weeks, large and stereotypic osteochondromas had formed in long bones and ribs. Companion mice were given daily IP doses of the type I BMP receptor inhibitor LDN-193189 starting on day 1 after tamoxifen injection, and treatment continued up to 6 to 8 weeks. Anatomical, histomorphometric and CT analyses showed that osteochondroma formation was markedly reduced by drug treatment. Bone volume quantification showed that the reduction reached nearly 65%. In vitro data with primary limb bud chondrogenic progenitors in micromass culture showed that LDN-193189 treatment dramatically reduced pSMAD1/5/8 phosphorylation and chondrogenesis, accounting for its strong therapeutic effects in mice. To our knowledge this study is the first to describe an effective treatment against osteochondroma formation in a mouse model of HME, a serious and often debilitating disease.

## Utility of Near Infrared Spectroscopy for Bone Quality Assessment

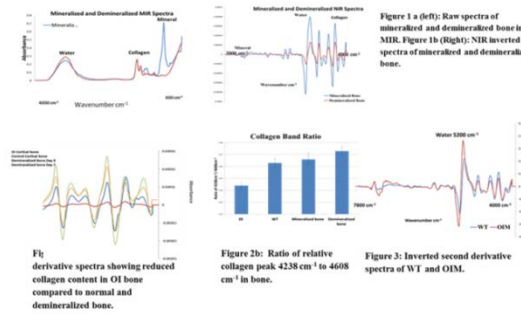
Ramyasri Ailavajhala<sup>1</sup>, Rutvin Kyada<sup>1</sup>, Heejin Yang<sup>1</sup>, Erin Carter<sup>2</sup>, Adele Boskey<sup>2</sup>, Cathleen Raggio<sup>2</sup>, Nancy Pleshko<sup>1</sup>

<sup>1</sup>Department of Bioengineering, Temple University, Philadelphia, PA

<sup>2</sup>Department of Orthopaedics Hospital for Special Surgery New York, NY

DISCLOSURES: Ramyasri Ailavajhala(N), Rutvin Kyada(N), Heejin Yang(N), Erin Carter(N), Adele Boskey (N), Cathleen Raggio (N), Nancy Pleshko (N)

**INTRODUCTION:** Bone fracture risk increases with age, disease states and therapeutic use. Although changes in bone mineral density are a common contributor to increase fracture risk, other factors such as bone geometry, mineral crystallinity, collagen and water content also contribute. To fully understand the factors that contribute to bone fragility, appropriate methods of analysis of bone composition and structure are required. In clinical and preclinical studies, magnetic resonance imaging (MRI) has been used to evaluate water in bone (1); however, this modality has limited spatial resolution and validation studies are still in progress. Near-infrared spectroscopy (NIRS) is a nondestructive technique that requires minimal or no sample preparation to evaluate molecular components of bone. NIRS uses higher frequency (4000-12000 cm<sup>-1</sup>) radiation than Mid IR (450-4000 cm<sup>-1</sup>), permitting a much greater depth of penetration (millimeters to centimeters). The NIRS absorption bands arise from molecular vibrations, and are overtones and combinations of the mid-IR fundamental vibrations of C-H, C-O, O-H and N-H bonds. Recently, NIRS has been shown to differentiate between bound and free water in intact cartilage (2). Although, this modality is not currently applicable for clinical studies, NIRS analyses is well suited to evaluate bone from preclinical studies. Spectral data can be acquired through the full tissue depth at 50 microns pixel resolution, and molecular information related to collagen and water , and possibly mineral, can be obtained. Here we demonstrate the utility NIRS for evaluation of bone quality parameters. Bone from *oim/oim* (OIM) and +/- (WT) mice were investigated for differences in water and collagen. OIM mice model moderate to severe osteogenesis imperfecta (OI), and their bone fragility phenotype results from a mutation in type 1 collagen that causes production of a type 1 collagen  $\alpha 1(I)$  homotrimer (3). **METHODS:** Tissues: Mineralized and demineralized bone were used as standards. Bovine tibias (n=2) were collected from 2 month old animals (Research 87, Boylston, MA). Tibias were cut by into segments with a bone band saw (Mar-Med Inc, Strongsville, OH), and ultrasonicated in 1% tergazyme solution for 2 hours at 38°C to remove bone marrow. Marrow free bones were sliced into 400  $\mu$ m thick, cross-sectioned slices using a diamond wafering saw (Buehler Isomat 1000, Lake bluff, IL). The slices were broken into small pieces about 4 mm x 4 mm and pulverized into bone powder by a SPEX SamplePrep Freezer/Mills (SPEX Mill 6770, Metuchen, NJ). One gram of bovine powder was added to 40 ml of 10 mM EDTA-Tris solution and stirred together for one week. Daily EDTA was replaced with new solution and the demineralization process was monitored for one week using both Mid-IR and NIR spectroscopy. Mouse bone: Humeri from OIM and WT mice (n=2 each, female 6.5 months old), from an IACUC approved study performed at Hospital for Special Surgery were investigated. Humeri were kept frozen in saline soaked gauze until data were obtained. Pieces of cortical bone were ~ 3 by 5 mm were dissected and marrow removed by centrifugation for 1 min at 10,000g followed by ultra-sonication at 38°C for 10 mins. Spectral data collection and processing for mineralized and demineralized bone: Mid-IR spectra of the mineralized bone were collected daily for one week using a Perkin Elmer 100 spectrometer (Shelton, CT) at 8 cm<sup>-1</sup> resolution and 32 co-added scans. The NIR data were collected using a Perkin Elmer Spotlight 400 imaging spectrometer at 4 cm<sup>-1</sup> resolution and 256 co-added scans. Spectra for both Mid-IR and NIRS were processed using Unscrambler (Camo, Norway) and peak height ratios were determined with Isys 5.0 software (Malvern Instruments, Columbia, MD). OIM and WT mice humeri spectral data and processing: The residual fat peak at 5792 cm<sup>-1</sup> was spectrally subtracted from OIM and WT bone from pure bone marrow spectra. Second derivative (Savitzky Golay, 57 points of smoothing) was applied to fat removed spectra in order to resolve peaks from raw spectra. **RESULTS:** In contrast to Mid-IR spectra where large difference between mineralized and demineralized bone are obvious in the phosphate region (figure 1a). NIR spectra of mineralized and demineralized of bone are very similar, especially with respect to frequencies of absorbances (figure 1b). Some subtle differences are present in the 7000 cm<sup>-1</sup> region, but the most prominent absorbances arise from collagen and water in both samples. The NIR spectra of OIM and WT mouse bone are also similar, and have most of the same collagen and water absorbances present in both. However, the collagen peak at 4238 cm<sup>-1</sup>, which is clearly seen in WT bone, as well as in mineralized and demineralized bovine bone, is not present in OIM bone (figure 2a) . These differences are quantified in figure 2b. In addition, there are differences in the water absorbances in the OIM and WT spectra (figure 3). The water peak near 5200 cm<sup>-1</sup> in the OIM occurs at a higher frequency compared to that in the WT spectra. In addition, there is relatively more water in the OIM bone compared to WT bone. **DISCUSSION:** The current study demonstrates ability of NIRS to detect subtle molecular changes in bone. Through the data presented here, bone quality can be assessed through shifts in the spectral contours caused by changes in the molecular composition. Quantitative data of peak heights ratios between collagen bands reflects the contour changes seen in the OI, control and demineralized bone. The origin of the 4238 cm<sup>-1</sup> absorbance is not precisely known, but does arise from a combination of CH and OH fundamental infrared absorbance's. Since OIM mice contain a mutation that causes abnormal collagen formation, the data presented here confirm that NIR spectra are sensitive to the collagen mutation in both the collagen and water components. **SIGNIFICANCE:** Evaluation of changes in bone quality in preclinical models of disease is critical for assessing novel therapeutics, and understanding the impact of genetic mutations. Here, we demonstrated that NIR spectroscopy, a modality that can be applied to evaluation of intact tissues, can yield information on water and collagen composition, Further studies will validate the origin of changes in the absorbance bands to aid in understanding of therapeutics.



**Acknowledgment:** NIH R01 AR056145

# Rescuing Chondrocyte Hypertrophic Differentiation Potential and Exploring Therapeutic Approaches for Enhancing Bone Formation in Mucopolysaccharidosis VII Dogs

Sun H. Peck, Jennifer L. Kang, Justin R. Bendigo, Patricia O'Donnell, Caitlin A. Fitzgerald, Jessica Bagel, Neil R. Malhotra, Eileen M. Shore, Margaret L. Casal, Lachlan J. Smith  
University of Pennsylvania, Philadelphia, PA

**Disclosures:** SHP (N), JLK (N), JRB (N), PO (N), CAF (N), JB (N), NRM (N), EMS (N), MLC (N), LJS (N)

**Introduction:** The mucopolysaccharidoses (MPS) are genetic, lysosomal storage diseases characterized by deficient activity of enzymes that degrade glycosaminoglycans (GAGs) [1]. MPS VII is characterized by mutations in the  $\beta$ -glucuronidase gene, leading to incomplete digestion and progressive accumulation of three GAG types [2]. MPS VII patients exhibit severe skeletal abnormalities, especially of the spine [3]. Persistent cartilaginous lesions are present in the vertebrae representing failed cartilage-to-bone conversion during postnatal development, which result in progressive kyphoscoliosis and spinal cord compression [4-7]. Using the naturally-occurring MPS VII canine model, we established that impaired hypertrophic differentiation of epiphyseal chondrocytes contributes to failed bone formation during early postnatal development [8], which in turn is associated with decreased Wnt/ $\beta$ -catenin signaling [9]. We also showed that Wnt pathway activation resulted in normalization of chondrocyte differentiation *in vitro* in MPS VII epiphyseal cartilage [10]. GAGs perform crucial roles in controlling the distribution and availability of Wnts, which are critical regulators of chondrocyte differentiation during endochondral ossification. Thus, we hypothesized that aberrant GAG accumulation in MPS VII contributes directly to impaired chondrocyte function and that in the absence of abnormal GAGs, hypertrophic differential potential could be rescued. To test this hypothesis, we undertook *in vitro* studies to compare differentiation potential of MPS VII chondrocytes in the presence and absence of their GAG-rich environment. Furthermore, to explore therapeutic approaches to correct MPS VII bone disease, we undertook a preliminary *in vivo* study in our canine model to establish a dosing regimen and safety profile using lithium, a Wnt pathway agonist, which has been previously shown to enhance bone formation and is approved clinically for other indications [11].

**Methods:** For this study, we used the naturally-occurring MPS VII canine model that closely mimics the skeletal phenotype of human patients [12]. *In Vitro Analysis of GAG Accumulation and Chondrocyte Hypertrophic Differentiation Potential:* With IACUC approval, unaffected control and MPS VII dogs (n=4 for each) were euthanized at 9 days-of-age, and lumbar vertebral epiphyseal cartilage was isolated. For monolayer cultures, cartilage was digested with collagenase until cells were released from the extracellular matrix. Isolated chondrocytes were expanded in basal medium (DMEM, 10% FBS, 1% PSF) then cultured in monolayer in either basal or osteogenic media. For explant cultures, epiphyseal cartilage was cultured as whole tissue explants in basal medium. Media was collected at 3, 7, and 14 days for monolayer cultures and at 5 days for explant cultures. Total media GAG content was measured using the dimethylmethylene blue assay and normalized to total cell count. Cells from monolayer cultures and explants were harvested, RNA extracted, and mRNA expression levels of chondrocyte differentiation markers (Sox9-proliferative; Runx2-prehypertrophic; Col10-hypertrophic) were measured using qPCR. Significant differences between groups ( $p<0.05$ ) were established using unpaired t-tests. *In Vivo Lithium Treatment:* To establish dosage needs of lithium, normal control dogs (n=2) were treated with twice daily doses of 5 mg/kg of powdered lithium carbonate packaged into gelatin capsules for 1 week for acclimation, then with twice daily doses of 10 mg/kg for 2 weeks, starting at 15 days-of-age. Dogs were monitored for side effects, and serum lithium levels were measured using a commercial assay (Crystal Chem).

**Results:** *In Vitro Analysis of GAG Accumulation and Chondrocyte Hypertrophic Differentiation:* In whole explant culture, MPS VII chondrocytes secreted significantly higher amounts of GAGs into the media compared to controls over time, while isolated chondrocytes showed no differences over 14 days of culture (Fig 1). Likewise, in whole explant culture, MPS VII chondrocytes showed impaired differentiation over time compared to controls, but both control and MPS VII chondrocytes exhibited similar propensity to differentiate over time in isolated cell culture (Fig 2). *In Vivo Lithium Treatment:* After the initial 1 week acclimation period, both dogs maintained serum lithium levels within the desired therapeutic range (0.2-1.5 mmol/L) over the following 2 weeks (Fig 3). Dogs exhibited a mild tremor which resolved within a few days. No significant adverse side effects from lithium treatments were observed.

**Discussion:** The results of this study show that MPS VII chondrocytes regain normal hypertrophic differentiation potential upon removal from their GAG-rich environment. Abnormal GAG accumulation in MPS VII epiphyseal cartilage may disrupt extracellular control of secreted growth factors, such as Wnts, which are necessary to initiate and sustain chondrocyte differentiation. We previously showed that activation of the Wnt pathway with exogenous factors can also normalize chondrocyte differentiation *in vitro*, and taken together, these results indicate that combinatorial therapies that normalize GAG accumulation and activate Wnt signaling may be able to rescue the differentiation potential of resident cells and ultimately normalize bone formation. As a preliminary step, we successfully treated neonatal dogs with lithium, establishing safety and optimizing an oral dosing regimen to sustain therapeutic serum levels. In ongoing *in vivo* studies, we are examining whether GAG reduction via exogenous enzyme replacement therapy (ERT) and Wnt/ $\beta$ -catenin pathway activation via lithium treatment are able to normalize chondrocyte function and bone formation in MPS VII dogs during postnatal growth.

**Significance:** MPS VII is associated with debilitating skeletal disease for which there is no treatment. Our results suggest that therapeutic strategies combining GAG reduction (ERT) and inducing endochondral bone formation (lithium) may effectively treat skeletal abnormalities in MPS VII patients.

**References:** [1] Neufeld+ 2001. [2] Sly+ J Pediatr, 1973. [3] Peck+ Mol Genet Met, 2016. [4] Pizzutillo+ J Pediatr Orthop, 1989. [5] de Kremer+ Am J Med Genet, 1992. [6] Yasin+ Spine, 2014. [7] Smith+ J Orthop Res, 2010. [8] Peck+ Mol Genet Met, 2015. [9] Peck+ ORS Trans, 2016. [10] Peck+ ASBMR Trans, 2016. [11] Clement-Lacroix+ PNAS, 2005. [12] Haskins+ Pediat Res, 1984.

**Acknowledgements:** Funding sources: NIH, Penn Orphan Diseases Center, National MPS Society and Penn Center for Musculoskeletal Disorders (P30 AR069619). The authors thank the staff and students at the Penn Vet School for animal care.

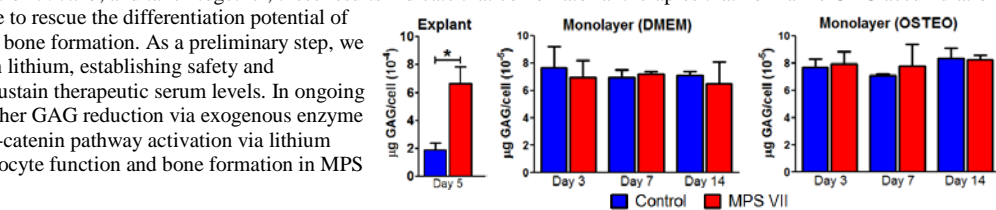


**Figure 1. Culture media GAG content.** Intact epiphyseal cartilage explants from MPS VII animals exhibited significantly higher GAG content secreted into the media compared to controls. Isolated chondrocytes in monolayer culture showed normalization of secreted GAG content regardless of media conditions. N=4; \* $p<0.05$ .

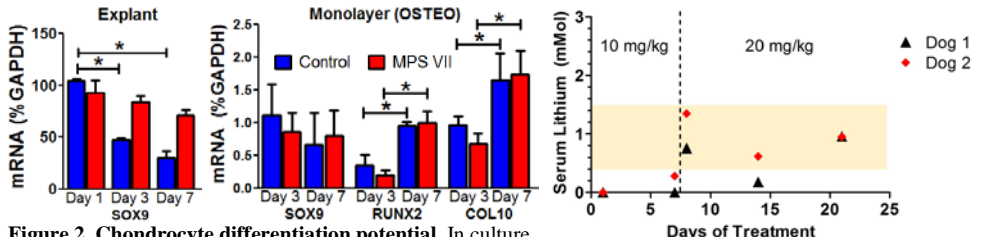


**Figure 2. Chondrocyte differentiation potential.** In culture, control chondrocytes in intact epiphyseal cartilage explants exhibited propensity to differentiate over time (decreasing SOX9 expression) while MPS VII chondrocytes did not (persistent SOX9 expression). In contrast, both control and MPS VII isolated chondrocytes grown in monolayer culture differentiated normally in the presence of osteogenic conditions. N=4, \* $p<0.05$ .

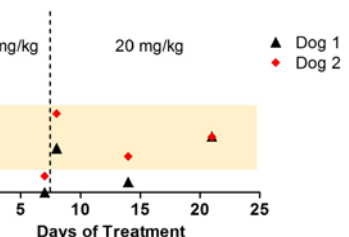


**Figure 3. Serum lithium levels in treated dogs.** 15-day old normal control animals were treated for 21 days with daily doses of lithium (10 mg/kg daily for 7 days, 20 mg/kg for following 14 days). Dashed line indicates day of increase in lithium dosage. Yellow shaded area indicates target non-toxic, therapeutic range for serum lithium concentration.

## **MODULATION OF OSTEOBLASTOGENESIS BY MATRICELLULAR R-SPONDIN-2**

**M. Noelle Knight, Michele Lowe, Jaimo Ahn, Kurt D. Hankenson**

More than 8.9 million osteoporotic fractures occur annually, resulting in a new osteoporotic fracture every three seconds worldwide. Existing therapeutics to prevent and treat osteoporosis are primarily limited to anti-resorptive agents that limit further bone loss, rather than anabolic agents that directly maintain and increase bone mass. One of the most promising targets for potential anabolic therapeutics is the Wnt signaling pathway due to its potent induction of osteoblastogenesis and bone formation. We have previously demonstrated that the matricellular Wnt co-activator R-spondin 2 (Rspo2) can promote osteoblast differentiation and mineralization in vitro, which results in an increase in canonical Wnt signaling. Interestingly, this enhanced osteoblastogenesis is not blocked by inhibition of the canonical Wnt signaling pathway through a dominant-negative T-cell Factor (TCF), suggesting the contribution of another mechanism of osteoinduction. We hypothesize that the modular domain structure of R-spondins provides a mechanism for the activation of multiple pathways, with the two cysteine-rich furin-like domains activating one pathway and the thrombospondin type 1 repeat (TSR1) domain activating another. Further supporting this modular dual-induction, R-spondins activate not only canonical Wnt signaling through beta-catenin but also some noncanonical signaling pathways. To address this hypothesis, we are investigating the Wnt signaling activity and differentiation potential of Rspo2-null mesenchymal progenitor cells (MPC), both alone and with the expression of a series of Rspo2 domain-deletion mutants. Rspo2-null MPC undergo less osteoblastogenesis and mineralization in vitro, with decreased expression of one of the main regulators of osteoblast differentiation, the transcription factor Osterix. However, these cells induce Alkaline Phosphatase and some downstream osteogenic genes similarly to wild-type cells, suggesting a partially differentiated or altered state under RSPO2-null conditions. Deletion of one of the furin domains and the TSR1 domain in mice recapitulates the skeletogenesis phenotype of the global knockout, confirming these as the functional domains with respect to osteogenesis. Ongoing in vivo studies utilizing an osteoblast-specific knockout mouse model show decreased skeletal size, as well as diminished stromal cell precursors. These experiments represent critical steps in advancing our understanding of osteoblastogenesis, and in harnessing the Wnt signaling pathway to design novel anabolic therapeutics for the urgent, unmet clinical need for osteoporosis treatment and prevention.

## Novel Techniques for the Evaluation of Physical Activity in a Large Animal Intervertebral Disc Degeneration Model

Justin R. Bendigo<sup>1,2</sup>, Sarah E. Gullbrand<sup>1,2</sup>, Brendan D. Stoeckl<sup>1</sup>, Zosia Zawacki<sup>1</sup>, Thomas P. Schaer<sup>1</sup>, Harvey E. Smith<sup>1,2</sup>, Robert L. Mauck<sup>1,2</sup>, Neil R. Malhotra<sup>1</sup>, Feini Qu<sup>1,2</sup>, Lachlan J. Smith<sup>1,2</sup>

<sup>1</sup>University of Pennsylvania, Philadelphia, PA, <sup>2</sup>Philadelphia VA Medical Center, Philadelphia, PA

**Disclosures:** JRB (N), SEG (N), BDS (4-Animation LLC), ZZ (N), TPS (N), HES (N), RLM (N), NRM (N), FQ (4-Animation LLC), LJS (N)

**Introduction:** Intervertebral disc degeneration (IDD) is a progressive, age-related condition that leads to structural and mechanical failure of the disc. This deterioration is commonly associated with low back pain (LBP). Therefore, pain is the most clinically significant characteristic of IDD, and the ideal animal model should recapitulate pain and functional impairment in addition to structural and mechanical alterations to the disc. Our group previously developed a large animal goat model of IDD that effectively recapitulates the structural and mechanical changes that occur with degeneration [1]; however, intervertebral disc degeneration in sheep or goats does not result in clinically perceptible pain, even at very advanced stages. Various methods currently exist to evaluate activity and pain in small animal models, including: the LABORAS platform, which measures vibration/force for position and behavior tracking [2]; hindpaw withdrawal in response to mechanical (von Frey Test) and thermal (Hargreaves Test) hyperalgesia signifying increased pain sensitivity [3]; and the Rotarod Test, which uses a rotating rod to measure balance and activity endurance [3]. These techniques are not readily translatable to large animal models. An objective tool to assess functional change that is consequent to painful degeneration would be invaluable to evaluation of therapeutics in a preclinical animal models. The objective of this study was to develop and validate two novel techniques for quantifying physical activity in an established caprine model of disc degeneration.

**Methods:** Two male large frame goats, ~2 years of age, were housed together in a 3-sided barn. IDD was induced at 4 lumbar levels per animal via intradiscal injection of 1U chondroitinase ABC. Our previous work showed that this insult results in moderate to severe degeneration of the disc after 12 weeks, as assessed via MRI, disc height, and histology [1]. Over this 12 week period, two methods of activity monitoring were investigated. Overhead Video-Based Motion Tracking: A GoPro HERO4 camera recording in SuperView mode was mounted to the barn ceiling to capture live images of the entire pen. Video was recorded for 1 hour per day when humans were not present to capture unprovoked activity. Motion was tracked for one goat in MATLAB using the DLTdv5 texture tracking program [4], which tracks a manually selected monochromatic texture region of interest – in this case the goat's body (Fig 1A). The center of this region for each video frame was then output to Excel as x-y coordinates mapped to the resolution of the video. Frames were grouped into 1-second increments, and the average x-y position was rounded to the nearest whole number. The distance formula was used to calculate change in position between each 1-second increment, and these values were summed over the hour-long video to yield total activity. Activity was monitored during 2 pre-operative weeks to establish baseline activity and from 1-12 weeks following induction of disc degeneration. Daily activity measurements were binned into two-week periods for analysis. Differences between time points were assessed via unpaired Student's *t*-tests compared to pre-op activity. To test for inter-observer reliability of the video tracking software, pre-op videos were tracked by two observers, and the activity levels were compared via unpaired Student's *t*-test. Step-Count Quantification using a Custom Wearable Device: Step count was also measured on a daily basis in a separate goat to characterize activity. A custom built wearable device [5] consisting of a sensor board with gyroscope, accelerometer, and magnetometer; microcontroller; radio; data logger; and lithium polymer battery was attached to the right forelimb proximal to the carpus (Fig 1B). A neodymium magnet was attached distal to the carpus. Discrete steps were identified by local maxima in the magnetic field strength, which occurred with carpal flexion during ambulation. Data from the device was uploaded to a computer each day over a period of 4 weeks prior to surgery, and for 12 weeks following surgical induction of disc degeneration. MATLAB was used to count the number of steps in a 30-minute window each day. Prolonged periods of elevated magnetic field strength – indicating that the goat was lying down – were excluded from the analysis. As with the video tracking data, activity was binned into two-week periods for analysis. Differences between time points were assessed via unpaired Student's *t*-tests compared to pre-op activity.

**Results:** Overhead Video-Based Motion Tracking: No significant difference in pre-op activity level was found between observers (Fig 1A). There was a significant increase ( $p<0.05$ ) in activity from 1-6 weeks post-operative compared to pre-op baseline, followed by a return to baseline activity from 7-12 weeks post-op (Fig 2B). Step-Count Quantification using a Custom Wearable Device: A significant reduction ( $p<0.05$ ) in activity 1-2 and 5-6 weeks post-op was observed compared to the pre-op baseline, with 7-12 weeks post-op also trending towards decreased activity ( $p=0.0614$  at 11-12 weeks) (Fig 2C).

**Discussion:** We developed two novel, independent methods for quantifying large animal activity in a model of lumbar disc degeneration and demonstrated that both methods are able to detect changes in activity over time. While activity levels differed between the two goats immediately post-surgery, both tracking methods show a long-term trend towards returning to or below baseline. Ongoing work will further validate these methodologies to explore and optimize relationships between disc degeneration and functional parameters in large animals. Concurrently we are assessing biomarker signatures such as serum inflammatory markers and immunohistochemistry for nociceptive nerve fibers. Recently, NIH leaders called for improved transparency and reproducibility in animal models [6, 7]. Our activity monitor methodologies described here combined with competent physical examination will offer a platform for improved *in vivo* assessment when using large animal models. Other applications for the wearable device include tracking limb movement during augmentation of orthopedic hardware in fragility fractures or tracking three dimensional head and neck kinematics in future work involving goats undergoing cervical total disc replacement.

**Significance:** Use of these novel activity monitoring techniques in large animal models of musculoskeletal disease will enhance the clinical relevance of these models by improving scientific rigor and model fidelity resulting in a more predictable translation to human clinical use.

**References:** [1] Gullbrand+, OA&C 2016 (In press) [2] Quinn+, Journal of Neuroscience Methods 2003 [3] Piel+, Gene 2014 [4] Hedrick+, Bioinspiration & Biomimetics 2008 [5] Qu+, ORS 2016 [6] Landis+, Nature 2012 [7] Collins+, Nature 2014

**Acknowledgments:** This study was supported by the Department of Veteran's Affairs, the Montague Research Award, and the Penn Vet Preclinical Translational Core.

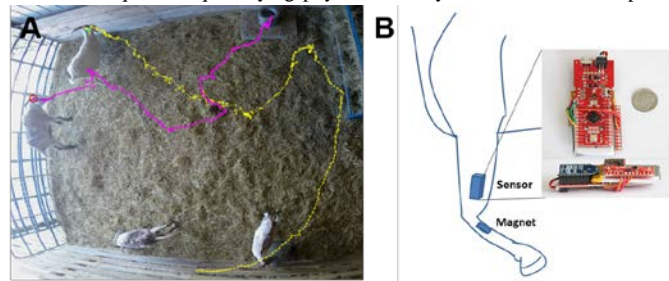


**Figure 1.** A. Overhead tracking of goat locomotion from video footage via the DLTdv5 MATLAB code. B. Schematic illustrating placement of the custom wearable device on the goat forelimb.

mapped to the resolution of the video. Frames were grouped into 1-second increments, and the average x-y position was rounded to the nearest whole number. The distance formula was used to calculate change in position between each 1-second increment, and these values were summed over the hour-long video to yield total activity. Activity was monitored during 2 pre-operative weeks to establish baseline activity and from 1-12 weeks following induction of disc degeneration. Daily activity measurements were binned into two-week periods for analysis. Differences between time points were assessed via unpaired Student's *t*-tests compared to pre-op activity. To test for inter-observer reliability of the video tracking software, pre-op videos were tracked by two observers, and the activity levels were compared via unpaired Student's *t*-test. Step-Count Quantification using a Custom Wearable Device: Step count was also measured on a daily basis in a separate goat to characterize activity. A custom built wearable device [5] consisting of a sensor board with gyroscope, accelerometer, and magnetometer; microcontroller; radio; data logger; and lithium polymer battery was attached to the right forelimb proximal to the carpus (Fig 1B). A neodymium magnet was attached distal to the carpus. Discrete steps were identified by local maxima in the magnetic field strength, which occurred with carpal flexion during ambulation. Data from the device was uploaded to a computer each day over a period of 4 weeks prior to surgery, and for 12 weeks following surgical induction of disc degeneration. MATLAB was used to count the number of steps in a 30-minute window each day. Prolonged periods of elevated magnetic field strength – indicating that the goat was lying down – were excluded from the analysis. As with the video tracking data, activity was binned into two-week periods for analysis. Differences between time points were assessed via unpaired Student's *t*-tests compared to pre-op activity.

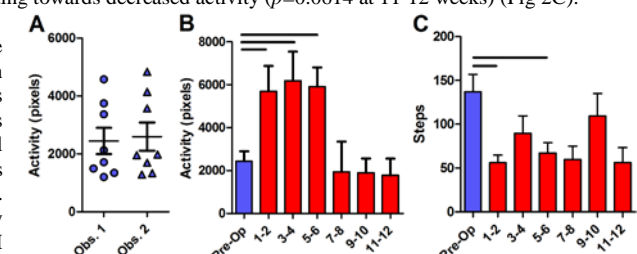


**Figure 2.** A. Inter-observer video tracking. B. Video tracking and C. custom wearable device tracking of daily activity pre-op and 1-12 weeks post-op in two separate goats

## **Determination of Novel BMP-Smad1/5 Signaling Interactions in Fibrodysplasia Ossificans Progressiva**

Allen, Robyn S., Eileen M. Shore, Mary C. Mullins  
University of Pennsylvania

Fibrodysplasia ossificans progressiva (FOP) is a rare and debilitating human genetic disorder that alters formation of skeletal elements and induces heterotopic ossification (HO). Classical FOP is caused by a single nucleotide substitution in the BMP/TGF $\beta$  cell surface receptor, ACVR1 (617G>A, R206H). This mutation results in gain-of-function of receptor signaling through the Phospho-Smad1/5 (pSmad) pathway. However, the mechanism through which the mutant receptor confers enhanced signaling activity remains uncertain. We used zebrafish embryo dorso-ventral patterning, which is established by a gradient of BMP pathway signaling that specifies ventral cell fates, to assay for mutant ACVR1 activity. We confirmed previous results that ACVR1-R206H misexpression causes over-activation of pSmad activity and ventralization of zebrafish embryos. We have now tested several rarer ACVR1 mutations of FOP for signaling activity in the zebrafish embryo assay and found similar results of over activity. Recent studies suggest that ACVR1-R206H and other FOP variant mutant receptors may have altered ligand affinity compared to WT ACVR1<sup>(1,2)</sup>. We are testing if BMP and other TGF $\beta$  family ligands enhance pSmad1/5 activation by ACVR1-R206H in *bmp7*-/- zebrafish embryos. In addition, we are testing the requirement of other BMP receptors for over-activation of pSmad1/5 signaling by ACVR1-R206H and ACVR1-WT, as signaling complex partners. These and further studies of the signaling interactions of ACVR1-R206H will allow for identification of novel therapeutic targets to treat FOP and give us unique insight into this fundamental and important cell signaling pathway.

## **Fracture healing in aged mice is characterized by sustained inflammation and decreases in cell proliferation**

John H Hebb<sup>1</sup>; Jason W Ashley<sup>1,2</sup>; Lee McDaniel<sup>3</sup>; Luke Lopas<sup>1</sup>; John Tobias<sup>1</sup>; Kurt D Hankenson<sup>1,4</sup>; Jaimo Ahn<sup>1</sup>

<sup>1</sup>University of Pennsylvania, Philadelphia, PA, <sup>2</sup>Eastern Washington University, Cheney, WA, <sup>3</sup>Georgetown University School of Medicine, Washington, D.C., <sup>4</sup>Michigan State University, East Lansing, MI,

**ABSTRACT INTRODUCTION:** There are over 18 million fractures per year with a resultant economic burden in excess of 100 billion USD annually. Given that fracture and subsequent re-fracture risk increases with age, advances in fracture care and treatment are necessary to control the costs associated with geriatric fracture and improve patient outcomes. Our current understanding of geriatric fracture healing at the cell and molecular levels is not well-developed. Thus, we investigated the molecular differences between old and young fracture healing processes by characterizing the gene expression profile of fracture calluses in young and old mice.

**METHODS:** 5 mo and 25 mo C57BL/6 mice underwent bilateral tibial fractures. 25-month-old (m/o) mice represent 50 to 75% survival (consistent with 70 to 85 year-old humans). Bones were harvested prior to fracture (0 days) or fracture callus was harvested at 5, 10, and 20 days post fracture (DPF) for analysis. Global gene expression was assessed using Affymetrix MoGene 1.0 ST microarrays across two batches using an identical protocol. Cten, heatmaps, top 10 up and down regulated gene tables (n=5 per age group), and Incromaps were used to visualize the data. All animal procedures were approved by the Institutional Animal Care and Use Committee.

**RESULTS:** Principal Component Analysis (PCA) and cross-sectional heatmap (the top 5 greatest fold-change genes, subject to p<0.005) analysis demonstrated that DPF followed by age have the most pronounced effect on changes in gene expression. In order to identify the top ten differentially expressed genes during fracture healing progression, genes with a size-adjusted step-up p-value of less than 0.005 were sorted according to fold-change comparing 5 versus 0, 10 vs 5, and 20 vs 10 DPF in each age group. Both un-fractured and 20 DPF aged mice show dysregulation of immune associated genes, in particular CXCL8, CCL8, and CCL5. At 10 DPF, aged mice show increases in a number of matrix associated genes, in particular Matn1, UCMA, SCUBE1, Col9A1, and Col9A3. In addition, at each time point, genes differentially expressed between young and old mice were loaded into CTen for a two group (young vs. old) comparison. This showed a saturation of CD8+ cells and macrophages in old mice relative to young mice. Conversely, there were more mast cells in young mice relative to old mice. Finally, consistent with the PCA data, the classic pathways of BMP, Indian Hedgehog, Notch and Wnt were noted to cluster based on time first and age second. Specifically, the Notch pathway was expressed higher at earlier time points, 0 and 5 DPF, compared to later time points for both young and old mice.

**DISCUSSION:** The data suggest a lag in fracture healing progression/maturation of aged mice compared to young, although a distinct time-dependent molecular progression seems to be present regardless of age, a finding consistent with our previous tissue-level data<sup>1</sup>. Our analysis also found differential regulation of immunologic pathways including enrichment of CD8+ T cells (which has been shown to negatively impact bone regeneration)<sup>2</sup> in the older animals, whereas we found mast cells (which have been identified as necessary for proper bone healing)<sup>3</sup> were enriched in young fractures. Consistent with differential cell enrichment, the data also suggested differential regulation of cytokine CCL8, the T cell chemoattractant CXCL9, and the T cell-secreted cytokine CCL5. Finally, higher earlier levels of Notch signaling in old and young fractures which decreases with time may suggest that sustaining signaling could better sustain the proliferative stages of healing. Taken together, our data suggest that geriatric fracture healing is characterized by an elevated inflammatory state and decreased proliferation of cells responsible for bone regeneration. While the molecular machinery and pathways governing bone healing are not lost with advanced age, underlying immune dysfunction and delayed healing pathway activation result in poorer healing.

**REFERENCES:** 1. Lopas + Clin Orthop Relat Res, 2014. 2. Reinke + Science translational medicine, 2013. 3. Behrends + European cells & materials, 2014

## Programming ‘On Demand’ Delivery from Mechanically Activated Microcapsules

Bhavana Mohanraj<sup>1</sup>, Gang Duan<sup>1</sup>, Daeyeon Lee<sup>1</sup>, Robert L. Mauck<sup>1,2</sup>, George R. Dodge<sup>1,2</sup>

<sup>1</sup>University of Pennsylvania <sup>2</sup>Philadelphia VA Medical Center

**Disclosures:** No disclosures.

**Introduction:** Self-regulated drug delivery systems control the release of therapeutics via stimuli-sensitive triggers (e.g. pH or enzyme activity [1]). To date, however, few systems exist that take advantage of the mechanical environment to tune biofactor release [2]. To this end, we recently developed a novel mechanically-activated microcapsule (MAMC) drug delivery platform to enable tunable release in response to mechanical perturbation [3]. To further develop the therapeutic application of MAMCs for musculoskeletal regeneration and repair, this study sought to extend the operative lifetime of MAMC mechano-activation, to query activation as a function of the stiffness of the 3D environment, and to demonstrate mechano-activated release of an active biologic factor to improve tissue growth.

**Methods:** MAMCs were fabricated using a glass capillary microfluidic device as in [4]. To evaluate the MAMC mechanical response, the inner aqueous phase contained FITC-dextran (2MDa), which was lost upon rupture (visualized by confocal). MAMCs were formed from PLGA 85:15, which has a slower degradation profile than PLGA 50:50 (as previously used [3]). MAMCs were incubated under physiologic conditions (PBS, 37°C) and mechano-activation was evaluated via ‘parallel-plate’ compression testing over 6 weeks. Next, to determine how the stiffness of the microenvironment impacts

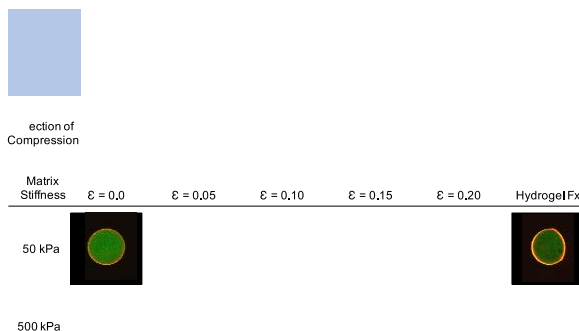


**Figure 2.** (A) MAMC strain in the direction of ( $E_{11}$ ) and perpendicular to ( $E_{22}$ ) compression shows MAMCs only deform in a stiff matrix (500kPa). (B) Visualization of a representative MAMC deforming in the hydrogel ( $n > 30$ , \* $p < 0.05$ , \*\* $p < 0.01$ , \*\*\* $p < 0.001$  vs 50kPa).

the surrounding matrix. In an “immature” matrix (50kPa), MAMC deformation was minimal, even upon hydrogel fracture (**Figure 2**). Conversely, MAMCs embedded within a “mature” matrix (500kPa) deformed with increasing hydrogel strain ( $p < 0.05$  for  $E_{11}$  and  $E_{22}$ , mature vs. immature). For MAMCs containing TGF- $\beta$ 3, ELISA showed that active TGF- $\beta$ 3 was released in a dose-dependent manner, proportional to the number of MAMCs ruptured (**Figure 3a**). Supernatant from intact TGF- $\beta$ 3 MAMCs showed minimal activity and blank MAMCs (BSA only) showed no activity. In the differentiation assay, exposure to TGF- $\beta$ 3 released from MAMCs increased GAG deposition in the pericellular space by day 4 (**Figure 3b**) and significantly increased construct GAG content by day 7, reaching levels similar to that of soluble TGF- $\beta$ 3 added to the medium (CM+, **Figure 3c**).

**Discussion:** Our findings show that the MAMC delivery system can be incorporated into strategies for tissue repair, specifically for engineered cartilage. MAMCs fabricated using a slower degrading polymer (PLGA 85:15) had an extended mechano-activation profile, indicating the potential for long-term delivery when the onset of mechanical loading is delayed (e.g. progressive load bearing after ACI). In the context of chondral defects, MAMC deformation depended on the stiffness of the surrounding matrix. This suggests that MAMC release may be programmed to actuate based on the maturity of the repair tissue. Finally, our findings show that the pro-chondrogenic factor TGF- $\beta$ 3 can be encapsulated within MAMCs, remains active, and induces chondrogenesis. This and other factors, including small molecules and anti-inflammatory agents, and their combinations can be released in response to the mechanical loading in the joint to regulate tissue repair. Importantly, this is not limited to one tissue or loading scenario, given that MAMCs can be tuned to activate across a range of mechanical inputs. As such, this technology is a valuable platform for self-regulated delivery across the musculoskeletal system.

**Significance:** MAMCs can be engineered to maintain a stable mechano-response over extended periods of time, to actuate as a function of the stiffness of the surrounding matrix, and can release active biologics to improve tissue repair and regeneration through *in situ* mechano-regulation of drug delivery.

**References:** [1] Kost+ Adv Drug Deliv Rev 2001, [2] Korin+ Science 2012, [3] Mohanraj+ 2016 ORS Annual Meeting #282, [4] Tu+ Langmuir 2012, [5] Farrell+ Eur Cells & Mat 2012, [6] Mauck+ Ann BME 2002.

**Acknowledgements:** This work is supported by an NSF GRFP and an NIH/NIAMS Training Grant (T32 AR007132).

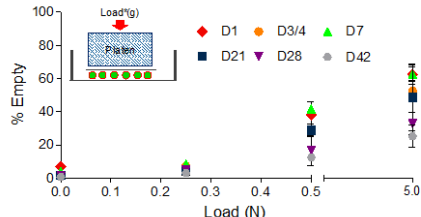


**Figure 1.** PLGA 85:15 MAMCs are mechano-responsive and structurally intact over 6 weeks. A stable response is observed over the first 3 weeks ( $p > 0.05$  vs. D1 at 0.5N;  $n = 3$ /load).

rupture, MAMCs were embedded in PEGDA hydrogels with “immature” (50kPa, 10%w/v) or “mature” (500kPa, 20%w/v) engineered cartilage properties. Using a confocal-mounted compression device [5], MAMC-containing hydrogels were compressed to 20% strain (at steps of 5%) and MAMC deformation measured. Finally, to determine if biologic factors remain functional during fabrication, the release and activity of TGF- $\beta$ 3 were measured by ELISA and differentiation assays. As a negative control, MAMCs containing only BSA were also evaluated. Differentiation was determined using a transwell assay with engineered cartilage. Bovine chondrocytes were embedded in agarose cylinders [6] and these constructs were placed in the lower chamber with the supernatant from intact or ruptured MAMCs and the MAMC solid fraction placed in the upper chamber. Constructs treated with aqueous TGF- $\beta$ 3 (CM+) served as a positive control, and constructs cultured in media lacking TGF served as a negative control. GAG production was assessed by Alcian Blue staining on Day 4 and construct GAG content on Day 7.

**Results:** MAMC fabrication using a slow-degrading PLGA 85:15 formulation resulted in extension of the lifetime of mechano-activation. MAMCs remained structurally intact and were sensitive to load over a period of up to 6 weeks (**Figure 1**). A stable mechano-response was observed for the first 3 weeks ( $p > 0.05$  vs. D1 at 0.5N) and only a slight decrease in sensitivity was noted at 4 and 6 weeks ( $p < 0.01$ ). In 3D matrices, MAMC deformation depended on the stiffness of

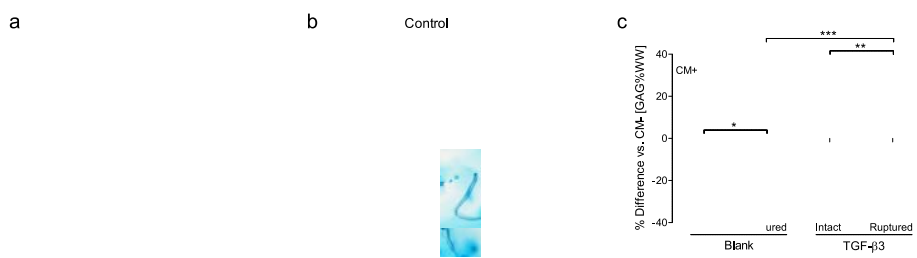


**Figure 3.** (A) TGF- $\beta$ 3 is measured in the supernatant of ruptured MAMCs in a “dose-dependent” manner ( $n = 3$ /group,  $^{\#}p < 0.001$  and  $^{\wedge}p < 0.01$  vs. blank,  $*p < 0.001$  vs. TGF- $\beta$ 3 intact). (B) TGF- $\beta$ 3 released from MAMCs is active, as visualized on day 4 by Alcian Blue staining (2ng/construct) and (C) GAG content on day 7, similar to that of CM+ (mean  $\pm$  SD: red  $\pm$  grey line) (10ng/construct,  $n = 4$ /group,  $*p < 0.05$ ,  $^{**}p < 0.01$ ).

## **Mechanical signaling in heartbeat coordination during development**

Anjali Rajaratnam, Christina Yingxian Chen, Kevin Chiou, Sangkyun Cho, Dennis Discher,  
Benjamin Prosser

The adult heart exhibits a coordinated contractile wavefront that spreads across the myocardium during each heart beat. This contractile wavefront is known to be driven by a propagating electrical signal that spreads from cell to cell via gap junctions. Yet surprisingly, in the absence of gap junctions the developing heart can still exhibit a coordinated beat, and inhibition of gap junctions by  $\beta$ -glycyrrhetic acid (BGA) does not diminish beating in embryonic hearts for an hour post drug treatment. In contrast, BGA ceases beating in adult hearts within minutes. Further experimental data and biophysical modeling suggest that mechanical signaling may thus play a more prominent role than electrical signaling in the propagation of the contractile wavefront in developing hearts. In this study we investigate the role of mechanosensing and mechanical signaling in neonatal rat cardiomyocytes by studying calcium dynamics in the presence of contractile and cytoskeletal inhibitors. The contractile inhibitors blebbistatin and cytochalasin D together cause a slower rise in the calcium transient when compared to control cells. This indicates that mechanically uncoupling cells negatively affects calcium kinetics. A similar result was found when microtubules were depolymerized using colchicine. In particular, it is known that microtubules participate in mechanochemotransduction through X-ROS signaling, a mechanism that increases the sensitivity of ryanodine receptor calcium release channels, in adult cardiomyocytes. We have also observed subtle delays between calcium transient peaks of cell pairs subjected to contractile and microtubule inhibitors, and experiments are underway to determine whether the delays observed in the calcium transient result in a slower calcium wavefront across a cell monolayer. Together these studies indicate a mechanical signaling mechanism that may aid heartbeat coordination in early hearts.

## **Generation and tenogenic differentiation of equine tendon-derived induced pluripotent stem cells**

Feikun Yang<sup>1</sup>, Filipa Pinto<sup>2</sup>, Aiwu Zhang<sup>1</sup>, Spencer Szczesny<sup>3</sup>, Robert L. Mauck<sup>3</sup>,  
Dean W. Richardson<sup>1</sup>

<sup>1</sup> Department of Clinic Studies at New Bolton Center, University of Pennsylvania, Kennett Square, PA 19348

<sup>2</sup> Institute for Regenerative Medicine, University of Pennsylvania, Philadelphia, PA 19104

<sup>3</sup> Department of Orthopaedic Surgery, Perelman School of Medicine, University of Pennsylvania, Philadelphia, PA 19104

Tendon, the unique form of connective tissue transferring force from muscle to bone, is highly prone to injury or overuse, leading to the development of tendinopathy in both humans and horses. Cell-based therapeutic strategies may afford major potential advantages in tendon repair because the natural healing of injured tendon is poor. Generation of induced pluripotent stem cells (iPSCs) should expand potential cell sources for “regenerative” therapy due to their functional similarity to embryonic stem cells. However, there is almost no information on iPSC application in tendon repair. By using lentiviral vectors expressing Oct4, Sox2, Klf4 and c-MYC (“Yamanaka factors”), we produced equine iPSCs derived from adult tendon cells (teno-iPSCs). The reprogrammed cell lines were morphologically similar to iPSCs reported from other species, and could be stably maintained in culture for over 40 passages with normal horse karyotype. Polymerase chain reaction (PCR) and immunofluorescent staining showed that teno-iPSCs expressed an array of equine specific pluripotency markers, including OCT4, NANOG, REX1, and TRA1-60. When cultured in liquid suspension in ultra-low attachment plates, the iPSC lines readily formed embryoid bodies with the expression of endodermal marker alpha-fetoprotein (AFP). *In vitro* adipogenesis assay further confirmed the pluripotency of teno-iPSCs. On the other hand, compared to bone-marrow derived mesenchymal stem cells (BMSCs), teno-iPSCs expressed higher level of tenogenic master transcription factor *Scleraxis* (SCX), indicating that the iPSCs retained parental epigenetic signature to some extent, which might facilitate their tenogenic differentiation. Treatment of teno-iPSCs with TGF-β3 or BMP12, growth factors reported to induce tenogenesis of BMSCs, slightly increased the mRNA level of SCX, but not *Mohawk* homeobox (MKX), another transcription factor crucial for tendon morphogenesis. The expression of decorin (DCN), one of the fundamental proteoglycans in the extracellular matrix of tendons, was increased by TGF-β3 but not by BMP12. Cyclic mechanical stretching on teno-iPSCs, which were seeded onto poly-ε-caprolactone (PCL)-based scaffold, increased the expression of SCX, MKX, and DCN. When teno-iPSCs were subjected to growth factor treatment combined with mechanical stimulation, the expression of MKX and DCN, but not SCX was enhanced by either TGF-β3 or BMP12. These data suggest that teno-iPSCs have high tenogenic differentiation capacity and that the combination of growth factor and mechanoinduction synergistically enhance the tenogenic differentiation of teno-iPSCs.

## **Methods to quantify glucose uptake in resting muscle using FDG PET/CT**

**Authors:** Richard White, Will Raynor, Tom Werner, Abass Alavi, Joshua Baker

### **Background/Purpose**

<sup>18</sup>F-fluorodeoxyglucose (FDG) positron emission tomography/computed tomography (PET/CT) is used to measure glucose uptake in specific tissues. This technology may be of interest as a modality to dynamically assess muscle metabolism. The purpose of this project is to assess the reliability of FDG PET/CT as a measure of muscle metabolism and to assess the construct validity of this measure within a population of at-risk individuals with rheumatoid arthritis (RA) compared to a healthy control population.

### **Methods**

An intravenous injection of <sup>18</sup>F-FDG (~500 MBq) was administered to 19 patients with RA. Whole body PET images and multislice CT scans were then collected on an integrated PET/CT system (Siemens Biograph 64). Manual regions of interest were drawn using OsiriX (OsiriX Foundation, Geneva, Switzerland, version 6.5.2), allowing for calculation of the mean standardized uptake value (SUVmean) and muscle cross-sectional area (CSA) in the thigh. PET measures in 15 RA subjects were compared to 15 healthy control subjects from Denmark matched on age ( $\pm 5$  years) and sex. PET measures in the RA subjects were also compared to the results of complete clinical and body composition assessments. Intra- and inter-reader reliability was assessed in a blinded fashion.

### **Results**

Intra-reader reliability was excellent for SUVmean (Rho: 0.96,  $p < 0.0001$ ) and muscle CSA (Rho: 0.99,  $p < 0.0001$ ). Inter-reader reliability was also excellent for both SUVmean (Rho: 0.94,  $p < 0.0001$ ) and muscle CSA (Rho: 0.90,  $p < 0.0001$ ). There was significantly lower muscle area (Median 212 [IQR 176, 242] cm<sup>2</sup> v. 295 [IQR 289, 344] cm<sup>2</sup>,  $p < 0.001$ ) and lower SUVmean (Median 0.55 [IQR 0.52, 0.63] v. 0.61 [IQR 0.57, 0.77],  $p = 0.03$ ) in 15 RA patients compared to 15 matched controls at the thigh. Among RA patients, muscle CSA at the thigh was strongly correlated with total appendicular lean mass index (0.82,  $p < 0.0001$ ). However, the SUVmean at the thigh was not significantly correlated with demographics, body mass, body composition, physical functioning, disease activity, or physical activity among patients with RA.

### **Conclusions**

Assessment of glucose uptake at the thigh is possible using FDG PET-CT and demonstrates good intra- and inter-reader reliability. Muscle activity was lower among an at-risk group of patients with RA compared to a healthy control population, suggesting some construct validity of the measure. However, there was no significant correlation with other measures of muscle health in this small sample.

## Role for IL15-IL15ra signaling axis on cortical bone mineralization

Emanuele Loro<sup>1</sup>, Girish Ramaswamy<sup>2</sup>, Abhishek Chandra<sup>2</sup>, Wei-Ju Tseng<sup>2</sup>, Manoj K. Mishra<sup>1</sup>, Eileen M. Shore<sup>2</sup> and Tejvir S. Khurana<sup>1</sup>.

<sup>1</sup>Department of Physiology and Pennsylvania Muscle Institute, Perelman School of Medicine, University of Pennsylvania, Philadelphia, PA, USA.

<sup>2</sup>Department of Orthopaedic Surgery, Perelman School of Medicine, University of Pennsylvania, Philadelphia, PA, USA.

Interleukin15 (Il15) and Il15 receptor  $\alpha$  (Il15ra) mediate pro-inflammatory signaling. We and others have shown they are also determinants of skeletal muscle properties and energy metabolism, exemplified by resistance to diet-induced obesity, higher activity and endurance noted in Il15ra<sup>-/-</sup> mice. The Il15/Il15ra axis is important for osteoclastogenesis, however, little is known about its role in osteoblast function and osteoblast/osteoclast coupling. Given the potential crosstalk between exercise activity, cytokine secretion and the musculoskeletal system, we investigated the effect of Il15ra ablation on bone mineralization.  $\mu$ CT and 3 point-bending showed that Il15ra<sup>-/-</sup> bones were protected from the age-related decline in trabecular bone, but were unexpectedly fragile in the cortical region. Interestingly, cultured mesenchymal stromal cells (MSC) from Il15ra<sup>-/-</sup> mice showed alterations in proliferation, mineralization and *rankl/opg* ratio, suggesting involvement of cell autonomous mechanisms. To investigate the molecular mechanisms underlying these differences, we analyzed the transcriptome of MSC's from control and Il15ra<sup>-/-</sup> after 5 days of osteogenic differentiation. Microarray analysis revealed that 1150 genes were differentially expressed (1.5 fold change and FDR<5%). Of these, 844 were upregulated and 306 were downregulated in Il15ra<sup>-/-</sup> cells compared to controls. Bioinformatic analyses using DAVID clustering revealed that the most represented Gene Ontology (GO) categories for the upregulated genes were related to metabolism (fatty acids metabolism), and immune response. In the downregulated list, cell cycle, retinoic acid metabolism, bone mineralization and embryonic forelimb morphogenesis were the most represented GO categories. Protein-protein interaction (PPI) network analysis using Cytoscape/PhenomeScape revealed the involvement of several genes/networks related to bone mineralization and phosphate homeostasis.

In particular, *enpp1* was significantly downregulated in il15ra<sup>-/-</sup> MSC. *Enpp1* mutations are associated with autosomal recessive Hypophosphatemic Rickets 2. In vitro studies on MC3T3 preosteoblasts confirmed that silencing of Il15ra using shRNA caused a cell autonomous decrease in Nucleotide Pyrophosphatase/Phosphodiesterase (NPP) activity, offering a mechanism for the lower cortical bone mineralization seen *in vivo* and *in vitro* in Il5ra<sup>-/-</sup> mice. Our results demonstrate that Il15ra plays an important role in osteoblast function, in cortical bone mineralization, and is required to ensure efficient osteoblast/osteoclast coupling.

## Combinatorial hydrogels and rapid single cell imaging to investigate chondrogenesis in 3D

Sebastián L. Vega<sup>1</sup>, Kwang Hoon Song<sup>1</sup>, Chao Wang<sup>2</sup>, Lin Han<sup>2</sup>, Jason A. Burdick<sup>1</sup>

<sup>1</sup>Department of Bioengineering, University of Pennsylvania, Philadelphia, PA

<sup>2</sup>School of Biomedical Engineering, Science and Health Systems, Drexel University, Philadelphia, PA

**Introduction:** The stem cell niche is a complex environment that exposes cells to an assortment of biochemical and physical cues.<sup>1</sup> For example, during cartilage development mesenchymal cells reside in a 3D environment that presents them with both cell-cell (e.g., cadherins) and cell-ECM adhesion (e.g., fibronectin) signals in a spatiotemporal manner.<sup>2</sup> Due to the inherent design of many material systems, decoupling mechanical properties from changes in chemical signals remains a challenge. Additionally, attempts to attribute individual biomaterial properties to cell behavior are further challenged by 2D cultures, which fail to adequately recreate native 3D milieus. To address these challenges, the goal of this study is to develop a biomaterial platform capable of presenting cells with a wide range of biochemical cues without altering mechanical properties. Here we used hyaluronic acid (HA) macromers functionalized with norbornene groups (NorHA) which allow for light-mediated thiol-ene reactions with di-thiol crosslinkers to create hydrogels with leftover reactive handles accessible for secondary reactions.<sup>3</sup> We patterned gradients of mono-thiolated peptides of the Arg-Gly-Asp (RGD) sequence from fibronectin to NorHA hydrogels and showed that we could spatially control the presentation of RGD over a wide range of concentrations without altering hydrogel mechanics. Rapid imaging and single cell analysis of encapsulated human mesenchymal stem cells (MSCs) also showed high viability and RGD-dependent changes in chondrogenic markers Sox9 and aggrecan within the combinatorial hydrogels.

**Methods:** *NorHA synthesis:* HA was converted to its tetrabutylammonium salt and then norbornene carboxylic acid was coupled to pendant alcohols on HA (Fig 1a). *Base hydrogel formation:* hydrogels were prepared by mixing NorHA macromer, di-thiol crosslinker, and 0.05 wt% photoinitiator (I2959), pipetting into PDMS molds (5x5x1 mm<sup>3</sup> squares), and photopolymerizing with UV light (10 mW/cm<sup>2</sup>) for 10 min (Fig 1b). *Biochemical gradient formation:* base hydrogels were incubated in a 5 mM solution of rhodamine-labeled mono-thiolated RGD peptide (GCGYGRGDSPG) and 0.05 wt% I2959 in PBS, and exposed to UV light for different times using an opaque sliding mask (Fig 1c). *Imaging:* using a Leica TCS SP8 confocal microscope with a motorized x-y stage, high-resolution 3D tile scan images of the top 200 μm of hydrogels were acquired. *RGD gradient characterization:* ImageJ and hydrogel confocal images were used to obtain a horizontal profile of RGD fluorescence. *Hydrogel mechanical characterization:* atomic force microscopy (AFM) was used to generate force curves on a 10x10 array using a 25 μm polystyrene spherical probe (0.03 N/m). Elastic moduli were obtained from force curve data using the Sneddon approximation of the Hertz indentation model. *Cell viability:* MSCs (5E6 cells/ml, Lonza) were encapsulated in base hydrogels, exposed to biochemical gradients, and cultured for 7 days in growth media. Viability was assessed using a Live/Dead (Invitrogen) per the manufacturer's instructions. *Cellular characterization:* MSC-laden hydrogels were fixed, permeabilized, blocked with 1% NGS followed by primary (Sox9 [1:200] or aggrecan [1:50] at 4°C for 16 h) and secondary (AlexaFluor 488, 1:200, 2 h) antibody incubations. *Single cell analysis:* hydrogel confocal images of 1-day Sox9 stained samples were divided into 10 regions in the horizontal direction, and total nuclei intensity was obtained and normalized to nuclear volume (Fig 1d). Similar procedure was applied to 7-day aggrecan-stained samples to calculate secreted aggrecan in different horizontal regions. At least 300 cells were analyzed per region.

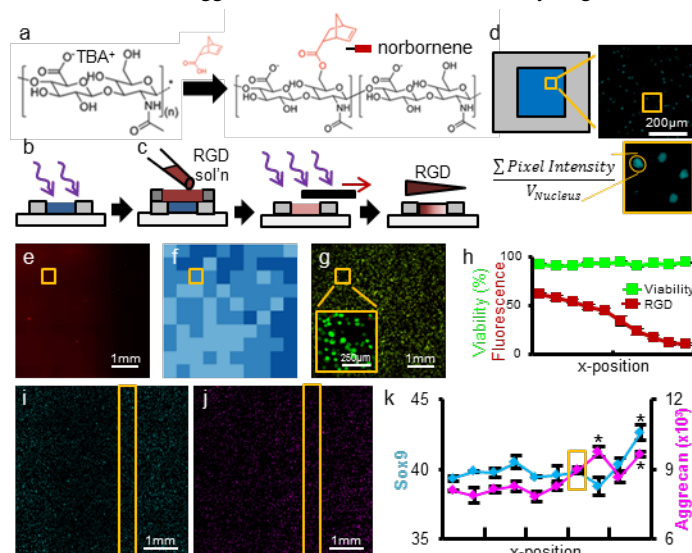


Fig 1. Refer to text for figure description.

**Results:** NorHA hydrogels created by fabrication scheme presented in Fig 1a-c feature an RGD gradient, as confirmed by confocal microscopy (Fig 1e). AFM force curves were used to generate an elastic moduli heat map, where darker blue regions correspond to a larger deviance (< 30%) from the average modulus ( $7.1 \pm 1.1$  kPa) (Fig 1f). MSCs encapsulated in hydrogels with spatially controlled biochemical cues show high bulk viability for at least 7 days in 3D culture (Fig 1g), and high resolution confocal images allow for viability assessment in spatially-defined regions within the hydrogel (Fig 1g, inset). Scatter plot of RGD fluorescence and cell viability in the horizontal direction shows a decreasing trend in peptide fluorescence without compromising cell viability (Fig 1h). Rapid confocal imaging (< 30 minutes per whole hydrogel) of 1-day Sox9 (Fig 1i) and 7-day aggrecan (Fig 1j) were acquired and used to quantify nuclear Sox9 and secreted aggrecan on a per-cell basis in 10 regions in the horizontal direction (e.g., one region showed in yellow rectangles in Fig 1i-j). Scatter plot of chondrogenic readouts show highest nuclear Sox9 (teal) and aggrecan (magenta) production in regions of low RGD (Fig 1k). **Conclusions:** The combinatorial hydrogel system presented can be used to assess many environmental signals within individual hydrogels and can be expanded to look at stem cell differentiation where the 3D environment is important for development and phenotypic stability. The spatial control of peptides allows for parallelization of experiments which can significantly reduce the number of studies required to attain significant data on cell-biomaterial interactions.

**References:** <sup>1</sup>(Scadden DT. Nature. 2006;441:1075-1079); <sup>2</sup>(DeLise AM. Osteoarthr and Cart. 2000;8:309-334); <sup>3</sup>(Gramlich WM. Biomat. 2013;34:9803-9811).

# Developmentally Relevant Cues within Hyaluronic Acid Hydrogels to Improve MSC Chondrogenesis

Mi Kwon, Sebastián L. Vega, Robert L. Mauck, Jason A. Burdick.  
University of Pennsylvania, Department of Bioengineering.

**Introduction:** In the condensation phase of chondrogenesis, stem cells aggregate via intercellular N-cadherin binding; however, this interaction is lost in hydrogel constructs, where cells are dispersed. We previously showed that mesenchymal stem cells (MSCs) encapsulated within hyaluronic acid hydrogels modified with N-Cadherin mimetic peptides (i.e., His-Ala-Val, HAV) underwent enhanced chondrogenesis and produced improved cartilaginous tissue when compared to unmodified hydrogels (see Bian et al, PNAS, 2013). However, there are still limitations to the use of MSCs in cartilage tissue engineering, such as incomplete differentiation. To further address this, we sought to investigate the dose and timing of the HAV sequence within engineered hydrogels. Notably, N-cadherin interactions are lost *in vivo* by the activity of the cell-surface metalloprotease ADAM10 during differentiation; thus, continuous presence of this peptide might not be optimal for MSC chondrogenesis.

**Materials and Methods:** Methacrylated HA (MeHA, 30% modified) was synthesized through the reaction of HA with methacrylic anhydride and further functionalized via a Michael addition reaction of methacrylates on MeHA with thiols on cysteine containing peptides (Fig. 1a). Human MSCs (Lonza) were encapsulated at a density of 20 million/mL in 1.5 wt% MeHA hydrogels (0.05 wt% Irgacure 2959, 2.0 mW/cm<sup>2</sup> UV light, 10 minutes). Constructs were cultured with 10 ng/mL TGF-β3 and analyzed via qPCR (Type II collagen, aggrecan, Sox-9) at 3, 7, and 14 days after cell seeding, with good cell viability confirmed at each timepoint. Single-cell and two-cell cluster analysis was performed after 3 days of culture using z-stacks acquired with a Leica SP8 inverted confocal microscope. Cells were stained with a β-catenin antibody (Abcam, 1:100) to probe for localization of β-catenin.

**Results and Discussion:** Human MSCs encapsulated in the HA macromers functionalized with the library of peptides (shown in Fig. 1a; study design described in Table 1) showed good viability (>90%) after encapsulation (Fig. 1b). These MSCs showed a concentration-dependent increase in chondrogenic gene expression (shown, type II collagen, Fig. 1c) with stable N-Cadherin mimetic peptides. This effect was abrogated in the presence of cleavable peptides with the same mimetic domain. N-cadherin mimetic peptides induced β-catenin translocation to the nucleus, with an effect comparable to true cell-cell contact in a two-cell MSC cluster in hydrogels without mimetic peptide (not shown).

Study Design							
	M	0S	1S	2S	0C	1C	2C
MeHA	+	+	+	+	+	+	+
Stable N-Cad	-	0 mM	1 mM	2 mM	-	-	-
Cleavable N-Cad	-	-	-	-	0 mM	1 mM	2 mM

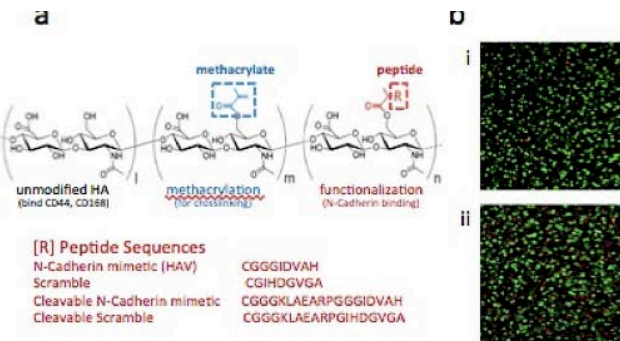


**Table 1.** Experimental design, with abbreviations of group names and the content of N-cadherin mimetic peptide functionalization, with all concentrations expressed with respect to final construct volume).

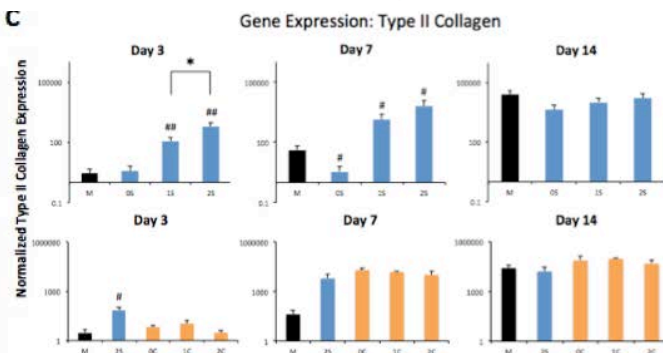


**Figure 1.** (a) Peptide-modified HA macromers. (b) Representative live/dead staining. (c) Type II Collagen expression in hydrogels with varying HAV peptide concentrations at three timepoints. All expression data quantified at day 3 and normalized to GAPDH and 2D monolayer control before encapsulation. \*P<0.05, \*\*P<0.01.

**Conclusions:** The concentration dependence on HAV of chondrogenic markers suggests that early differentiation is tunable by simply increasing the simulated developmentally relevant cell-cell contacts available. Furthermore, abolishment of type II collagen upregulation on this timescale with corresponding ADAM10-cleavable peptides confirms that cells are indeed able to regulate their microenvironment in this context. The β-catenin translocation data suggests this mimetic peptide indeed influences cell behavior in a manner comparable to its real counterpart.

**Acknowledgements:** This work was funded in part by NIH/NIAMS training grant T32-AR007132.

**References:** L. Bian, M. Guvendiren, R.L. Mauck, and J.A. Burdick. Hydrogels that mimic developmentally relevant matrix and N-Cadherin interactions enhance MSC chondrogenesis. PNAS (2013) 110:10117-10122.

## G<sub>α</sub> Controls Cortical Bone Quality by Regulating Osteoclast Differentiation via pCREB and β-Catenin Pathways

Girish Ramaswamy<sup>1,5</sup>, Hyunsoo Kim<sup>4</sup>, Deyu Zhang<sup>1,5</sup>, Vitali Lounev<sup>1,5</sup>, Joy Wu<sup>6</sup>, Yongwon Choi<sup>4</sup>, Frederick S Kaplan<sup>1,2,5</sup>, Robert J. Pignolo<sup>1,2,5</sup>, Eileen M. Shore<sup>1,3,5</sup>

Department of <sup>1</sup>Orthopaedic Surgery, <sup>2</sup>Medicine, <sup>3</sup>Genetics, <sup>4</sup>Pathology and Laboratory Medicine, and the <sup>5</sup>Center for Research in FOP and Related Disorders, and, Perelman School of Medicine at the University of Pennsylvania, Philadelphia, PA, <sup>6</sup>Division of Endocrinology, Stanford University School of Medicine, Stanford, CA

The *Gnas* gene encodes multiple transcripts, including the α-subunit of the stimulatory G-protein (G<sub>α</sub>) of adenylyl cyclase. We previously showed that heterozygous deletion of the paternal allele of *Gnas* (*Gnas*<sup>+/−</sup>) decreases cAMP, enhances osteoblastogenesis and inhibits adipogenesis relevant to heterotopic ossification. This study examined the effects of heterozygous *Gnas* inactivation during skeletal development and bone remodeling.

We previously described that trabecular BV/TV and architecture were unaffected but that cortical BV/TV and cortical thickness were significantly reduced (~15%) in *Gnas*<sup>+/−</sup> mice with dramatic reduction (> 25%) in stiffness and peak load in *Gnas*<sup>+/−</sup> femurs by 3-pt bending. However, no changes in osteoblast number and mineral apposition rate were detected in *Gnas*<sup>+/−</sup> mice, suggesting that cortical bone defects were not due to mutation effects on osteoblasts.

In contrast, significantly elevated osteoclast numbers (Fig. 1) at the endosteal surface of femurs in 3 and 9 month old *Gnas* mutants were detected by TRAP staining. Flow cytometry showed no differences in the bone marrow osteoclast precursor population (Cd3<sup>−</sup> Cd45R<sup>−</sup> Cd11b<sup>−/low</sup> Cd115<sup>high</sup>) of *Gnas*<sup>+/−</sup> mice. However, differentiation of *Gnas*<sup>+/−</sup> bone marrow macrophages (BMM) formed significantly higher numbers of multi-nucleated TRAP<sup>+</sup> osteoclasts and larger resorption pits, suggesting that cortical bone defects in *Gnas*<sup>+/−</sup> mice are due to enhanced osteoclast differentiation and function.

Significantly lower levels of pCREB and higher levels of Nfatc1 were detected during osteoclast differentiation in *Gnas*<sup>+/−</sup> cells. Treatment of *Gnas*<sup>+/−</sup> BMMs with Forskolin, a cAMP/PKA activator, during osteoclast differentiation elevated pCREB, reduced Nfact1 to levels comparable to WT and importantly reduced TRAP<sup>+</sup> osteoclasts.

Significantly increased mRNA expression of Wnt inhibitors (*Sost* and *Sfrp4*) and a higher percent of *Sost*<sup>+</sup> osteocytes were present in cortical bone from *Gnas*<sup>+/−</sup> mice. Reduced total β-catenin and its target Cyclin D1 in *Gnas*<sup>+/−</sup> cells during osteoclast differentiation were detected by immunoblot suggesting an overall decrease in Wnt/β-catenin signaling in the mutants.

Collectively, our data support that reduced G<sub>α</sub> signaling leads to increased osteoclast numbers and activity *in vivo* and increased differentiation through decreased Wnt/β-catenin and cAMP/pCREB signaling. This study reveals a new role for G<sub>α</sub> signaling in maintaining cortical bone quality by regulating osteoclastogenesis.

## Effects of Hypoxia and TGF- $\beta$ Exposure during Monolayer Expansion on the Survival and Matrix Producing Capacity of Mesenchymal Stem Cells

Sun H. Peck<sup>1,2</sup>, Justin R. Bendigo<sup>1,2</sup>, Sarah E. Gullbrand<sup>1,2</sup>, John W. Tobias<sup>2</sup>, George R. Dodge<sup>1,2</sup>, Robert L. Mauck<sup>1,2</sup>, Neil R. Malhotra<sup>2</sup>, Lachlan J. Smith<sup>1,2</sup>  
<sup>1</sup>Philadelphia VA Medical Center, Philadelphia, PA; <sup>2</sup>University of Pennsylvania, Philadelphia, PA

**Disclosures:** SHP (N), JRB (N), SEG (N), JWT (N), GRD (N), RLM (N), NRM (N), LJS (N)

**Introduction:** Degeneration of the intervertebral discs is implicated as a major cause of lower back pain [1]. There is a need for treatment options that not only alleviate symptoms but also reconstitute native tissue structure and mechanical function within the disc. Over the past several years, application of mesenchymal stem cells (MSCs) for disc regeneration, particularly for the nucleus pulposus (NP), has received considerable attention. Previous studies have shown that MSCs are capable of undergoing differentiation into a NP-like phenotype under certain culture conditions [2-4]; however, a key challenge to successful application of MSCs for NP regeneration is the harsh *in vivo* environment, which is characterized by low nutrition and oxygen tension, both of which may negatively impact the survival and biosynthetic properties of MSCs [5]. The objective of this study was to investigate whether exposing MSCs to hypoxia during monolayer expansion enhances subsequent survival and regenerative potential in the nutrient and oxygen poor NP environment. Furthermore, we investigated whether priming MSCs towards an NP-like phenotype by exposing them to TGF- $\beta$ 3 during monolayer expansion enhances subsequent regenerative potential.

**Methods:** *Cell Isolation and Expansion:* Bone marrow-derived MSCs were isolated from 3 juvenile (<6 months of age) bovine femurs and tibia, pooled, and expanded to confluence through a single initial passage in monolayer in normoxia (21% O<sub>2</sub>) and basal medium (DMEM (4.5 g/L glucose) and 10% FBS). The cells were then passaged and expanded in basal medium in one of four different conditions for 1 week: 1. Normoxia (21% O<sub>2</sub>; standard MSC expansion conditions); 2. Normoxia+TGF- $\beta$ 3 (10 ng/mL); 3. Hypoxia (2% O<sub>2</sub>); 4. Hypoxia+TGF- $\beta$ 3 (10 ng/mL). *Pellet Culture:* After the monolayer expansion protocol described above, cells were passaged and cultured in pellets (250,000 cells/pellet) in a simulated NP-like environment (hypoxia (2% O<sub>2</sub>) and chemically defined media with low glucose (1 g/L DMEM and no growth factors)). After 2 weeks of culture, pellets were harvested and either fixed in formalin and processed for paraffin histology (n=2) or analyzed for biochemical composition (n=5). For histology, sections were stained with Alcian blue (glycosaminoglycans, GAG) or picrosirius red (collagen). For analysis of biochemical composition, DNA, GAG, and collagen contents were quantified using the PicoGreen (Thermo Fisher), dimethylmethylen blue, or hydroxyproline assays respectively. DNA was analyzed per pellet, and GAG and collagen were normalized to DNA. Significant differences ( $p<0.05$ ) between groups were established using 2-way ANOVA with Bonferroni post-hoc tests ( $p<0.05$ ). *Microarray Analysis:* Bovine MSCs were isolated and expanded under the four conditions described above, with cells from 3 different donor animals maintained as distinct biological replicates. Cells were harvested, high quality RNA (RIN>9) was isolated from each sample, and global gene expression was measured using the WTPlus Bovine Gene Chip (Affymetrix GeneChip system). Gene expression data were normalized using Robust Multi-array Average. Significant differences in gene expression were determined using 3-way mixed model ANOVA ( $p<0.05$ ; adjusted for false discovery rate).

**Results:** *Pellet Culture:* DNA content for pellets with MSCs expanded in hypoxia, both with and without TGF- $\beta$ 3, was significantly higher than for those with MSCs expanded in normoxia, both with and without TGF- $\beta$ 3 (Fig 1A). DNA content was lowest for pellets with MSCs expanded in normoxia with TGF- $\beta$ 3 and highest for pellets with MSCs expanded in hypoxia with TGF- $\beta$ 3. There was no significant effect of monolayer expansion condition on pellet GAG content (normalized to DNA, Fig 1B). Collagen content exhibited the opposite trend to DNA and was highest for pellets with MSCs expanded in normoxia with TGF- $\beta$ 3 ( $p<0.05$  vs both normoxia without TGF- $\beta$ 3 and hypoxia with TGF- $\beta$ 3, Fig 1C). Histological results supported these findings (Figs 1D and E), where pellets with MSCs expanded under hypoxia, with and without TGF- $\beta$ 3, were larger than those with MSCs expanded under normoxia, suggesting higher cell numbers. *Microarray Analysis:* Principal component analysis (PCA, Fig 2A) indicated significant effects of MSC donor on the global gene expression in response to each expansion condition. The effects of altering oxygen tension alone (without TGF- $\beta$ 3) during monolayer expansion on MSC gene expression were moderate. MSCs expanded under hypoxia exhibited differential expression of genes implicated in the cell stress response (B4GALT6: galactosyltransferase; LPL: lipoprotein lipase; NGF: nerve growth factor; PK: pyruvate kinase) compared to normoxia expanded MSCs (Fig 2B). Exposure to TGF- $\beta$ 3 during monolayer expansion resulted in the greatest effects on global gene expression, irrespective of oxygen tension. In particular, there were significant effects on expression of genes involved in growth and inflammation, including those of the TGF- $\beta$ , NF $\kappa$ B, and caspase activation pathways (Fig 2C).

**Discussion:** The results of this study suggest that exposure to hypoxia during monolayer expansion leads to improved survival (higher DNA content) when these cells are subsequently cultured in simulated NP-like conditions with limited oxygen and nutrition. Interestingly, exposure to hypoxia during monolayer expansion had no significant impact on the subsequent matrix (GAG or collagen) producing capacity of MSCs in the absence of TGF- $\beta$ 3. In contrast, exposure to TGF- $\beta$ 3 under normoxic conditions during expansion significantly inhibited subsequent MSC survival and boosted collagen production on a per cell basis with no effect on GAG. This may suggest induction of a post-mitotic and pro-fibrotic phenotype, which may be detrimental to the capacity of MSCs to regenerate NP tissue. Microarray results support this view, with TGF- $\beta$ 3 exerting significant effects on signaling pathways that regulate fibrosis and inflammation, which eclipsed any beneficial effects of hypoxia alone. Ongoing work will seek to verify these findings, by determining the type of collagen (I or II) being produced and measuring levels of pro-inflammatory factors in the culture media. Finally, microarray results highlighted the significant effects of donor on the response of MSCs to environmental stimuli, potentially due to variations in age and sex, the impact of which should be considered during future translational studies.

**Significance:** The results of this study demonstrate that alterations in monolayer expansion environment significantly impact the survival and matrix producing capacity of MSCs and provide a foundation for optimizing the regenerative capacity of these cells in the intervertebral disc.

**References:** [1] Mirza+ Spine, 2007. [2] Smith+ Tiss Eng A, 2013. [3] Perglio+ Spine J, 2013. [4] Gupta+ Tiss Eng A, 2011. [5] Farrell+ OAC, 2014.

**Acknowledgements:** Department of Veteran's Affairs, Penn Center for Musculoskeletal Disorders (P30 AR069619)

**Figure 1. Composition of MSC pellets after monolayer expansion in different oxygen and TGF- $\beta$ 3 conditions.** A. DNA content, B. GAG per DNA, and C. Collagen per DNA. D. Alcian blue staining for GAG. E. Picrosirius red staining for collagen. N=5; \* $p<0.05$ ; scale bar = 0.2 mm.

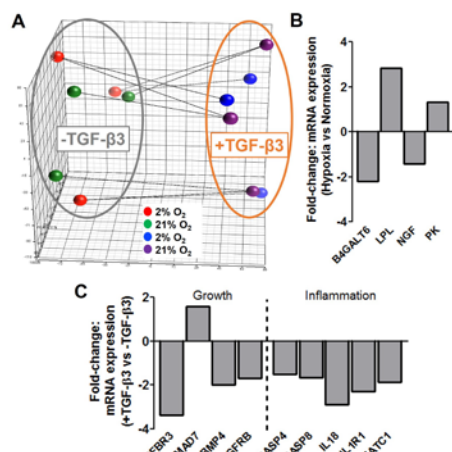
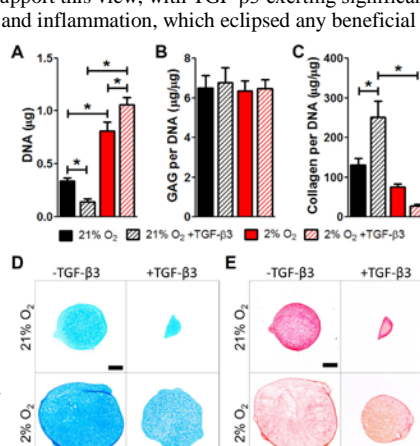


**Figure 2. Microarray results.** A. Principal component analysis (PCA) plot. Lines connect all samples from a single animal. B. Effects of hypoxia on gene expression in the absence of TGF- $\beta$ 3. C. Effects of TGF- $\beta$ 3 on growth and inflammation pathway gene expression. N=3; all  $p<0.05$ .

## **Conditional deletion of PDGFR $\beta$ diminishes osteoblast association with blood vessels and impairs fracture healing**

Robert J. Tower

Blood vessels are absolutely essential for bone formation, but the molecular mechanisms behind this angiogenic-osteogenic coupling remain poorly understood. In vascular biology, platelet-derived growth factor receptor beta (PDGFR $\beta$ ) is vital for the recruitment of pericytes to blood vessels while PDGF-BB, the main ligand of PDGFR $\beta$ , is chemotactic and mitogenic for osteoblastic cells *in vitro*. Here we investigate the role of osteoblast PDGFR $\beta$  in bone development, homeostasis and repair and investigate its potential role in angiogenic-osteogenic coupling. Conditional deletion of PDGFR $\beta$  in osteoblast-lineage cells showed no observable defects under physiological conditions, but showed delayed periosteal cell expansion, impaired callus formation and delayed healing following tibia fracture. Mutant calluses were smaller with a reduced composition of cartilage, bone and marrow and increased fibrotic tissue and adipocytes. *In vitro* studies revealed that osteoblasts are recruited to endothelial tubules and help promote tubule formation and stabilization in part through the PDGF pathway. *In vivo*, conditional deletion of PDGFR $\beta$  led to a decreased association between osteoprogenitors and blood vessels, as well as reductions in the average blood vessel size and their infiltration into the soft callus. These results demonstrate a role for PDGF signaling between blood vessels and osteoblast and suggest a possible pericytic role for osteoblasts in a fracture environment.